Long-Term Degradation of Lithium-ion Batteries

SCOTT G. MARQUIS
St Anne's College
University of Oxford

To my Mum, my Dad, and my Granny Betty...

ABSTRACT

In this thesis, we develop efficient mathematical models of lithium-ion batteries and the key degradation mechanism, Solid–electrolyte interphase (SEI) growth. By doing this, we provide a modular mathematical framework for lithium-ion battery modelling from which an appropriate fidelity model can be selected and extended. Our approach is to develop detailed physics-based models motivated by standard electrochemical modelling approaches and then employ asymptotic methods to systematically simplify these models. An important output of this work is an open-source battery modelling software called PyBaMM (Python Battery Mathematical Modelling) that allows other researchers to easily use and interact with the models we develop.

ACKNOWLEDGMENTS

I would first like to thank my supervisors Colin Please and Jon Chapman for their guidance and support throughout my DPhil. Their encouragement to collaborate with others and explore topics as they took my interest has made my DPhil both exciting and enjoyable. In particular, I am incredibly grateful that they provided me with the opportunity to contribute to the inception and development of an open-source battery modelling software called PyBaMM.

I would like to thank the entire PyBaMM development team, in particular, Valentin Sulzer and Robert Timms for discussions and collaborations that have greatly enriched my DPhil experience. I would also like to thank David Howey and the members of his research group for enthusiastic discussions that have deepened my understanding of lithium-ion batteries and focused me on the practical implications of my work. I am also thankful for everyone in InFoMM Cohort 3 for making my time in Oxford so enjoyable.

Finally, I want to thank my wonderful parents, Sandra and Stuart, for their constant love and support without which I would not have completed my undergraduate studies. I am forever grateful to them for everything they have done for me.

CONTENTS

LIST OF TABLES

LISTINGS

ACRONYMS

cSP   Corrected single-particle

DAE   Differential algebraic equation

DFN   Doyle–Fuller–Newman

DFNCC Doyle–Fuller–Newman with current collectors

ECM   Equivalent circuit model

OCP   Open-circuit potential

OCV   Open-circuit voltage

ODE   Ordinary differential equation

PDE   Partial differential equation

P2D   Pseudo two-dimensional

SEI   Solid–electrolyte interphase

SoC   State-of-charge

SPM   Single-particle model

SPMe   Single-particle model with electrolyte

SPM   Single-particle model with current collectors

SPMeCC Single-particle model with electrolyte and current collectors

INTRODUCTION

1.1 OVERVIEW

With the shift to vehicle electrification and renewable energy sources, lithium-ion batteries are emerging as one of the most important technologies of the 21st century. The first lithium-ion batteries were developed during the 1970s and 1980s by Jon B. Goodenough and collaborators at the University of Oxford [16]. Since then we have witnessed large increases in energy and power density, and huge reductions in the cost of production. These advances have brought electric vehicles to the centre of the plans of car manufacturers and created a boom in lithium-ion battery manufacturing. To further advance these technologies, and properly manage them, there is a clear need to develop our quantitative understanding of lithium-ion batteries.

The term *battery* can be used to refer to individual *cells*, *modules* (a connected set of cells), or *packs* (a connected set of modules). Lithium-ion cells come in three major formats: cylindrical cells (e.g. the 18650 cells used by Tesla), pouch cells, and prismatic cells. Our attention is directed towards individual lithium-ion pouch cells although our modelling approaches can be adapted to the other cell formats.

Lithium-ion pouch cells consist of many repeated electrochemical layers. Each electrochemical layer consists of two electrodes, a porous separator, an electrolyte, and two current collectors, as depicted in Figure 1.1. Each electrode consists of active material particles (shown as
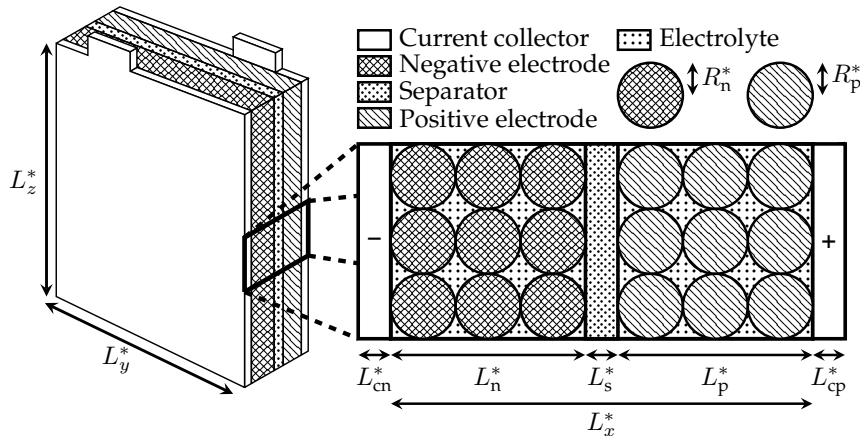
Figure 1.1: Schematic of a single layer of a lithium-ion pouch cell. Active material particles are shaded cross-stitch and diagonally for the negative and positive active materials, respectively.

spheres) within which lithium can be stored, and a binder (not shown) which holds the electrode together and maintains an electrical connection between the active material particles and the current collectors. Additionally, a tab is located at the top of each current collector, to provide an electrical connection to the layer. Typically, the negative and positive tabs of each layer (referred to as *soft tabs*) are connected to a master negative tab and a master positive tab (referred to as *hard tabs*) so that each electrochemical layer is connected in parallel.

Upon discharge, lithium intercalated in the negative electrode particles migrates to the surface of the particles where an electrochemical reaction occurs. This electrochemical reaction produces a lithium ion, which is free to move through the electrolyte and an electron which is free to move through the electrode. The electron travels through the electrode, into the current collector and tab, and through an external circuit. Meanwhile, the lithium ion migrates through the electrolyte towards the positive electrode. At the surface of the positive electrode particles, the lithium ion and electron combine through another electrochemical reaction to form a lithium atom intercalated in the positive electrode particle. To charge the battery, a voltage is applied across the cell and the whole process occurs in reverse.

The picture we have described above is of an idealised lithium-ion cell. In reality, many degradation mechanisms occur within the cell that result in deviations from this idealisation. A few of the major mechanisms are: the growth of the solid–electrolyte–interphase (SEI), which is a side reaction that consumes lithium; lithium plating, another side reaction that consumes lithium; and loss of active material, where particles either crack or become fully detached from the electrode and hence cannot be used to store lithium. Even these main mechanisms are not well understood quantitatively. For an overview of known degradation mechanisms in lithium-ion batteries, see [10]. Each of these degradation mechanisms results in capacity fade and/or power fade of the cell, which render the cell less valuable.

1.2 MOTIVATION

Many important factors influence the design of lithium-ion cells. A few examples are the chemical composition of the electrodes and electrolyte [1], the size distributions of active material particles [39], [76], the thickness of the electrodes, the porosity of the electrodes [96], the format of the cell (cylindrical or pouch), cell dimensions [38], and tab placement [38]. The ideal lithium-ion cell would have a high energy and power density, have limited degradation, and be low cost. However, design trade-offs must be made between these objectives. For example, to increase the power density of a lithium-ion cell, we could increase the surface area of the active material by having smaller particles. Unfortunately, increasing the surface area of the particles has been found to

increase the rate of degradation [24]. Understanding degradation is, therefore, a key challenge in the design of lithium-ion cells.

Degradation is also key in the management of lithium-ion cells (e.g. in vehicle-to-grid applications [62] and grid storage [60], [72]). In [72], significant improvements in system management were demonstrated by employing physics-based mathematical models of a lithium-ion cell instead of simpler alternatives. Thus highlighting the potential benefits of developing better mathematical models of lithium-ion cells and degradation mechanisms.

In this thesis, we divide the task of understanding degradation into two key challenges. These are

1. Develop efficient mathematical models of a lithium-ion cell.

2. Develop an accurate model of the growth of the SEI.

The motivation behind the first challenge is to address the fact the simulating degradation, which occurs over many cycles and very long timescales, is a computationally intensive task. Brute force simulation of a complex model of a full lithium-ion cell is not an efficient option particularly when using parameter estimations routines for unknown parameters in degradation models and incorporating cell models into larger systems (e.g. battery packs with cooling modules). Therefore, having an efficient model of a full lithium-ion cell is a prerequisite for modelling degradation and developing our quantitative understanding.

The second challenge is motivated the lack of accurate and validated mathematical models of the growth of the SEI. We have chosen to focus our attention on the growth of the SEI because it is considered to be one of the most important degradation mechanisms. Addressing this challenge also serves as an example of how to extend battery models to include other degradation mechanisms.

1.3 OUTLINE AND CONTRIBUTIONS

In this section, we provide an outline of this thesis and indicate the novel contributions of our work. For each chapter, we state the associated research papers that we have produced. We also detail our contributions to collaborative papers.

In Chapter 2, we provide a gentle introduction to the core concepts of battery modelling. We then address the first of our two key challenges (develop efficient mathematical models of a lithium-ion cell) in Chapters 3 and 4. The second key challenge (develop an accurate model of the growth of the SEI) is addressed in Chapter 5. Finally, in Chapter 6, we draw our conclusions. All of the models that we develop within this thesis are implemented within the open-source battery modelling software PyBaMM (Python Battery Mathematical Modelling) [86]. We provide an overview of PyBaMM in Appendix A.

The work in Chapter 3 forms the basis of the published research article:

- S. G. Marquis, V. Sulzer, R. Timms, C. P. Please, and S. J. Chapman, "An asymptotic derivation of a single particle model with electrolyte," *Journal of The Electrochemical Society*, vol. 166, no. 15, A3693–A3706, 2019

In this work, we provide the first asymptotic derivation of a model commonly used in the battery modelling community: the single-particle model (SPM). We also extend this model and provide the first asymptotic version of the single-particle model with electrolyte (SPMe). We then identify a common issue with other ad-hoc versions of the SPMe from the literature and demonstrate how this is corrected. Mathematically, the approach taken in this chapter is similar to that adopted in [85] for lead-acid batteries and also [53]. In [53], a non-standard model of a lithium-ion battery that neglected the effects of the active material particles was adopted. However, our analysis of common parameter values suggests that capturing the effects within the particles is critical. Another mathematical contribution in this area is the work in [75]. In [75], a different asymptotic limit is taken to the one we take in Chapter 3 however both give rise to similar reduced models. We also undertook related work on parameter estimation with the SPMe

- A. Aitio, S. G. Marquis, P. Ascencio, and D. Howey, "Bayesian parameter estimation applied to the Li-ion battery single particle model with electrolyte dynamics," *arXiv preprint*, vol. arXiv, p. 2001.09890, 2020, (Accepted to IFAC 2020)

but we do not include this work in this thesis. Here, we contributed a sub-millisecond spectral implementation of the SPMe in MATLAB.

The work in Chapter 4 forms the basis of two submitted research papers

- R. Timms, S. G. Marquis, V. Sulzer, C. P. Please, and S. J. Chapman, "Asymptotic reduction of a lithium-ion pouch cell model," *arXiv preprint*, vol. arXiv, p. 2005.05127, 2020, (Submitted to SIAM)

- S. G. Marquis, R. Timms, V. Sulzer, C. P. Please, and S. J. Chapman, "A suite of reduced-order models of a single-layer lithium-ion pouch cell," *arXiv preprint*, vol. arXiv, p. 2008.03691, 2020, (Submitted to Journal of The Electrochemical Society)

This work was mainly a collaboration I had with R. Timms. Broadly, the division of work was as follows. I was mainly responsible for the mathematical analysis associated with electrical and chemical components of the problem (e.g. the current collectors and internal cell electrochemistry) whilst R. Timms was responsible for the mathematical analysis associated with the thermal aspects of the problem. A large proportion

of work in this chapter is dedicated to developing a modular implementation of the suite of models that were derived from the asymptotic reduction. This was implemented within the PyBaMM, with which V.Sulzer was also involved. I was involved heavily in most of the key aspects of this implementation such as inputting of the model equations, developing discretisation schemes, and interfacing to efficient numerical solvers. The asymptotic analysis conducted in this chapter is similar to that conducted in [84] for lead-acid batteries. However, there are a few key geometric differences between lithium-ion and lead-acid batteries, namely that lead-acid batteries do not have current collectors. As a result, the reduced models are different. The models that we develop as a result of our asymptotic analysis have a '2+1' structure. Such simplifications are sometimes referred to as "potential pair" models and are usually made in an ad-hoc manner (e.g. [25], [38], [40], [42]). We provide the first systematic asymptotic derivation of these models. We also provide the first full numerical comparison of the various combinations of simplifications made in this chapter and Chapter 3.

In Chapter 5, we develop a novel detailed mathematical model of the SEI. We then apply asymptotic methods to this model to develop simplified SEI growth models. This work is the first application of asymptotic methods to the modelling of the SEI. We are also the first to account for the interactions between the SEI growth reaction and the intercalation reaction. We then adopt an experimentally motivated model of a full lithium-ion cell from [82] to allow us to compare our SEI model to experimental data. In [82], SEI models are only compared to experimental data for a single temperature at a single time. In contrast, we are the first to compare our SEI model to the full set of available capacity fade data and demonstrate that our model captures the thermal, temporal, and state-of-charge (SoC) dependence of SEI growth.

As previously mentioned, the models in this thesis have been implemented within the open-source software PyBaMM. We have submitted a software engineering paper on this work

- V. Sulzer, S. G. Marquis, R. Timms, M. Robinson, and S. J. Chapman, "Python Battery Mathematical Modelling (PyBaMM)," *ECSarXiv*, vol. 7, 2020, (Submitted to the Journal of Open Research Software)

Related to this, we have also been involved with the numerical implementation of the work in the paper

- T. G. Tranter, R. Timms, T. Heenan, S. G. Marquis, V. Sulzer, A. Jnawali, M. D. R. Kok, C. P. Please, S. J. Chapman, P. R. Shearing, and D. J. L. Brett, "Probing heterogeneity in li-ion batteries with coupled multiscale models of electrochemistry and thermal transport using tomographic domains," *Journal of The Electrochemical Society*, vol. 167, no. 11, p. 110 538, 2020.

INTRODUCTION TO BATTERY MODELLING

2.1 INTRODUCTION

In this chapter, we provide a gentle introduction to battery modelling. We begin by introducing some commonly used terminology and then define the mathematical notation that we will adopt for the rest of this thesis. We then introduce some key concepts from electrochemistry. Following this, we state the standard model of a lithium-ion battery, the Doyle–Fuller–Newman (DFN) model, and provide a set of parameter values for this model. We then discuss some important properties of the DFN model which we will use in later chapters.

2.2 TERMINOLOGY

This section is intended to serve as a quick reference for some of the most commonly used terminology in the study of batteries. We will also re-write these concepts in mathematical notation as required throughout the thesis.

- *C-rate* — The C-rate is a measure of the current being drawn from a cell. A C-rate of one, denoted 1 C, corresponds the current which fully discharges the battery from the maximum to the minimum voltage in 1 hour. A rate of 2 C is twice that current. The C-rate is dependent upon the particular cell and the choice of maximum and minimum voltages.

- *Open-circuit potential (OCP)* — The OCP is the potential difference at which an individual electrochemical reaction is in equilibrium.

- *Open-circuit voltage (OCV)* — The OCV is the potential difference across a lithium-ion cell for which the current flowing through the cell is zero (i.e. the cell is in equilibrium). The terms OCP and OCV are sometimes used interchangeably within the battery community, but we will reserve the OCP for the equilibrium of individual electrochemical reactions (e.g. on the surfaces of the electrode) and OCV for the equilibrium of the full cell.

- *Overpotential* — The overpotential of an electrochemical reaction is the difference between the actual potential difference and the OCP. Thus the overpotential is a measure of how far from equilibrium an electrochemical reaction is. This type of overpotential is often referred to as the *reaction overpotential*. Overpotentials can also be defined for other electrochemical components. For

example, the potential drops associated with Ohmic losses are considered a type of overpotential.

- *Galvanostatic and potentiostatic* — A galvanostatic problem is one in which the current is held fixed and the potential determined. In contrast, a potentiostatic problem is one in which the potential difference is held fixed and the current determined.

- *State-of-charge (SoC)* — The state of charge of a cell, SoC $\in [0, 1]$, indicates the extent to which a cell is charged. When SoC $= 1$ the cell is fully charged and when SoC $= 0$ the cell is fully discharged. The 'fully charged' and 'fully discharged' states are defined to be where the cell reaches a manufacturer defined maximum and minimum voltage during an infinitely slow charge and discharge. Because of internal cell resistances, a particular measured voltage can correspond to multiple SoCs depending upon the applied current. Although commonly used in the study of batteries, we will generally try to avoid using SoC and instead work with cut-off voltage limits and physical concentrations.

- *Nominal capacity* — The nominal capacity of a cell, measured in A h, is the total amount of charge that can be drawn from a cell when discharging very slowly from SoC $= 1$ to SoC $= 0$. The cell must be discharged slowly to avoid exceeding the voltage limits of the cell as a result of internal resistances. In practice, the nominal capacity of a cell is not accessible due to these internal resistances.

2.3   NOTATION

In this section, we comment on the notational conventions that we adopted throughout this thesis. Firstly, we use a superscript '$*$' to denote dimensional quantities, with dimensionless quantities denoted without this superscript. We denote electric potentials by ϕ, current densities by $\boldsymbol{i}$, lithium concentration by c (in the electrolyte c denotes the lithium-ion concentrations), molar fluxes by $\boldsymbol{N}$, and temperature by T. To distinguish potentials, fluxes and concentrations in the electrolyte from those in the solid phase of the electrode, we use a subscript 'e' for electrolyte variables and a subscript 's' for solid-phase variables. To indicate the region within which each variable is defined, we include an additional subscript 'k', which takes one of the following values: 'n' (negative electrode), 'p' (positive electrode), 'cn' (negative current collector), 'cp' (positive current collector), or 's' (separator). For example, the notation $\phi_{\mathrm{s,n}}^*$ refers to the dimensional electric potential in the solid phase of the negative electrode. When stating the governing equations, we take the region in which an equation holds to be implicitly defined by the subscript of the variables.

As indicated in Figure 1.1, the negative current collector, negative electrode, separator, positive electrode, and positive current collector are of thickness L_{cn}^*, L_n^*, L_s^*, L_p^*, and L_{cp}^*, respectively. We denote the distance between the negative and positive current collectors by $L_x^* = L_n^* + L_s^* + L_p^*$, the width of the cell by L_y^* and the height of the cell by L_z^*. The active material particles in the negative and positive electrodes are assumed to be spheres with radii R_n^* and R_p^*, respectively. The battery models that we employ in this thesis consist of both a macro spatial scale and a micro spatial scale. On the macroscale, we use the spatial coordinates $\boldsymbol{x}^* = (x^*, y^*, z^*) \in [-L_{cn}^*, L_x^* + L_{cp}^*] \times [0, L_y^*] \times [0, L_z^*]$ to indicate the location through the thickness, width, and height of the cell. At each macroscale point a microscale particle problem exists. Since behaviour in the particles is assumed to be spherically symmetric, we use a single microscale spatial coordinate $r^* \in [0, R_k^*]$, $k \in \{n, p\}$, to indicate the location within the active material particles. Time is denoted by t^*. We define

$$\Omega_{cn}^* = [-L_{cn}^*, 0] \times \Omega^*, \qquad \Omega_n^* = [0, L_n^*] \times \Omega^*,$$
$$\Omega_s^* = [L_n^*, L_x^* - L_p^*] \times \Omega^*, \qquad \Omega_p^* = [L_x^* - L_p^*, L_x^*] \times \Omega^*,$$
$$\Omega_{cp}^* = [L_x^*, L_x^* + L_{cp}^*] \times \Omega^*,$$

corresponding to the negative current collector, negative electrode, separator, positive electrode, and positive current collector, respectively, where $\Omega^* = [0, L_y^*] \times [0, L_z^*]$ is the projection of the battery onto the (y^*, z^*)-plane. We use the notation $\partial\Omega_{tab,k}^*$ to refer to the negative and positive tabs ($k \in \{cn, cp\}$), $\partial\Omega_{ext,k}^*$ to refer to the external boundaries of region $k \in \{cn, n, s, p, cp\}$, and $\partial\Omega_{k_1,k_2}^*$ to refer to the interface between regions k_1 and k_2. Finally, for $k \in \{cn, cp\}$ we use $\partial\Omega_{tab,k,\perp}^*$ to denote the projection of the tabs onto the (y^*, z^*)-plane, and $\partial\Omega_{ext,k,\perp}^* = \partial\Omega^* \setminus \partial\Omega_{tab,k,\perp}^*$ to denote the non-tab region of the boundary of the projection. We will denote the dimensionless versions of each of these regions by omitting the superscript '$*$'.

Throughout we shall make use of the following notation to represent averaged quantities

$$\bar{f}_n^* = \frac{1}{L_n^*} \int_0^{L_n^*} f_n^* \mathrm{d}x^*, \qquad \text{(Negative electrode)} \quad (2.1a)$$

$$\bar{f}_s^* = \frac{1}{L_s^*} \int_{L_n^*}^{L_x^* - L_p^*} f_s^* \mathrm{d}x^*, \qquad \text{(Separator)} \quad (2.1b)$$

$$\bar{f}_p^* = \frac{1}{L_p^*} \int_{L_x^* - L_p^*}^{L_x^*} f_p^* \mathrm{d}x^*, \qquad \text{(Positive electrode)} \quad (2.1c)$$

$$\langle f_k^* \rangle = \frac{1}{L_y^* L_z^*} \int_0^{L_z^*} \int_0^{L_y^*} f_k^* \mathrm{d}y^* \mathrm{d}z^*, \qquad \text{(Transverse average)} \quad (2.1d)$$

along with the obvious dimensionless versions (i.e. just remove superscript stars).

2.4   ELECTROCHEMISTRY BASICS

Before introducing the standard model of a lithium-ion battery, we overview the important basics of electrochemical modelling which are employed heavily in battery modelling. Two key electrochemical components are: the electrochemical reactions and the electrolyte. We introduce the standard modelling approaches for each of these components here. More in-depth introductions to these concepts can be found in [55], [64], [70].

2.4.1   *Modelling electrochemical reactions*

Electrochemical reactions are central to battery modelling and are usually modelled using the phenomenological Butler–Volmer equation. To illustrate the assumptions that go into developing the Butler–Volmer equation, we consider an intercalation reaction taking place on a graphite electrode submerged in an electrolyte. The reaction takes the form

$$LiC_6 \rightleftharpoons Li^+ + e^- + C_6, \tag{2.2}$$

where LiC_6 represents lithium carbonate (graphite with lithium intercalated within it), Li^+ represents lithium ions in the electrolyte, e^- represents electrons within the graphite electrode, and C_6 represents unlithiated graphite. In the forward reaction, that is

$$LiC_6 \rightarrow Li^+ + e^- + C_6, \tag{2.3}$$

lithium is transferred into the electrolyte at a rate proportional to the concentration of lithium within the electrode. Additionally, the rate of reaction is also dependent upon the potential difference between the graphite and the electrolyte. The potential dependence is chosen such that a greater applied potential difference ($\phi_s^* - \phi_e^*$), where ϕ_s^* is the potential in the solid and ϕ_e^* is the potential in the electrolyte) results in a higher rate of reaction. We do this because a greater potential difference gives greater incentive for the positively charged lithium ions to travel into the electrolyte of lower electric potential. The reaction is also assumed to have an Arrhenius dependence upon the temperature. Charge in the form of a positively charged lithium ion is transferred during this reaction. By taking a positive current to correspond to ions being transferred from the electrode into the electrolyte, we can write the total current density transferred by the reaction as

$$j_{s,e}^* = F^* k_{s,e}^* c_s^* \exp\left(\frac{\alpha_{s,e} F^*}{R_g^* T^*} \left(\phi_s^* - \hat{\phi}_e^* \right) \right), \tag{2.4}$$

where $k_{s,e}^*$ is the forward reaction rate constant, c_s^* is the concentration of lithium in the graphite, $\alpha_{s,e}$ is the charge transfer coefficient, F^* is Faraday's constant, R_g^* is the gas constant, T^* is temperature, ϕ_s^* is the electric potential in the solid, and $\hat{\phi}_e^*$ is the electric potential in the electrolyte. Similarly, in the backwards reaction given by

$$LiC_6 \leftarrow Li^+ + e^- + C_6, \tag{2.5}$$

lithium is transferred into the graphite at a rate proportional to the concentration of lithium in the electrolyte, c_e^*, and the concentration of empty graphite sites within the electrode, $(c_{s,max}^* - c_s^*)$ where $c_{s,max}^*$ is the maximum concentration of lithium within graphite. The rate is also dependent upon the potential difference across the layer. However, this time a greater potential difference will lead to a smaller rate of reaction because there will be a greater energy barrier to overcome for lithium ions to leave the electrolyte. Again, the temperature dependence is captured by an Arrhenius dependence. The total current density transferred by the reaction is then

$$j_{e,s}^* = -F^* k_{e,s}^* (c_{s,max}^* - c_s^*) c_e^* \exp\left(-\frac{\alpha_{e,s} F^*}{R_g^* T^*}\left(\phi_s^* - \hat{\phi}_e^*\right)\right), \tag{2.6}$$

where $k_{e,s}^*$ is the reaction rate constant and $\alpha_{e,s}$ is the charge transfer coefficient. For a reaction in which a single unit of charge is transferred, such as the one we have here, it can be shown that $\alpha_{s,e} + \alpha_{e,s} = 1$ [64]. Furthermore, it is common to take $\alpha_{s,e} = \alpha_{s,e} = 1/2$, which we will adopt from now on [70]. Given that these forward and backward reactions occur simultaneously, we can write the total interfacial current, $j^* = j_{s,e}^* + j_{e,s}^*$, as

$$
\begin{aligned}
j^* ={}& F^* k_{s,e}^* c_s^* \exp\left(\frac{F^*}{2R_g^* T^*}\left(\phi_s^* - \hat{\phi}_e^*\right)\right) \\
& - F^* k_{e,s}^* (c_{s,max}^* - c_s^*) c_e^* \exp\left(-\frac{F^*}{2R_g^* T^*}\left(\phi_s^* - \hat{\phi}_e^*\right)\right).
\end{aligned}
\tag{2.7}
$$

When the total reaction current is zero, the electrochemical reaction is said to be in equilibrium. The potential difference at which the reaction is in equilibrium is called the *open-circuit potential* (OCP). Setting $j^* = 0$ in (2.7) and denoting the OCP by $\hat{U}^*(c_s^*, c_e^*) = (\phi_s^* - \hat{\phi}_e^*)\big|_{j^*=0}$, we find

$$\hat{U}^*(c_s^*, c_e^*) = \frac{R_g^* T^*}{F^*} \log\left(\frac{k_{e,s}^* (c_{s,max}^* - c_s^*) c_e^*}{k_{s,e}^* c_s^*}\right). \tag{2.8}$$

We now express (2.7) in terms of $\hat{U}^*(c_s^*, c_e^*)$ by using (2.8) to get

$$j^* = j_0^* \sinh\left(\frac{F^*\hat{\eta}^*}{2R_g^*T^*}\right), \tag{2.9a}$$

where

$$j_0^* = m^*(c_s^*)^{1/2}(c_{s,\max}^* - c_s^*)^{1/2}(c_e^*)^{1/2} \tag{2.9b}$$

is the *exchange current density* and

$$\hat{\eta} = \phi_s^* - \hat{\phi}_e^* - \hat{U}^*(c_s^*, c_e^*) \tag{2.9c}$$

is the *reaction overpotential*. Here, we have introduced an effective reaction constant for notational convenience defined as

$$m^* = 2F^*(k_{s,e}^* k_{e,s}^*)^{1/2}. \tag{2.10}$$

Equations (2.9) are the Butler–Volmer equations for the reaction (2.2).

In practice, the functional form for $\hat{U}^*(c_s^*, c_e^*)$ presented in (2.8) is not employed. This is because it does poorly in representing the experimentally observed behaviour of batteries. Instead experimentally measured OCP functions are used. One could choose to measure $\hat{U}^*(c_s^*, c_e^*)$, however, the main drawback to this approach is that $\hat{U}^*(c_s^*, c_e^*)$ is a function of both the electrolyte properties and the electrode properties and would therefore need to be re-tabulated for every combination of electrode and electrolyte chemistry. Instead, we formulate our model in terms of the OCP of graphite relative to a lithium reference electrode. To measure this new OCP, a lithium reference electrode is inserted into the electrolyte, a wire connected to the graphite electrode, and the voltage is varied until the flow of current through the circuit is zero. On the surface of the lithium reference electrode, a reaction occurs of the form

$$\text{Li} \rightleftharpoons \text{Li}^+ + \text{e}^- \tag{2.11}$$

where Li represents lithium in the lithium reference electrode, Li$^+$ represents lithium ions in the electrolyte, and e$^-$ represents electrons in the lithium reference electrode. We define ϕ_e^* to be the potential in the lithium reference electrode when (2.11) is in equilibrium. Therefore, we have

$$\phi_e^* = \hat{\phi}_e^* + \frac{R_g^*T^*}{F^*}\log\left(\frac{k_{e,\text{Li}}^* c_e^*}{k_{\text{Li},e}^*}\right). \tag{2.12}$$

where $k_{\text{Li},e}^*$ is the forward reaction rate associated with (2.11), and $k_{e,\text{Li}}^*$ is the backward reaction rate associated with (2.11). This new potential, ϕ_e^*, is also identified as the electrochemical potential in the electrolyte.

Assuming that the concentration of lithium ions in the electrolyte is the same near both the graphite and the lithium reference electrode, the OCP of the graphite relative to the lithium reference electrode is then given by

$$
\begin{aligned}
U^*(c_s^*) &= \left. (\phi_s^* - \phi_e^*) \right|_{j^*=0}, \\
&= \left. (\phi_s^* - \hat{\phi}_e^*) \right|_{j^*=0} + (\hat{\phi}_e^* - \phi_e^*) \\
&= \hat{U}^*(\hat{c}_s^*, \hat{c}_e^*) + \hat{\phi}_e^* - \phi_e^* \\
&= \frac{R_g^* T^*}{F^*} \log \left(\frac{k_{e,s}^* k_{Li,e}^* (c_{s,max}^* - c_s^*)}{k_{s,e}^* k_{e,Li}^* c_s^*} \right),
\end{aligned}
\tag{2.13}
$$

which is independent of the electrolyte concentration. We can now use (2.13) to re-write (2.9) as

$$
j^* = j_0^* \sinh \left(\frac{F^* \eta^*}{2 R_g^* T^*} \right),
\tag{2.14a}
$$

$$
j_0^* = m^* (c_s^*)^{1/2} (c_{s,max}^* - c_s^*)^{1/2} (c_e^*)^{1/2},
\tag{2.14b}
$$

$$
\eta = \phi_s^* - \phi_e^* - U^*(c_s^*),
\tag{2.14c}
$$

which is the form of the Butler–Volmer equations that is commonly used in battery modelling. An experimentally measured OCP is normally used instead of the analytic form stated in (2.13). This experimentally measured OCP is now independent of the electrolyte and so is significantly easier to tabulate for various electrochemical setups.

2.4.2 *Modelling electrolytes*

An electrolyte is a material that consists of ionic species which can conduct a current through the material. In contrast to electric conductors, in an electrolyte, it is the ionic species that carry the current and not electrons. A typical electrolyte consists of positively charged ionic species (cations), negatively charged ionic species (anions), and neutral solvent species. There can be any number of each species but we restrict ourselves to the case of a *binary electrolyte*, which consists of a single cation and a single anion species in a solvent. This case allows for simplifications to be made during the analysis that result in a simpler final numerical implementation of the model. Additionally, we consider the specific case in which the ions have a charge of ± 1 unit of charge. We provide an introduction to the modelling of infinitely dilute electrolytes, which is the so-called Nernst–Planck theory. The resulting equations are the same as those derived by the more involved Stefan–Maxwell theory of moderately concentrated electrolytes. However, the definitions of grouped parameters such as the effective diffusivity and effective conductivity are different. In practice, the effective diffusivity and effective conductivity are experimentally measured so

these subtleties are not of concern here. For a full comparison of the Nernst–Planck and Stefan–Maxwell theories see [11].

In the case of an infinitely dilute binary electrolyte the concentrations of the two ionic species are assumed to be negligibly small compared to the concentration of the solvent, which forms the majority of the electrolyte. We denote the concentrations of the positively charged ions and negatively charged ions by

$$c_+^*, \ c_-^*,$$

respectively. We also denote the fluxes of the positively charged ions and negatively charged ions by

$$\boldsymbol{N}_+^*, \ \boldsymbol{N}_-^*,$$

respectively. Each species is assumed to be driven down gradients in it's own concentration according to Fick's law. Additionally, each species is also assumed to migrate in the presence of a gradient in the electric potential. Firstly, the rate of migration is assumed to be proportional to the gradient of the electric potential, such that a larger gradient in potential will lead to a greater flux of ions. Secondly, this rate is assumed to be proportional to the concentration of ions, such that a greater flux will be observed when there is a higher concentration of ions. Thirdly, this migration rate is also assumed to be proportional to the *mobility* of ions, which is measured in $\mathrm{m^2\,V^{-1}\,s^{-1}}$ and captures the extent to which the ions will move within a particular solvent in the presence of an electric field. Finally, the rate is assumed to be proportional to the charge of the ion; in our case the charge of each species is $\pm e^*$ where e^* is the value of elementary charge (the magnitude of the charge of a single electron). We neglect the effects of convection within the electrolyte although this is considered in [55]. Therefore the fluxes of the two species are given by

$$\boldsymbol{N}_+^* = -D_+^*(c_+^*)\nabla^* c_+^* - e^*\mu_+^*(c_+^*)c_+^*\nabla^*\hat{\phi}_{\mathrm{e}}^*, \tag{2.15a}$$

$$\boldsymbol{N}_-^* = -D_-^*(c_-^*)\nabla^* c_-^* + e^*\mu_-^*(c_-^*)c_-^*\nabla^*\hat{\phi}_{\mathrm{e}}^*, \tag{2.15b}$$

where $D_+^*(c_+^*)$ and $D_-^*(c_-^*)$ are the positive and negative ion diffusivities, $\mu_+^*(c_+^*)$ and $\mu_-^*(c_-^*)$ are the positive and negative ion mobilities, and $\hat{\phi}_{\mathrm{e}}^*$ is the electric potential in the electrolyte. Here, the sign of the mobility term is chosen such that the positive species moves down gradients in electric potential and the negative species moves up gradients in the electric potential. In battery modelling, it is uncommon to express the electrolyte equations in terms of the elementary unit of charge and the mobilities. Instead, the equations are usually re-written using the Einstein relation

$$D^*(c^*) = \mu^*(c^*)k_{\mathrm{B}}^* T^*, \tag{2.16}$$

where k_B^* is the Boltzmann constant and T^* is temperature, in conjunction with Faraday's constant, F, and the gas constant, R_g^*, which are given by

$$F^* = N_A^* e^*, \quad R_g^* = N_A^* k_B^*,$$ (2.17)

where N_A^* is Avogadro's constant. Equations (2.15) then become

$$\boldsymbol{N}_+^* = -D_+^*(c_+^*)\left(\nabla^* c_+^* + \frac{F^*}{R_g^* T^*} c_+^* \nabla^* \hat{\phi}_e^*\right),$$ (2.18a)

$$\boldsymbol{N}_-^* = -D_-^*(c_-^*)\left(\nabla^* c_-^* - \frac{F^*}{R_g^* T^*} c_-^* \nabla^* \hat{\phi}_e^*\right).$$ (2.18b)

Applying the principle of conservation of mass to each ionic species gives

$$\frac{\partial c_+^*}{\partial t^*} = -\nabla^* \cdot \boldsymbol{N}_+^*,$$ (2.19a)

$$\frac{\partial c_-^*}{\partial t^*} = -\nabla^* \cdot \boldsymbol{N}_-^*.$$ (2.19b)

We thereby have two partial differential equations, (2.18) with (2.19), for three unknowns: c_+^*, c_-^*, and $\hat{\phi}_e^*$. In the absence of an external magnetic field, we obtain an additional equation from Maxwell's equations in the form of Poisson's equation

$$\nabla^* \cdot \left(\epsilon^* \nabla^* \hat{\phi}_e^*\right) = F^* \left(c_-^* - c_+^*\right),$$ (2.20)

where ϵ^* is the permittivity of the electrolyte. Equations (2.18), (2.19), and (2.20) alongside appropriate boundary conditions and initial conditions provide a fully closed system. However, in the modelling of batteries, it is common to simplify this system. To make this simplification, we first nondimensionalise (2.20) by scaling the electric potential with the thermal voltage, the spatial gradients by some typical lengthscale, L_{typ}^*, and the concentrations of ions by some typical concentration, $c_{e,typ}^*$, as

$$\hat{\phi}_e^* = \frac{R_g^* T^*}{F^*} \hat{\phi}_e, \quad \nabla^* = \frac{1}{L_{typ}^*} \nabla,$$ (2.21)

$$c_+^* = c_{e,typ}^* c_+, \quad c_-^* = c_{e,typ}^* c_-.$$ (2.22)

Substituting these scalings into (2.20) gives

$$\lambda \nabla^2 \hat{\phi}_e = c_- - c_+.$$ (2.23)

where

$$\lambda = 2 \left(\frac{\lambda^*}{L_{\mathrm{typ}}^*} \right)^2 \tag{2.24}$$

and

$$\lambda^* = \sqrt{\frac{\epsilon^* R_{\mathrm{g}}^* T^*}{2(F^*)^2 (c_{\mathrm{e,typ}}^*)^2}} \tag{2.25}$$

is the Debye length. For a typical electrolyte used in a lithium-ion battery, we have $\lambda^* \approx 1\,\mathrm{nm}$. The typical thickness of a lithium-ion cell is on the order of $L_{\mathrm{typ}}^* \approx 100\,\mathrm{\mu m}$. Therefore, we have $\lambda \ll 1$. In the bulk electrolyte (away from boundaries) an outer problem for (2.23) can solved to find

$$c_+ = c_- + \mathcal{O}(\lambda). \tag{2.26}$$

Thus in this outer region the concentrations of the two ionic species are approximately equal. In the electrochemical community this condition is referred to as *charge neutrality*.

On a domain near the boundaries of size $\mathcal{O}(\sqrt{\lambda})$, an inner problem must be solved. This inner problem has been studied in detail in [74]. Typically, within this inner region, a very large concentration of one ionic species and low concentration of the other species is observed. In the electrochemical community, this region is referred to as the *double layer* or the *Debye layer*. It is common to neglect a full description of this region and instead assume it is incorporated into the phenomenological Butler–Volmer relations that describe the electrochemical reactions across the boundaries. Sometimes a capacitance effect is introduced to account for charge buildup within the double layer, but we will neglect this since the effect is small.

In the outer charge-neutral region, we define

$$c_{\mathrm{e}}^* := c_+^* = c_-^*.$$

This condition takes the place of (2.20) leaving two equations (2.18) with (2.19) for two unknowns, c_{e}^* and $\hat{\phi}_{\mathrm{e}}^*$. It is common to slightly rearrange these two equations. We first define the current to be

$$\begin{aligned}
\boldsymbol{i}_{\mathrm{e}}^* &= F^*(\boldsymbol{N}_+^* - \boldsymbol{N}_-^*) \\
&= \kappa_{\mathrm{e}}^*(c_{\mathrm{e}}^*) \left(-\nabla^* \hat{\phi}_{\mathrm{e}}^* + (1 - 2t^+(c_{\mathrm{e}}^*)) \frac{R_{\mathrm{g}}^* T^*}{F^*} \nabla^* \log(c_{\mathrm{e}}^*) \right)
\end{aligned} \tag{2.27}$$

where

$$\kappa_e^*(c_e^*) = \frac{(F^*)^2 (D_+^*(c_e^*) + D_-^*(c_e^*))c_e^*}{R_g^* T^*},$$

$$t^+(c_e) = \frac{D_+^*(c_e^*)}{D_+^*(c_e^*) + D_-^*(c_e^*)}.$$

Here $\kappa_e^*(c_e^*)$ is the effective conductivity, and $t^+(c_e^*)$ is the positive transference number. Then subtracting (2.19b) from (2.19a) gives

$$\nabla^* \cdot \boldsymbol{i}_e^* = 0. \tag{2.28}$$

We replace the equation for the conservation of negative ionic species, (2.18b) and (2.19b), with the current conservation equation (2.28) and the current defined in (2.27). For the conservation of the positive ionic species we re-write the positive flux in terms of effective electrolyte parameters as

$$\boldsymbol{N}_e^* := \boldsymbol{N}_+^* = -D_e^*(c_e^*)\nabla^* c_e^* + \frac{t^+(c_e^*)}{F^*}\boldsymbol{i}_e^* \tag{2.29}$$

where

$$D_e^*(c_e^*) = \frac{2D_+^*(c_e^*)D_-^*(c_e^*)}{D_+^*(c_e^*) + D_-^*(c_e^*)},$$

is the effective diffusivity.

Finally, we formulate the electrolyte equations in terms of the electrochemical potential in the electrolyte, ϕ_e^*. This ensures that we employ the same definition of the potential in the electrolyte model that we do in Butler–Volmer equations (2.14) where the OCP is defined relative to a lithium reference electrode. We do this using

$$\nabla^* \hat{\phi}_e^* = \nabla^* \phi_e^* - \frac{R_g^* T^*}{F^*}\nabla^* \log(c_e^*) \tag{2.30}$$

which is a direct consequence of (2.12). Therefore, the Nernst–Planck governing equations for a binary electrolyte are

$$\frac{\partial c_e^*}{\partial t^*} = -\nabla^* \cdot \boldsymbol{N}_e^*, \tag{2.31a}$$

$$\boldsymbol{N}_e^* = -D_e^*(c_e^*)\nabla^* c_e^* + \frac{t^+(c_e^*)}{F^*}\boldsymbol{i}_e^*, \tag{2.31b}$$

$$\nabla^* \cdot \boldsymbol{i}_e^* = 0, \tag{2.31c}$$

$$\boldsymbol{i}_e^* = \kappa_e^*(c_e^*)\left(-\nabla^* \phi_e^* + 2(1 - t^+(c_e^*))\frac{R_g^* T^*}{F^*}\nabla^* \log(c_e^*)\right). \tag{2.31d}$$

There are three important functional parameters in this model: the effective diffusivity $D_e^*(c_e^*)$, the effective conductivity $\kappa_e^*(c_e^*)$, and the positive transference number $t^+(c_e^*)$. These parameters are measured

experimentally and so for our purposes we can ignore their definitions in terms of the diffusivities of the individual ionic species, which differ from those of the Stefan–Maxwell theory. The model equations (2.31) are the same as those derived in Stefan–Maxwell theory (for the specific cases commonly considered in battery modelling) [11]. Henceforth, we shall take $t^+(c_e^*) = t^+$ since the transference number is constant for all of the parameter sets we consider.

2.5   DOYLE–FULLER–NEWMAN (DFN) MODEL

The classical model of a lithium-ion battery was developed by Doyle, Fuller, and Newman (DFN model) [21], [55]. The model captures the electrochemical behaviour in the through-cell direction (x^*-direction) and neglects any current collector and thermal effects. As a result, the model is independent of both y^* and z^*. The model naturally decomposes into a set of 'submodels', with one for each component of the cell. Here we introduce each component and the corresponding modelling equations.

2.5.1   *Electrodes*

The electrodes in a lithium-ion cell are electrically conducting porous materials which consist of active material, where lithium can intercalate, and an electrically conducting binder material. The pores of the electrode are flooded with an electrolyte. Within the framework of the DFN model, the active material is treated as spherical particles, with diffusion being the transport mechanism for lithium transport within the solid [21]. The behaviour within the particle is assumed to be spherically symmetric. The timescale associated with diffusion within the active material is long compared with the timescale associated with the transport of electrons, and the model, therefore, requires two components which describe processes occurring over disparate length scales: a macroscale description of charge conservation (electron transport), and a microscale description of mass conservation (lithium transport) [21].

2.5.1.1   *Charge conservation in the electrodes*

The current in the electrodes is described by Ohm's law. To account for the transfer of current between the electrode and electrolyte (which occurs via electrochemical reactions), an additional current source/sink

term is included. The governing equations for current in the electrode are therefore

$$\frac{\partial i_{s,k}^*}{\partial x^*} = -a_k^* j_k^*, \qquad\qquad k \in \{n, p\}, \qquad\qquad (2.32a)$$

$$i_{s,k}^* = -\sigma_{s,k}^* \frac{\partial \phi_k^*}{\partial x^*}, \qquad\qquad k \in \{n, p\}, \qquad\qquad (2.32b)$$

where a_k^* is the surface area per unit volume of the electrode, and j_k^* is the interfacial current density. On the boundary between the negative current collector and the negative electrode, we set the potential to a reference value. We also consider the cell under galvanostatic conditions. Therefore, we have the following boundary conditions at either end of the cell

$$\phi_{s,n}^* = 0, \qquad\qquad x^* \in \partial\Omega_{n,cn}^*, \qquad\qquad (2.32c)$$

$$i_{s,p}^* = \mathcal{I}^*, \qquad\qquad x^* \in \partial\Omega_{p,cp}^*, \qquad\qquad (2.32d)$$

where $\mathcal{I}^*$ is the applied current density. Finally, the separator is taken to be electrically insulating so that no charge is transferred from the electrodes to the separator (charge can be transferred through the separator region but only by ion transport in the electrolyte which floods the pores of the separator). Therefore, on the electrode–separator boundary, we have

$$i_{s,k}^* = 0, \qquad x^* \in \partial\Omega_{k,s}^*, \qquad\qquad k \in \{n, p\}. \qquad (2.32e)$$

2.5.1.2 *Mass conservation in the active material*

As in [21], we treat the active material on the microscale as spherical particles of uniform radius, in which spherically symmetric diffusion of lithium is described by Fick's law

$$\frac{\partial c_{s,k}^*}{\partial t^*} = -\frac{1}{(r^*)^2} \frac{\partial}{\partial r^*} \left((r^*)^2 N_{s,k}^* \right), \qquad k \in \{n, p\}, \qquad (2.33a)$$

$$N_{s,k}^* = -D_{s,k}^*(c_{s,k}^*) \frac{\partial c_{s,k}^*}{\partial r^*}, \qquad k \in \{n, p\}, \qquad (2.33b)$$

where $c_{s,k}^*$ is the concentration of lithium in the active material, $N_{s,k}^*$ is the flux of lithium ions in the active material, $D_{s,k}^*(c_{s,k}^*)$ is the diffusivity of lithium in the active material, r^* is the radial spatial coordinate, and t^* is time. We assume that the particle is entirely surrounded by electrolyte and that lithium transfer with the electrolyte occurs uniformly across each particle's outer surface, giving

$$N_{s,k}^*\big|_{r^*=0} = 0, \quad N_{s.k}^*\big|_{r^*=R_k^*} = \frac{j_k^*}{F^*}. \quad k \in \{n, p\}, \qquad (2.33c)$$

where F^* is Faraday's constant. Further, we assume that the concentration within the particles in each electrode is initially uniform in space

$$c_{s,k}^*\big|_{t^*=0} = c_{s,k,0}^*, \quad k \in \{n, p\},\tag{2.33d}$$

where $c_{s,k,0}^*$ is a constant. It should be noted that this microscale model for the active material holds at every point $x^* \in \Omega_k^*$ for $k \in \{n, p\}$ of the macroscale model. In this sense, the radial direction r^* can be viewed as a 'pseudodimension'. It is this that gives the DFN it's alternative name, the pseudo-two-dimensional (P2D) model. This also means that $c_{s,k}^*$ is in general a function of r^*, x^*, and t^*.

2.5.2 *Electrolyte*

We model the electrolyte using a homogenised version of the electrolyte equations we introduced earlier (2.31). The derivation of these homogenised electrolyte equations via the method of multiple scales can be found in [73]. In performing the homogenisation, there are three main modifications to (2.31). The first modification is to account for the electrolyte volume fraction in the transfer of mass. The second modification is that diffusivities and conductivities are converted to their homogenised counterparts which account for the tortuosity of the porous structure. We shall take the tortuosity to be given through the Bruggeman relation, ϵ_k^b, where ϵ_k is the electrolyte volume fraction in the region k, and b is the Bruggeman coefficient [58]. The third main modification is the addition of a source term which accounts for the transfer of lithium between the macroscale electrolyte and the active material particles at every macroscale point.

2.5.2.1 *Charge conservation in the electrolyte*

As a result of these considerations, the governing equations for the current in the electrolyte are

$$\frac{\partial i_{e,k}^*}{\partial x^*} = a_k^* j_k^*, \qquad k \in \{n, p\},\tag{2.34a}$$

$$\frac{\partial i_{e,s}^*}{\partial x^*} = 0,\tag{2.34b}$$

$$i_{e,k}^* = \epsilon_k^b \kappa_e^*(c_{e,k}^*)\left(-\frac{\partial \phi_{e,k}^*}{\partial x^*}\right.$$
$$\left.+2(1 - t^+)\frac{R_g^* T_\infty^*}{F^*}\frac{\partial}{\partial x^*}\left(\log(c_{e,k}^*)\right)\right), \ k \in \{n, s, p\},\tag{2.34c}$$

where $i_{e,k}^*$ is the current in the electrolyte, $c_{e,k}^*$ is the lithium-ion concentration, $\kappa_e^*(c_{e,k}^*)$ is the effective electrolyte conductivity, $\phi_{e,k}^*$ is the electrochemical potential in the electrolyte, t^+ is the transference num-

ber, R_g^* is the gas constant, and T_∞^* is the temperature. No charge is transferred directly from the electrolyte into the current collectors, so that

$$i_{e,k}^* = 0, \qquad x^* \in \partial\Omega_{ck,k}^*, \qquad k \in \{n, p\}, \qquad (2.34d)$$

Finally, on the electrode–separator boundaries the electrical potential and current in the electrolyte must be continuous

$$\phi_{e,k}^* = \phi_{e,s}^*, \qquad x^* \in \partial\Omega_{k,s}^*, \qquad k \in \{n, p\}, \qquad (2.34e)$$

$$i_{e,k}^* = i_{e,s}^*, \qquad x^* \in \partial\Omega_{k,s}^*, \qquad k \in \{n, p\}. \qquad (2.34f)$$

Note that the electrochemical potential in the electrolyte appears to only be determined up to a constant. However, this constant will be determined through the electrochemical reactions.

2.5.2.2 *Mass conservation in the electrolyte*

The concentration of lithium ions in the electrolyte is determined by solving an effective diffusion equation with an additional source term describing lithium transfer to the active material

$$\epsilon_k \frac{\partial c_{e,k}^*}{\partial t^*} = -\frac{\partial N_{e,k}^*}{\partial x^*} + \frac{1}{F^*}\frac{\partial i_{e,k}^*}{\partial x^*}, \qquad k \in \{n, s, p\}, \quad (2.35a)$$

$$N_{e,k}^* = -\epsilon_k^b D_e^*(c_{e,k}^*)\nabla^* c_{e,k}^* + \frac{t^+}{F^*} i_{e,k}^*, \qquad k \in \{n, s, p\} \quad (2.35b)$$

where we have used (2.34a) and (2.34b) to give a concise description of the flux of lithium ions across the interface between the electrolyte and solid particle. Here, $N_{e,k}^*$ is the lithium-ion flux in the electrolyte and $D_e^*(c_{e,k}^*)$ is the effective diffusivity of the electrolyte. There is no flux of lithium ions from the electrolyte into the current collectors and so we have

$$N_{e,k}^* = 0, \qquad x^* \in \partial\Omega_{ck,k}^*, \qquad k \in \{n, p\}. \qquad (2.35c)$$

We also require that the concentration and flux of lithium ions be continuous across the electrode/separator boundaries

$$c_{e,k}^* = c_{e,s}^* \qquad x^* \in \partial\Omega_{k,s}^*, \qquad k \in \{n, p\}, \qquad (2.35d)$$

$$N_{e,k}^* = N_{e,s}^*, \qquad x^* \in \partial\Omega_{k,s}^*, \qquad k \in \{n, p\}, \qquad (2.35e)$$

and assume that the concentration of lithium ions in the electrolyte is initially uniform in space

$$c_{e,k}^*\big|_{t^*=0} = c_{e,0}^*, \quad k \in \{n, s, p\}, \qquad (2.35f)$$

where $c_{e,0}^*$ is a constant.

2.5.3   *Electrochemical reactions*

On the surface of the active material particles, electrochemical reactions occur that transfer lithium ions between the active material and the electrolyte. In the negative electrode region, we have the intercalation reaction
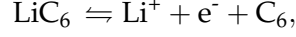
$$LiC_6 \rightleftharpoons Li^+ + e^- + C_6,$$

where LiC_6 represents lithium carbonate (graphite with lithium intercalated within it), Li^+ represents lithium ions in the electrolyte, e^- represents electrons within the graphite electrode, and C_6 represents unlithiated graphite. In the positive electrode region we have

$$LiX \rightleftharpoons Li^+ + e^- + X,$$
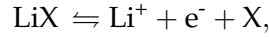
where LiX represents lithium within some transition metal (e.g. nickel/-manganese), Li^+ represents lithium ions in the electrolyte, e^- represents electrons within the positive electrode, and X represents unlithiated postive electrode active material. We model both of these electrochemical reactions using the symmetric Butler–Volmer kinetics introduced in §2.4.1. The reaction flux density, j_k^*, is then given by

$$j_k^* = j_{0,k}^* \sinh\left(\frac{F^*\eta_k^*}{2R_g^* T_\infty^*}\right)\bigg|_{r^*=R_k^*}, \quad k \in \{n, p\}, \tag{2.36a}$$

$$j_{0,k}^* = m_k^*(c_{s,k}^*)^{1/2}(c_{s,k,max}^* - c_{s,k}^*)^{1/2}(c_{e,k}^*)^{1/2}\big|_{r^*=R_k^*} \tag{2.36b}$$
$$k \in \{n, p\},$$

$$\eta_k^* = \phi_{s,k}^* - \phi_{e,k}^* - U_k^*(c_{s,k}^*)\big|_{r^*=R_k^*}, \quad k \in \{n, p\}, \tag{2.36c}$$

where j_{0k}^* is the exchange current density, η_k^* is the surface reaction overpotential, $U_k^*(c_{s,k}^*)$ is the OCP relative to a lithium reference electrode of electrode k, and m_k^* is the effective reaction rate constant.

2.5.4   *Reformulation of the DFN model*

It is useful to reformulate the DFN model (2.32)-(2.36). This reformulation will be helpful for our asymptotic analysis in later section. The main idea is to take advantage of current conservation to re-write boundary conditions on the electrode–separator boundaries. By summing (2.32a) and (2.34a), we obtain

$$\frac{\partial}{\partial x^*}\left(i_{s,k}^* + i_{e,k}^*\right) = 0, \qquad k \in \{n, p\}. \tag{2.37}$$

Integrating this with respect to x^* and applying (2.32d) and (2.34d) for the case k=p, we get

$$i_{s,p}^* + i_{e,p}^* = \mathcal{I}^*. \tag{2.38}$$

Then using (2.32e), (2.34b), and (2.34f), we have that

$$i_{e,s}^* = \mathcal{I}^*. \tag{2.39}$$

Finally, integrating (2.37) for the case k=n, and applying (2.32e) and (2.34f) gives

$$i_{s,n}^* + i_{e,n}^* = \mathcal{I}^*. \tag{2.40}$$

Therefore, using (2.38) and (2.40), we can replace (2.32) with

$$\mathcal{I}^* - i_{e,k}^* = \sigma_{s,k}^* \frac{\partial \phi_{s,k}^*}{\partial x^*}, \qquad k \in \{n, p\}, \tag{2.41a}$$

$$\phi_{s,n}^* = 0, \qquad x^* \in \partial\Omega_{n,cn}^* \tag{2.41b}$$

where we note that the constant of integration for $\phi_{s,p}^*$ is determined by the electrochemical reactions (2.36). Similarly, we can also replace (2.34) with

$$\frac{\partial i_{e,k}^*}{\partial x^*} = a_k^* j_k^*, \qquad k \in \{n, p\}, \tag{2.42a}$$

$$i_{e,s}^* = \mathcal{I}^*, \tag{2.42b}$$

$$i_{e,k}^* = \epsilon_k^b \kappa_e^*(c_{e,k}^*) \left(-\frac{\partial \phi_{e,k}^*}{\partial x^*} \right.$$
$$\left. + 2(1 - t^+) \frac{R^* T_\infty^*}{F^*} \frac{\partial}{\partial x^*} \left(\log(c_{e,k}^*) \right) \right), \quad k \in \{n, s, p\}, \tag{2.42c}$$

$$i_{e,k}^* = 0, \qquad x^* \in \partial\Omega_{ck,k}^*, \qquad k \in \{n, p\}, \tag{2.42d}$$

$$i_{e,k}^* = \mathcal{I}^*, \qquad x^* \in \partial\Omega_{s,k}^*, \qquad k \in \{n, p\}, \tag{2.42e}$$

The reformulated DFN then comprises of (2.33), (2.35), (2.36), (2.41), and (2.42).

2.6   PARAMETER VALUES

For reference, all of the parameters in the DFN are defined in Tables 2.1 and 2.2, along with typical values for a copper negative current collector, graphite negative electrode, LiPF$_6$ in EC:DMC electrolyte, lithium cobalt oxide positive electrode, and aluminium positive current collector, adapted from [51], [52], [54]. In addition to the parameter values in Tables 2.1 and 2.2, the model also requires functional forms to be provided for $U_n^*(c_{s,n}^*)$, $U_p^*(c_{s,n}^*)$, $D_e^*(c_e^*)$, and $\kappa_e^*(c_e^*)$. We present the forms that we employ in Figure 2.1.

Parameter	Units	Description	Value
F^*	$C\,mol^{-1}$	Faraday's constant	96487
R_g^*	$J\,mol^{-1}\,K^{-1}$	Universal gas constant	8.314
T_∞^*	K	Reference temperature	298.15
b	-	Bruggeman coefficient	1.5
t^+	-	Transference number	0.4
L_x^*	µm	Cell thickness	225
L_y^*	mm	Cell width	207
L_z^*	mm	Cell height	137
I^*	$A\,m^{-2}$	Typical current density	24

Table 2.1: Typical dimensional parameter values taken from [51]. The parameters are for a carbon negative current collector, graphite negative electrode, LiPF$_6$ in EC:DMC electrolyte, LCO positive electrode, and aluminium positive current collector. (Part 1).

Parameter	Units	Description	cn	n	s	p	cp
L_k^*	μm	Region thickness	25	100	25	100	25
$c_{e,typ}^*$	$\mathrm{mol\,m^{-3}}$	Typical lithium concentration in electrolyte	-	1×10^3	1×10^3	1×10^3	-
$D_{e,typ}^*$	$\mathrm{m^2\,s^{-1}}$	Typical electrolyte diffusivity	-	5.34×10^{-10}	5.34×10^{-10}	5.34×10^{-10}	-
ϵ_k	-	Electrolyte volume fraction	-	0.3	1	0.3	-
$c_{s,k,max}^*$	$\mathrm{mol\,m^{-3}}$	Maximum lithium concentration in solid	-	2.498×10^4	-	5.122×10^4	-
σ_k^*	$\mathrm{\Omega^{-1}\,m^{-1}}$	Solid conductivity	5.96×10^7	100	-	10	3.55×10^7
$D_{s,k}^*$	$\mathrm{m^2\,s^{-1}}$	Solid diffusivity	-	3.9×10^{-14}	-	1×10^{-13}	-
R_k^*	μm	Particle radius	-	10	-	10	-
a_k^*	$\mathrm{\mu m^{-1}}$	Electrode surface area per unit volume	-	0.18	-	0.15	-
m_k^*	$\mathrm{A\,m^{-2}\,(m^3\,mol^{-1})^{1.5}}$	Reaction rate	-	2×10^{-5}	-	6×10^{-7}	-
$c_{k,0}^*$	$\mathrm{mol\,m^{-3}}$	Initial lithium concentration in solid	-	1.999×10^4	-	3.073×10^4	-

Table 2.2: Typical dimensional parameter values taken from [51]. The parameters are for a carbon negative current collector, graphite negative electrode, LiPF$_6$ in EC:DMC electrolyte, LCO positive electrode, and aluminium positive current collector. (Part 2).
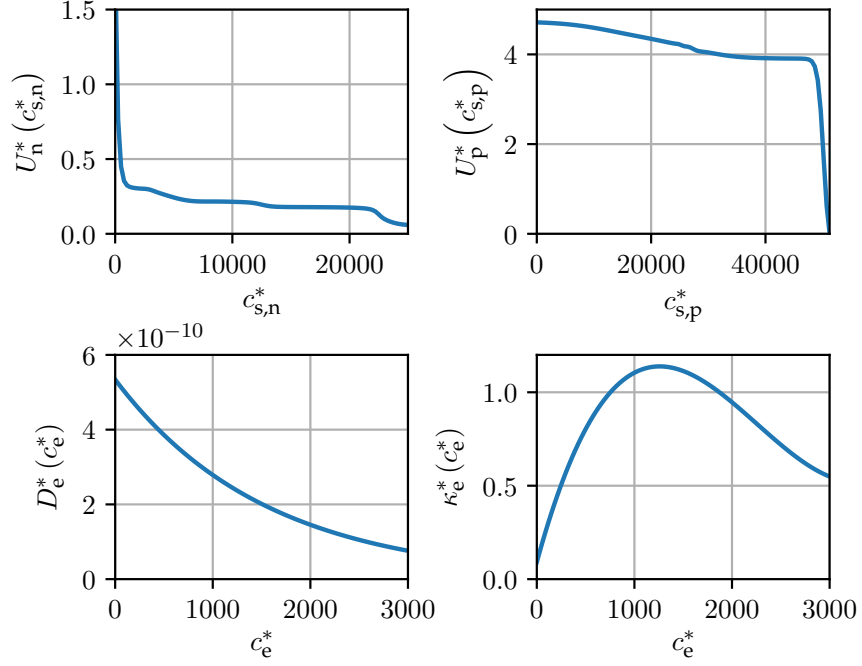
Figure 2.1: Experimentally measured functional forms of $U_n^*(c_{s,n}^*)$, $U_p^*(c_{s,n}^*)$, $D_e^*(c_e^*)$, and $\kappa_e^*(c_e^*)$, taken from [51].

2.7 COMMENTS ON THE DFN MODEL

In this section, we discuss variations of the DFN model and some helpful properties that aid intuition and understanding. These properties will also be useful for our asymptotic analysis later.

2.7.1 *Galvanostatic, potentiostatic, and power control*

The DFN model in galvanostatic form is given by (2.32)-(2.36). For the galvanostatic problem a current is applied and the voltage is to be determined. We formulated our model in terms of the through-cell current density, $\mathcal{I}^*$, but since the model neglects the effects of the current collectors, this is easily related to the applied current, I_{app}^* (measured in A), through

$$\mathcal{I}^* = \frac{I_{app}^*}{L_y^* L_z^*}. \tag{2.43}$$

The voltage across the layer is simply obtained from

$$\mathcal{V}^* = \phi_{s,p}^*\big|_{\partial\Omega_{p,\,cp}^*} - \phi_{s,n}^*\big|_{\partial\Omega_{n,\,cn}^*}, \tag{2.44}$$

and since resistances in the current collectors are neglected, the terminal voltage (as measure by connecting a voltmeter to the negative and positive tabs) is simply given by

$$V^* = \mathcal{V}^*. \tag{2.45}$$

The model can be re-written in potentiostatic form, where V^* (and in turn $\mathcal{V}^*$) is prescribed, by replacing (2.32d) by

$$\phi_{s,p}^* = \mathcal{V}^*, \quad x^* \in \partial\Omega_{p,cp}^*. \tag{2.46}$$

The through-cell current density then is obtained from

$$\mathcal{I}^* = i_{s,p}^* \big|_{\partial\Omega_{p,cp}^*}$$

Alternatively, a power controlled version of the model can be implemented using either (2.32d) or (2.46) and determining I_{app}^* and V^* (and in turn $\mathcal{I}^*$ and $\mathcal{V}^*$) from the additional constraint

$$I_{app}^* V^* = P^*, \tag{2.47}$$

where P^* is the prescribed power.

2.7.2 *Components of the voltage*

We can obtain the voltage of the cell, $\mathcal{V}^*$, directly from (2.44). However, one can obtain a better understanding of the electrochemical behaviour of the cell by breaking the voltage into individual contributing components; this is also helpful for understanding our asymptotic results later. To do this, we consider a particular path that a unit of charge follows through the cell. Charge enters the cell through the boundary $\partial\Omega_{n,cn}^*$ and is carried through the solid phase of the negative electrode by electrons to some point $x_n^* \in \Omega_n^*$. At this point, an electrochemical reaction occurs so that the charge is transferred into the electrolyte. It is then carried through the electrolyte by ionic species until it reaches a point $x_p^* \in \Omega_p^*$ where another electrochemical reaction occurs transferring it into the solid phase of the positive electrode. Finally, the charge is again carried by electrons through the positive electrode until it reaches the positive current collector. The voltage can be written in terms of the potential drops associated with each section of this path as

$$
\begin{aligned}
\mathcal{V}^* = \; & \phi_{s,p}^* \big|_{\partial\Omega_{p,cp}^*} - \phi_{s,p}^* \big|_{x^*=x_p^*} && \text{(Positive electrode)} \\
& + \phi_{s,p}^* \big|_{x^*=x_p^*} - \phi_{e,p}^* \big|_{x^*=x_p^*} && \text{(Positive reaction)} \\
& + \phi_{e,p}^* \big|_{x=x_p^*} - \phi_{e,n}^* \big|_{x=x_n^*} && \text{(Electrolyte)} && \text{(2.48)} \\
& + \phi_{e,n}^* \big|_{x^*=x_n^*} - \phi_{s,n}^* \big|_{x^*=x_n^*} && \text{(Negative reaction)} \\
& + \phi_{s,n}^* \big|_{x^*=x_n^*} - \phi_{s,n}^* \big|_{\partial\Omega_{n,cn}^*} && \text{(Negative electrode)}.
\end{aligned}
$$

We define the open-circuit voltage (OCV) to be

$$U_{eq}^* = U_p^*(c_{s,p}^*)\big|_{r^*=R_p^*,\, x^*=x_p^*} - U_n^*(c_{s,n}^*)\big|_{r^*=R_n^*,\, x^*=x_n^*},$$

the solid-phase Ohmic losses to be

$$\Delta\Phi_{Solid}^* = \left(\phi_{s,p}\big|_{x=1} - \phi_{s,p}\big|_{x=x_p}\right) + \left(\phi_{s,n}\big|_{x=x_n} - \phi_{s,n}\big|_{x=0}\right),$$

and using the definition of the reaction overpotential given in (2.36c), we define the total reaction overpotential to be

$$\eta_r^* = \eta_p^*\big|_{x^*=x_p^*} - \eta_n^*\big|_{x^*=x_n^*}.$$

Additionally, by integrating (2.34c) from x_n^* to x_p^*, we split the potential drop in the electrolyte into two components

$$\phi_{e,p}^*\big|_{x^*=x_p^*} - \phi_{e,n}\big|_{x^*=x_n^*} = \eta_c^* + \Delta\Phi_{Elec}^*,$$

where η_c^* is the concentration overpotential given by

$$\eta_c^* = 2(1+t^+)\frac{R^*T_\infty^*}{F^*}\log\left(\frac{c_{e,p}^*\big|_{x^*=x_p^*}}{c_{e,n}^*\big|_{x^*=x_n^*}}\right),$$

and $\Delta\Phi_{Elec}^*$ is the electrolyte Ohmic losses given by

$$\Delta\Phi_{Elec}^* = -\int_{x_n^*}^{x_p^*}\frac{i_{e,k}^*}{\epsilon_k^b\kappa_e^*(c_{e,k}^*)}\mathrm{d}x^*$$

With these definitions (2.48) becomes

$$\mathcal{V}^* = U_{eq}^* + \eta_r^* + \eta_c^* + \Delta\Phi_{Elec}^* + \Delta\Phi_{Solid}^*. \tag{2.49}$$

Because the values of each of the components of the voltage are dependent upon the choice of path (e.g. choosing reaction points close to the current collectors leads to lower solid-phase Ohmic losses and higher electrolyte Ohmic losses than choosing reaction points next to the separator), we average (2.49) over all possible paths, leading to

$$\mathcal{V}^* = \bar{U}_{eq}^* + \bar{\eta}_r^* + \bar{\eta}_c^* + \overline{\Delta\Phi}_{Elec}^* + \overline{\Delta\Phi}_{Solid}^*. \tag{2.50}$$

where it is understood that the bar notation in this context indicates averages over the electrodes as

$$\bar{U}_{eq}^* = \bar{U}_p^*(c_{s,p}^*)\big|_{r^*=R_p^*} - \bar{U}_n^*(c_{s,n}^*)\big|_{r^*=R_n^*},$$

etc. Adopting (2.50) is useful for understanding the contribution of each term to the voltage. It is also useful for comparing the reduced-order models that we derive later.

(a)

(b)
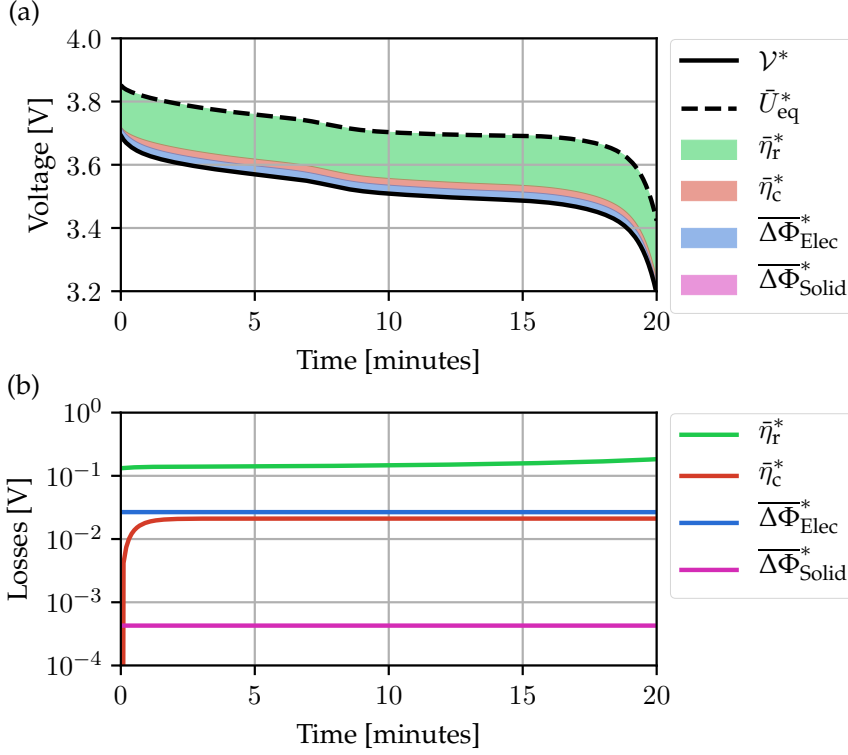
Figure 2.2: Components of the voltage: (a) sum of the OCV and loss terms; (b) absolute values of the loss terms. These results were generated using the DFN model with the parameter set in Tables 2.1 and 2.2.

In Figure 2.2, we have plotted the contribution from each component of (2.50) for a twenty-minute, constant-current discharge. The first term, $\bar{U}_{\mathrm{eq}}^*$, is the OCV and is the voltage that would be observed during an infinitely slow discharge. In Figure 2.2 (a), we can see that most of the distinctive shape of the voltage curve is a direct result of the OCV. It follows that good experimental measurements of the OCPs of each electrode are essential for accurate reproduction of the voltage. Additionally, capturing the evolution of the concentration on the surface of the active material particles (of which the OCPs are a strong function) is also very important. The other terms in (2.50) each correspond to a different internal cell resistances, which cause voltage losses. The most important of these is the reaction overpotential, $\bar{\eta}_{\mathrm{r}}^*$, which is associated with the voltage losses due to electrochemical reactions. This is followed in importance by the two sources of losses in the electrolyte: the concentration overpotential, $\bar{\eta}_{\mathrm{c}}^*$; and the electrolyte Ohmic losses, $\overline{\Delta\Phi}_{\mathrm{Elec}}^*$. In Figure 2.2 (b), we can see the distinction between these two terms. The concentration overpotential, is a strong function of electrolyte concentration and thus a transient response is observed on the electrolyte diffusion timescale. The electrolyte Ohmic losses, on the other hand, are instantaneous (there is only a small dependency upon the electrolyte concentration through the electrolyte

conductivity). Distinguishing these two losses can help estimate parameter values. The least important term is the solid-phase Ohmic losses, which is orders of magnitude lower than the other components for this particular parameter set.

From Figure 2.2, we can hypothesise that a good reduced-order model of the DFN would focus on accurately capturing the OCV and the reaction overpotential, and hence the evolution of the concentration on the surface of the active material particles. A correction to this model would then involve incorporating the electrolyte effects. In later chapters, we perform asymptotic analysis to derive such reduced-order models that confirm this.

2.7.3 *Conservation of lithium*

In our asymptotic analysis in later chapters, we make use of lithium conservation properties. We show here that the total amount of lithium in the active material particles is conserved. We also show that the total amount of lithium in the electrolyte is conserved. By integrating (2.42a) over electrodes n and p separately and applying the boundary conditions (2.42d) and (2.42e), it can be shown that

$$\int_0^{L_n^*} j_n^* \mathrm{d}x^* = \frac{\mathcal{I}^*}{a_n^*}, \quad \int_{L_x^* - L_p^*}^{L_x^*} j_p^* \mathrm{d}x^* = -\frac{\mathcal{I}^*}{a_p^*}. \tag{2.51}$$

To obtain an evolution equation for the total lithium contained within a single active material particle, we integrate (2.33a) over a single active material particle and apply (2.33c) to get

$$\frac{\partial}{\partial t^*}\left(4\pi \int_0^{R_k^*} (r^*)^2 c_{s,k}^* \mathrm{d}r^*\right) = -4\pi (R_k^*)^2 \frac{j_k^*}{F^*}, \tag{2.52}$$

where the factor of 4π has arisen from integration over the sphere. We identify the term contained within the brackets as the total lithium content in a single active material particle. To derive an evolution equation for the total lithium content in an entire electrode, we must integrate (2.52) over the electrode whilst accounting for the density of particles. A consistent way to obtain the particle density is divide the surface area density, a_k^*, by the total surface area of a single particle, $4\pi (R_k^*)^2$. Thus integrating (2.52) over each electrode and applying (2.51), we have

$$\frac{\partial}{\partial t^*}\left(\frac{a_n^* L_y^* L_z^*}{(R_n^*)^2} \int_0^{L_n^*} \int_0^{R_n^*} (r^*)^2 c_{s,n}^* \mathrm{d}r^* \mathrm{d}x^*\right) = -\frac{L_y^* L_z^* \mathcal{I}^*}{F^*} \tag{2.53a}$$

$$\frac{\partial}{\partial t^*}\left(\frac{a_p^* L_y^* L_z^*}{(R_p^*)^2} \int_{L_x^* - L_p^*}^{L_x^*} \int_0^{R_p^*} (r^*)^2 c_{s,p}^* \mathrm{d}r^* \mathrm{d}x^*\right) = \frac{L_y^* L_z^* \mathcal{I}^*}{F^*}, \tag{2.53b}$$

where we identify the terms contained within the brackets as the total lithium content in the active material of the negative electrode and the total lithium content in the active material of the positive electrode, respectively. Note that L_y^* and L_z^* terms are a result of integration over the y^* and z^* directions. It is then clear from summing (2.53a) and (2.53b) that the total lithium content contained within the active material of the cell is constant. Thus any lithium leaving one of the electrodes must instantaneously be offset by lithium entering the other electrode.

We now consider lithium conservation in the electrolyte. Integration of (2.35a) over each electrode and the separator, separately, followed by the application of (2.35c), (2.42d), (2.42e), and (2.51) yields

$$\frac{\partial}{\partial t^*}\left(\epsilon_n L_y^* L_z^* \int_0^{L_n^*} c_{e,n}^* \mathrm{d}x^*\right) = L_y^* L_z^* N_{e,n}^*\big|_{\partial\Omega_{s,n}^*} + \frac{L_y^* L_z^* \mathcal{I}^*}{F^*}, \quad (2.54a)$$

$$\frac{\partial}{\partial t^*}\left(\epsilon_s L_y^* L_z^* \int_0^{L_n^*} c_{e,s}^* \mathrm{d}x^*\right) = L_y^* L_z^* N_{e,s}^*\big|_{\partial\Omega_{s,p}^*}$$
$$- L_y^* L_z^* N_{e,s}^*\big|_{\partial\Omega_{s,n}^*}, \quad (2.54b)$$

$$\frac{\partial}{\partial t^*}\left(\epsilon_p L_y^* L_z^* \int_0^{L_p^*} c_{e,p}^* \mathrm{d}x^*\right) = -L_y^* L_z^* N_{e,p}^*\big|_{\partial\Omega_{s,p}^*}$$
$$- \frac{L_y^* L_z^* \mathcal{I}^*}{F^*}, \quad (2.54c)$$

where we identify the terms in the brackets as the total lithium content in the negative electrolyte, separator electrolyte, and positive electrolyte, respectively. By summing (2.54a), (2.54b), and (2.54c); and using the continuity conditions (2.35e), it is clear that the total lithium content in the electrolyte is constant. By integrating (2.54a) and (2.54c) with respect to t^*, summing them, applying (2.35e) and (2.35f), and re-writing in terms of averaged quantities, we can express this in the form of the relation

$$\epsilon_n L_n^* \bar{c}_{e,n}^* + \epsilon_s L_s^* \bar{c}_{e,s}^* + \epsilon_p L_p^* \bar{c}_{e,p}^* = (\epsilon_n L_n^* + \epsilon_s L_s^* + \epsilon_p L_p^*) c_{e,0}^*. \quad (2.55)$$

2.8 SUMMARY

In this chapter, we have introduced the terminology, notation, and key concepts that we employ throughout the rest of this thesis. The DFN model will play a central role in our development of simple models of full lithium-ion cells and we will regularly interpret our results in terms of OCPs and overpotentials. We will use the Butler–Volmer and Nernst–Planck equations as building blocks for our SEI model, where it will also be crucial to distinguish between the electric and electrochemical potentials in the electrolyte.

ASYMPTOTIC REDUCTION OF THE DFN MODEL

3.1 INTRODUCTION

In this chapter, we employ asymptotic methods to simplify the DFN model as given by (2.33), (2.35), (2.36), (2.41), and (2.42). We begin by introducing typical scalings and writing the DFN in dimensionless form. We then identify key dimensionless parameters and perform a systematic asymptotic reduction in the distinguished limit in which the electrical conductivities are of comparable size to the ratio of the typical discharge timescale to the lithium-ion migration timescale. We make a uniform asymptotic expansion and, at leading order, recover the classical single particle model (SPM). By extending the asymptotic expansion to first order, we obtain an additional PDE for the concentration of lithium ions in the electrolyte and an additional algebraic correction to the voltage. We summarise our reduced models and compare their computational complexity and accuracy with the DFN model. Following the discussion on computational complexity, we compare our model with a selection of ad-hoc models from the literature, showing that our model best recovers the behaviour of the DFN model. Finally, we also compare our model with the asymptotic model derived in [75].

3.2 LITERATURE REVIEW

The DFN model is too computationally expensive for studies of long-term degradation and applications within battery management systems. As a result, there have been many previous efforts to develop simplified models of lithium-ion batteries. The most popular approach adopted in industry is equivalent circuit models (ECM) [31], [41], [65], [78]. ECMs use circuit elements such as resistors and capacitors to model the behaviour of a lithium-ion cell. Mathematically, these circuits can be thought of as systems of time-dependent ordinary differential equations (ODEs). These models are empirically driven, with parameter values for resistances and capacitances being adjusted to a particular set of data. As a result, ECMs perform well for the particular operating conditions of the training data but generally perform poorly as degradation processes occur and the cell deviates from its initial state. Further, because it is not clear what the exact physical connection between circuit elements and physical processes are, it is unclear how to extend ECMs to account for degradation [64].

The most popular physics-based reduced-order model is the single-particle model (SPM) [12], [26], [77], [89]. In this model, it is assumed that all of the particles in each electrode act in the same way. As a result, a single representative particle can be solved for in each electrode, dramatically reducing computation power. It is also assumed the electrolyte effects can be neglected. This model performs well at low currents but deviates significantly from the DFN at higher currents. Therefore, there have been several ad-hoc attempts to extend the SPM so that it is valid at higher currents [27], [36], [61], [67], [68], [88]. Each of these extensions includes an expression to estimate the electrolyte effects which are normally neglected by the SPM. Approaches here range from using interpolating polynomials for the electrolyte [68] to slightly more systematic approaches where a long list of assumptions are made to decoupling the electrolyte PDEs from the rest of the problem [61].

There have been some previous applications of asymptotic methods to batteries. In [85], asymptotic methods were applied to detailed models of lead-acid batteries to develop reduced-order models. In [53], a model of a lithium-ion battery that neglects the active material particles was developed and then systematically reduced using asymptotic methods. Asymptotic methods have also been applied to the DFN model in [75]. In [75], asymptotic methods were applied to the DFN model to systematically reduce it. This involved taking a different asymptotic limit to the one taken here to derive a model similar to ours. We will compare these two models later.

3.3   NONDIMENSIONALISATION

In order to facilitate the asymptotic analysis to follow, we write the classical DFN model in dimensionless form. This is achieved by introducing characteristic scales for each of the variables. The through-cell x^*-coordinate is scaled with L_x^* and in each of the particles, we scale lengths by the particle radius. As our typical timescale, we take a representative discharge time of the cell τ_d^*, which is defined in Table 3.2. The current densities in both the electrode and electrolyte are scaled by a typical operating current density, I^*. We choose to scale the potentials, overpotentials, and OCPs by a typical potential scale, Φ^*, which we take to be the thermal voltage $\Phi^* = R_g^* T_\infty^* / F^*$. The scaled potential in the negative electrode is measured relative to ground (0 V), whereas the scaled potential in the positive electrode is measured relative to the reference OCV, $U_{ref}^* = U_{p,ref}^* - U_{n,ref}^*$, which is the voltage measured across the cell when no current is applied for a particular set of reference concentrations, $c_{s,n,ref}^*$ and $c_{s,p,ref}^*$. The scaled potential in the electrolyte is measured relative to the reference OCP in the negative electrode, $U_{n,ref}^*$. The lithium concentration in the electrolyte is scaled by the typical value $c_{e,typ}^*$, whereas the lithium concentrations in the solid particles are scaled with their maximum concentrations, $c_{s,k,max}^*$.

The electrolyte conductivity and electrolyte diffusivity are scaled by their typical values $\kappa_{e,typ}^*$, and $D_{e,typ}^*$, respectively. In our analysis, we will work with the solid diffusivities as a function of concentration, $D_{s,k}^*(c_{s,k}^*)$, (even though they are constant in our parameter set). We therefore also scale the solid diffusivities by a typical value $D_{s,k,typ}^*$. Fluxes then scale in the natural way. To summarise, the dimensionless variables are related to their dimensional counterparts in the following way:

global:

$$x^* = L_x^* x, \quad t^* = \tau_d^* t,$$
$$\mathcal{I}^* = I^* \mathcal{I} \quad \kappa_e^* = \kappa_{typ}^* \kappa_e, \quad D_e^* = D_{e,typ}^* D_e;$$

for $k \in \{n, p\}$:

$$r_k^* = R_k^* r_k, \quad c_{s,k}^* = c_{s,k,max}^* c_{s,k}$$
$$D_{s,k}^* = D_{s,k,typ}^* D_{s,k},$$
$$N_{s,k}^* = \frac{D_{s,k,typ}^* c_{s,k,max}^*}{R_k^*} N_{s,k},$$
$$j_k^* = \frac{I^*}{a_k^* L_x^*} j_k, \quad j_{0,k}^* = \frac{I^*}{a_k^* L_x^*} j_{0,k},$$
$$\eta_k^* = \frac{R^* T_\infty^*}{F^*} \eta_k, \quad U_k^* = U_{k,ref}^* + \frac{R^* T_\infty^*}{F^*} U_k;$$

for $k \in \{cn, n, p, cp\}$:   (3.1)

$$i_{s,k}^* = I^* i_{s,k};$$

for $k \in \{cn, n\}$:

$$\phi_{s,k}^* = \frac{R^* T_\infty^*}{F^*} \phi_{s,k};$$

for $k \in \{p, cp\}$:

$$\phi_{s,k}^* = \left(U_{p,ref}^* - U_{n,ref}^* \right) + \frac{R^* T_\infty^*}{F^*} \phi_{s,k};$$

for $k \in \{n, s, p\}$:

$$c_{e,k}^* = c_{e,typ}^* c_{e,k}, \quad N_{e,k}^* = \frac{D_{e,typ}^* c_{e,typ}^*}{L_x^*} N_{e,k},$$
$$\phi_{e,k}^* = -U_{n,ref}^* + \frac{R^* T_\infty^*}{F^*} \phi_{e,k}, \quad i_{e,k}^* = I^* i_{e,k}.$$

For clarity, in Table 3.1 we have included the full set of the dimensionless variables that result from making the scalings (3.1). Through non-dimensionalisation, we identify a number of key timescales in our model which relate to various physical processes. These are provided and interpreted in Table 3.2. For the discharge timescale, we have used that the available lithium in the cell is $\mathcal{O}(c^*_{\mathrm{s,n,max}} L^*_x L^*_y L^*_z)$ and that this is consumed at a rate $\mathcal{O}(I^* L^*_y L^*_z / F^*)$. This give rise to a timescale that is not quite the same as the discharge time (otherwise its value would be $3600/\mathcal{C}$, since a 1 C discharge takes 3600 seconds). The difference arises for three reasons: (i) the negative electrode is of size L^*_{n} and not L^*_x; (ii) the volume of active material is lower than the superficial volume; (iii) the actual capacity of the cell is lower than the theoretical capacity. The OCP tends to $\pm\infty$ when the battery is fully charged/discharged; the actual capacity is that available between two (finite) voltage limits, which we take to be 3.2 V and 4.7 V in defining $\mathcal{C}$. In addition, we identify a number of dimensionless parameters which are presented alongside their respective interpretations and typical values in Tables 3.3 and 3.4.

Symbol	Interpretation	Region k $\in \{\cdots\}$
$\phi_{\mathrm{s,k}}$	Electric potential in solid	n, p,
$\phi_{\mathrm{e,k}}$	Electric potential in the electrolyte	n, s, p
$i_{\mathrm{s,k}}$	Current density in the solid	n, p,
$i_{\mathrm{e,k}}$	Current density in the electrolyte	n, s, p
$c_{\mathrm{s,k}}$	Lithium concentration in the active material	n, p
$c_{\mathrm{e,k}}$	Lithium-ion concentration in the electrolyte	n, s, p
$N_{\mathrm{s,k}}$	Lithium flux in the active material	n, p
$N_{\mathrm{e,k}}$	Lithium-ion flux in the electrolyte	n, s, p
j_{k}	Interfacial current density	n, p
$j_{0,\mathrm{k}}$	Exchange current density	n, p
η_{k}	Surface reaction overpotential	n, p
U_{k}	Open circuit potential	n, p

Table 3.1: Variables in dimensionless DFN model.

Symbol	Expression	Interpretation	Value (s)
τ_{d}^*	$F^* c_{\mathrm{n,max}}^* L_x^* / I^*$	Discharge timescale	$2.260 \times 10^4 / \mathcal{C}$
τ_{n}^*	$(R_{\mathrm{n}}^*)^2 / D_{\mathrm{n,typ}}^*$	Diffusion timescale in the negative electrode solid material	2.564×10^3
τ_{p}^*	$(R_{\mathrm{p}}^*)^2 / D_{\mathrm{p,typ}}^*$	Diffusion timescale in the positive electrode solid material	1×10^3
τ_{e}^*	$(L_x^*)^2 / D_{\mathrm{e,typ}}^*$	Diffusion timescale in the electrolyte	1.816×10^2
$\tau_{r_{\mathrm{n}}}^*$	$F^* / (m_{\mathrm{n,typ}}^* a_{\mathrm{n}}^* (c_{\mathrm{e,typ}}^*)^{1/2})$	Reaction timescale in the negative electrode	8.475×10^2
$\tau_{r_{\mathrm{p}}}^*$	$F^* / (m_{\mathrm{p,typ}}^* a_{\mathrm{p}}^* (c_{\mathrm{e,typ}}^*)^{1/2})$	Reaction timescale in the positive electrode	3.390×10^4

Table 3.2: Timescales associated with the physical processes occurring in the battery model. For the isothermal case, $m_{\mathrm{k,typ}}^* = m_{\mathrm{k}}^*$.

Parameter	Expression	Interpretation	cn	n	s	p	cp
L_k	L_k^*/L_x^*	Ratio of region thickness to cell thickness	0.1111	0.4444	0.1111	0.4444	0.1111
$\mathcal{C}_k$	τ_k^*/τ_d^*	Ratio of solid diffusion and discharge timescales	-	$0.1135\mathcal{C}$	-	$0.04425\mathcal{C}$	-
$\mathcal{C}_{r,k}$	$\tau_{r,k}^*/\tau_d^*$	Ratio of reaction and discharge timescales	-	$0.0375\mathcal{C}$	-	$1.5\mathcal{C}$	-
σ_k	$(R^*T_\infty^*/F^*)/(I^*L_x^*/\sigma_k^*)$	Ratio of thermal voltage to the typical Ohmic drop in the solid	$2.84 \times 10^8/\mathcal{C}$	$475.8/\mathcal{C}$	-	$47.58/\mathcal{C}$	$1.69 \times 10^8/\mathcal{C}$
a_k	$a_k^*R_k^*$	Product of particle radius and surface area per unit volume	-	1.8	-	1.5	-
γ_k	$c_{k,max}^*/c_{n,max}^*$	Ratio of maximum lithium concentrations in solid	-	1	-	2.0501	-
$c_{k,0}$	$c_{k,0}^*/c_{k,max}^*$	Dimensionless initial lithium concentration in solid	-	0.8	-	0.6	-

Table 3.3: Typical dimensionless parameter values derived from dimensional parameters in Tables 2.1 and 2.2. Here $\mathcal{C} = I^*/(24\,\mathrm{Am}^{-2})$ is the C-Rate where we have taken a 1 C rate to correspond to a typical x^*-direction current density of 24 Am^{-2}. This is for a cell with an initial stoichiometry of 0.8 in the negative electrode and 0.6 in the positive electrode with a voltage cutoff of 3.2 V. (Part 1).

Parameter	Expression	Interpretation	Value
$\mathcal{C}_e$	τ_e^* / τ_d^*	Ratio of electrolyte transport and discharge timescales	$8.036 \times 10^{-3}\,\mathcal{C}$
γ_e	$c_{e,typ}^* / c_{n,max}^*$	Ratio of maximum lithium concentration in the negative electrode solid and typical electrolyte concentration	4.003×10^{-2}
$\hat{\kappa}_e$	$(R^* T_\infty^* / F^*)/(I^* L_x^* / \kappa_{e,typ}^*)$	Ratio of thermal voltage to the typical Ohmic drop in the electrolyte	$4.981/\mathcal{C}$

Table 3.4: Typical dimensionless parameter values derived from dimensional parameters in Tables 2.1 and 2.2. Here $\mathcal{C} = I^*/(24\,\mathrm{Am^{-2}})$ is the C-Rate where we have taken a 1 C rate to correspond to a typical x^*-direction current density of $24\,\mathrm{Am^{-2}}$. This is for a cell with an initial stoichiometry of 0.8 in the negative electrode and 0.6 in the positive electrode with a voltage cutoff of 3.2 V. (Part 2).

3.4   DIMENSIONLESS DFN MODEL

Here, we summarise the dimensionless version of the reformulated DFN model as given by (2.33), (2.35), (2.36), (2.41), and (2.42). Using the scalings from (3.1), the electrode equations (2.41) become

$$\mathcal{I} - i_{\mathrm{e,k}} = \sigma_{\mathrm{s,k}} \frac{\partial \phi_{\mathrm{s,k}}}{\partial x} \qquad\qquad \mathrm{k} \in \{\mathrm{n, p}\}, \tag{3.2a}$$

$$\phi_{\mathrm{s,n}} = 0 \qquad\qquad x \in \partial\Omega_{\mathrm{n,cn}} \tag{3.2b}$$

the active material equations (2.33) become

$$\mathcal{C}_{\mathrm{k}} \frac{\partial c_{\mathrm{s,k}}}{\partial t} = -\frac{1}{r_{\mathrm{k}}^2} \frac{\partial}{\partial r_{\mathrm{k}}} \left(r_{\mathrm{k}} N_{\mathrm{s,k}} \right), \qquad\qquad \mathrm{k} \in \{\mathrm{n, p}\}, \tag{3.3a}$$

$$N_{\mathrm{s,k}} = -D_{\mathrm{s,k}}(c_{\mathrm{s,k}}) \frac{\partial c_{\mathrm{s,k}}}{\partial r}, \qquad\qquad \mathrm{k} \in \{\mathrm{n, p}\}, \tag{3.3b}$$

$$N_{\mathrm{s,k}}\big|_{r=0} = 0, \quad N_{\mathrm{s.k}}\big|_{r_{\mathrm{k}}=1} = \frac{\mathcal{C}_{\mathrm{k}} j_{\mathrm{k}}}{a_{\mathrm{k}} \gamma_{\mathrm{k}}}. \qquad\qquad \mathrm{k} \in \{\mathrm{n, p}\}, \tag{3.3c}$$

$$c_{\mathrm{s,k}}\big|_{t=0} = c_{\mathrm{s,k,0}}, \qquad\qquad \mathrm{k} \in \{\mathrm{n, p}\}; \tag{3.3d}$$

the electrolyte current equations (2.42) become

$$\frac{\partial i_{\mathrm{e,k}}}{\partial x} = j_{\mathrm{k}}, \qquad\qquad \mathrm{k} \in \{\mathrm{n, p}\}, \tag{3.4a}$$

$$i_{\mathrm{e,s}} = \mathcal{I}, \tag{3.4b}$$

$$i_{\mathrm{e,k}} = \epsilon_{\mathrm{k}}^{\mathrm{b}} \hat{\kappa}_{\mathrm{e}} \kappa_{\mathrm{e}}(c_{\mathrm{e,k}}) \left(-\frac{\partial \phi_{\mathrm{e,k}}}{\partial x} + 2(1 - t^+) \frac{\partial}{\partial x} \left(\log(c_{\mathrm{e,k}}) \right) \right), \tag{3.4c}$$

$$\mathrm{k} \in \{\mathrm{n, s, p}\},$$

$$i_{\mathrm{e,k}} = 0, \qquad\qquad x \in \partial\Omega_{\mathrm{ck,k}}, \qquad\qquad \mathrm{k} \in \{\mathrm{n, p}\}, \tag{3.4d}$$

$$i_{\mathrm{e,k}} = \mathcal{I}, \qquad\qquad x \in \partial\Omega_{\mathrm{k,s}}, \qquad\qquad \mathrm{k} \in \{\mathrm{n, p}\}, \tag{3.4e}$$

the electrolyte diffusion equations (2.35) become

$$\mathcal{C}_{\mathrm{e}} \epsilon_{\mathrm{k}} \frac{\partial c_{\mathrm{e,k}}}{\partial t} = -\gamma_{\mathrm{e}} \frac{\partial N_{\mathrm{e,k}}}{\partial x} + \mathcal{C}_{\mathrm{e}} \frac{\partial i_{\mathrm{e,k}}}{\partial x}, \qquad\qquad \mathrm{k} \in \{\mathrm{n, s, p}\}, \tag{3.5a}$$

$$N_{\mathrm{e,k}} = -\epsilon_{\mathrm{k}}^{\mathrm{b}} D_{\mathrm{e}}(c_{\mathrm{e,k}}) \frac{\partial c_{\mathrm{e,k}}}{\partial x} + \frac{\mathcal{C}_{\mathrm{e}} t^+}{\gamma_{\mathrm{e}}} i_{\mathrm{e,k}}, \qquad \mathrm{k} \in \{\mathrm{n, s, p}\}, \tag{3.5b}$$

$$N_{\mathrm{e,k}} = 0, \quad x \in \partial\Omega_{\mathrm{ck,k}}, \qquad\qquad \mathrm{k} \in \{\mathrm{n, p}\}, \tag{3.5c}$$

$$c_{\mathrm{e,k}} = c_{\mathrm{e,s}}, \quad N_{\mathrm{e,k}} = N_{\mathrm{e,s}}, \; x \in \partial\Omega_{\mathrm{k,s}}, \quad \mathrm{k} \in \{\mathrm{n, p}\}, \tag{3.5d}$$

$$c_{\mathrm{e,k}}\big|_{t=0} = 1, \qquad\qquad \mathrm{k} \in \{\mathrm{n, s, p}\}; \tag{3.5e}$$

and the electrochemical reaction equations (2.36) become

$$j_k = j_{0,k} \sinh\left(\frac{\eta_k}{2}\right)\bigg|_{r=1}, \qquad\qquad k \in \{n,p\}, \qquad (3.6a)$$

$$j_{0,k} = \frac{\gamma_k}{\mathcal{C}_{e,k}}(c_{s,k})^{1/2}(1-c_{s,k})^{1/2}(c_{e,k})^{1/2}\big|_{r=1} \qquad k \in \{n, p\}, \qquad (3.6b)$$

$$\eta_k = \phi_{s,k} - \phi_{e,k} - U_k(c_{s,k})\big|_{r_k=1}, \qquad\qquad k \in \{n, p\}. \qquad (3.6c)$$

We also note that the dimensionless version of (2.55) is

$$\epsilon_n L_n \bar{c}_{e,n} + \epsilon_s L_s \bar{c}_{e,s} + \epsilon_p L_p \bar{c}_{e,p} = (\epsilon_n L_n + \epsilon_s L_s + \epsilon_p L_p), \qquad (3.7)$$

which is a consequence of lithium being conserved in the electrolyte.

3.5   ASYMPTOTIC REDUCTION

We consider the limit in which the electrical conductivity in the electrodes and electrolyte is high (such that the typical potential drop in each material is small relative to the thermal voltage) and the timescale for the migration of lithium ions in the electrolyte is small relative to the typical timescale of a discharge. This corresponds to the limit $\mathcal{C}_e \to 0$, where $\mathcal{C}_e$ is the ratio of the typical timescale for lithium ion migration to the typical discharge timescale, $\sigma_k \to \infty$, where σ_k is ratio of the thermal voltage to the typical Ohmic drop in the solid, and $\hat{\kappa}_e \to \infty$, where $\hat{\kappa}_e$ is the ratio of the thermal voltage to the typical Ohmic drop in the electrolyte. We consider the distinguished limit in which each overpotential term in (2.50) appears at leading or first order in our asymptotic expansion. We take $\sigma_k \mathcal{C}_e$ and $\hat{\kappa}_e \mathcal{C}_e$ to both tend to a constant as $\mathcal{C}_e \to 0$, $\sigma_k \to \infty$, and $\hat{\kappa}_e \to \infty$ by setting

$$\sigma_k = \frac{\sigma'_k}{\mathcal{C}_e}, \quad \sigma'_k = \mathcal{O}(1), \quad k \in \{n, p\},$$
$$\hat{\kappa}_e = \frac{\hat{\kappa}'_e}{\mathcal{C}_e}, \quad \hat{\kappa}'_e = \mathcal{O}(1). \qquad\qquad (3.8)$$

We then expand all variables in powers of $\mathcal{C}_e$ in the form

$$c_{s,k} = c_{s,k}^{(0)} + \mathcal{C}_e c_{s,k}^{(1)} + \mathcal{C}_e^2 c_{s,k}^{(2)} + \dots,$$

etc.

3.5.1 *Leading-order analysis*

At leading order in $\mathcal{C}_e$, the electrode potential equations (3.2) become

$$\frac{\partial \phi_{s,k}^{(0)}}{\partial x} = 0 \qquad\qquad k \in \{n, p\}, \qquad (3.9a)$$

$$\phi_{s,n}^{(0)} = 0 \qquad\qquad x \in \partial\Omega_{n,cn}; \qquad (3.9b)$$

the active material equations (3.3) become

$$\mathcal{C}_k \frac{\partial c_{s,k}^{(0)}}{\partial t} = -\frac{1}{r_k^2}\frac{\partial}{\partial r_k}\left(r_k N_{s,k}^{(0)}\right), \qquad k \in \{n, p\}, \qquad (3.10a)$$

$$N_{s,k}^{(0)} = -D_{s,k}(c_{s,k}^{(0)})\frac{\partial c_{s,k}^{(0)}}{\partial r}, \qquad k \in \{n, p\}, \qquad (3.10b)$$

$$N_{s,k}^{(0)}\big|_{r=0} = 0, \quad N_{s,k}^{(0)}\big|_{r_k=R_k} = \frac{\mathcal{C}_k j_k^{(0)}}{a_k \gamma_k}, \qquad k \in \{n, p\}, \qquad (3.10c)$$

$$c_{s,k}^{(0)}\big|_{t=0} = c_{s,k,0}; \qquad (3.10d)$$

the electrolyte current equations (3.4) become

$$\frac{\partial i_{e,k}^{(0)}}{\partial x} = j_k^{(0)}, \qquad\qquad k \in \{n, p\}, \qquad (3.11a)$$

$$i_{e,s}^{(0)} = \mathcal{I}, \qquad (3.11b)$$

$$\frac{\partial \phi_{e,k}^{(0)}}{\partial x} = 2(1-t^+)\frac{\partial}{\partial x}\left(\log\left(c_{e,k}^{(0)}\right)\right) \qquad k \in \{n, s, p\}, \qquad (3.11c)$$

$$i_{e,k}^{(0)} = 0, \quad x \in \partial\Omega_{ck,k}, \qquad k \in \{n, p\}, \qquad (3.11d)$$

$$i_{e,k}^{(0)} = \mathcal{I}, \quad x \in \partial\Omega_{k,s}, \qquad k \in \{n, p\}, \qquad (3.11e)$$

the electrolyte diffusion equations (3.5) become

$$0 = -\gamma_e \frac{\partial N_{e,k}^{(0)}}{\partial x}, \qquad\qquad k \in \{n, s, p\}, \qquad (3.12a)$$

$$N_{e,k}^{(0)} = -\epsilon_k^b D_e(c_{e,k}^{(0)})\frac{\partial c_{e,k}^{(0)}}{\partial x}, \qquad k \in \{n, s, p\}, \qquad (3.12b)$$

$$N_{e,k}^{(0)} = 0, \quad x \in \partial\Omega_{ck,k}, \qquad k \in \{n, p\}, \qquad (3.12c)$$

$$c_{e,k}^{(0)} = c_{e,s}^{(0)}, \; N_{e,k}^{(0)} = N_{e,s}^{(0)}, \; x \in \partial\Omega_{k,s}, \qquad k \in \{n, p\}, \qquad (3.12d)$$

$$c_{e,k}^{(0)}\big|_{t=0} = 1, \qquad\qquad k \in \{n, s, p\}; \qquad (3.12e)$$

and the electrochemical reaction equations (3.6) become

$$j_k^{(0)} = j_{0,k}^{(0)} \sinh\left(\frac{\eta_k^{(0)}}{2}\right)\bigg|_{r=1}, \qquad k \in \{n, p\}, \quad (3.13a)$$

$$j_{0,k}^{(0)} = \frac{\gamma_k}{\mathcal{C}_{e,k}}(c_{s,k}^{(0)})^{1/2}(1 - c_{s,k}^{(0)})^{1/2}(c_{e,k}^{(0)})^{1/2}\big|_{r=1} \quad k \in \{n, p\}, \quad (3.13b)$$

$$\eta_k^{(0)} = \phi_{s,k}^{(0)} - \phi_{e,k}^{(0)} - U_k(c_{s,k}^{(0)})\big|_{r_k=1}, \qquad k \in \{n, p\}. \quad (3.13c)$$

Firstly, from (3.12), we have that

$$c_{e,k}^{(0)} = 1 \qquad x \in \Omega_k, \qquad k \in \{n, s, p\}, \qquad (3.14a)$$

$$N_{e,k}^{(0)} = 0, \qquad x \in \Omega_k, \qquad k \in \{n, s, p\}. \qquad (3.14b)$$

By using (3.14) in (3.11) we have that $\phi_{e,k}^{(0)}$ is independent of x. Additionally from (3.9), we have that $\phi_{s,k}^{(0)}$ is independent of x. Since $c_{e,k}^{(0)}$, $\phi_{e,k}^{(0)}$, and $\phi_{s,k}^{(0)}$ are all independent of x and $c_{s,k}^{(0)}$ is initially independent of x, it follows that $c_{s,k}^{(0)}, j_k^{(0)}, j_{0,k}^{(0)}, \eta_k^{(0)}$, and $U_k(c_{s,k}^{(0)})\big|_{r_k=1}$ are also independent of x. Therefore, integrating (3.11a) over each electrode and applying the boundary conditions (3.11d) and (3.11e), gives

$$i_{e,n}^{(0)} = \frac{x\mathcal{I}}{L_n}, \quad i_{e,s}^{(0)} = \mathcal{I}, \quad i_{e,p}^{(0)} = \frac{(1-x)\mathcal{I}}{L_p}, \qquad (3.15)$$

$$j_n^{(0)} = \frac{\mathcal{I}}{L_n}, \quad j_p^{(0)} = -\frac{\mathcal{I}}{L_p}. \qquad (3.16)$$

From (3.9), we have

$$\phi_{s,n}^{(0)} = 0, \quad x \in \Omega_n. \qquad (3.17)$$

Therefore, since $\phi_{e,k}^{(0)}$ is independent of x, rearranging (3.13c) for k=n gives

$$\phi_{e,k}^{(0)} = -U_n(c_{s,n}^{(0)})\big|_{r_n=1} - \eta_n^{(0)}, \quad x \in \Omega_k, \quad k \in \{n, s, p\}. \qquad (3.18)$$

We can then rearrange (3.13c) for k=p and use that $\phi_{s,p}^{(0)}$ is independent of x to obtain

$$\phi_{e,p}^{(0)} = U_p(c_{s,p}^{(0)})\big|_{r_p=1} - U_n(c_{s,n}^{(0)})\big|_{r_n=1} + \eta_p^{(0)} - \eta_n^{(0)}, \quad x \in \Omega_p. \quad (3.19)$$

Finally, we rearrange (3.13a) to get

$$\eta_k^{(0)} = 2\sinh^{-1}\left(\frac{j_k^{(0)}}{j_{0,k}^{(0)}}\right), \quad x \in \Omega_k, \quad k \in \{n, p\}. \qquad (3.20)$$

3.5.2   *Summary of the single-particle model*

The dimensionless leading-order model is given by (3.10), (3.13b), and (3.15)-(3.20). In this limit, each particle in the electrode acts in the same way to lowest order in $\mathcal{C}_e$. Therefore, the model only consists of a single representative particle in each electrode. This gives the model it's name: the single-particle model (SPM) [12], [61]. In the SPM, the voltage is simply given by $\mathcal{V}^{(0)} = \phi_{s,p}^{(0)}$. To provide an easy reference and to draw parallels with the voltage breakdown introduced in §2.7.2, we also summarise the SPM in dimensional form. Here, we shall drop the asymptotic order notation. In each of the representative particles, we have

$$\frac{\partial c_{s,k}^*}{\partial t^*} = -\frac{1}{(r^*)^2}\frac{\partial}{\partial r^*}\left((r^*)^2 N_{s,k}^*\right), \qquad k \in \{n, p\}, \qquad (3.21a)$$

$$N_{s,k}^* = -D_{s,k}^*(c_{s,k}^*)\frac{\partial c_{s,k}^*}{\partial r^*}, \qquad k \in \{n, p\}, \qquad (3.21b)$$

$$N_{s,k}^*\big|_{r^*=0} = 0, \qquad k \in \{n, p\}, \qquad (3.21c)$$

$$N_{s,k}^*\big|_{r^*=R_k^*} = \begin{cases} \frac{\mathcal{I}^*}{F^* a_n^* L_n^*}, & k = n \\ -\frac{\mathcal{I}^*}{F^* a_p^* L_p^*} & k = p \end{cases} \qquad k \in \{n, p\}, \qquad (3.21d)$$

$$c_{s,k}^*\big|_{t^*=0} = c_{s,k,0}^*, \qquad k \in \{n, p\}, \qquad (3.21e)$$

with the voltage, expressed in the form of §2.7.2, given by

$$\mathcal{V}^* = \bar{U}_{eq}^* + \bar{\eta}_r^* \qquad (3.21f)$$

$$\bar{U}_{eq}^* = U_p^*(c_{s,p}^*)\big|_{r^*=R_p^*} - U_n^*(c_{s,n}^*)\big|_{r^*=R_n^*} \qquad (3.21g)$$

$$\bar{\eta}_r^* = \eta_p^* - \eta_n^* \qquad (3.21h)$$

$$\eta_p^* = -\frac{2R_g^* T_\infty^*}{F^*}\sinh^{-1}\left(\frac{\mathcal{I}^*}{j_{0,p}^* a_p^* L_p^*}\right) \qquad (3.21i)$$

$$\eta_n^* = \frac{2R_g^* T_\infty^*}{F^*}\sinh^{-1}\left(\frac{\mathcal{I}^*}{j_{0,n}^* a_n^* L_n^*}\right) \qquad (3.21j)$$

$$j_{0,k}^* = m_k^*(c_{s,k}^*)^{1/2}(c_{s,k,max}^* - c_{s,k}^*)^{1/2}(c_{e,0}^*)^{1/2} \quad k \in \{n, p\}. \quad (3.21k)$$

The remaining internal cell variables are given by

$$\phi_{s,n}^* = 0, \quad \phi_{s,p}^* = \mathcal{V}^*, \tag{3.21l}$$

$$i_{s,n}^* = \mathcal{I}^* - \frac{x^* \mathcal{I}^*}{L_n^*} \quad i_{s,p}^* = \mathcal{I}^* - \frac{(L_x^* - x^*)\mathcal{I}^*}{L_p^*} \tag{3.21m}$$

$$i_{e,n}^* = \frac{x^* \mathcal{I}^*}{L_n^*}, \quad i_{e,s}^* = \mathcal{I}^*, \quad i_{e,p}^* = \frac{(L_x^* - x^*)\mathcal{I}^*}{L_p^*}, \tag{3.21n}$$

$$j_n^* = \frac{\mathcal{I}^*}{a_n^* L_n^*}, \quad j_p^* = -\frac{\mathcal{I}^*}{a_p^* L_p^*}, \tag{3.21o}$$

$$\phi_{e,k}^* = -U_n^*(c_{s,n}^*)\big|_{r^*=R_n^*} - \eta_n^*, \quad k \in \{n, s, p\} \tag{3.21p}$$

$$c_{e,k}^* = c_{e,0}^*, \quad N_{e,k}^* = 0, \quad k \in \{n, s, p\}. \tag{3.21q}$$

Written in this form, it is clear that the SPM only estimates the OCV and reaction overpotential in the voltage expression (2.50). In Figure 2.2, we saw that these two terms are the main contributors to the terminal voltage and so this is consistent with what we would expect from a leading-order model. The SPM does particularly well at low C-rates but at higher C-rates, electrolyte effects in particular become more important. To correct for this, we proceed to first order in the asymptotic expansion.

3.5.3 *First-order analysis*

At $\mathcal{O}(\mathcal{C}_e)$, the electrode potential equations (3.2) become

$$\mathcal{I} - i_{e,k}^{(0)} = \sigma_k' \frac{\partial \phi_{s,k}^{(1)}}{\partial x} \qquad k \in \{n, p\}, \tag{3.22a}$$

$$\phi_{s,n}^{(1)} = 0 \qquad x \in \partial\Omega_{n,cn}; \tag{3.22b}$$

the active material equations (3.3) become

$$\mathcal{C}_k \frac{\partial c_{s,k}^{(1)}}{\partial t} = -\frac{1}{r_k^2} \frac{\partial}{\partial r_k}\left(r_k N_{s,k}^{(1)}\right), \quad k \in \{n, p\}, \tag{3.23a}$$

$$N_{s,k}^{(1)} = -D_{s,k}(c_{s,k}^{(0)}) \frac{\partial c_{s,k}^{(1)}}{\partial r} - D_{s,k}'(c_{s,k}^{(0)}) c_{s,k}^{(1)} \frac{\partial c_{s,k}^{(0)}}{\partial r}, \tag{3.23b}$$
$$k \in \{n, p\},$$

$$N_{s,k}^{(1)}\big|_{r=0} = 0, \quad N_{s,k}^{(1)}\big|_{r_k=R_k} = \frac{\mathcal{C}_k j_k^{(1)}}{a_k \gamma_k}. \quad k \in \{n, p\}, \tag{3.23c}$$

$$c_{s,k}^{(1)}\big|_{t=0} = 0, \quad k \in \{n, p\}; \tag{3.23d}$$

and the electrolyte current equations (3.4) become

$$\frac{\partial i_{e,k}^{(1)}}{\partial x} = j_k^{(1)}, \quad k \in \{n, p\}, \tag{3.24a}$$

$$i_{e,s}^{(1)} = 0, \tag{3.24b}$$

$$i_{e,k}^{(0)} = \epsilon_k^b \hat{\kappa}_e' \kappa_e(c_{e,k}^{(0)}) \left(-\frac{\partial \phi_{e,k}^{(1)}}{\partial x} + 2(1 - t^+)\frac{1}{c_{e,k}^{(0)}}\frac{\partial c_{e,k}^{(1)}}{\partial x} \right), \tag{3.24c}$$

$$k \in \{n, s, p\},$$

$$i_{e,k}^{(1)} = 0, \quad x \in \partial\Omega_{ck,k} \cup \partial\Omega_{k,s}, \quad k \in \{n, p\}, \tag{3.24d}$$

where we have omitted the terms from (3.24c) that become zero upon substitution of (3.14a) and (3.18). At $\mathcal{O}(\mathcal{C}_e)$, the electrolyte diffusion equations (3.5) become

$$\epsilon_k \frac{\partial c_{e,k}^{(0)}}{\partial t} = -\gamma_e \frac{\partial N_{e,k}^{(1)}}{\partial x} + \frac{\partial i_{e,k}^{(0)}}{\partial x}, \quad k \in \{n, s, p\}, \tag{3.25a}$$

$$N_{e,k}^{(1)} = -\epsilon_k^b D_e(c_{e,k}^{(0)})\frac{\partial c_{e,k}^{(1)}}{\partial x} + \frac{t^+}{\gamma_e}i_{e,k}^{(0)}, \quad k \in \{n, s, p\} \tag{3.25b}$$

$$N_{e,k}^{(1)} = 0, \quad x \in \partial\Omega_{ck,k}, \quad k \in \{n, p\}, \tag{3.25c}$$

$$c_{e,k}^{(1)} = c_{e,s}^{(1)}, \quad N_{e,k}^{(1)} = N_{e,s}^{(1)}, \quad x \in \partial\Omega_{k,s}, \quad k \in \{n, p\}, \tag{3.25d}$$

$$c_{e,k}^{(1)}\big|_{t=0} = 0, \quad k \in \{n, s, p\}; \tag{3.25e}$$

where we have omitted the terms from (3.25b) that become zero upon substitution of (3.14a) and (3.18). The electrochemical reaction equations (3.6) become

$$j_k^{(1)} = j_{0,k}^{(1)} \sinh\left(\frac{\eta_k^{(0)}}{2}\right) + \frac{j_{0,k}^{(0)}\eta_k^{(1)}}{2} \cosh\left(\frac{\eta_k^{(0)}}{2}\right), \tag{3.26a}$$

$$k \in \{n, p\},$$

$$j_{0,k}^{(1)} = \frac{j_{0,k}^{(0)}}{2}\left(\frac{c_{s,k}^{(1)}}{c_{s,k}^{(0)}} - \frac{c_{s,k}^{(1)}}{1 - c_{s,k}^{(0)}} + \frac{c_{e,k}^{(1)}}{c_{e,k}^{(0)}}\right)\Bigg|_{r_k=1}, \quad k \in \{n, p\}, \tag{3.26b}$$

$$\eta_k^{(1)} = \phi_{s,k}^{(1)} - \phi_{e,k}^{(1)} - c_{s,k}^{(1)}\big|_{r_k=1}\frac{\partial U_k}{\partial c_{s,k}}\bigg|_{c_{s,k}=c_{s,k}^{(0)}}, \quad k \in \{n, p\}. \tag{3.26c}$$

Substituting (3.14a) and (3.15) into (3.25a), integrating over each Ω_k, and applying the boundary conditions (3.25c) and (3.25d) gives

$$N_{e,n}^{(1)} = \frac{\mathcal{I}x}{\gamma_e L_n}, \quad N_{e,s}^{(1)} = \frac{\mathcal{I}}{\gamma_e}, \quad N_{e,p}^{(1)} = \frac{\mathcal{I}(1-x)}{\gamma_e L_p}. \tag{3.27}$$

Then, substituting (3.14a), (3.15), and (3.27) into (3.25b) and applying the constraint on conservation of lithium in the electrolyte, (3.7), gives

$$
c_{e,n}^{(1)} = \frac{(1 - t^+)\mathcal{I}}{\gamma_e 6 D_e(1)} \left(2 \left(\frac{L_p^2}{\epsilon_p^b} - \frac{L_n^2}{\epsilon_n^b} \right) \right.
$$
$$
\left. + \frac{2 L_s}{\epsilon_s^b} (1 + L_p - L_n) + \frac{3}{\epsilon_n^b L_n} (L_n^2 - x^2) \right),
$$
(3.28a)

$$
c_{e,p}^{(1)} = \frac{(1 - t^+)\mathcal{I}}{6\gamma_e D_e(1)} \left(2 \left(\frac{L_p^2}{\epsilon_p^b} - \frac{L_n^2}{\epsilon_n^b} \right) \right.
$$
$$
\left. + \frac{3}{\epsilon_s^b} (L_n^2 - L_p^2 + 1 - 2x) \right),
$$
(3.28b)

$$
c_{e,p}^{(1)} = \frac{(1 - t^+)\mathcal{I}}{6\gamma_e D_e(1)} \left(2 \left(\frac{L_p^2}{\epsilon_p^b} - \frac{L_n^2}{\epsilon_n^b} \right) \right.
$$
$$
\left. + \frac{3 L_s}{\epsilon_s^b} (L_p - L_n - 1) + \frac{3}{L_p \epsilon_p^b} ((x - 1)^2 - L_p^2) \right).
$$
(3.28c)

Integrating (3.24a) over Ω_n and Ω_p and applying the boundary conditions (3.24d) gives

$$
\bar{j}_k^{(1)} = 0, \quad k \in \{n, p\}.
$$
(3.29)

Therefore, integrating (3.23) over Ω_n and Ω_p gives the problem

$$
\mathcal{C}_k \frac{\partial \bar{c}_{s,k}^{(1)}}{\partial t} = -\frac{1}{r_k^2} \frac{\partial}{\partial r_k} \left(r_k \bar{N}_{s,k}^{(1)} \right), \quad k \in \{n, p\},
$$
(3.30a)

$$
\bar{N}_{s,k}^{(1)} = -D_{s,k}(c_{s,k}^{(0)}) \frac{\partial \bar{c}_{s,k}^{(1)}}{\partial r} - D'_{s,k}(c_{s,k}^{(0)}) \bar{c}_{s,k}^{(1)} \frac{\partial c_{s,k}^{(0)}}{\partial r},
$$
$$
k \in \{n, p\},
$$
(3.30b)

$$
\bar{N}_{s,k}^{(1)} \big|_{r=0} = 0, \quad \bar{N}_{s,k}^{(1)} \big|_{r_k = R_k} = 0. \quad k \in \{n, p\},
$$
(3.30c)

$$
\bar{c}_{s,k}^{(1)} \big|_{t=0} = 0, \quad k \in \{n, p\},
$$
(3.30d)

to which the solution is

$$
\bar{c}_{s,k}^{(1)} = 0, \quad k \in \{n, p\}.
$$
(3.31)

Hence the first-order correction to the lithium concentration in the average particle in each electrode is zero. Using (3.15) in (3.22) gives

$$
\phi_{s,n}^{(1)} = -\frac{\mathcal{I}x}{2\sigma_n' L_n} (2 L_n - x)
$$
(3.32a)

$$
\phi_{s,p}^{(1)} = \mathcal{V}^{(1)} + \frac{\mathcal{I}(x - 1)(1 - 2 L_p - x)}{2\sigma_p' L_p},
$$
(3.32b)

where $\mathcal{V}^{(1)} = \phi_{s,p}^{(1)}\big|_{\partial\Omega_{p,cp}}$ is a constant of integration that remains to be determined. By averaging (3.26c) over Ω_n and Ω_p and applying (3.31), we have

$$\bar{\eta}_k^{(1)} = \bar{\phi}_{s,k}^{(1)} - \bar{\phi}_{e,k}^{(1)}, \quad k \in \{n, p\}. \tag{3.33}$$

We can now average (3.32b) over Ω_p and use (3.33) with k=p, to obtain

$$\mathcal{V}^{(1)} = \bar{\phi}_{e,p}^{(1)} + \bar{\eta}_p^{(1)} - \frac{\mathcal{I}L_p}{3\sigma_p'}, \tag{3.34}$$

which is the first-order correction to the terminal voltage. To fully determine the first-order terminal voltage, it only remains to determine $\bar{\phi}_{e,p}^{(1)}$ and $\bar{\eta}_p^{(1)}$. By integrating (3.24c) over Ω_k for $k \in \{n, s, p\}$ and using (3.33) with k=n to determine the constant of integration, we have

$$\phi_{e,n}^{(1)} = \Phi_e + 2(1 - t^+)(c_{e,n}^{(1)} - \bar{c}_{e,n}^{(1)})$$
$$- \frac{\mathcal{I}}{\hat{\kappa}_e'\kappa_e(1)}\left(\frac{x^2 - L_n^2}{2\epsilon_n^b L_n} + \frac{L_n}{\epsilon_s^b}\right), \tag{3.35a}$$

$$\phi_{e,s}^{(1)} = \Phi_e + 2(1 - t^+)(c_{e,s}^{(1)} - \bar{c}_{e,n}^{(1)}) - \frac{\mathcal{I}x}{\hat{\kappa}_e'\kappa_e(1)\epsilon_s^b}, \tag{3.35b}$$

$$\phi_{e,p}^{(1)} = \Phi_e + 2(1 - t^+)(c_{e,p}^{(1)} - \bar{c}_{e,n}^{(1)})$$
$$- \frac{\mathcal{I}}{\hat{\kappa}_e'\kappa_e(1)}\left(\frac{x(2 - x) + L_p^2 - 1}{2\epsilon_p^b L_p} + \frac{1 - L_p}{\epsilon_s^b}\right), \tag{3.35c}$$

where

$$\Phi_e = \bar{\phi}_{s,n}^{(1)} - \bar{\eta}_n^{(1)} - \frac{\mathcal{I}L_n}{\hat{\kappa}_e'\kappa_e(1)}\left(\frac{1}{3\epsilon_n^b} - \frac{1}{\epsilon_s^b}\right). \tag{3.35d}$$

Finally, averaging (3.26a) over Ω_n and Ω_p and rearranging for $\bar{\eta}_k^{(1)}$ gives

$$\bar{\eta}_k^{(1)} = -\frac{2\bar{j}_{0,k}^{(1)}}{j_{0,k}^{(0)}}\tanh\left(\frac{\eta_k^0}{2}\right) \tag{3.35e}$$

where we average (3.26b) and use (3.14) and (3.31) to get

$$\bar{j}_{0,k}^{(1)} = \frac{j_{0,k}^{(0)}\bar{c}_{e,k}^{(1)}}{2}. \tag{3.35f}$$

We have now fully determined $\mathcal{V}^{(1)}$, $c_{e,k}^{(1)}$, $\phi_{s,k}^{(1)}$, $\phi_{e,k}^{(1)}$, $\bar{\eta}_k^{(1)}$, $\bar{c}_{s,k}^{(1)}$, $\bar{j}_k^{(1)}$, and $\bar{j}_{0,k}^{(1)}$ as algebraic expressions which require negligible additional computational effort to evaluate. However, to determine $c_{s,k}^{(1)}$, $j_k^{(1)}$, $j_{0,k}^{(1)}$, $i_{e,k}^{(1)}$, and $i_{s,k}^{(1)}$ requires significant additional computational effort because one must then resolve the concentrations in all of the particles instead

of a single averaged particle. We will discuss this later but since the terminal voltage is the key output of interest to battery engineers, we will simply employ the leading-order approximations for these variables in our reduced-order models.

3.5.4   *Transient response*

In the previous analysis, we only considered the steady state solution for $c_{e,k}^{(0)}$ and $c_{e,k}^{(1)}$. However, we can account for the transient effects by scaling time with the electrolyte diffusion timescale as

$$t^* = \tau_e \hat{t}$$

instead of the discharge timescale. We can now solve a new short time problem by transforming the dimensionless equations (3.2)-(3.6) using

$$t = \mathcal{C}_e \hat{t}$$

and denoting short time variables as

$$\hat{c}_{e,k}, \ \hat{c}_{s,k}, \ \text{etc.} \tag{3.36}$$

We consider the limit in (3.8) and make asymptotic expansions in these short time variables of the form

$$\hat{c}_{e,k} = \hat{c}_{e,k}^{(0)} + \mathcal{C}_e \hat{c}_{e,k}^{(1)} + \dots \tag{3.37}$$

etc. We shall only consider the analysis to determine the electrolyte concentration as the analysis for the other variables is trivial (i.e on the short timescale the solid concentration remains constant, and the current and potentials are given in the same form as before). At leading order, the electrolyte concentration equations (3.5) become

$$\epsilon_k \frac{\partial \hat{c}_{e,k}^{(0)}}{\partial \hat{t}} = -\gamma_e \frac{\partial \hat{N}_{e,k}^{(0)}}{\partial x}, \qquad\qquad k \in \{n, s, p\}, \tag{3.38a}$$

$$\hat{N}_{e,k}^{(0)} = -\epsilon_k^b D_e(\hat{c}_{e,k}^{(0)}) \frac{\partial \hat{c}_{e,k}^{(0)}}{\partial x}, \qquad\qquad k \in \{n, s, p\}, \tag{3.38b}$$

$$\hat{N}_{e,k}^{(0)} = 0, \quad x \in \partial\Omega_{ck,k}, \qquad\qquad k \in \{n, p\}, \tag{3.38c}$$

$$\hat{c}_{e,k}^{(0)} = \hat{c}_{e,s}^{(0)}, \quad \hat{N}_{e,k}^{(0)} = \hat{N}_{e,s}^{(0)}, \ x \in \partial\Omega_{k,s}, \quad k \in \{n, p\}, \tag{3.38d}$$

$$\hat{c}_{e,k}^{(0)}\big|_{\hat{t}=0} = 1, \qquad\qquad k \in \{n, s, p\}, \tag{3.38e}$$

which yields the solution

$$\hat{c}_{e,k}^{(0)} = 1 \tag{3.39}$$

and thus clearly satisfies the matching condition

$$\lim_{\hat{t} \to \infty} \hat{c}_{e,k}^{(0)} = \lim_{t \to 0} c_{e,k}^{(0)} \tag{3.40}$$

At $\mathcal{O}(\mathcal{C}_e)$, the electrolyte concentration equations (3.5) become

$$\epsilon_k \frac{\partial \hat{c}_{e,k}^{(1)}}{\partial \hat{t}} = -\gamma_e \frac{\partial \hat{N}_{e,k}^{(1)}}{\partial x} + \frac{\partial i_{e,k}^{(0)}}{\partial x}, \qquad k \in \{n, s, p\}, \tag{3.41a}$$

$$N_{e,k}^{(1)} = -\epsilon_k^b D_e(1) \frac{\partial \hat{c}_{e,k}^{(1)}}{\partial x} + \frac{t^+}{\gamma_e} i_{e,k}^{(0)}, \qquad k \in \{n, s, p\}, \tag{3.41b}$$

$$\hat{N}_{e,k}^{(1)} = 0, \quad x \in \partial\Omega_{ck,k}, \qquad k \in \{n, p\}, \tag{3.41c}$$

$$\hat{c}_{e,k}^{(1)} = \hat{c}_{e,s}^{(1)}, \; \hat{N}_{e,k}^{(1)} = \hat{N}_{e,s}^{(1)}, \quad x \in \partial\Omega_{k,s}, \quad k \in \{n, p\}, \tag{3.41d}$$

$$\hat{c}_{e,k}^{(1)}\big|_{\hat{t}=0} = 0, \qquad k \in \{n, s, p\}, \tag{3.41e}$$

where we have used $\hat{i}_{e,k}^{(0)} = i_{e,k}^{(0)}$ and $\hat{c}_{e,k}^{(0)} = 1$. We can see that this electrolyte concentration, $\hat{c}_{e,k}^{(1)}$ will satisfy the matching condition

$$\lim_{\hat{t} \to \infty} \hat{c}_{e,k}^{(1)} = c_{e,k}^{(1)}, \tag{3.41f}$$

because $c_{s,k}^{(1)}$ is the steady-state solution of (3.41). Since $i_{e,n}^{(0)} = \frac{x\mathcal{I}}{L_n}$, $i_{e,s}^{(0)} = \mathcal{I}$, and $i_{e,p}^{(0)} = \frac{(1-x)\mathcal{I}}{L_p}$ and $\mathcal{I}$ is in general a function of time, it is most appropriate to solve (3.41) using computational methods. The most general approach is to consider a composite electrolyte problem that is valid on both the electrolyte diffusion timescale and the discharge timescale. To do this, we write the composite variables

$$c_{e,k}^{(c)} = \underbrace{\hat{c}_{e,k}^{(1)}}_{\text{Short time}} + \underbrace{c_{e,k}^{(1)}}_{\text{Long time}} - \underbrace{c_{e,k}^{(1)}}_{\text{Matched}} = \hat{c}_{e,k}^{(1)} \tag{3.42a}$$

$$N_{e,k}^{(c)} = \underbrace{\hat{N}_{e,k}^{(1)}}_{\text{Short time}} + \underbrace{N_{e,k}^{(1)}}_{\text{Long time}} - \underbrace{N_{e,k}^{(1)}}_{\text{Matched}} = \hat{N}_{e,k}^{(1)}. \tag{3.42b}$$

Therefore, the composite problem, written in terms of t, is given by

$$\mathcal{C}_e \epsilon_k \frac{\partial c_{e,k}^{(c)}}{\partial t} = -\gamma_e \frac{\partial N_{e,k}^{(c)}}{\partial x} + \frac{\partial i_{e,k}^{(0)}}{\partial x}, \qquad k \in \{n, s, p\}, \tag{3.43a}$$

$$N_{e,k}^{(c)} = -\epsilon_k^b D_e(1) \frac{\partial c_{e,k}^{(c)}}{\partial x} + \frac{t^+}{\gamma_e} i_{e,k}^{(0)}, \qquad k \in \{n, s, p\}, \tag{3.43b}$$

$$N_{e,k}^{(c)} = 0, \quad x \in \partial\Omega_{ck,k}, \qquad k \in \{n, p\}, \tag{3.43c}$$

$$c_{e,k}^{(c)} = c_{e,s}^{(c)}, \; N_{e,k}^{(c)} = N_{e,s}^{(c)}, \; x \in \partial\Omega_{k,s}, \quad k \in \{n, p\}, \tag{3.43d}$$

$$c_{e,k}^{(c)}\big|_{t=0} = 0, \qquad k \in \{n, s, p\}. \tag{3.43e}$$

We can then use this composite form in the expressions derived in the previous section with $c_{e,k}^{(1)}$ replaced by $c_{e,k}^{(c)}$.

As an aside, in the particular case where $\mathcal{I}$ is a constant and $\epsilon_n = \epsilon_s = \epsilon_p$, (3.41) can be solved by separation of variables, with the solution given by

$$
\begin{aligned}
\hat{c}_{e,k}^{(1)} &= c_{e,k}^{(1)} \\
&+ \sum_{m=1}^{\infty} \alpha_m \exp\left(-\gamma_e \epsilon_k^{b-1} D_e(1)\pi^2 m^2 \hat{t}\right) \sin(m\pi x),
\end{aligned}
\tag{3.44a}
$$

$$
\alpha_m = -2 \int_0^1 c_{e,k}^{(1)} \sin(m\pi x)\mathrm{d}x.
\tag{3.44b}
$$

For a constant current discharge, we found that taking the first term in this series accurately recovered the predicted terminal voltage. A similar solution can also be found for a jump between two arbitrary constant currents.

3.5.5 *Summary of the single-particle model with electrolyte*

The dimensionless version of the single-particle model with electrolyte (SPMe) is given by a combination of the leading-order equations (3.10), (3.13b), and (3.15)-(3.20) and the first-order equations (3.32), (3.34), (3.35), (3.35e), (3.35f), and (3.43). Note that we make use of the composite electrolyte concentration equations. Similar to how we treated the SPM, we now summarise the SPMe in dimensional form. We shall combine leading and first-order equations where convenient to present a condensed and easy to interpret form of the model. We will also make two small modifications to the model, that we have found help the model perform better in certain situations.The first modification involves noticing that

$$
D_e(c_{e,k}^{(0)}) = D_e(c_{e,k}^{(0)} + \mathcal{C}_e c_{e,k}^{(c)}) + \mathcal{O}(\mathcal{C}_e).
\tag{3.45}
$$

Therefore, we can replace the linear diffusion coefficient in the first-order composite electrolyte diffusion equation (3.43) by its nonlinear counterpart whilst maintaining $\mathcal{O}(\mathcal{C}_e^2)$ accuracy. The second modification is to notice that

$$
\log\left(\frac{1 + \mathcal{C}_e c_{e,k}^{(1)}}{1 + \mathcal{C}_e \bar{c}_{e,k}^{(1)}}\right) = \mathcal{C}_e(c_{e,k}^{(1)} - \bar{c}_{e,k}^{(1)}) + \mathcal{O}(\mathcal{C}_e^2).
\tag{3.46}
$$

Therefore, we can absorb the terms of the form $(c_{e,k}^{(1)} - \bar{c}_{e,k}^{(1)})$ in (3.35) into a combined-order expression involving 'log' whilst maintaining $\mathcal{O}(\mathcal{C}_e^2)$ accuracy. Both of these modifications reverse the linearisation of nonlinear functions performed during our asymptotic analysis.

In the following, we state the dimensional SPMe. The combined leading- and first-order electrode-averaged lithium concentration in the active material is given by the problem

$$\frac{\partial \bar{c}^*_{s,k}}{\partial t^*} = -\frac{1}{(r^*)^2}\frac{\partial}{\partial r^*}\left((r^*)^2 \bar{N}^*_{s,k}\right), \quad k \in \{n, p\} \tag{3.47a}$$

$$\bar{N}^*_{s,k} = -D^*_{s,k}(\bar{c}^*_{s,k})\frac{\partial \bar{c}^*_{s,k}}{\partial r^*}, \quad k \in \{n, p\}, \tag{3.47b}$$

$$\bar{N}^*_{s,k}\big|_{r^*_k=0} = 0, \quad \bar{N}^*_{s,k}\big|_{r^*_k=R^*_k} = \begin{cases} \frac{\mathcal{I}^*}{F^* a^*_n L^*_n}, & k = n, \\[2mm] -\frac{\mathcal{I}^*}{F^* a^*_p L^*_p}, & k = p, \end{cases} \tag{3.47c}$$
$$k \in \{n, p\},$$

$$\bar{c}^*_{s,k}\big|_{t^*=0} = c^*_{s,k,0}, \quad k \in \{n, p\}; \tag{3.47d}$$

and in the electrolyte, we have the combined leading- and first-order problem

$$\epsilon_k \frac{\partial c^*_{e,k}}{\partial t^*} = -\frac{\partial N^*_{e,k}}{\partial x^*} + \begin{cases} \frac{\mathcal{I}^*}{F^* L^*_n}, & k = n, \\[2mm] 0, & k = s, \quad k \in \{n, s, p\}, \\[2mm] -\frac{\mathcal{I}^*}{F^* L^*_p}, & k = p, \end{cases} \tag{3.47e}$$

$$N^*_{e,k} = -\epsilon^b_k D^*_e(c^*_{e,k})\frac{\partial c^*_{e,k}}{\partial x^*} + \begin{cases} \frac{x^* t^+ \mathcal{I}^*}{F^* L^*_n}, & k = n, \\[2mm] \frac{t^+ \mathcal{I}^*}{F^*}, & k = s, \\[2mm] \frac{(L^* - x^*) t^+ \mathcal{I}^*}{F^* L^*_p}, & k = p, \end{cases} \tag{3.47f}$$
$$k \in \{n, s, p\},$$

$$\begin{aligned} N^*_{e,k} &= 0, & x^* &\in \partial\Omega^*_{ck,k}, & k &\in \{n, p\}, & &\text{(3.47g)} \\ c^*_{e,k} &= c^*_{e,s}, & x^* &\in \partial\Omega^*_{k,s}, & k &\in \{n, p\}, & &\text{(3.47h)} \\ N^*_{e,k} &= N^*_{e,s}, & x^* &\in \partial\Omega^*_{k,s}, & k &\in \{n, p\}, & &\text{(3.47i)} \\ c^*_{e,k}\big|_{t^*=0} &= c^*_{e,0}, & & & k &\in \{n, s, p\}. & &\text{(3.47j)} \end{aligned}$$

The combined leading- and first-order voltage is given by

$$\mathcal{V}^* = \bar{U}^*_{eq} + \bar{\eta}^*_r + \bar{\eta}^*_c + \bar{\Delta\Phi}^*_{Elec} + \bar{\Delta\Phi}^*_{Solid}, \tag{3.47k}$$

where $\bar{U}_{eq}$ is the combined leading- and first-order electrode-averaged OCV and is given by

$$\bar{U}^*_{eq} = U^*_p\left(\bar{c}^*_{s,p}\big|_{r^*=R^*_p}\right) - U^*_n\left(\bar{c}^*_{s,n}\big|_{r^*=R^*_n}\right); \tag{3.47l}$$

$\bar{\eta}_r^*$ is the combined leading- and first-order electrode-averaged reaction overpotential and is given by

$$\bar{\eta}_r^* = \bar{\eta}_p^* - \bar{\eta}_n^* \tag{3.47m}$$

$$\bar{\eta}_n^* = \frac{2R_g^* T_\infty^*}{F^*} \sinh^{-1}\left(\frac{\mathcal{I}^*}{a_n^* \bar{j}_{0,n}^* L_n^*}\right), \tag{3.47n}$$

$$\bar{\eta}_p^* = -\frac{2R_g^* T_\infty^*}{F^*} \sinh^{-1}\left(\frac{\mathcal{I}^*}{a_p^* \bar{j}_{0,p}^* L_p^*}\right), \tag{3.47o}$$

where $\bar{j}_{0,n}^*$ and $\bar{j}_{0,p}^*$ are the combined leading and first-order average negative and positive exchange current densities given by

$$\bar{j}_{0,n}^* = \frac{m_n^*}{L_n^*} \int_0^{L_n^*} (c_{s,n}^*)^{1/2} (c_{s,n,max}^* - c_{s,n}^*)^{1/2} (c_{e,n}^*)^{1/2} \, dx^*, \tag{3.47p}$$

$$\bar{j}_{0,p}^* = \frac{m_p^*}{L_p^*} \int_{L^* - L_p^*}^{L^*} (c_{s,p}^*)^{1/2} (c_{s,p,max}^* - c_{s,p}^*)^{1/2} (c_{e,p}^*)^{1/2} \, dx^*. \tag{3.47q}$$

The combined leading- and first-order electrolyte concentration overpotential is given by

$$\bar{\eta}_c^* = 2(1 - t^+)\frac{R_g^* T_\infty^*}{F^*} \log\left(\frac{\bar{c}_{e,p}^*}{\bar{c}_{e,n}^*}\right); \tag{3.47r}$$

the combined leading- and first-order electrolyte Ohmic losses are

$$\overline{\Delta\Phi}_{Elec}^* = -\frac{\mathcal{I}^*}{\kappa_e^*(c_{e,0}^*)}\left(\frac{L_n^*}{3\epsilon_n^b} + \frac{L_s^*}{\epsilon_s^b} + \frac{L_p^*}{3\epsilon_p^b}\right); \tag{3.47s}$$

and the combined leading- and first-order solid-phase Ohmic losses are

$$\overline{\Delta\Phi}_{Solid}^* = -\frac{\mathcal{I}^*}{3}\left(\frac{L_p^*}{\sigma_p^*} + \frac{L_n^*}{\sigma_n^*}\right). \tag{3.47t}$$

The remaining key variables are given by the following algebraic expressions. The combined leading- and first-order negative and positive electrode potentials are given by

$$\phi_{s,n}^* = -\frac{\mathcal{I}^* x^*}{2\sigma_n^* L_n^*}(2L_n^* - x^*), \tag{3.47u}$$

$$\phi_{s,p}^* = \mathcal{V}^* + \frac{\mathcal{I}^*(x^* - L_x^*)(L_x^* - 2L_p^* - x^*)}{2\sigma_p^* L_p^*}; \tag{3.47v}$$

the combined leading- and first-order electrolyte potential is given by

$$
\phi_{e,n}^* = \Phi_e^* + 2(1 - t^+)\frac{R_g^* T_\infty^*}{F^*} \log\left(\frac{c_{e,n}^*}{\bar{c}_{e,n}^*}\right)
$$
$$
- \frac{\mathcal{I}^*}{\kappa_e^*(c_{e,0}^*)}\left(\frac{(x^*)^2 - (L_n^*)^2}{2\epsilon_n^b L_n^*} + \frac{L_n^*}{\epsilon_s^b}\right),
$$
(3.47w)

$$
\phi_{e,s}^* = \Phi_e^* + 2(1 - t^+)\frac{R_g^* T_\infty^*}{F^*} \log\left(\frac{c_{e,s}^*}{\bar{c}_{e,n}^*}\right) - \frac{\mathcal{I}^* x^*}{\kappa_e^*(c_{e,0}^*)\epsilon_s^b},
$$
(3.47x)

$$
\phi_{e,n}^* = \Phi_e^* + 2(1 - t^+)\frac{R_g^* T_\infty^*}{F^*} \log\left(\frac{c_{e,p}^*}{\bar{c}_{e,n}^*}\right)
$$
$$
- \frac{\mathcal{I}^*}{\kappa_e^*(c_{e,0}^*)}\left(\frac{x^*(2L_x^* - x^*) + (L_p^*)^2 - (L_x^*)^2}{2\epsilon_p^b L_p^*}\right.
$$
$$
\left. + \frac{L_x^* - L_p^*}{\epsilon_s^b}\right),
$$
(3.47y)

where

$$
\Phi_e^* = \bar{\phi}_{s,n} - \bar{\eta}_n + \frac{\mathcal{I}^* L_n^*}{\kappa_e(c_{e,0}^*)}\left(\frac{1}{\epsilon_n^b} - \frac{1}{\epsilon_s^b}\right);
$$

and the combined leading- and first-order average negative and positive interfacial current densities are given by

$$
\bar{j}_n^* = \frac{\mathcal{I}^*}{F^* a_n^* L_n^*}, \quad \bar{j}_p^* = -\frac{\mathcal{I}^*}{F^* a_p^* L_p^*}.
$$
(3.47z)

Written in this form, we can see that the SPMe adopts the OCV predicted by the SPM but also corrects for electrolyte effects in the reaction overpotential, concentration overpotential, and electrolyte Ohmic losses in the voltage expression (2.50). The SPMe also accounts for the solid-phase Ohmic losses. There is a key difference in how we should interpret the active material equations in the SPM and the SPMe, which is why we have written the SPMe equations with an 'overbar' and the SPM equation without an 'overbar'. In the SPM, all active material particles behave in the same way and therefore we can solve for the concentration in a single *representative* particle. However, for the SPMe, we only solve for a *theoretical average* particle and are not necessarily determining the concentration in any particular particle. Without making this distinction, one may have chosen to evaluate the voltage by considering a particular path through the cell as in (2.49), which does not guarantee the same asymptotic accuracy. We will see in following sections that this error is implemented in the ad-hoc versions of the SPMe.

3.6 MODEL COMPARISON

3.6.1 *Finite-volume implementation*

In this section, we compare the DFN model (as given by (2.33), (2.35), (2.36), (2.41), and (2.42)), SPM (3.21), and the SPMe (3.47). We implement the DFN model by discretising the spatial dimensions using the finite-volume method to convert the system of PDEs into a system of differential-algebraic equations (DAEs) of index one. Before solving this system, a set of consistent initial conditions for the potentials are found numerically using Newton's method. The time evolution of the system is then performed using the SUNDIALs DAE solvers interfaced through PyBaMM [29], [86]. Similarly, we use the finite-volume method to discretise the spatial dimensions of the SPM and SPMe and again use SUNDIALs for the time evolution. We use the same mesh to discretise the SPM, SPMe, and DFN model. In the x^*-direction, we use 30 points in the negative electrode, 20 points in the separator, and 30 points in the positive electrode. In the r^*-direction, we use 15 points. Numerical errors associated with the spatial discretisation, are therefore of order 10^{-2}. However, we have limited their influence upon the comparison by applying the same numerical method to each model and checking convergence. Since we aim to compare models and not numerical methods, we only concern ourselves with the relative reduction in computational complexity obtained by using the SPMe instead of the DFN model, whilst retaining the same numerical method. Here, we use the finite-volume method, but of course, alternative methods could be applied to both models to further increase speed and/or reduce memory requirements of each.

Computational complexity consists of space complexity (memory) and time complexity. To demonstrate the reduction in space complexity, we consider our finite-volume implementation with 30 points in the electrodes, 20 points in the separator, and 15 points in the particles. In this case, the DFN model requires $2 \times (30 \times 15) = 900$ states for the concentration of lithium in the particles, 80 states for the concentration of lithium ions in the electrolyte, 80 states for the electrolyte potential, and 60 states for the electrode potentials. This leads to a total of 1120 internal states, which are to be stored at each time step. On the other hand, the SPMe requires only 30 states for the concentration of lithium in the particles and 80 states for the concentration of lithium ions in the electrolyte. Therefore, for this discretisation, the SPMe requires just over 10% of the memory required by the DFN model. With regards to time complexity, the DFN model is limited in two respects. Firstly, it is limited by the large number of states which must be computed at every time step and secondly it is limited by the stiff nature of the system, which arises from the discretisation of the mixed parabolic and elliptic PDEs resulting in a system of DAEs. As previously discussed,

the SPMe addresses the first of these limitations. It also addresses the second limitation because the model consists of three parabolic PDEs, which upon discretisation lead to a well-conditioned system of ODEs amenable to taking larger time steps than the stiff DAE system of the DFN model. Furthermore, being a system of DAEs the DFN model suffers from convergence issues if inconsistent initial conditions are provided or if there is a large change in current, for example, in switching between charging and discharging. This is an inherent issue with DAE based algorithms and efforts have been made to limit the range of inconsistent initial conditions [50]. However, this robustness problem persists and convergence of the DFN model cannot always be ensured for non-constant currents.

3.6.2 *Voltage comparison*

We compare the SPM, SPMe, and DFN model by considering the case of a single constant-current discharge over a range of C-rates. The initial stoichiometries of the negative and positive electrodes are 0.8 and 0.6, respectively, and we terminate the discharge when the terminal voltage reaches 3.2 V. For this cell, a C-rate of 1 C corresponds to a discharge current density of 24 A/m^2. As provided in Tables 3.3 and 2.2, we have $\mathcal{C}_e = 5.1 \times 10^{-3}\mathcal{C}$ where $\mathcal{C}$ is the C-rate. The predicted terminal voltage of each model is presented in Figure 3.1 and root mean square (RMS) errors in Table 3.5.
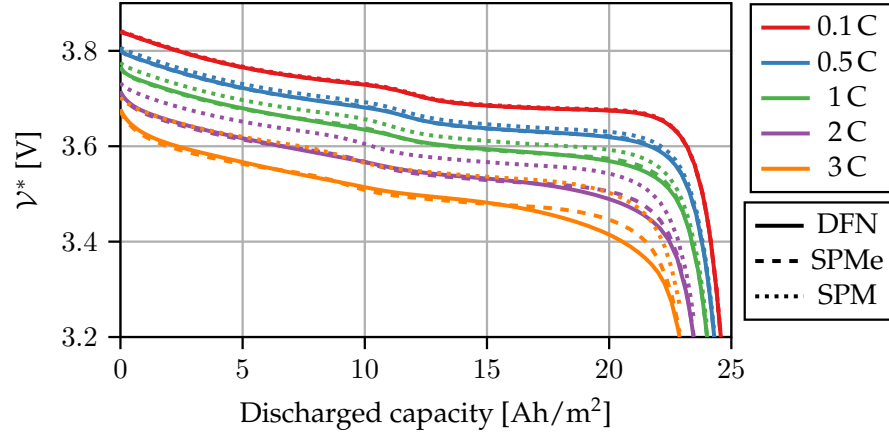
Figure 3.1: Constant-current discharge comparison of DFN model (as given by (2.33), (2.35), (2.36), (2.41)), SPM (3.21), and SPMe (3.47) over a range of typical C-rates. The RMS voltage error for the reduced models with respect to the DFN model is provided in Table 3.5.

At low C-rates, all three models match well with an RMS voltage error of just 1.72 mV for the SPM at 0.1 C. However, at higher C-rates we observe that the SPM prediction deviates from the DFN model solution, producing an RMS voltage error of 19.86 mV at 1 C and 62.78 mV at 3 C. The SPMe greatly improves upon this, with a RMS voltage error

	0.1 C	0.5 C	1 C	2 C	3 C
SPM	1.72 mV	9.62 mV	19.86 mV	40.67 mV	62.78 mV
SPMe	0.17 mV	1.34 mV	3.04 mV	7.36 mV	13.34 mV

Table 3.5: RMS voltage error between the reduced models and the DFN model for the finite-volume implementation with 30 points in each domain.

of just 3.04 mV at 1 C and 13.34 mV at 3 C. Unfortunately, there is a discrepancy in the voltage curves near then end of the discharge at 3 C. To investigate the source of this discrepancy, we plot the error in each component of the voltage during a 3 C discharge in Figure 3.2.
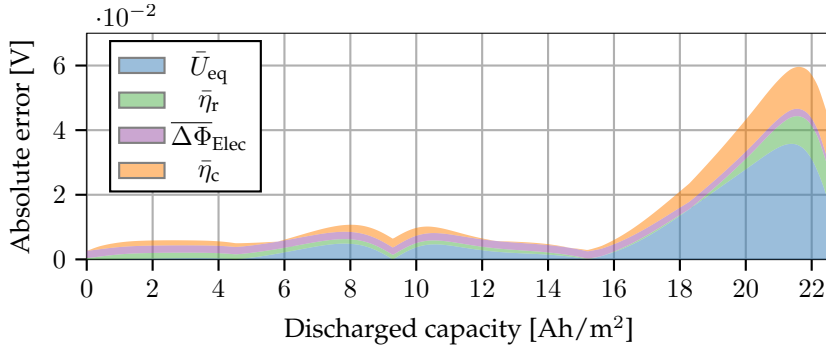
Figure 3.2: Voltage component errors of the SPMe vs. DFN.

We observe that for the majority of the discharge all components of the SPMe voltage agree well with the voltage predicted by the DFN model. However, near the end of the discharge, there is a large increase in the error of our solution, as observed in Figure 3.1. Around 60-70% of this error is due to a poor estimation of the electrode-averaged OCV. This error occurs when the OCV becomes highly nonlinear. If we extend our asymptotic expansion of the OCP, $U_k(c_k)$, to second order, we obtain the term $\mathcal{C}_e^2 U_k''(c_{s,k}^0)(c_{s,k}^1)^2/2$. Hence, when the OCV is highly nonlinear, $U_k''(c_{s,k}^0)$ becomes large and the higher-order terms neglected from the SPMe become significant. We account for this behaviour later but the resulting model requires a significantly larger computational budget than the SPM and SPMe.

3.6.3 *Grid dependence and computation time*

In Figure 3.3, we compare the solutions of the SPMe and DFN model with 5, 10, 20 and 30 points in each domain (negative electrode, separator, positive electrode, negative particle, positive particle) across a range of C-rates. Here, we measure the RMS voltage error against the DFN model solution with 30 points in each domain. It is important here to only focus upon the relative timings of the models and not absolute times. It should also be noted that this comparison is for a

constant-current discharge; the non-constant case has been reported to give rise to even longer computation times for the DFN model [13]. The key observation from Figure 3.3 is that for a relatively small increase in RMS voltage error, particularly at low C-rates, an order of magnitude decrease in computation time is achieved by using the SPMe instead of the DFN model. Achieving such large decreases in computation time is consistent across all C-rates and numbers of grid points used. Further, we can observe that the SPMe generally increases the accuracy of the SPM by an order of magnitude for a particular C-rate whilst maintaining a similar computation time. When a small number of grid points (e.g. 10 points) are used, and a current above 0.5 C is applied, the SPMe produces a solution that is not limited by the discretisation error. Therefore, to achieve the asymptotic accuracy of the SPMe, a coarser spatial discretisation is often sufficient, which allows for further increases in speed and savings in memory.
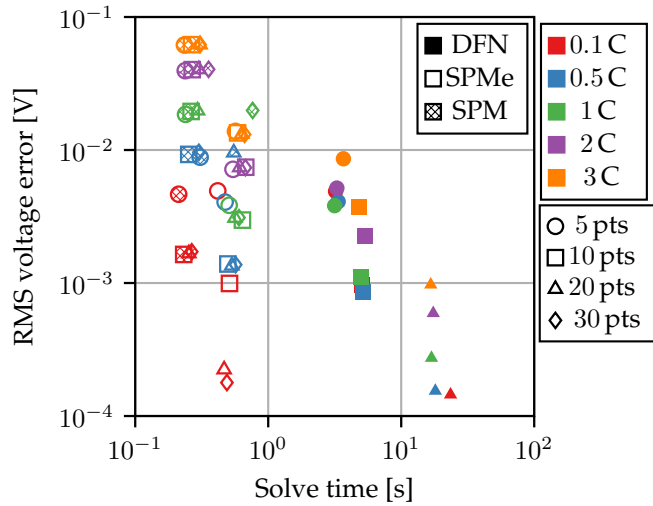
Figure 3.3: RMS voltage error relative to the DFN model with 30 x^*-grid points in each of the domains: negative electrode, separator, and positive electrode; as well as 30 r^*-grid points in the particles. This reference model with 30 points in each domain has an average (across C-rates) run time of 120 s. Here, 'n pts' refers to n points in each of the domains: negative electrode, separator, and positive electrode as well as n points in each of the particles.

3.6.4   *Comparison of internal states*

To further confirm the accuracy of the SPMe, we compare the internal states predicted by the SPMe and DFN model. These are presented for a 1 C constant current discharge in Figure 3.4. We observe good agreement between the two sets of model predictions. The apparent discrepancy in the negative electrode potential is only due to the scale employed in Figure 3.4. This discrepancy is in fact $\mathcal{O}(\mathcal{C}_e^2)$. The discrepancy in the negative electrode stoichiometry is a result of the SPMe
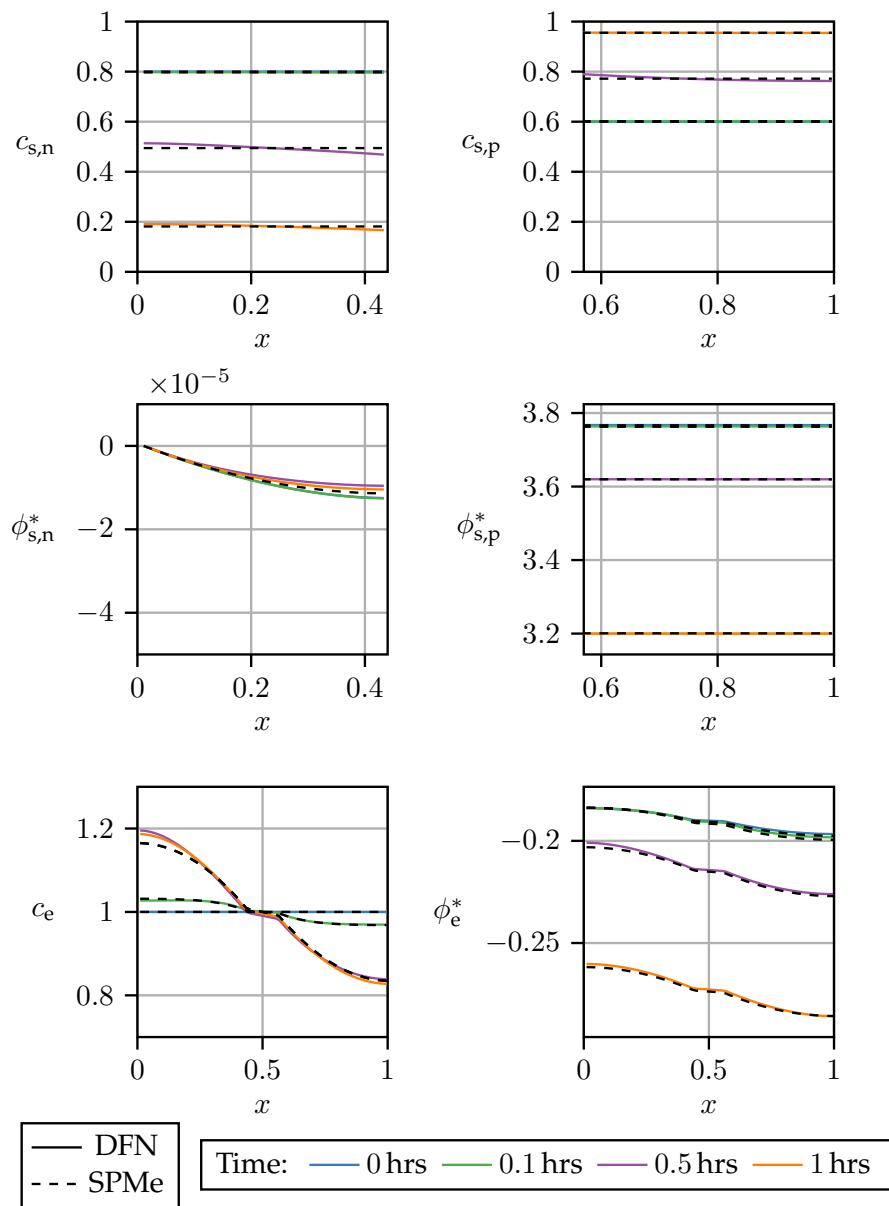
Figure 3.4: Comparison of DFN model and SPMe internal states during a 1 C constant current discharge. The DFN model solution is given by the solid lines and the SPMe solution by the closest black dashed line. Note that some of the black dashed lines lie upon others so it appears that there are fewer black dashed lines than solid lines.

using only the leading-order equations in $\mathcal{C}_e$ within the electrode particles; this is equivalent to considering only the electrode-averaged concentration in the particles. This is the same approximation as employed by the SPM and the SPMe is therefore only accurate to $\mathcal{O}(\mathcal{C}_e)$ for the concentration in the particles.

In Figure 3.5, we compare the internal states of the SPMe and DFN model across a range of C-rates. Here, we display the lithium concentration in the x^*-averaged particle to demonstrate the ability of our model to capture the concentration profile inside particles as well as the surface concentration. We observe good agreement of the internal states, with the exception the electrolyte potentials at large C-rates, which is a result of the assumption of high electrolyte conductivity.

3.6.5 *Drive cycle comparison*

Whilst comparing the models using a constant current discharge is useful for gaining insight into where discrepancies occur, it is not fully representative of an actual cell use case. To replicate actual operating conditions better, we run the DFN, SPMe, and SPM on the US06 standard test drive cycle. The input current density is presented in Figure 3.6 and ranges from $-50\,\mathrm{A\,m^{-2}}$ to $100\,\mathrm{A\,m^{-2}}$, where a negative current corresponds to charging. Therefore, this cycle has a max C-rate of just over $5\,\mathrm{C}$. This input current density profile corresponds to an initial charge of the cell followed by a rest period just before the thirty-second mark. After this rest period, the car begins the driving phase, drawing a positive current from the cell. Occasionally, a negative current is observed during the driving phase which is a result of regenerative braking recharging the cell.

In Figures 3.6 (b) and (c), we can see clearly that the SPMe performs significantly better than the SPM at recovering the voltage of the DFN. In particular, we observe an order of magnitude reduction in error across the entire drive cycle. We can also observe that on regions of high current, the poorer performance of the SPM is more pronounced. This reduction in error can be important for SoC estimation algorithms because even small variations in the voltage prediction can be misinterpreted as large variations in the SoC.
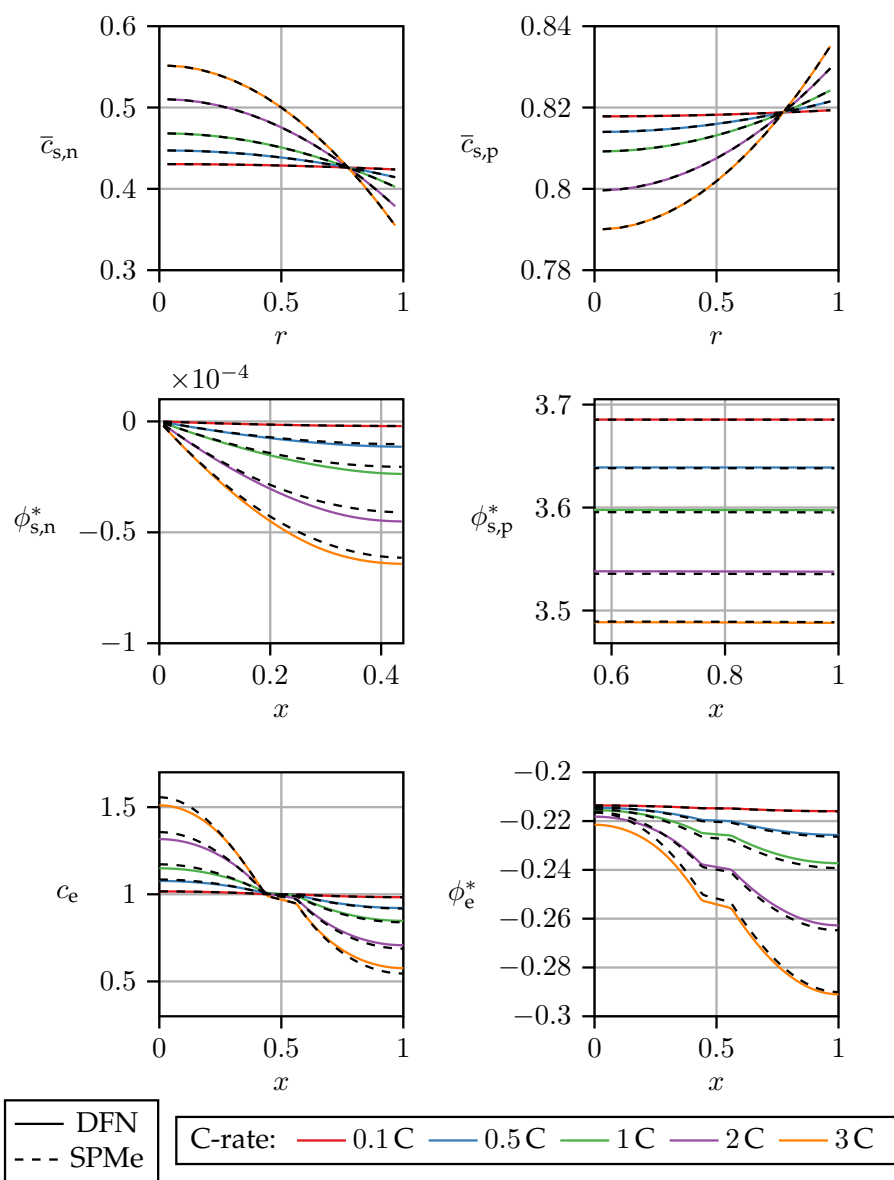
Figure 3.5: Comparison of internal state across multiple C-rates after a discharged capacity of $15\,\mathrm{Ah/m^2}$. The DFN model solution is given by the solid lines and the SPMe solution by the closest black dashed line. Note that we plot the x^*-averaged particle concentration here instead of the surface concentration plotted in Figure 3.4.
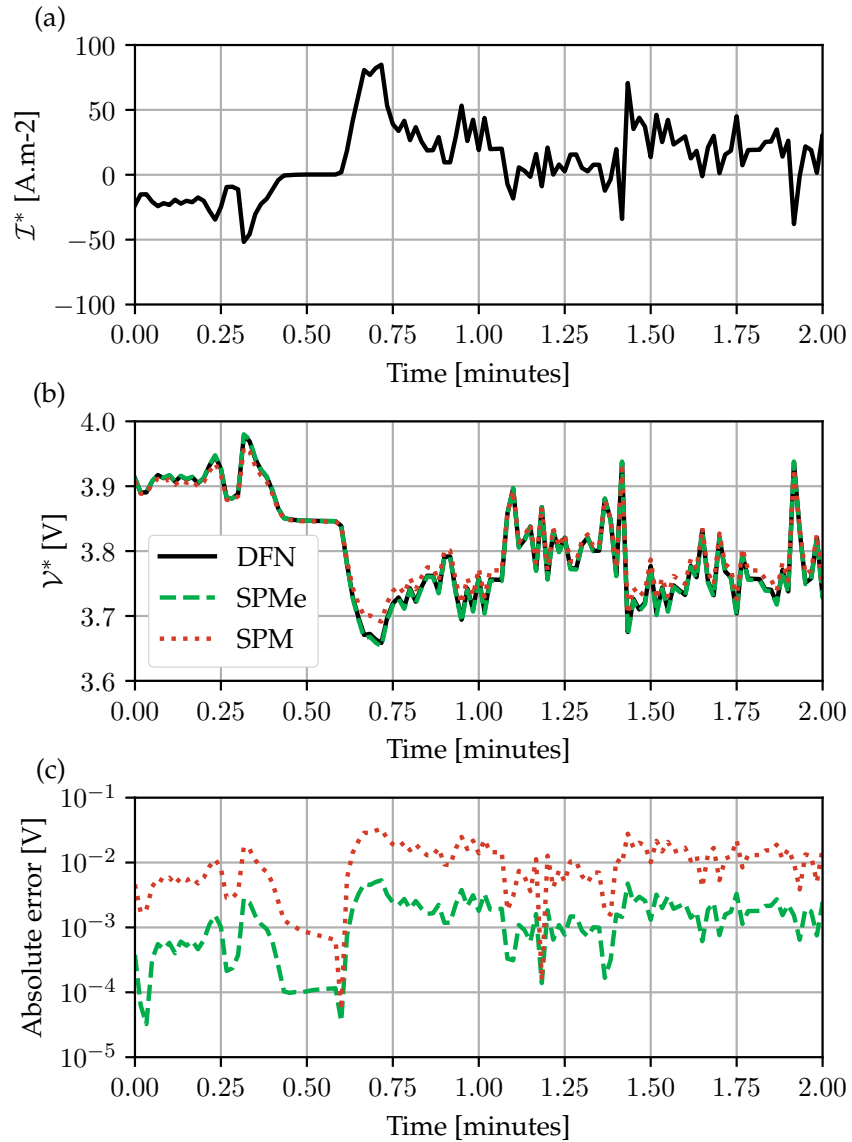
Figure 3.6: Comparison of DFN, SPMe, and SPM running a two minute snapshot of the US06 standard drive cycle: (a) Input current density for each model; (b) predicted voltage; (c) SPMe vs DFN, SPM vs DFN voltage errors.

3.7 ALTERNATIVE VERSIONS OF THE SPME

3.7.1 *Comparison with ad-hoc models*

Several alternative models in the literature extend the SPM in an ad-hoc manner to account for electrolyte effects [27], [36], [61], [67], [68], [88]. In this section, we highlight the key differences between these models and the asymptotic SPMe (3.47) presented here. We have chosen to compare a subset of the models, which cover the variety of ad-hoc models available of similar computational complexity. In some papers, the model is discretised during development. We view the choice of discretisation to be a numerical method instead of a feature of the model itself. Therefore, we have converted each model into the continuum form to highlight the differences in the underlying models. We do not aim to study the benefits and drawbacks of different numerical methods.

A common theme in the literature is to implicitly replace the electrode-averaged concentration overpotential and electrode-averaged electrolyte Ohmic losses with pointwise versions but still use the OCV and reaction overpotential obtained from the active material solution in a single particle. It is also common to neglect the solid-phase Ohmic losses (this is a reasonable assumption since we have already observed this to be small). The general form of the voltage expression used in the literature is

$$\mathcal{V}^* = \bar{U}_{\text{eq}}^* + \bar{\eta}_{\text{r}}^* + \eta_{\text{c}}^*\big|_{x_{\text{n}}^*=0,x_{\text{p}}^*=L_x^*} + \Delta\Phi_{\text{Elec}}^*\big|_{x_{\text{n}}^*=0,x_{\text{p}}^*=L_x^*}. \tag{3.48}$$

This expression consists of a combination of both electrode-averaged and pointwise terms, and therefore accuracy of $\mathcal{O}(\mathcal{C}_{\text{e}}^2)$ cannot be ensured. This error arises because the single particle in the SPMe is taken to mean a representative particle (i.e. all particles behave the same) instead of a theoretical average particle and so the ad-hoc models simply choose a particular current path to evaluate the voltage. To make matters worse, they often choose a path involving particles adjacent to the current collectors where the true particle concentration is the furthest from the average.

We begin by considering the model proposed by Perez et. al. in [61]. In this model, the electrode-averaged concentration overpotential (3.47r) and the electrode-averaged electrolyte Ohmic losses (3.47s) are replaced by the pointwise versions

$$\eta_c^*\big|_{x_{\text{n}}^*=0,x_{\text{p}}^*=L_x^*} = 2(1-t^+)\frac{R_{\text{g}}^*T_{\infty}^*}{F^*}\log\left(\frac{c_{\text{e,p}}^*\big|_{x^*=L_x^*}}{c_{\text{e,n}}^*\big|_{x^*=0}}\right), \tag{3.49a}$$

$$\Delta\Phi_{\text{Elec}}^*\big|_{x_{\text{n}}^*=0,x_{\text{p}}^*=L_x^*} = -\frac{\mathcal{I}^*}{2\bar{\kappa}_{\text{e,eff}}^*}\left(L_{\text{n}}^* + 2L_{\text{s}}^* + L_{\text{p}}^*\right), \tag{3.49b}$$

respectively (note that to get (3.49b) we have corrected the sign of the expression in [61]). Here, $\bar{\kappa}^*_{\text{e,eff}}$ is the effective conductivity averaged across the entire cell, with the x^*-averaged effective conductivity defined as

$$\kappa^*_{\text{e,eff}} = \sum_{\text{k=n,s,p}} \frac{L^*_k}{L^*_x} \epsilon^b_k \bar{\kappa}^*_{\text{e,k}}(c^*_{\text{e,k}}).$$

The voltage is then given by (3.48). Additionally, (3.49b) requires that $\kappa^*_{\text{e,eff}} \approx \bar{\kappa}^*_{\text{e,eff}}$ throughout the cell. With this assumption, $\mathcal{O}(\mathcal{C}^2_e)$ accuracy cannot be ensured for all values of ϵ_n, ϵ_s, and ϵ_p. Finally, solid-phase Ohmic losses are neglected and Ohmic losses due to the presence of SEI are included; we shall neglect the SEI terms in our comparisons, noting that (3.47) can be easily extended to include them.

The model presented by Prada et. al. [67] also employs (3.49a) for the concentration overpotential but the electrolyte Ohmic losses are taken to be

$$\Delta\Phi^*_{\text{Elec}}\big|_{x^*_n=0, x^*_p=L^*_x} = -\frac{\mathcal{I}^*}{2}\left(\frac{L^*_n}{\epsilon^b_n\bar{\kappa}^*_{\text{e,n}}} + 2\frac{L^*_s}{\epsilon^b_s\bar{\kappa}^*_{\text{e,s}}} + \frac{L_p}{\epsilon^b_p\bar{\kappa}^*_{\text{e,p}}}\right), \quad (3.50)$$

where $\bar{\kappa}^*_{\text{e,k}}$ is the electrolyte conductivity averaged over region k. Whilst (3.50) does not rely upon the assumption that $\kappa^*_{\text{e,eff}} \approx \bar{\kappa}^{\text{eff}}_e$, its form is still a result of considering the pointwise electrolyte potential difference instead of the electrode-averaged difference. In addition to these differences, Prada et. al. [67] take the average exchange-current densities $\bar{j}^*_{0,n}$ and $\bar{j}^*_{0,p}$ to be constant. In terms of accurately reproducing the results of the DFN model, this simplification has a clear disadvantage as the reaction overpotentials are strong functions of the lithium and lithium-ion concentrations.

The model developed by Han et. al [27] is the same as that presented by Prada et. al. [67] without the additional assumption of constant exchange-current densities. That is, Han et. al. [27] employ (3.49a) and (3.50), which are the pointwise concentration overpotential, and electrolyte Ohmic losses, respectively. Han et. al. [27] note the tendency for their model to over-correct the voltage. We suspect the use of pointwise terms is the cause.

The model presented by Kemper et. al. [36] is somewhat different from the others we have discussed. Firstly, the model is presented as a set of ODEs instead of PDEs. These ODEs are derived by spatially discretising the underlying PDEs. Whilst this particular discretisation may be useful, we consider this to be a numerical method and not a feature of the model itself. Since we aim to compare the underlying simplified models directly, we have converted these ODEs back into PDEs. The resulting PDEs that describe the concentrations in the electrode particles and the electrolyte are equivalent to those used in our model. However, the expression for the terminal voltage is different

and it is not clear how to prescribe meaning to each of the individual components in the way we have done here. The full statement of these equations can be found in our paper [48].

We compare the variations of the SPMe in the literature and our asymptotic SPMe. For this section, we use a finite-volume implementation of each of the models implemented in MATLAB with ODE15s being used for the time integration. We consider a range of constant-current discharge rates and then consider the RMS voltage error of each model relative to the DFN model. For each model, we discretise using 30 points in each electrode, 20 in the separator, and 15 in each particle. Our results are presented in Figure 3.7, where we compare the models in [27], [36], [61]. Each version of the SPMe consists of three parabolic PDEs, one in the negative particle, one in the positive particle, and one in the electrolyte alongside an algebraic expression for the voltage. As a result, each SPMe must store $2 \times 15 + (30 + 20 + 30) = 120$ states at each time step. Therefore, the memory requirements of each model are similar. Upon evaluation, each version of the model takes on average 0.07 s. We observe that across all discharge rates, the asymptotic SPMe outperforms the ad-hoc models from the literature. In particular, the asymptotic SPMe is consistently an order of magnitude more accurate than the models in Perez et. al. [61] and Kemper et. al [36]. Furthermore, at higher C-rates, the RMS voltage errors in the models from the literature approach being of the order of 0.1 V whereas the RMS voltage errors of our SPMe only reach the order of 0.01 V. Additionally, as we would expect, our model converges to the DFN model solution at a faster rate than the other models. We attribute the main gains of our model to the consistent electrode-averaged OCPs, overpotentials, and Ohmic losses in our terminal voltage expression.
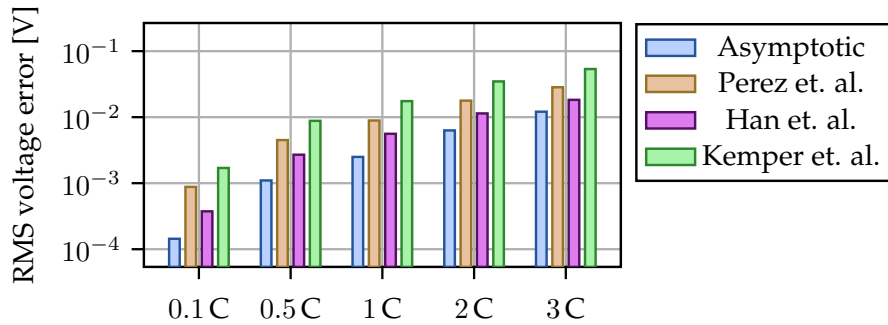
Figure 3.7: Comparison of versions of the SPMe: Asymptotic (3.47), Perez et. al. [61], Han et. al. [27], and Kemper et. al. [36]. The models are compared by considering the RMS voltage error of the simplified model voltage prediction vs the DFN model.

3.7.2   *Comparison with the corrected single particle model*

In [75], an alternative asymptotic limit was explored that also gives rise of a variant of the SPMe. The limit taken in [75] corresponds to the case in which the OCV exhibits large changes relative to the thermal voltage. Their limit recovers a variant of the SPM at leading order because the reaction overpotentials are small. In contrast, in our limit the small gradients in the electrolyte concentration, electrolyte potential, and electrode potentials give rise to the homogeneous behavior of electrode particles and hence the SPM. Both limits recover a variant of the SPM at leading order and a similar correction term at first order. The main difference between the two resulting models is that instead of employing an analytic expression for $\phi_{e,k}^*$, [75] solve the elliptic equation

$$
i_{e,k}^* = \epsilon_k^b \kappa_e^*(c_{e,k}^*) \left(-\frac{\partial \phi_{e,k}^*}{\partial x^*} \right.
$$
$$
\left. + 2(1-t^+)\frac{R^* T^*}{F^*}\frac{\partial}{\partial x^*}\left(\log\left(c_{e,k}^*\right) \right) \right), \tag{3.51}
$$

$$
i_{e,n}^* = \frac{x^* \mathcal{I}^*}{L_n^*}, \quad i_{e,s}^* = \mathcal{I}^*, \quad i_{e,p}^* = \frac{(L_x^* - x^*)\mathcal{I}^*}{L_p^*}. \tag{3.52}
$$

Therefore, the model in [75], which is referred to as the corrected single-particle (cSP) model, becomes a system of DAEs upon spatial discretisation. In contrast, (3.47) is a purely parabolic problem and one can, therefore, employ ODE solvers after discretisation. Because of this increased complexity in the model structure, we choose not to include it in our previous comparisons. In terms of computation time, the cSP takes on the order of 2 seconds, whereas the SPMe takes around 1 second to run a constant current discharge in PyBaMM. In Figure 3.8 and Figure 3.9, we compare the voltage and electrolyte potential predicted by the cSP and the SPMe for the parameter set in [75]. In Figure 3.8, we can see that employing the more expensive cSP instead of the SPMe does not offer any clear benefit for reproducing the voltage. In Figure 3.9, we observe that there is a gain in the accuracy of the prediction of the electrolyte potential. For most applications, we believe that this gain in accuracy is not worth the additional computational effort required to solve the cSP. Please note that in [75], a comparison between the SPMe and the cSP wsa also provided. However, there was an error in comparison included in the original manuscript, which has been corrected in [90] and brings the results in agreement with those presented here.
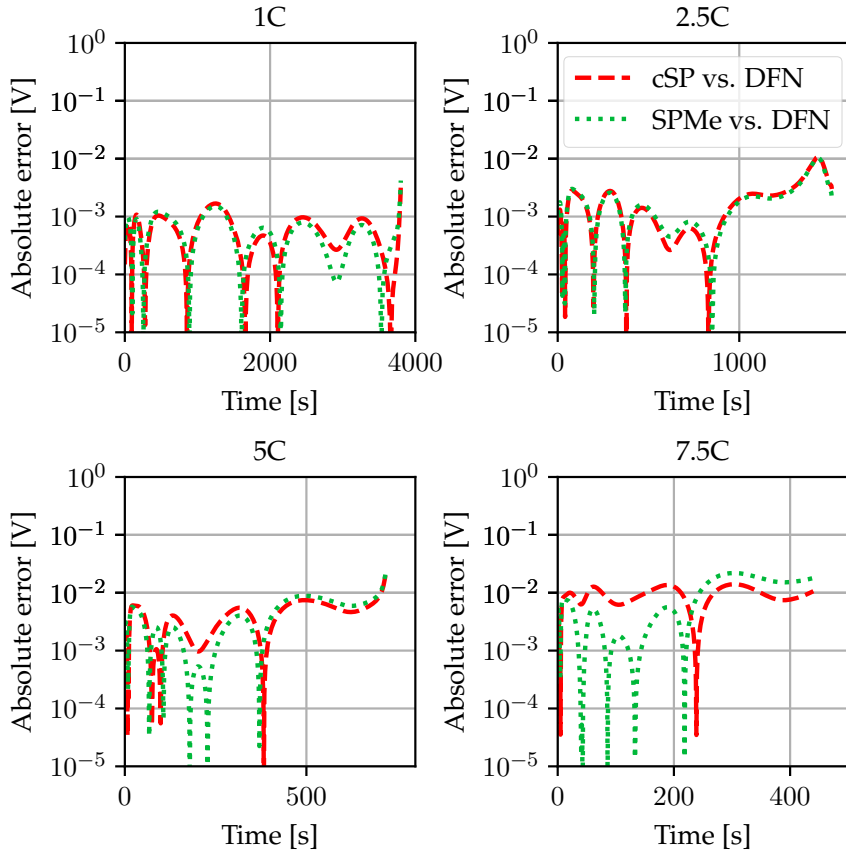
Figure 3.8: Voltage errors vs. DFN for the cSP and SPMe.
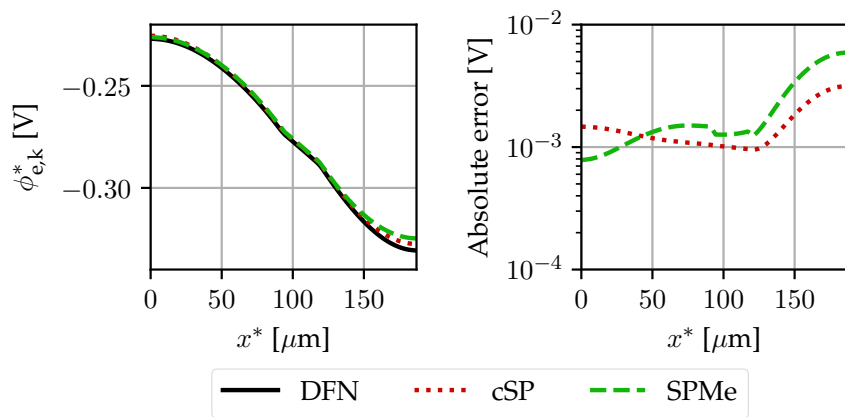
Figure 3.9: Comparison of the electrolyte potential predicted by the cSP and SPMe at 576 seconds into a $5\,\mathrm{C}$ discharge.

3.8 EXTENDING THE SPME

In Figure 3.1 and Figure 3.2, we observed that a discrepancy arises between the SPMe and the DFN voltage predictions when the OCPs are nonlinear. In this section, we present an extension that corrects for this behaviour. We consider the same limit as (3.8) but additionally take

$$U_k''(c_{s,k}^{(0)}) = \mathcal{O}(\mathcal{C}_e^{-1}). \tag{3.53}$$

The asymptotic analysis follows very similarly to before so to avoid repetition, we will simply highlight the key differences. Firstly, in §3.5.3, we have that

$$\bar{U}_k(c_{s,k}) = U_k(c_{s,k}^{(0)}) + \mathcal{O}(\mathcal{C}_e^2). \tag{3.54}$$

where $c_{s,k}^{(0)}$ is independent of x. Here, we instead have

$$\bar{U}_k(c_{s,k}) = U_k(c_{s,k}^{(0)}) + \mathcal{C}_e^2 \overline{(c_{s,k}^{(1)})^2} U_k''(c_{s,k}^{(0)}) + \mathcal{O}(\mathcal{C}_e^2). \tag{3.55}$$

where

$$\overline{(c_{s,k}^{(1)})^2} = \frac{1}{|\Omega_k|} \int_{\Omega_k} (c_{s,k}^{(1)})^2 \mathrm{d}x. \tag{3.56}$$

Therefore, in this limit, we must determine both the average particle concentration given by $c_{s,k}^{(0)}$ and the variance in the particle concentrations given by (3.56). Whereas before we only required the average particle concentration. Ideally, we could now solve an additional PDE in each electrode for the particle concentration variance. However we quickly run into a problem when squaring and averaging the first-order particle equations (3.23). Here, the squared source term, $(j_k^{(1)})^2$, involves various cross-terms of $c_{s,k}^{(1)}$ and not $c_{s,k}^{(1)}$ alone. Therefore, we must solve for $c_{s,k}^{(1)}$ itself in each particle and thus vastly increase computational complexity. In practice the simplest way to do this is to recombine the leading- and first-order particle equations; this avoids issues such as particle concentrations exceeding their maximum and minimum values.

In dimensional form, the resulting equations are the same as those in (3.47) but with the active material equations (3.47a)-(3.57d) replaced by

$$\frac{\partial c_{s,k}^*}{\partial t^*} = -\frac{1}{(r^*)^2}\frac{\partial}{\partial r^*}\left((r^*)^2 N_{s,k}^*\right), \qquad k \in \{n, p\} \qquad (3.57a)$$

$$N_{s,k}^* = -D_{s,k}^*(c_{s,k}^*)\frac{\partial c_{s,k}^*}{\partial r^*}, \qquad k \in \{n, p\}, \qquad (3.57b)$$

$$N_{s,k}^*\big|_{r_k^*=0} = 0, \quad N_{s,k}^*\big|_{r_k^*=R_k^*} = \tilde{j}_k^* \qquad k \in \{n, p\}, \qquad (3.57c)$$

$$c_{s,k}^*\big|_{t^*=0} = c_{s,k,0}^*, \qquad k \in \{n, p\}; \qquad (3.57d)$$

where the $\tilde{j}_k^*$ is the corrected interfacial current density given by

$$\tilde{j}_n^* = \frac{\mathcal{I}^*}{a_n^* L_n^*} + (j_n^* - \bar{j}_n^*) \quad \tilde{j}_p^* = -\frac{\mathcal{I}^*}{a_p^* L_p^*} + (j_n^* - \bar{j}_n^*) \qquad (3.57e)$$

where

$$j_k^* = j_{0,k}^* \sinh\left(\frac{\eta_k^*}{2}\right), \qquad (3.57f)$$

$$j_{0,k}^* = m_k^*(c_{s,k}^*)^{1/2}(c_{s,k,max}^* - c_{s,k}^*)^{1/2}(c_{e,k}^*)^{1/2} \qquad (3.57g)$$

$$\eta_k^* = \phi_{s,k}^* - \phi_{e,k}^* - U_k^*(c_{s,k}^*)\big|_{r^*=R_k^*} \qquad (3.57h)$$

and $c_{e,k}^*$, $\phi_{s,k}^*$, and $\phi_{e,k}^*$ are given by their expressions in (3.47) with

$$U_k^*(\bar{c}_{s,k}^*)$$

replaced by

$$\frac{1}{|\Omega_k^*|}\int_{\Omega_k^*} U_k^*(c_{s,k}^*)\mathrm{d}x^*.$$

The corrected interfacial current density, $\tilde{j}_k^*$ is asymptotically equivalent to the calculated interfacial current density, j_k^*, up to terms of size $\mathcal{O}(\mathcal{C}_e^2)$ but the higher-order terms are chosen such that the analytical average current density is enforced.

In Figure 3.10, we compare the DFN, SPMe, and the extended SPMe introduced in this section. We observe that the discrepancy between the SPMe and DFN when the OCP is nonlinear is corrected by the proposed extension. Further, by making this extension the extended SPMe is seen to give a good estimate of the terminal voltage up to 10 C.
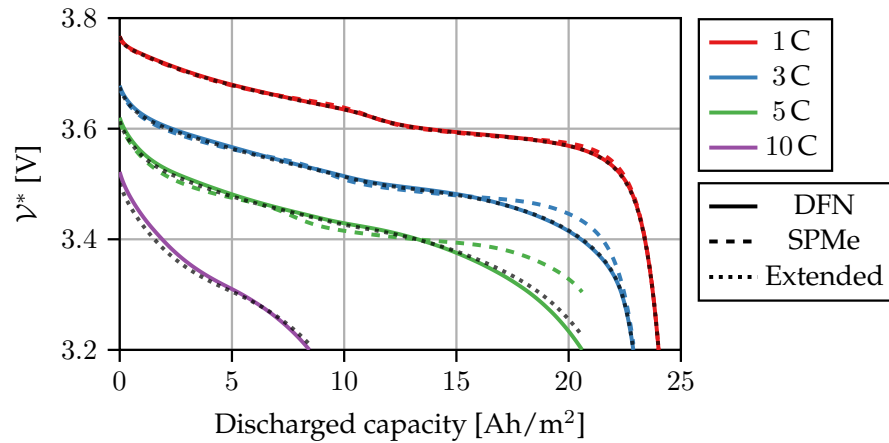
Figure 3.10: Comparison of the terminal voltage predicted by the DFN, SPMe, and extended SPMe.

The extended SPMe introduced in this section is significantly more computationally expensive than the original SPMe. This is a result of solving for the concentration in every particle in each electrode instead of just a single average particle. We have considered this case mainly to demonstrate that improving the calculation of the average OCP does indeed correct for the discrepancy in the SPMe voltage. However, this model also has a computational advantage over the DFN because we have eliminated the elliptic part of the problem. Thus upon discretisation in space, we recover a system of ODEs that are simpler to solve than the DAE system produced by the DFN.

3.9 SUMMARY

In this chapter, we have employed asymptotic methods to simplify the DFN model. At leading-order, we recovered the classical SPM and by proceeding to first-order we derived a correction term. By comparing the DFN, SPMe, and SPM, we found that the SPMe offers a good trade-off between speed and accuracy. We then identified and addressed a key error in ad-hoc versions of the SPMe. This error results in the ad-hoc versions being less accurate than our asymptotic version of the same computational complexity. We also identified the source of a discrepancy in the terminal voltage and determined the additional effort required to address the problem. The majority of the work in this chapter is contained within our published paper [48]. The SPMe as derived here has been implemented within PyBaMM so that it is easily available for use by other researchers and industrialists [86].

ASYMPTOTIC REDUCTION OF A POUCH CELL MODEL

4.1 INTRODUCTION

In this chapter, we develop a thermal three-dimensional model of a lithium-ion pouch cell inspired by the one-dimensional DFN model. We introduce typical scalings and write this model in dimensionless form. We then exploit the small aspect ratio of the cell and the high current collector conductivity to asymptotically reduce this model. We will find that there are two distinguished limits: one in which the model reduces to a set of through-cell one-dimensional models coupled through a two-dimensional problem for the boundary conditions, and a second in which only a single through-cell one-dimensional problem needs to be solved, with an additional two-dimensional problem needed to calculate an in-series resistance. We provide a numerical comparison of these reduced models with the full models. We then combine this analysis with the analysis conducted in Chapter 3 to develop a hierarchy of nine reduced-order models of a lithium-ion pouch cell. We give a critical numerical comparison of each of these models in both isothermal and thermal settings, and study their performance on realistic drive cycle data. Finally, we make recommendations regarding model selection, taking into account the available computational resources and the quantities of interest in a particular study.

4.2 LITERATURE REVIEW

The multiscale and multidimensional nature of lithium-ion pouch cells has been accounted for serval times within the literature (e.g. [6], [23], [30], [37], [40], [56]), with many models based on extensions or adaptations of the porous electrode model developed by Doyle, Fuller and Newman [21] (the DFN model), or reductions thereof.

While fully-coupled three-dimensional electrochemical and thermal models provide useful information for predicting cell behaviour, they are often too computationally expensive to be practically useful, and simplifications must be made. One approach is to treat the electrochemical problem as a network of resistors, coupled to a three-dimensional thermal model [25], [38], [42]. A current-voltage relation is given for each of the resistors in the network, which can either be a complicated description based on porous electrode theory [42], or a simplified description, such as a nonlinear resistor fitted to an electrochemical model [25] or data [37]. This approach reduces the three-dimensional

electrochemical model to a system of one-dimensional electrochemical models coupled via a two-dimensional electrical problem in the current collectors, and a three-dimensional thermal model across the entire cell. These simplifications, sometimes referred to as "potential pair" models, are usually made in an ad-hoc manner (e.g. [25], [38], [40], [42]). Asymptotic methods have been applied to simplify a three-dimensional model of a lead-acid battery [84]. However, there are key differences between lead-acid batteries and lithium-ion batteries (e.g. lead-acid batteries do not have separate current collectors).

4.3 POUCH CELL MODEL

We begin by providing a detailed exposition of the three-dimensional thermal pouch cell model that we have developed. The electrochemical model consists of a three-dimensional version of the standard DFN model (2.32)-(2.36) [21], with an additional equation relating to charge balance in the current collectors, which we model as Ohmic resistors. This is supplemented with an equation for energy balance, which includes source terms arising from Ohmic, irreversible, and reversible heat generation within the cell. Descriptions of each of the cell components, along with modelling assumptions, and the resulting governing equations, are laid out in the following sections.

4.3.1 *Current collectors*

In the current collectors conservation of charge along with Ohm's law gives

$$\nabla^* \cdot \boldsymbol{i}^*_{s,ck} = 0, \qquad\qquad k \in \{n, p\}, \qquad (4.1a)$$

$$\boldsymbol{i}^*_{s,ck} = -\sigma^*_{ck} \nabla^* \phi^*_{s,ck}, \qquad\qquad k \in \{n, p\}, \qquad (4.1b)$$

where $\boldsymbol{i}^*_{s,ck}$ is the current density, $\phi^*_{s,ck}$ is the electric potential, and σ^*_{ck} is the electrical conductivity. We assume no charge is exchanged through the external boundary of the current collectors except at the tabs so that

$$\boldsymbol{i}^*_{s,ck} \cdot \boldsymbol{n} = 0, \qquad \boldsymbol{x}^* \in \partial\Omega^*_{ext,ck}, \qquad\qquad k \in \{n, p\}. \qquad (4.1c)$$

We need to set a reference potential, or ground state, against which other potentials are measured. We assume a uniform potential across the surface of the negative tab and set this potential to be zero

$$\phi^*_{s,cn} = 0, \quad \boldsymbol{x}^* \in \partial\Omega^*_{tab,n}. \qquad (4.1d)$$

The boundary condition that describes the charging rate of the cell can be implemented in several ways. If the voltage is specified then we can take the potential at the positive tab to be given. Alternatively, the applied current may be specified, which can be implemented in different

ways: either by assuming the electric potential at the positive tab is spatially uniform, but unknown, and letting the total applied current be given; or by assuming that the applied current is uniform across one tab and letting the voltage be determined by the average potential on the tab. Adopting the former approach provides the following two conditions describing the current flow through the tabs

$$\int_{\partial\Omega^*_{\text{tab,n}}} \boldsymbol{i}^*_{\text{s,cn}} \cdot \boldsymbol{n} \, \mathrm{d}x^* = -I^*_{\text{app}},$$

and so   (4.1e)

$$\int_{\partial\Omega^*_{\text{tab,p}}} \boldsymbol{i}^*_{\text{s,cp}} \cdot \boldsymbol{n} \, \mathrm{d}x^* = I^*_{\text{app}},$$

where $\boldsymbol{n}$ is the outward pointing unit normal. In practice the first of these conditions is not needed, since we set the potential to zero on the negative tab, and conservation of current ensures the integral conditions (4.1e) are satisfied. If instead we assume a uniform current density across the tabs the integral condition at the positive tab is replaced with

$$\boldsymbol{i}^*_{\text{s,cp}} \cdot \boldsymbol{n} = -\frac{I^*_{\text{app}}}{A^*_{\text{tab,p}}}, \quad \boldsymbol{x}^* \in \partial\Omega^*_{\text{tab,p}}, \tag{4.1f}$$

where $A^*_{\text{tab,k}} = L^*_{\text{ck}} L^*_{\text{tab,k}}$ is the area of tab k, L^*_{ck} is the current collector thickness, and $L^*_{\text{tab,k}}$ is the tab width. Finally, the electric potential and the normal component of the current density are continuous across the current collector–electrode interface

$$\phi^*_{\text{s,ck}} = \phi^*_{\text{s,k}}, \qquad \boldsymbol{x}^* \in \partial\Omega^*_{\text{ck,k}}, \qquad k \in \{n, p\}, \tag{4.1g}$$

$$\boldsymbol{i}^*_{\text{s,ck}} \cdot \boldsymbol{n} = \boldsymbol{i}^*_{\text{s,k}} \cdot \boldsymbol{n}, \qquad \boldsymbol{x}^* \in \partial\Omega^*_{\text{ck,k}}, \qquad k \in \{n, p\}, \tag{4.1h}$$

where $\phi^*_{\text{s,k}}$ and $\boldsymbol{i}^*_{\text{s,k}}$ are the electric potential and current density in electrode k.

4.3.2 Electrochemistry

The governing equations for the electrochemical part of the problem (i.e. the electrodes, active material, and electrolyte) extend naturally from the DFN equations stated in (2.32)-(2.36), with the one-dimensional gradients being replaced by three-dimensional gradients, the inclusion of an additional boundary condition on the external walls of the cell,

and the addition of temperature dependence. The electrode equations are then given by

$$\nabla^* \cdot \boldsymbol{i}_{s,k}^* = -a_k^* j_k^*, \qquad\qquad\qquad\qquad k \in \{n, p\}, \qquad (4.2a)$$

$$\boldsymbol{i}_{s,k}^* = -\sigma_{s,k}^* \nabla^* \phi_k^*, \qquad\qquad\qquad k \in \{n, p\}, \qquad (4.2b)$$

$$\boldsymbol{i}_{s,k}^* \cdot \boldsymbol{n} = 0, \qquad \boldsymbol{x}^* \in \partial\Omega_{k,s}^*, \qquad k \in \{n, p\}, \qquad (4.2c)$$

$$\boldsymbol{i}_{s,k}^* \cdot \boldsymbol{n} = 0, \qquad \boldsymbol{x}^* \in \partial\Omega_{\text{ext},k}^*, \qquad k \in \{n, p\}. \qquad (4.2d)$$

Additionally on the boundaries between the electrodes and current collectors, the continuity conditions (4.1g) and (4.1h) hold. The temperature dependent active material equations are

$$\frac{\partial c_{s,k}^*}{\partial t^*} = -\frac{1}{(r^*)^2} \frac{\partial}{\partial r^*}\left((r^*)^2 N_{s,k}^*\right), \qquad k \in \{n, p\}, \qquad (4.3a)$$

$$N_{s,k}^* = -D_{s,k}^*(c_{s,k}^*, T_k^*)\frac{\partial c_{s,k}^*}{\partial r^*}, \qquad k \in \{n, p\}, \qquad (4.3b)$$

$$N_{s,k}^*\big|_{r^*=0} = 0, \quad N_{s.k}^*\big|_{r^*=R_k^*} = \frac{j_k^*}{F^*}. \qquad k \in \{n, p\}, \qquad (4.3c)$$

$$c_{s,k}^*\big|_{t^*=0} = c_{s,k,0}^*, \qquad\qquad\qquad\qquad\qquad (4.3d)$$

where $D_{s,k}^*(c_{s,k}^*, T_k^*)$ is the temperature dependent diffusivity of lithium in the active material and T_k^* is the (macroscopic) temperature. The governing equations for the current in the electrolyte are

$$\nabla^* \cdot \boldsymbol{i}_{e,k}^* = a_k^* j_k^*, \qquad k \in \{n, p\}, \qquad\qquad\qquad (4.4a)$$

$$\nabla^* \cdot \boldsymbol{i}_{e,s}^* = 0, \qquad\qquad\qquad\qquad\qquad\qquad\qquad (4.4b)$$

$$\boldsymbol{i}_{e,k}^* = \epsilon_k^b \kappa_e^*(c_{e,k}^*, T_k^*)\left(-\nabla^* \phi_{e,k}^*\right.$$
$$\left. +2(1-t^+)\frac{R^* T_k^*}{F^*}\nabla^*\left(\log(c_{e,k}^*)\right)\right), \qquad (4.4c)$$
$$k \in \{n, s, p\},$$

$$\phi_{e,k}^* = \phi_{e,s}^*, \quad \boldsymbol{x}^* \in \partial\Omega_{e,s}^*, \quad k \in \{n, p\}, \qquad (4.4d)$$

$$\boldsymbol{i}_{e,k}^* \cdot \boldsymbol{n} = \boldsymbol{i}_{e,s}^* \cdot \boldsymbol{n}, \quad \boldsymbol{x}^* \in \partial\Omega_{k,s}^*, \quad k \in \{n, p\}. \qquad (4.4e)$$

$$\boldsymbol{i}_{e,k}^* \cdot \boldsymbol{n} = 0, \quad \boldsymbol{x}^* \in \partial\Omega_{ck,k}^*, \quad k \in \{n, p\} \qquad (4.4f)$$

$$\boldsymbol{i}_{e,k}^* \cdot \boldsymbol{n} = 0, \quad \boldsymbol{x}^* \in \partial\Omega_{ext,k}^*, \quad k \in \{n, s, p\}. \qquad (4.4g)$$

where $\kappa_e^*(c_{e,k}^*, T_k^*)$ is the temperature dependent electrolyte conductivity. Note that the electrochemical potential in the electrolyte, ϕ_e^*, is only determined up to a constant. This will be determined relative to the reference electrode potential on the negative tab through the electrochemical reactions. The electrolyte diffusion equations are

$$\epsilon_k \frac{\partial c_{e,k}^*}{\partial t^*} = -\nabla^* \cdot \boldsymbol{N}_{e,k}^* + \frac{1}{F^*}\nabla^* \cdot \boldsymbol{i}_{e,k}^*, \qquad k \in \{n, s, p\}, \qquad (4.5a)$$

$$\boldsymbol{N}_{e,k}^* = -\epsilon_k^b D_e^*(c_{e,k}^*, T_k^*)\nabla^* c_{e,k}^* + \frac{t^+}{F^*}\boldsymbol{i}_{e,k}^*, \qquad k \in \{n, s, p\}, \qquad (4.5b)$$

$$N_{e,k}^* \cdot n = 0, \qquad x^* \in \partial\Omega_{ck,k}^*, \qquad k \in \{n, p\}, \quad (4.5c)$$

$$N_{e,k}^* \cdot n = 0, \qquad x^* \in \partial\Omega_{ext,k}^*, \qquad k \in \{n, s, p\}, \quad (4.5d)$$

$$c_{e,k}^* = c_{e,s}^* \qquad x^* \in \partial\Omega_{k,s}^*, \qquad k \in \{n, p\}, \quad (4.5e)$$

$$N_{e,k}^* \cdot n = N_{e,s}^* \cdot n, \qquad x^* \in \partial\Omega_{k,s}^*, \qquad k \in \{n, p\}, \quad (4.5f)$$

$$c_{e,k}^*\big|_{t^*=0} = c_{e,0}^*, \qquad\qquad k \in \{n, s, p\}, \quad (4.5g)$$

where $D_e^*(c_{e,k}^*, T_k^*)$ is the temperature dependent diffusivity of the electrolyte. Finally, the interfacial current density, j_k^*, is given by

$$j_k^* = j_{0,k}^* \sinh\left(\frac{F^*\eta_k^*}{2R_g^*T_k^*}\right), \quad k \in \{n, p\}, \tag{4.6a}$$

$$j_{0,k}^* = m_k^*(T_k^*)(c_{s,k}^*)^{1/2}(c_{s,k,max}^* - c_{s,k}^*)^{1/2}(c_{e,k}^*)^{1/2}\Big|_{r^*=R_k^*} \tag{4.6b}$$
$$k \in \{n, p\},$$

$$\eta_k^* = \phi_{s,k}^* - \phi_{e,k}^* - U_k^*(c_{s,k}^*, T_k^*)\big|_{r^*=R_k^*}, \quad k \in \{n, p\}, \tag{4.6c}$$

where $U_k^*(c_{s,k}^*, T_k^*)$ is the temperature dependent OCP, and $m_k^*(T_k^*)$ is the temperature dependent effective reaction rate constant.

4.3.3 *Energy conservation*

The governing equation for energy conservation is

$$\rho_k^* c_{p,k}^* \frac{\partial T_k^*}{\partial t^*} = \nabla^* \cdot (\lambda_k^* \nabla^* T_k^*) + Q_{Ohm,k}^* + Q_{rxn,k}^* + Q_{rev,k}^*, \tag{4.7a}$$
$$k \in \{cn, n, s, p, cp\},$$

where ρ_k^* is the density, $c_{p,k}^*$ is the specific heat, and λ_k^* is the thermal conductivity. Within the electrode region, the model accounts for Ohmic heating $Q_{Ohm,k}^*$ due to resistance in the solid and electrolyte, irreverisble heating due to electrochemical reactions $Q_{rxn,k}^*$, and reversible heating due to entropic changes in the the electrode $Q_{rev,k}^*$ [9], given by

$$Q_{Ohm,k}^* = -\left(i_{s,k}^* \cdot \nabla^* \phi_{s,k}^* + i_{e,k}^* \cdot \nabla^* \phi_{e,k}^*\right), \quad k \in \{n, p\}, \tag{4.7b}$$

$$Q_{rxn,k}^* = a_k^* j_k^* \eta_k^*, \qquad\qquad k \in \{n, p\}, \tag{4.7c}$$

$$Q_{rev,k}^* = a_k^* j_k^* T_k^* \frac{\partial U_k^*}{\partial T_k^*}\bigg|_{T_k^*=T_\infty^*}, \qquad k \in \{n, p\}. \tag{4.7d}$$

In the current collectors and separator there is no heat generation due to electrochemical effects, and we need only consider the Ohmic heat generation terms given by

$$Q_{Ohm,k}^* = -i_{s,k}^* \cdot \nabla^* \phi_{s,k}^*, \quad k \in \{cn, cp\}, \tag{4.7e}$$

$$Q_{Ohm,s}^* = -i_{e,s}^* \cdot \nabla^* \phi_{e,s}^*. \tag{4.7f}$$

For the thermal part of the problem, we assume Newton cooling on all boundaries, including the tabs,

$$-\lambda_k^* \nabla^* T_k^* \cdot \boldsymbol{n} = h^* (T_k^* - T_\infty^*), \quad \boldsymbol{x}^* \in \partial\Omega_{\text{ext}}^*, \tag{4.7g}$$
$$k \in \{\text{cn, n, s, p, cp}\},$$

where h^* is the (possibly spatially dependent) heat transfer coefficient. Some authors have considered the effects of different cooling scenarios, such as tab cooling vs. surface cooling, on battery operation. For instance, Hunt *et al.* [32] conducted experiments showing that surface cooling can lead to a greater loss of capacity compared with tab cooling when discharging cells at high rates. These different cooling scenarios can be investigate by choosing particular cooling functions h^* (for example, h^* may be larger on the tabs).

We require the temperature and heat flux to be continuous at the interfaces between the components of the cell

$$T_{\text{ck}}^* = T_k^*, \qquad\qquad \boldsymbol{x}^* \in \partial\Omega_{\text{ck,k}}^*, \quad k \in \{\text{n, p}\}, \tag{4.7h}$$
$$\lambda_{\text{ck}}^* \nabla^* T_{\text{ck}}^* \cdot \boldsymbol{n}, = \lambda_k^* \nabla^* T_k^* \cdot \boldsymbol{n}, \quad \boldsymbol{x}^* \in \partial\Omega_{\text{ck,k}}^*, \quad k \in \{\text{n, p}\}, \tag{4.7i}$$
$$T_k^* = T_{\text{s}}^*, \qquad\qquad \boldsymbol{x}^* \in \partial\Omega_{\text{k,s}}^*, \quad k \in \{\text{n, p}\}, \tag{4.7j}$$
$$\lambda_k^* \nabla^* T_k^* \cdot \boldsymbol{n} = \lambda_{\text{s}}^* \nabla^* T_{\text{s}}^* \cdot \boldsymbol{n}, \quad \boldsymbol{x}^* \in \partial\Omega_{\text{k,s}}^*, \quad k \in \{\text{n, p}\}, \tag{4.7k}$$

and prescribe an initial uniform temperature T_0^*, that is

$$T_k^*\big|_{(t^*=0)} = T_0^*, \quad k \in \{\text{cn, n, s, p, cp}\}. \tag{4.7l}$$

4.4   THERMAL PARAMETER VALUES

In Tables 2.1 and 2.2, and Figure 2.1, we provided a set of parameter values for the one-dimensional DFN that we introduced in §2.5. In our pouch cell model, we will use these parameter values along with a few modifications and additions. We introduce the temperature dependencies to the parameters in the following way. The temperature dependent OCPs are given by

$$U_k^*(c_{\text{s,k}}^*, T_k^*) = U_k^*(c_{\text{s,k}}^*) + (T_k^* - T_\infty^*)\frac{\partial U_k^*}{\partial T_k^*}\bigg|_{T_k^*=T_\infty^*} \tag{4.8a}$$

where $U_k^*(c_{\text{s,k}}^*)$ is given in Figure 2.1 and the entropic change, $\frac{\partial U_k^*}{\partial T_k^*}\big|_{T_k^*=T_\infty^*}$, is given as a function of the lithium concentration in the active material and is presented in Figure 4.1.
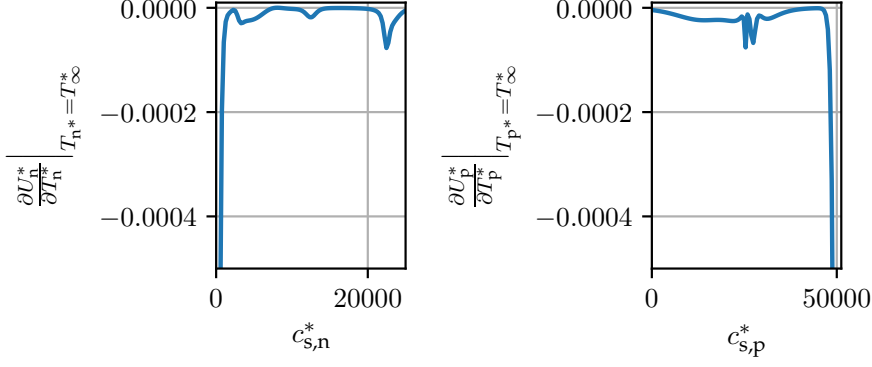
Figure 4.1: Experimentally measured functional forms of entropic change, taken from [51].

The temperature dependence of the electrolyte diffusivity, electrolyte conductivity, solid diffusivity, and reaction rate are accounted for using the following Arrenhius dependencies

$$D_e(c_{e,k}^*, T_k^*) = D_e^*(c_{e,k}^*) \exp\left(\frac{E_{D_e}^*}{R_g^*} \left(\frac{1}{T_{\infty^*}} - \frac{1}{T_k^*} \right) \right), \tag{4.8b}$$

$$\kappa_e(c_{e,k}^*, T_k^*) = \kappa_e^*(c_{e,k}^*) \exp\left(\frac{E_{\kappa_e}^*}{R_g^*} \left(\frac{1}{T_{\infty^*}} - \frac{1}{T_k^*} \right) \right), \tag{4.8c}$$

$$D_{s,k}^*(T_k^*) = D_{s,k}^* \exp\left(\frac{E_{D_{s,k}}^*}{R_g^*} \left(\frac{1}{T_\infty^*} - \frac{1}{T_k^*} \right) \right), \tag{4.8d}$$

$$m_k^*(T_k^*) = m_k^* \exp\left(\frac{E_{m_k}^*}{R_g^*} \left(\frac{1}{T_\infty^*} - \frac{1}{T_k^*} \right) \right), \tag{4.8e}$$

where the values of the activation energies are given in Table 4.1. The additional dimensional parameters in the thermal model are given in Table 4.1.

4.5 DIMENSIONLESS POUCH CELL MODEL

We introduce a set of scalings to nondimensionalise the pouch cell model. The temperature is measured relative to the ambient temperature, T_∞^*, and we scale the deviation by some typical temperature difference, ΔT^*, to be determined later. The transverse coordinates, y^* and z^* are scaled with a typical transverse dimension L^* (which could be L_y^*, L_z^* or $(L_y^* L_z^*)^{1/2}$ for example). We then scale the applied current I_{app}^* by some typical through-cell current density, I^*, multiplied by the scale for the transverse area, $(L^*)^2$. For details on the other scalings,

Parameter	Units	Description	cn	n	s	p	cp
$E_{D_e}^*$	$J\,mol^{-1}$	Activation energy for electrolyte diffusivity			3.704×10^4		
$E_{\kappa_e}^*$	$J\,mol^{-1}$	Activation energy for electrolyte conductivity			3.470×10^4		
$E_{D_{s,k}}^*$	$J\,mol^{-1}$	Activation energy for solid diffusivity	-	4.277×10^4	-	1.855×10^4	-
$E_{m_k}^*$	$J\,mol^{-1}$	Activation energy for reaction rate	-	3.748×10^4	-	3.957×10^4	-
h^*	$W\,m^{-2}\,K^{-1}$	Heat transfer coefficient			10		
ρ_k^*	$kg\,m^{-3}$	Density	8954	1657	397	3262	2707
$c_{p,k}^*$	$J\,kg^{-1}\,K^{-1}$	Specific heat capacity	385	700	700	700	897
λ_k^*	$W\,m^{-1}\,K^{-1}$	Thermal conductivity	401	1.7	0.16	2.1	237
ρ_{eff}^*	$J\,K^{-1}\,m^{-3}$	Lumped effective thermal density			1.812×10^6		
λ_{eff}^*	$W\,m^{1-}\,K^{-1}$	Effective thermal conductivity			59.396		
T_0^*	K	Initial temperature			298.15		

Table 4.1: Typical dimensional parameter values relevant for the thermal extension of the DFN taken from [51]. The parameters are for a carbon negative current collector, graphite negative electrode, $LiPF_6$ in EC:DMC electrolyte, LCO positive electrode, and aluminium positive current collector.

please refer to §3.3. To summarise, the dimensionless variables are related to their dimensional counterparts in the following way

global

$$x^* = L_x^* x, \quad y^* = L^* y, \quad z^* = L^* z, \quad t^* = \tau_d^* t,$$
$$I_{app}^* = I^* (L^*)^2 I_{app} \quad \kappa_e^* = \kappa_{typ}^* \kappa_e, \quad D_e^* = D_{e,typ}^* D_e;$$

for $k \in \{n, p\}$:

$$r_k^* = R_k^* r_k, \quad c_{s,k}^* = c_{s,k,max}^* c_{s,k} \quad D_{s,k}^* = D_{s,k,typ}^* D_{s,k},$$
$$N_{s,k}^* = \frac{D_{s,k,typ}^* c_{s,k,max}^*}{R_k^*} N_{s,k},$$
$$j_k^* = \frac{I^*}{a_k^* L_x^*} j_k, \quad j_{0,k}^* = \frac{I^*}{a_k^* L_x^*} j_{0,k}, \quad m_k^* = m_{k,typ}^* m_k,$$
$$\eta_k^* = \frac{R^* T_\infty^*}{F^*} \eta_k, \quad U_k^* = U_{k,ref}^* + \frac{R^* T_\infty^*}{F^*} U_k;$$

for $k \in \{cn, n, p, cp\}$:

$$\boldsymbol{i}_{s,k}^* = I^* \boldsymbol{i}_{s,k};$$

for $k \in \{cn, n\}$:

$$\phi_{s,k}^* = \frac{R^* T_\infty^*}{F^*} \phi_{s,k};$$

for $k \in \{p, cp\}$:

$$\phi_{s,k}^* = \left(U_{p,ref}^* - U_{n,ref}^* \right) + \frac{R^* T_\infty^*}{F^*} \phi_{s,k};$$

for $k \in \{n, s, p\}$:

$$c_{e,k}^* = c_{e,typ}^* c_{e,k}, \quad \boldsymbol{N}_{e,k}^* = \frac{D_{e,typ}^* c_{e,typ}^*}{L_x^*} \boldsymbol{N}_{e,k},$$
$$\phi_{e,k}^* = -U_{n,ref}^* + \frac{R^* T^*}{F^*} \phi_{e,k}, \quad \boldsymbol{i}_{e,k}^* = I^* \boldsymbol{i}_{e,k};$$

for $k \in \{cn, n, s, p, cp\}$:

$$T_k^* = (\Delta T^*) T_k + T_\infty^*.$$

The resulting dimensionless parameters are presented in Tables 3.3, 3.4, 4.2, and 2.2. The key timescales in the model are the same as those presented in Table 3.2, with the addition of

$$\tau_{th}^* = \frac{\rho_{eff}^* (L^*)^2}{\lambda_{eff}^*} \approx 5.724 \times 10^2, \tag{4.9}$$

which is the planar (y^*-z^*) thermal diffusion timescale.

Parameter	Expression	Interpretation	cn	n	s	p	cp
$A_{\text{tab,k}}$	$A^*_{\text{tab,k}}/(L^*_x L^*)$	Dimensionless tab area	-	0.0324	-	0.0324	-
ρ_{k}	$\rho^*_{\text{k}} c^*_{\text{p,k}}/\rho^*_{\text{eff}}$	Dimensionless volumetric heat capacity	1.903	0.6403	0.1535	1.2605	1.3403
λ_{k}	$\lambda^*_{\text{k}}/\lambda^*_{\text{eff}}$	Dimensionless thermal conductivity	6.7513	0.0286	0.0027	0.0354	3.9901
$\mathcal{B}$	$I^* R^* T^*_\infty \tau^*_{\text{th}}/(\rho^*_{\text{eff}} F^* \Delta T^* L^*_x)$	Dimensionless heat generation coefficient			0.3608		
$\mathcal{C}_{\text{th}}$	$\tau^*_{\text{th}}/\tau^*_{\text{d}}$	Ratio of planar thermal diffusion and discharge timescales			$0.02533\mathcal{C}$		
Θ	$\Delta T^*/T^*_\infty$	Ratio of typical temperature variation and reference temperature			$0.008\,\mathcal{C}$		
h	$h^* L^*_x/\lambda^*_{\text{eff}}$	Dimensionless heat transfer coefficient			3.7881×10^{-5}		

Table 4.2: Typical dimensionless parameter values derived from dimensional parameters in Tables 2.1, 2.2, and 4.1. Here $\mathcal{C} = I^*/(24\,\text{Am}^{-2})$ is the C-Rate where we have taken a 1C rate to correspond to a typical x^*-direction current density of $24\,\text{Am}^{-2}$. This is for a cell with an initial stoichiometry of 0.8 in the negative electrode and 0.6 in the positive electrode with a voltage cutoff of 3.2 V. (Part 1).

Parameter	Expression	Interpretation	Value
T_0	$(T_0^* - T_\infty^*)/\Delta T^*$	Dimensionless initial temperature	0
δ	L_x^*/L^*	Aspect ratio	1.642×10^{-3}
L_y	L_y^*/L^*	Dimensionless cell width	1.511
L_z	L_z^*/L^*	Dimensionless cell height	1

Table 4.3: Typical dimensionless parameter values derived from dimensional parameters in Tables 2.1, 2.2, and 4.1 (Part 2).

Here, we summarise the dimensionless pouch cell model. In the following, we use the scaled gradient operator

$$\nabla_\delta \equiv \frac{\partial}{\partial x}\boldsymbol{e}_1 + \delta\frac{\partial}{\partial y}\boldsymbol{e}_2 + \delta\frac{\partial}{\partial z}\boldsymbol{e}_3, \tag{4.10}$$

where $\boldsymbol{e}_i$ is the unit vector in the ith direction, and $\delta = L_x^*/L^*$ is the aspect ratio of the cell (which arises because of the different scaling in the x^* and y^*, z^* directions). The current collector and electrode equations (4.1) and (4.2) become

$$\nabla_\delta \cdot \boldsymbol{i}_{\mathrm{s,k}} = 0, \qquad\qquad \mathrm{k} \in \{\mathrm{cn, cp}\}, \tag{4.11a}$$
$$\boldsymbol{i}_{\mathrm{s,k}} = -\sigma_\mathrm{k}\nabla_\delta\phi_{\mathrm{s,k}}, \qquad\qquad \mathrm{k} \in \{\mathrm{cn, cp}\}, \tag{4.11b}$$
$$\nabla_\delta \cdot \boldsymbol{i}_{\mathrm{s,k}} = -j_\mathrm{k}, \qquad\qquad \mathrm{k} \in \{\mathrm{n, p}\}, \tag{4.11c}$$
$$\boldsymbol{i}_{\mathrm{s,k}} = -\sigma_\mathrm{k}\nabla_\delta\phi_{\mathrm{s,k}}, \qquad\qquad \mathrm{k} \in \{\mathrm{n, p}\}, \tag{4.11d}$$

with boundary conditions

$$\phi_{\mathrm{s,cn}} = 0, \qquad \boldsymbol{x} \in \partial\Omega_{\mathrm{tab,cn}}, \tag{4.11e}$$

$$\delta\int_{\partial\Omega_{\mathrm{tab,cp}}} \boldsymbol{i}_{\mathrm{s,cp}} \cdot \boldsymbol{n} \, \mathrm{d}A = I_{\mathrm{app}}, \tag{4.11f}$$

$$\boldsymbol{i}_{\mathrm{s,k}} \cdot \boldsymbol{n} = 0, \qquad \boldsymbol{x} \in \partial\Omega_{\mathrm{ext,k}} \qquad \mathrm{k} \in \{\mathrm{cn, n, p, cp}\} \tag{4.11g}$$
$$\boldsymbol{i}_{\mathrm{s,ck}} \cdot \boldsymbol{n} = \boldsymbol{i}_{\mathrm{s,k}} \cdot \boldsymbol{n}, \qquad \boldsymbol{x} \in \partial\Omega_{\mathrm{ck,k}}, \qquad \mathrm{k} \in \{\mathrm{n, p}\}, \tag{4.11h}$$
$$\boldsymbol{i}_{\mathrm{s,k}} \cdot \boldsymbol{n} = 0, \qquad \boldsymbol{x} \in \partial\Omega_{\mathrm{k,s}}, \qquad \mathrm{k} \in \{\mathrm{n, p}\}, \tag{4.11i}$$
$$\phi_{\mathrm{s,ck}} = \phi_{\mathrm{s,k}}, \qquad \boldsymbol{x} \in \partial\Omega_{\mathrm{ck,k}}, \qquad \mathrm{k} \in \{\mathrm{n, p}\}. \tag{4.11j}$$

The active material equations (4.3) become

$$C_k \frac{\partial c_{s,k}}{\partial t} = -\frac{1}{r_k^2} \frac{\partial}{\partial r_k} \left(r_k^2 N_{s,k} \right), \qquad k \in \{n, p\}, \qquad (4.12a)$$

$$N_{s,k} = -D_{s,k}(c_{s,k}, T_k) \frac{\partial c_{s,k}}{\partial r_k} \qquad k \in \{n, p\}, \qquad (4.12b)$$

$$N_{s,k}\big|_{r_k=0} = 0, \quad \frac{a_k \gamma_k}{C_k} N_{s,k}\big|_{r_k=1} = j_k, \qquad k \in \{n, p\}, \qquad (4.12c)$$

$$c_{s,k}\big|_{t=0} = c_{s,k,0}, \qquad k \in \{n, p\}. \qquad (4.12d)$$

The electrolyte potential equations (4.4) become

$$\nabla_\delta \cdot \boldsymbol{i}_{e,k} = \begin{cases} j_k, & k = n, p, \\ 0, & k = s, \end{cases} \quad k \in \{n, s, p\}, \qquad (4.13a)$$

$$\begin{aligned} C_e \boldsymbol{i}_{e,k} = \epsilon_k^b \hat{\kappa}_e \kappa_e(c_{e,k}, T_k) \, (&-\nabla_\delta \phi_{e,k} \\ &+2(1-t^+)(1+\Theta T_k)\nabla_\delta (\log c_{e,k}) - \nabla_\delta \phi_{e,k}) , \\ & k \in \{n, s, p\}, \end{aligned} \qquad (4.13b)$$

$$\boldsymbol{i}_{e,k} \cdot \boldsymbol{n} = 0, \quad \boldsymbol{x} \in \partial\Omega_{ck,k}, \quad k \in \{n, p\}, \qquad (4.13c)$$

$$\boldsymbol{i}_{e,k} \cdot \boldsymbol{n} = 0, \quad \boldsymbol{x} \in \partial\Omega_{ext,k}, \quad k \in \{n, s, p\}. \qquad (4.13d)$$

The electrolyte concentration equations (4.5) become

$$C_e \gamma_e \epsilon_k \frac{\partial c_{e,k}}{\partial t} = -\gamma_e \nabla_\delta \cdot \boldsymbol{N}_{e,k} + C_e \nabla_\delta \cdot \boldsymbol{i}_{e,k}, \quad k \in \{n, p\}, \qquad (4.14a)$$

$$\boldsymbol{N}_{e,k} = -\epsilon_k^b D_e(c_{e,k}, T_k) \nabla_\delta c_{e,k} + \frac{C_e t^+}{\gamma_e} \boldsymbol{i}_{e,k}, \quad k \in \{n, p\}, \qquad (4.14b)$$

with boundary conditions

$$\boldsymbol{N}_{e,k} \cdot \boldsymbol{n} = 0, \quad \boldsymbol{x} \in \partial\Omega_{ext,k}, \qquad k \in \{n, s, p\}, \qquad (4.14c)$$

$$\boldsymbol{N}_{e,k} \cdot \boldsymbol{n} = 0, \quad \boldsymbol{x} \in \partial\Omega_{ck,k}, \qquad k \in \{n, p\}, \qquad (4.14d)$$

$$\boldsymbol{N}_{e,k} \cdot \boldsymbol{n} = \boldsymbol{N}_{e,s} \cdot \boldsymbol{n}, \quad \boldsymbol{x} \in \partial\Omega_{k,s}, \qquad k \in \{n, p\}, \qquad (4.14e)$$

$$c_{e,k} = c_{e,s} \quad \boldsymbol{x} \in \partial\Omega_{k,s}, \qquad k \in \{n, p\}, \qquad (4.14f)$$

$$c_{e,k}\big|_{t=0} = c_{e,0}, \qquad k \in \{n, s, p\}. \qquad (4.14g)$$

The electrochemical reactions equations (4.6) become

$$j_k = j_{0,k} \sinh \left(\frac{\eta_k}{2(1+\Theta T_k)} \right), \qquad k \in \{n, p\}, \qquad (4.15a)$$

$$j_{0,k} = \frac{\gamma_k}{C_{r,k}} m_k(T_k) c_{s,k}^{1/2} (1-c_{s,k})^{1/2} c_{e,k}^{1/2} \big|_{r_k=1}, \qquad k \in \{n, p\}, \qquad (4.15b)$$

$$\eta_k = \phi_{s,k} - \phi_{e,k} - U_k(c_{s,k}, T_k)\big|_{r_k=1}, \qquad k \in \{n, p\}. \qquad (4.15c)$$

Finally, the energy conservation equation (4.7) becomes

$$\delta^2 \mathcal{C}_{\text{th}}\rho_{\text{k}}\frac{\partial T_{\text{k}}}{\partial t} = \nabla_\delta \cdot (\lambda_{\text{k}}\nabla_\delta T_{\text{k}}) + \delta^2 \mathcal{B}\left(Q_{\text{ohm,k}} + Q_{\text{rxn,k}} + Q_{\text{rev,k}}\right), \text{(4.16a)}$$

$$\text{k} \in \{\text{cn}, \text{n}, \text{s}, \text{p}, \text{cp}\},$$

$$Q_{\text{Ohm,k}} = -\left(\boldsymbol{i}_{\text{s,k}} \cdot \nabla_\delta \phi_{\text{s,k}} + \boldsymbol{i}_{\text{e,k}} \cdot \nabla_\delta \phi_{\text{e,k}}\right), \quad \text{k} \in \{\text{n}, \text{p}\}, \qquad \text{(4.16b)}$$

$$Q_{\text{Ohm,s}} = -\boldsymbol{i}_{\text{e,s}} \cdot \nabla_\delta \phi_{\text{e,s}}, \qquad \text{(4.16c)}$$

$$Q_{\text{Ohm,k}} = -\boldsymbol{i}_{\text{s,k}} \cdot \nabla_\delta \phi_{\text{s,k}}, \quad \text{k} \in \{\text{cn}, \text{cp}\} \qquad \text{(4.16d)}$$

$$Q_{\text{rxn,k}} = j_{\text{k}}\eta_{\text{k}}, \quad \text{k} \in \{\text{n}, \text{p}\}, \qquad \text{(4.16e)}$$

$$Q_{\text{rev,k}} = j_{\text{k}}(\Theta^{-1} + T_{\text{k}})\frac{\partial U_{\text{k}}}{\partial T_{\text{k}}}\bigg|_{T_{\text{k}}=0}, \quad \text{k} \in \{\text{n}, \text{p}\}, \qquad \text{(4.16f)}$$

with $Q_{\text{rxn,k}} = Q_{\text{rev,k}} = 0$ for $\text{k} \in \{\text{cn}, \text{s}, \text{cp}\}$. The thermal boundary conditions are given by

$$-\lambda_{\text{k}}\nabla_\delta T_{\text{k}} \cdot \boldsymbol{n} = h(\boldsymbol{x})T_{\text{k}}, \quad \boldsymbol{x} \in \partial\Omega_{\text{ext}}, \qquad \text{(4.16g)}$$

$$\text{k} \in \{\text{cn}, \text{n}, \text{s}, \text{p}, \text{cp}\},$$

$$T_{\text{ck}} = T_{\text{k}}, \quad \boldsymbol{x} \in \partial\Omega_{\text{ck,k}}, \quad \text{k} \in \{\text{n}, \text{p}\}, \qquad \text{(4.16h)}$$

$$\lambda_{\text{ck}}\nabla_\delta T_{\text{ck}} \cdot \boldsymbol{n} = \lambda_{\text{k}}\nabla_\delta T_{\text{k}} \cdot \boldsymbol{n}, \quad \boldsymbol{x} \in \partial\Omega_{\text{ck,k}}, \quad \text{k} \in \{\text{n}, \text{p}\}, \qquad \text{(4.16i)}$$

$$T_{\text{k}} = T_{\text{s}}, \quad \boldsymbol{x} \in \partial\Omega_{\text{k,s}}, \quad \text{k} \in \{\text{n}, \text{p}\}, \qquad \text{(4.16j)}$$

$$\lambda_{\text{k}}\nabla_\delta T_{\text{k}} \cdot \boldsymbol{n} = \lambda_{\text{s}}\nabla_\delta T_{\text{s}} \cdot \boldsymbol{n}, \quad \boldsymbol{x} \in \partial\Omega_{\text{k,s}}, \quad \text{k} \in \{\text{n}, \text{p}\}, \qquad \text{(4.16k)}$$

$$T_{\text{k}}\big|_{t=0} = T_0, \quad \text{k} \in \{\text{cn}, \text{n}, \text{s}, \text{p}, \text{cp}\}. \qquad \text{(4.16l)}$$

4.6 ASYMPTOTIC ANALYSIS

In this section, we exploit the small aspect ratio of a typical pouch cell by considering the limit $\delta \to 0$. To enable a balance of terms in the current conservation equations we rescale the transverse currents by writing

$$\boldsymbol{i}_{\text{s,k}} = i_{\text{s,k,1}}\boldsymbol{e}_1 + \frac{\boldsymbol{i}_{\text{s,k},\perp}}{\delta}, \qquad \text{k} \in \{\text{cn}, \text{n}, \text{p}, \text{cp}\},$$

$$\boldsymbol{i}_{\text{e,k}} = i_{\text{e,k,1}}\boldsymbol{e}_1 + \frac{\boldsymbol{i}_{\text{e,k},\perp}}{\delta}, \qquad \text{k} \in \{\text{n}, \text{s}, \text{p}\}, \qquad \text{(4.17)}$$

where $\boldsymbol{i}_{\text{s,k},\perp}$ and $\boldsymbol{i}_{\text{e,k},\perp}$ are the y-z components of the solid and electrolyte current, respectively. We define

$$\nabla_\perp \equiv \frac{\partial}{\partial y}\boldsymbol{e}_2 + \frac{\partial}{\partial z}\boldsymbol{e}_3, \qquad \text{(4.18)}$$

for notational convenience.

4.6.1   *The large conductivity limit*

We consider the physically-relevant limit of large (dimensionless) conductivity in the current collectors. There is a distinguished limit when $\sigma_k = \sigma'_k/\delta^2$ for $k \in \{cn, cp\}$, where $\sigma'_k = \mathcal{O}(1)$ as $\delta \to 0$. Further, to retain both heat loss from the current collector surfaces (area $O(1)$) and heat loss from the cell edges including the tabs (area $O(\delta)$) at leading order we consider the limit in which $h = \delta^2 h'$ for $\boldsymbol{x} \in \{-L_{cn}, 1+L_{cp}\} \times \Omega$, and $h = \delta h''$ for the remaining external boundaries, with h' and h'' of $\mathcal{O}(1)$ as $\delta \to 0$. Such a scaling for the heat transfer coefficient is applicable for cooling under free convection, but h may be considerably larger for forced cooling (e.g. [14], [17], [34]). All other parameters are taken to be $\mathcal{O}(1)$. We expand each variable in powers of δ^2 as $\delta \to 0$ in the form

$$\phi_{s,k} = \phi_{s,k}^{(0)} + \delta^2 \phi_{s,k}^{(2)} + \cdots . \tag{4.19}$$

4.6.1.1   *Charge conservation in the solids*

Using (4.17)-(4.18) the governing equations for charge transport in the current collectors, (4.11a)-(4.11b), read

$$\frac{\partial i_{s,k,1}}{\partial x} + \nabla_\perp \cdot \boldsymbol{i}_{s,k,\perp} = 0, \quad k \in \{cn, cp\}, \tag{4.20a}$$

$$\delta^2 i_{s,k,1} = -\sigma'_k \frac{\partial \phi_{s,k}}{\partial x}, \quad \boldsymbol{i}_{s,k,\perp} = -\sigma'_k \nabla_\perp \phi_{s,k}, \quad k \in \{cn, cp\}, \tag{4.20b}$$

along with the rescaled boundary conditions at the tabs

$$\phi_{s,cn} = 0, \qquad\qquad \boldsymbol{x} \in \partial\Omega_{tab,cn}, \tag{4.21a}$$

$$\boldsymbol{i}_{s,cp,\perp} \cdot \boldsymbol{n} = \frac{I_{app}}{A_{tab,cp}}, \qquad\qquad \boldsymbol{x} \in \partial\Omega_{tab,cp}, \tag{4.21b}$$

the no flux conditions (4.11g)–(4.11i), and continuity of the potential and current at the electrode/separator interfaces $x = L_n, 1 - L_p$. After expanding in powers of δ^2, we immediately see from (4.20b) that $\phi_{s,cn}^{(0)}$ and $\phi_{s,cp}^{(0)}$ are independent of x, and therefore $\boldsymbol{i}_{s,cp,\perp}^{(0)}$ and $\boldsymbol{i}_{s,cp,\perp}^{(0)}$ are also independent of x. Then, integration of the leading-order terms in (4.20a) and application of the appropriate boundary conditions gives

$$L_{cn}\nabla_\perp \cdot \boldsymbol{i}_{s,cn,\perp}^{(0)} = -\mathcal{I}_n(y,z), \quad L_{cp}\nabla_\perp \cdot \boldsymbol{i}_{s,cp,\perp}^{(0)} = \mathcal{I}_p(y,z) \tag{4.22}$$

where $\mathcal{I}_n$ and $\mathcal{I}_p$ are the leading-order currents densities through the electrode/current collector interfaces:

$$\begin{aligned}
\mathcal{I}_n(y,z) &:= i_{s,cn,1}^{(0)}\big|_{x=0} = i_{s,n,1}^{(0)}\big|_{x=0}, \\
\mathcal{I}_p(y,z) &:= i_{s,cp,1}^{(0)}\big|_{x=1} = i_{s,p,1}^{(0)}\big|_{x=1}.
\end{aligned} \tag{4.23}$$

Using (4.20b) to write (4.22) in terms of potentials, gives

$$L_{\mathrm{cn}}\sigma'_{\mathrm{cn}}\nabla^2_\perp \phi^{(0)}_{\mathrm{s,cn}} = \mathcal{I}_{\mathrm{n}}, \quad L_{\mathrm{cp}}\sigma'_{\mathrm{cp}}\nabla^2_\perp \phi^{(0)}_{\mathrm{s,cp}} = -\mathcal{I}_{\mathrm{p}}, \quad (y,z) \in \Omega \ \ (4.24a)$$

with boundary conditions

$$\phi^{(0)}_{\mathrm{s,cn}} = 0, \quad (y,z) \in \partial\Omega_{\mathrm{tab,cn},\perp}, \tag{4.24b}$$

$$-\sigma'_{\mathrm{cp}}\nabla_\perp \phi^{(0)}_{\mathrm{s,cp}} \cdot \boldsymbol{n} = \frac{I_{\mathrm{app}}}{A_{\mathrm{tab,cp}}}, \quad (y,z) \in \partial\Omega_{\mathrm{tab,cp},\perp}, \tag{4.24c}$$

$$\nabla_\perp \phi^{(0)}_{\mathrm{s,k}} \cdot \boldsymbol{n} = 0, \quad (y,z) \in \partial\Omega_{\mathrm{ext,k},\perp}, \quad \mathrm{k} \in \{\mathrm{cn, cp}\}. \tag{4.24d}$$

In the electrodes, after using (4.17)-(4.18) the governing equations (4.11c)-(4.11d) read

$$\frac{\partial i_{\mathrm{s,k,1}}}{\partial x} + \nabla_\perp \cdot \boldsymbol{i}_{\mathrm{s,k},\perp} = -j_{\mathrm{k}}, \quad \mathrm{k} \in \{\mathrm{n, p}\}, \tag{4.25a}$$

$$i_{\mathrm{s,k,1}} = -\sigma_{\mathrm{k}}\frac{\partial \phi_{\mathrm{s,k}}}{\partial x}, \quad \boldsymbol{i}_{\mathrm{s,k},\perp} = -\delta^2 \sigma_{\mathrm{k}}\nabla_\perp \phi_{\mathrm{s,k}}, \quad \mathrm{k} \in \{\mathrm{n, p}\}, \tag{4.25b}$$

At leading order $\boldsymbol{i}^{(0)}_{\mathrm{s,k},\perp} = 0$ for $\mathrm{k} \in \{\mathrm{n, p}\}$, so that

$$\frac{\partial i^{(0)}_{\mathrm{s,k,1}}}{\partial x} = -j^{(0)}_{\mathrm{k}}, \quad i^{(0)}_{\mathrm{s,k,1}} = -\sigma_{\mathrm{k}}\frac{\partial \phi^{(0)}_{\mathrm{s,k}}}{\partial x}, \quad \mathrm{k} \in \{\mathrm{n, p}\}, \tag{4.26a}$$

with the boundary conditions

$$\left.\phi^{(0)}_{\mathrm{s,n}}\right|_{x=0} = \phi^{(0)}_{\mathrm{s,cn}}, \qquad \left.i^{(0)}_{\mathrm{s,n,1}}\right|_{x=L_{\mathrm{n}}} = 0, \tag{4.26b}$$

$$\left.\phi^{(0)}_{\mathrm{s,p}}\right|_{x=1} = \phi^{(0)}_{\mathrm{s,cp}}, \qquad \left.i^{(0)}_{\mathrm{s,p,1}}\right|_{x=1-L_{\mathrm{p}}} = 0. \tag{4.26c}$$

4.6.1.2 *Charge conservation in the electrolyte*

A similar calculation holds for charge conservation in the electrolyte. Using (4.17)-(4.18) in (4.13b) the transverse current in the electrolyte is

$$\boldsymbol{i}_{\mathrm{e,k},\perp} = \delta^2 \epsilon^{\mathrm{b}}_{\mathrm{k}}\hat{\kappa}_{\mathrm{e}}\kappa_{\mathrm{e}}(c_{\mathrm{e,k}}, T_{\mathrm{k}}) \left(-\nabla_\perp \phi_{\mathrm{e,k}} \right.$$
$$\left. +2(1-t^+)(1+\Theta T_{\mathrm{k}})\nabla_\perp \left(\log c_{\mathrm{e,k}}\right)\right), \quad \mathrm{k} \in \{\mathrm{n, s, p}\},$$

Thus, to leading order in δ, we have $\boldsymbol{i}_{e,k,\perp}^{(0)} = 0$ for $k \in \{n, s, p\}$, and the flow of current in the electrolyte is also predominantly in the x-direction. Then, at leading order in δ, equations (4.13) give

$$\frac{\partial i_{e,k,1}^{(0)}}{\partial x} = \begin{cases} j_k^{(0)}, & k = n, p, \\ 0, & k = s, \end{cases} \qquad k \in \{n, s, p\}, \tag{4.27a}$$

$$i_{e,k,1}^{(0)} = \epsilon_k^b \hat{\kappa}_e \kappa_e(c_{e,k}^{(0)}, T_k^{(0)}) \left(-\frac{\partial \phi_{e,k}^{(0)}}{\partial x} \right. \tag{4.27b}$$
$$\left. + 2(1 - t^+)(1 + \Theta T_k^{(0)}) \frac{\partial}{\partial x} \left(\log c_{e,k}^{(0)} \right) \right),$$
$$k \in \{n, s, p\},$$

with boundary conditions given by (4.13c)–(4.13d), and continuity conditions given by

$$i_{e,n,1}^{(0)}\big|_{x=0} = 0, \quad i_{e,p,1}^{(0)}\big|_{x=1} = 0, \tag{4.27c}$$

$$\phi_{e,n}^{(0)}\big|_{x=L_n} = \phi_{e,s}^{(0)}\big|_{x=L_n}, \quad i_{e,n,1}^{(0)}\big|_{x=L_n} = i_{e,s,1}^{(0)}\big|_{x=L_n}, \tag{4.27d}$$

$$\phi_{e,s}^{(0)}\big|_{x=1-L_p} = \phi_{e,p}^{(0)}\big|_{x=1-L_p}, \quad i_{e,s,1}^{(0)}\big|_{x=1-L_p} = i_{e,p,1}^{(0)}\big|_{x=1-L_p}. \tag{4.27e}$$

Note that (4.26a), (4.27a) imply $i_{s,k,1}^{(0)} + i_{e,k,1}^{(0)}$ is independent of x, so that

$$i_{s,k,1}^{(0)} + i_{e,k,1}^{(0)} = \mathcal{I}_k \qquad k \in \{n, p\}, \tag{4.27f}$$

which can be used to eliminate $i_{s,k,1}^{(0)}$ in (4.26a). Note also that integrating (4.27a) in x and using (4.27c)-(4.27f) gives

$$\mathcal{I}_n = L_n \bar{j}_n^{(0)} = i_{e,s,1}^{(0)} = -L_p \bar{j}_p^{(0)} = \mathcal{I}_p = \mathcal{I},$$

say, where $\mathcal{I} = \mathcal{I}(y, z)$ is the through-cell current density.

4.6.1.3 *Lithium conservation*

For the lithium concentrations in the solid and electrolyte we find at leading order

$$\mathcal{C}_k \frac{\partial c_{s,k}^{(0)}}{\partial t} = -\frac{1}{r_k^2} \frac{\partial}{\partial r_k} \left(r_k^2 N_{s,k}^{(0)} \right), \quad k \in \{n, p\}, \tag{4.28a}$$

$$N_{s,k}^{(0)} = -D_{s,k}(c_{s,k}^{(0)}, T_k^{(0)}) \frac{\partial c_{s,k}^{(0)}}{\partial r_k}, \quad k \in \{n, p\}, \tag{4.28b}$$

$$\mathcal{C}_\mathrm{e}\epsilon_\mathrm{k}\gamma_\mathrm{e}\frac{\partial c_{\mathrm{e,k}}^{(0)}}{\partial t} = -\gamma_\mathrm{e}\frac{\partial N_{\mathrm{e,k}}^{(0)}}{\partial x} + \mathcal{C}_\mathrm{e}\frac{\partial i_{\mathrm{e,k}}^{(0)}}{\partial x}, \quad \mathrm{k}\in\{\mathrm{n,s,p}\}, \tag{4.28c}$$

$$N_{\mathrm{e,k}}^{(0)} = -\epsilon_\mathrm{k}^\mathrm{b}D_\mathrm{e}(c_{\mathrm{e,k}}^{(0)},T_\mathrm{k}^{(0)})\frac{\partial c_{\mathrm{e,k}}^{(0)}}{\partial x} + \frac{\mathcal{C}_\mathrm{e}t^+}{\gamma_\mathrm{e}}i_{\mathrm{e,k}}^{(0)}, \quad \mathrm{k}\in\{\mathrm{n,s,p}\}, \tag{4.28d}$$

with boundary conditions

$$N_{\mathrm{s,k}}^{(0)}\big|_{r_\mathrm{k}=0} = 0, \quad \frac{a_\mathrm{k}\gamma_\mathrm{k}}{\mathcal{C}_\mathrm{k}}N_{\mathrm{s,k}}^{(0)}\big|_{r_\mathrm{k}=1} = j_\mathrm{k}^{(0)}, \quad \mathrm{k}\in\{\mathrm{n,p}\}, \tag{4.28e}$$

$$N_{\mathrm{e,n}}^{(0)}\big|_{x=0} = 0, \quad N_{\mathrm{e,p}}^{(0)}\big|_{x=1} = 0, \tag{4.28f}$$

$$c_{\mathrm{e,n}}^{(0)}\big|_{x=L_\mathrm{n}} = c_{\mathrm{e,s}}^{(0)}\big|_{x=L_\mathrm{n}}, \quad N_{\mathrm{e,n}}^{(0)}\big|_{x=L_\mathrm{n}} = N_{\mathrm{e,s}}^{(0)}\big|_{x=L_\mathrm{n}}, \tag{4.28g}$$

$$c_{\mathrm{e,s}}^{(0)}\big|_{x=1-L_\mathrm{p}} = c_{\mathrm{e,p}}^{(0)}\big|_{x=1-L_\mathrm{p}}, \quad N_{\mathrm{e,s}}^{(0)}\big|_{x=1-L_\mathrm{p}} = N_{\mathrm{e,p}}^{(0)}\big|_{x=1-L_\mathrm{p}}, \tag{4.28h}$$

and initial conditions

$$c_{\mathrm{s,k}}^{(0)}(x,y,z,r,0) = c_{\mathrm{s,k,0}}, \quad \mathrm{k}\in\{\mathrm{n,p}\}, \tag{4.28i}$$

$$c_{\mathrm{e,k}}^{(0)}(x,y,z,0) = 1, \quad \mathrm{k}\in\{\mathrm{n,s,p}\}. \tag{4.28j}$$

4.6.1.4 *Electrochemistry*

At leading order in δ, the electrochemical reactions are given by

$$j_\mathrm{k}^{(0)} = j_{0,\mathrm{k}}^{(0)}\sinh\left(\frac{\eta_\mathrm{k}^{(0)}}{2(1+\Theta T_\mathrm{k}^{(0)})}\right), \quad \mathrm{k}\in\{\mathrm{n,p}\}, \tag{4.29a}$$

$$j_{0,\mathrm{k}}^{(0)} = \frac{\gamma_\mathrm{k}}{\mathcal{C}_{\mathrm{r,k}}}m_\mathrm{k}(T_\mathrm{k}^{(0)})(c_{\mathrm{s,k}}^{(0)})^{1/2}(1-c_{\mathrm{s,k}}^{(0)})^{1/2}(c_{\mathrm{e,k}}^{(0)})^{1/2}\big|_{r_\mathrm{k}=1}, \tag{4.29b}$$

$$\mathrm{k}\in\{\mathrm{n,p}\},$$

$$\eta_\mathrm{k}^{(0)} = \phi_{\mathrm{s,k}}^{(0)} - \phi_{\mathrm{e,k}}^{(0)} - U_\mathrm{k}(c_{\mathrm{s,k}}^{(0)},T_\mathrm{k}^{(0)})\big|_{r_\mathrm{k}=1}, \quad \mathrm{k}\in\{\mathrm{n,p}\}. \tag{4.29c}$$

4.6.1.5 *Energy conservation*

At leading order in (4.16) we find

$$\frac{\partial^2 T_\mathrm{k}^{(0)}}{\partial x^2} = 0, \quad \mathrm{k}\in\{\mathrm{cn,n,s,p,cp}\} \tag{4.30}$$

with $T_\mathrm{k}^{(0)}$ and $\lambda_\mathrm{k}\partial T_\mathrm{k}^{(0)}/\partial x$ continuous at $x=0,1,L_\mathrm{n}$ and $1-L_\mathrm{p}$, and

$$\frac{\partial T_{\mathrm{cn}}^{(0)}}{\partial x}\bigg|_{x=-L_\mathrm{cn}} = \frac{\partial T_{\mathrm{cp}}^{(0)}}{\partial x}\bigg|_{x=1+L_\mathrm{cp}} = 0, \tag{4.31}$$

giving $T^{(0)} = T^{(0)}(y, z, t)$, where we can drop the subscript k on the leading-order temperature since it is x-independent and the same across all of the cell components. At the next order, we find

$$\mathcal{C}_{\text{th}}\rho_{\text{k}}\frac{\partial T^{(0)}}{\partial t} = \lambda_{\text{k}}\left(\frac{\partial^2 T_{\text{k}}^{(2)}}{\partial x^2} + \nabla_\perp^2 T^{(0)}\right)$$
$$+ \mathcal{B}\left(Q_{\text{Ohm,k}}^{(0)} + Q_{\text{rxn,k}}^{(0)} + Q_{\text{rev,k}}^{(0)}\right), \quad (4.32)$$
$$\text{k} \in \{\text{cn, n, s, p, cp}\},$$

where

$$Q_{\text{Ohm,k}}^{(0)} = \sigma_{\text{k}}\left(\frac{\partial \phi_{\text{s,k}}^{(0)}}{\partial x}\right)^2 - i_{\text{e,k,1}}^{(0)}\frac{\partial \phi_{\text{e,k}}^{(0)}}{\partial x}, \qquad \text{k} \in \{\text{n, p}\}, \qquad (4.33a)$$

$$Q_{\text{Ohm,s}}^{(0)} = -i_{\text{e,s,1}}^{(0)}\frac{\partial \phi_{\text{e,s}}^{(0)}}{\partial x}, \qquad\qquad\qquad\qquad (4.33b)$$

$$Q_{\text{Ohm,k}}^{(0)} = \sigma_{\text{k}}'|\nabla_\perp \phi_{\text{s,k}}^{(0)}|^2, \qquad\qquad \text{k} \in \{\text{cn, cp}\} \qquad (4.33c)$$

and $Q_{\text{rxn,k}}^{(0)}$ and $Q_{\text{rev,k}}^{(0)}$ are the leading-order terms in (4.16e)-(4.16f). Integrating across the whole cell from $x = -L_{\text{cn}}$ to $x = 1 + L_{\text{cp}}$ gives

$$\mathcal{C}_{\text{th}}\sum_{\text{k}}\left(\rho_{\text{k}}L_{\text{k}}\right)\frac{\partial T^{(0)}}{\partial t} = \sum_{\text{k}}\left(\lambda_{\text{k}}L_{\text{k}}\right)\nabla_\perp^2 T^{(0)}$$
$$+ \mathcal{B}\int_{-L_{\text{cn}}}^{1+L_{\text{cp}}} Q_{\text{k}}^{(0)}\,\mathrm{d}x \qquad (4.34)$$
$$+ \left[\lambda_{\text{k}}\frac{\partial T_{\text{k}}^{(2)}}{\partial x}\right]_{-L_{\text{cn}}}^{1+L_{\text{cp}}},$$

where $Q_{\text{k}}^{(0)} = Q_{\text{Ohm,k}}^{(0)} + Q_{\text{rxn,k}}^{(0)} + Q_{\text{rev,k}}^{(0)}$, and it is understood that the integral of $Q_{\text{k}}^{(0)}$ is the sum of the integrals over each cell component. The final term of (4.34) may be evaluated through the use of the boundary condition (4.16g), which gives

$$\lambda_{\text{cn}}\frac{\partial T_{\text{cn}}^{(2)}}{\partial x}\bigg|_{-L_{\text{cn}}} = h_{\text{cn}}'T^{(0)}, \quad \lambda_{\text{cp}}\frac{\partial T_{\text{cp}}^{(2)}}{\partial x}\bigg|_{1+L_{\text{cp}}} = -h_{\text{cn}}'T^{(0)}, \qquad (4.35)$$

where

$$h_{\text{cn}}'(y, z) = h'(-L_{\text{cn}}, y, z), \quad h_{\text{cp}}'(y, z) = h'(1 + L_{\text{cp}}, y, z),$$

are the heat transfer coefficients for the negative and positive current collectors, respectively. Since our choice of nondimensionalisation is such that

$$\sum_k \rho_k L_k = \sum_k \lambda_k L_k = \sum_k L_k = L_{cn} + 1 + L_{cp} = L,$$

say, the governing equation for the leading-order temperature may be written

$$\mathcal{C}_{th} \frac{\partial T^{(0)}}{\partial t} = \nabla_\perp^2 T^{(0)} + \mathcal{B} \bar{Q}^{(0)} - \frac{(h'_{cn} + h'_{cp})}{L} T^{(0)}, \tag{4.36a}$$

where

$$\bar{Q}^{(0)} = \frac{1}{L} \int_{-L_{cn}}^{1+L_{cp}} Q_k^{(0)} \, \mathrm{d}x$$

is the x-averaged heat source term. Equation (4.36a) is subject to the initial condition

$$T^{(0)}(y, z, 0) = T_0, \tag{4.36b}$$

and the boundary condition

$$-\nabla_\perp T^{(0)} \cdot \boldsymbol{n} = \overline{h''} T^{(0)} \quad (y, z) \in \partial\Omega, \tag{4.36c}$$

where

$$\overline{h''} = \frac{1}{L} \int_{-L_{cn}}^{1+L_{cp}} h'' \, \mathrm{d}x$$

is the x-averaged edge heat transfer coefficient.

4.6.1.6 *Summary*

To leading order the reduced model is the two-dimensional pair-potential problem

$$L_{cn} \sigma'_{cn} \nabla_\perp^2 \phi_{s,cn}^{(0)} = \mathcal{I}, \qquad L_{cp} \sigma'_{cp} \nabla_\perp^2 \phi_{s,cp}^{(0)} = -\mathcal{I} \qquad \text{in } \Omega \tag{4.37a}$$

with boundary conditions

$$\phi_{s,cn}^{(0)} = 0 \quad \text{on } \partial\Omega_{tab,cn,\perp}, \tag{4.37b}$$

$$\nabla_\perp \phi_{s,cn}^{(0)} \cdot \boldsymbol{n} = 0 \quad \text{on } \partial\Omega_{ext,cn,\perp} \tag{4.37c}$$

$$-\sigma'_{cp} \nabla_\perp \phi_{s,cp}^{(0)} \cdot \boldsymbol{n} = \frac{I_{app}}{A_{tab,cp}} \quad \text{on } \partial\Omega_{tab,cp,\perp}, \tag{4.37d}$$

$$\nabla_\perp \phi_{s,cp}^{(0)} \cdot \boldsymbol{n} = 0 \quad \text{on } \partial\Omega_{ext,cp,\perp}, \tag{4.37e}$$

where $\mathcal{I}$ is the through-cell current given (at each point (y, z)) by a one-dimensional DFN model (4.26)-(4.29), coupled to the two-dimensional thermal problem

$$\mathcal{C}_{\text{th}}\frac{\partial T^{(0)}}{\partial t} = \nabla_\perp^2 T^{(0)} + \mathcal{B}\bar{Q}^{(0)} - \frac{(h'_{\text{cn}} + h'_{\text{cp}})}{L}T^{(0)} \quad \text{in } \Omega, \qquad (4.37\text{f})$$

$$- \nabla_\perp T^{(0)} \cdot \boldsymbol{n} = \overline{h''}T^{(0)} \quad \text{on } \partial\Omega. \qquad (4.37\text{g})$$

with initial condition $T^{(0)} = T_0$, where the heat source is

$$\begin{aligned}\bar{Q}^{(0)} = \frac{1}{L}\int_0^1 \mathcal{Q}^{(0)}\ \mathrm{d}x &+ \frac{L_{\text{cn}}}{L}\sigma'_{\text{cn}}|\nabla_\perp\phi_{\text{s,cn}}^{(0)}|^2 \\ &+ \frac{L_{\text{cp}}}{L}\sigma'_{\text{cp}}|\nabla_\perp\phi_{\text{s,cp}}^{(0)}|^2,\end{aligned} \qquad (4.37\text{h})$$

where $\mathcal{Q}^{(0)} = Q_{\text{Ohm,k}}^{(0)} + Q_{\text{rxn,k}}^{(0)} + Q_{\text{rev,k}}^{(0)}$ (k $\in$ {n, s, p}) is the heat source in the one-dimensional DFN model.

4.6.2   *The very large conductivity limit*

The model derived in §4.6.1 is the distinguished limit in which the resistance to current travelling down the current collector is comparable to that to current travelling through the cell. In applications, in order to ensure the whole cell is used uniformly, the current collectors are designed to be thick enough that the potential on them is approximately uniform. In this section we analyse this situation by considering the sub-limit $\sigma'_k \gg 1$.

In §4.6.1 we also took the edge cooling coefficient to be asymptotically larger than the surface cooling coefficient so that both effects appeared in the leading-order heat balance. In this section, we weaken the effect of edge cooling by considering the sub-limit $h'' \ll 1$. We also suppose that the surface cooling coefficients h'_k do not vary spatially so that the temperature is also approximately uniform.

We will see that with these approximations the model simplifies considerably. For ease of exposition we quantify the limits by introducing a single small parameter ε such that $\sigma'_k = \sigma''_k/\varepsilon$, $h'' = h'''\varepsilon$ with σ''_k, $h''' = \mathcal{O}(1)$ as $\varepsilon \to 0$. We now expand the leading-order term of §4.6.1 in each variable in powers of ε as

$$\phi_{\text{s,k}}^{(0)} = \phi_{\text{s,k}}^{(00)} + \varepsilon\phi_{\text{s,k}}^{(01)} + \cdots, \qquad (4.38)$$

as $\varepsilon \to 0$. We will retain both the leading term and the first correction in this expansion in ε, while neglecting the first correction in the expansion in δ^2; thus our results are asymptotically accurate providing $\delta^2 \ll \varepsilon$. After rewriting σ'_k and h'' (4.37) become

$$L_{\text{cn}}\sigma''_{\text{cn}}\nabla_\perp^2\phi_{\text{s,cn}}^{(0)} = \varepsilon\mathcal{I}, \qquad L_{\text{cp}}\sigma''_{\text{cp}}\nabla_\perp^2\phi_{\text{s,cp}}^{(0)} = -\varepsilon\mathcal{I} \qquad \text{in } \Omega \quad (4.39\text{a})$$

$$\phi_{\text{s,cn}}^{(0)} = 0 \quad \text{on } \partial\Omega_{\text{tab,cn},\perp}, \tag{4.39b}$$

$$\nabla_\perp \phi_{\text{s,cn}}^{(0)} \cdot \boldsymbol{n} = 0 \quad \text{on } \partial\Omega_{\text{ext,cn},\perp} \tag{4.39c}$$

$$-\sigma_{\text{cp}}'' \nabla_\perp \phi_{\text{s,cp}}^{(0)} \cdot \boldsymbol{n} = \frac{\varepsilon I_{\text{app}}}{A_{\text{tab,cp}}} \quad \text{on } \partial\Omega_{\text{tab,cp},\perp}, \tag{4.39d}$$

$$\nabla_\perp \phi_{\text{s,cp}}^{(0)} \cdot \boldsymbol{n} = 0 \quad \text{on } \partial\Omega_{\text{ext,cp},\perp}, \tag{4.39e}$$

$$\mathcal{C}_{\text{th}} \frac{\partial T^{(0)}}{\partial t} = \nabla_\perp^2 T^{(0)} + \mathcal{B}\bar{Q}^{(0)} - \frac{(h_{\text{cn}}' + h_{\text{cp}}')}{L} T^{(0)} \quad \text{in } \Omega, \tag{4.39f}$$

$$-\nabla_\perp T^{(0)} \cdot \boldsymbol{n} = \varepsilon \overline{h'''} T^{(0)} \quad \text{on } \partial\Omega. \tag{4.39g}$$

with initial condition $T^{(0)} = T_0$. It is useful to also write down a global current conservation equation, by integrating the second equation in (4.39a) over Ω and using (4.39d) to give

$$I_{\text{app}} = \int_\Omega \mathcal{I} \, \mathrm{d}y \, \mathrm{d}z. \tag{4.39h}$$

4.6.2.1 *Leading-order problem*

At leading order in ε we find the potentials are uniform as expected, with

$$\phi_{\text{s,cn}}^{(00)} = 0, \qquad \phi_{\text{s,cp}}^{(00)} = V^{(00)}(t), \tag{4.40}$$

where $V^{(00)}(t)$ is the (unknown) leading-order terminal voltage. Since (4.39g) gives

$$-\nabla_\perp T^{(00)} \cdot \boldsymbol{n} = 0 \quad \text{on } \partial\Omega,$$

the leading-order temperature $T^{(00)}$ will be spatially uniform if the heat source $\bar{Q}^{(00)}$ is spatially uniform. Additionally, if $T^{(00)}$ is spatially uniform then at each point (y, z) the one-dimensional DFN model (4.27)-(4.29) sees the same temperature $T^{(00)}$ and potential difference $V(t)$, so that (providing the initial condition is independent of y and z) the solution to each of these models is independent of y and z, and the through-cell current $\mathcal{I}^{(00)}$ and heating $\bar{Q}^{(00)}$ are uniform. Thus a single one-dimensional DFN problem suffices to determine $V^{(00)}$ as a functional of $\mathcal{I}^{(00)}$ and $T^{(00)}$. Let us write this output of the DFN model as

$$\phi_{\text{s,cp}} - \phi_{\text{s,cn}} = \mathcal{V}(\mathcal{I}, T), \tag{4.41}$$

so that $V^{(00)} = \mathcal{V}(\mathcal{I}^{(00)}, T^{(00)})$. The current $\mathcal{I}^{(00)}$ is given by (4.39h) as

$$\mathcal{I}^{(00)} = \frac{I_{\text{app}}}{L_y L_z}, \tag{4.42}$$

while the leading-order temperature is determined from the ordinary differential equation

$$
\mathcal{C}_{\text{th}}\frac{\mathrm{d}T^{(00)}}{\mathrm{d}t} = \mathcal{B}\bar{\mathcal{Q}}(\mathcal{I}^{(00)}, T^{(00)}) - \frac{(h'_{\text{cn}} + h'_{\text{cp}})}{L}T^{(00)},
\tag{4.43a}
$$

with initial condition $T^{(00)}(0) = T_0$, where

$$
\bar{\mathcal{Q}}(\mathcal{I}, T) = \frac{1}{L}\int_0^1 \mathcal{Q}^{(0)} \,\mathrm{d}x,
\tag{4.44}
$$

is the x-averaged heat source in the one-dimensional DFN model, which, like $\mathcal{V}$ is a functional of the temperature T and current $\mathcal{I}$.

4.6.2.2 *First-order correction*

The first-order corrections to the current collector potentials satisfy

$$
L_{\text{cn}}\sigma''_{\text{cn}}\nabla_\perp^2\phi_{\text{s,cn}}^{(01)} = \frac{I_{\text{app}}}{L_yL_z}, \quad \text{in } \Omega
\tag{4.45a}
$$

$$
L_{\text{cp}}\sigma''_{\text{cp}}\nabla_\perp^2\phi_{\text{s,cp}}^{(01)} = -\frac{I_{\text{app}}}{L_yL_z}, \quad \text{in } \Omega
\tag{4.45b}
$$

$$
\phi_{\text{s,cn}}^{(01)} = 0 \quad \text{on } \partial\Omega_{\text{tab,cn},\perp}, \qquad \nabla_\perp\phi_{\text{s,cn}}^{(01)}\cdot\boldsymbol{n} = 0 \quad \text{on } \partial\Omega_{\text{ext,cn},\perp}
\tag{4.45c}
$$

$$
-\sigma''_{\text{cp}}\nabla_\perp\phi_{\text{s,cp}}^{(01)}\cdot\boldsymbol{n} = \frac{I_{\text{app}}}{A_{\text{tab,cp}}} \quad \text{on } \partial\Omega_{\text{tab,cp},\perp},
\tag{4.45d}
$$

$$
\nabla_\perp\phi_{\text{s,cp}}^{(01)}\cdot\boldsymbol{n} = 0 \quad \text{on } \partial\Omega_{\text{ext,cp},\perp},
\tag{4.45e}
$$

We note that $\phi_{\text{s,cp}}^{(01)}$ is only determined up to a function of time, which is fixed by solving the through-cell DFN problem at $\mathcal{O}(\varepsilon)$. However, we will see that we can evaluate this term without solving multiple DFN models parameterised by y and z. We use (4.41) to write

$$
\phi_{\text{s,cp}}^{(01)} - \phi_{\text{s,cn}}^{(01)} = \frac{\delta\mathcal{V}}{\delta\mathcal{I}}\mathcal{I}^{(01)} + \frac{\delta\mathcal{V}}{\delta T}T^{(01)}
$$

where the functional derivatives are evaluated at $(\mathcal{I}^{(00)}, T^{(00)})$, and are therefore independent of y and z. Integrating over Ω gives

$$
\langle\phi_{\text{s,cp}}^{(01)}\rangle - \langle\phi_{\text{s,cn}}^{(01)}\rangle = \frac{\delta\mathcal{V}}{\delta\mathcal{I}}\langle\mathcal{I}^{(01)}\rangle + \frac{\delta\mathcal{V}}{\delta T}\langle T^{(01)}\rangle
\tag{4.46}
$$

where

$$
\langle\cdot\rangle = \frac{1}{L_yL_z}\int_\Omega \cdot \,\mathrm{d}y\,\mathrm{d}z.
$$

But (4.39h) gives

$$\langle \mathcal{I}^{(01)} \rangle = 0,$$

so the only contribution from the DFN at $O(\varepsilon)$ is from the temperature perturbation.

Recalling that the terminal voltage is the average of the potential over the positive tab,

$$V^{(01)} = \frac{L_{cp}}{A_{tab,cp}} \int_{\partial\Omega_{tab,cp,\perp}} \phi_{s,cp}^{(01)} \, ds \,,$$

and (4.45a) and (4.45e) are enough to determine $\langle \phi_{s,cn}^{(01)} \rangle$ and $V^{(01)} - \langle \phi_{s,cp}^{(01)} \rangle$, which can be interpreted as the potential drops across the negative and positive current collectors respectively. Since these are proportional to I_{app} (which may be time dependent) they can be most easily formulated in terms of current collector resistances by writing

$$\langle \phi_{s,cn}^{(01)} \rangle = -R_{cn} I_{app}, \qquad V^{(01)} - \langle \phi_{s,cp}^{(01)} \rangle = -R_{cp} I_{app}, \qquad (4.47)$$

where

$$R_{cn} = \frac{\langle f_n \rangle}{L_y L_z L_{cn} \sigma_{cn}''}, \qquad R_{cp} = \frac{1}{L_y L_z \sigma_{cp}'' A_{tab,cp}} \int_{\partial\Omega_{tab,cp,\perp}} f_p \, ds \quad (4.48)$$

with

$$\nabla_\perp^2 f_n = -1, \qquad \nabla_\perp^2 f_p = 1 \qquad \text{in } \Omega, \qquad (4.49a)$$

$$f_n = 0 \quad \text{on } \partial\Omega_{tab,cn,\perp}, \qquad (4.49b)$$

$$\nabla_\perp f_n \cdot \boldsymbol{n} = 0 \quad \text{on } \partial\Omega_{ext,cn,\perp}, \qquad (4.49c)$$

$$\nabla_\perp f_p \cdot \boldsymbol{n} = \frac{L_y L_z L_{cp}}{A_{tab,cp}} \quad \text{on } \partial\Omega_{tab,cp,\perp}, \qquad (4.49d)$$

$$\nabla_\perp f_p \cdot \boldsymbol{n} = 0 \ \text{on } \partial\Omega_{ext,cp,\perp}, \qquad \langle f_p \rangle = 0. \qquad (4.49e)$$

Combining (4.47) with (4.46) gives the perturbation to the terminal voltage as

$$V^{(01)} = \frac{\delta \mathcal{V}}{\delta T} \langle T^{(01)} \rangle - R_{cp} I_{app} - R_{cn} I_{app}. \qquad (4.50)$$

At next order in (4.39f)-(4.39g) we find

$$
\mathcal{C}_{\text{th}}\frac{\partial T^{(01)}}{\partial t} = \nabla_\perp^2 T^{(01)} + \mathcal{B}\frac{\delta \bar{\mathcal{Q}}}{\delta T}T^{(01)} - \frac{(h'_{\text{cn}} + h'_{\text{cp}})}{L}T^{(01)}
$$
$$
+ \frac{\mathcal{B}L_{\text{cn}}\sigma''_{\text{cn}}}{L}|\nabla_\perp \phi^{(01)}_{\text{s,cn}}|^2
$$
$$
+ \frac{\mathcal{B}L_{\text{cp}}\sigma''_{\text{cp}}}{L}|\nabla_\perp \phi^{(01)}_{\text{s,cp}}|^2 \quad \text{in } \Omega,
$$
$$
-\nabla_\perp T^{(01)} \cdot \boldsymbol{n} = \overline{h'''}T^{(00)} \quad \text{on } \partial\Omega,
$$

where the functional derivative is evaluated at $T^{(00)}$. Integrating over y and z gives

$$
\mathcal{C}_{\text{th}}\frac{\partial \langle T^{(01)}\rangle}{\partial t} = \mathcal{B}\frac{\delta \bar{\mathcal{Q}}}{\delta T}\langle T^{(01)}\rangle - \frac{(h'_{\text{cn}} + h'_{\text{cp}})}{L}\langle T^{(01)}\rangle
$$
$$
- \frac{T^{(00)}}{L_y L_z}\int_{\partial\Omega}\overline{h'''}\,\mathrm{d}s + H_{\text{cn}}I^2_{\text{app}} \tag{4.51}
$$
$$
+ H_{\text{cp}}I^2_{\text{app}} \quad \text{in } \Omega,
$$

where the coefficients related to Ohmic heating in the current collectors are

$$
H_{\text{cn}} = \frac{\mathcal{B}L_{\text{cn}}}{L(L_y L_z L_{\text{cn}})^2\sigma''_{\text{cn}}}\langle|\nabla_\perp f_{\text{n}}|^2\rangle, \tag{4.52a}
$$
$$
H_{\text{cp}} = \frac{\mathcal{B}L_{\text{cp}}}{L(L_y L_z L_{\text{cp}})^2\sigma''_{\text{cp}}}\langle|\nabla_\perp f_{\text{p}}|^2\rangle. \tag{4.52b}
$$

In principle (4.51) allows the correction to the average temperature to be determined, whence (4.50) gives the correction to the terminal voltage. Rather than evaluating $\delta\mathcal{V}/\delta T$ and $\delta\bar{\mathcal{Q}}/\delta T$ the most convenient way to capture the perturbation is to note that

$$
\mathcal{V}(\mathcal{I}^{(00)}, T^{(00)} + \varepsilon\langle T^{(01)}\rangle) = \mathcal{V}(\mathcal{I}^{(00)}, T^{(00)})
$$
$$
+ \varepsilon\frac{\delta\mathcal{V}}{\delta T}(\mathcal{I}^{(00)}, T^{(00)})\langle T^{(01)}\rangle
$$
$$
+ O(\varepsilon^2),
$$

so that

$$
V^{(00)} + \varepsilon V^{(01)} = \mathcal{V}(\mathcal{I}^{(00)}, T^{(00)} + \varepsilon\langle T^{(01)}\rangle)
$$
$$
- \varepsilon R_{\text{cp}}I_{\text{app}} - \varepsilon R_{\text{cn}}I_{\text{app}} + O(\varepsilon^2).
$$

Thus we may solve a single one-dimensional DFN using the y, z-averaged temperature, and the error will be $O(\varepsilon^2)$.

4.6.2.3 *Summary*

Writing $\langle T \rangle = T^{(00)} + \varepsilon \langle T^{(01)} \rangle$ gives

$$V = \mathcal{V}(\mathcal{I}^{(00)}, \langle T \rangle) - \varepsilon R_{\text{cp}} I_{\text{app}} - \varepsilon R_{\text{cn}} I_{\text{app}} + O(\varepsilon^2, \delta^2), \tag{4.53a}$$

$$\mathcal{C}_{\text{th}} \frac{\partial \langle T \rangle}{\partial t} = \mathcal{B} \bar{\mathcal{V}}(\mathcal{I}^{(00)}, \langle T \rangle) - \frac{(h'_{\text{cn}} + h'_{\text{cp}})}{L} \langle T \rangle$$
$$- \frac{\varepsilon \langle T \rangle}{L_y L_z} \int_{\partial \Omega} \overline{h'''} \, \mathrm{d}s \tag{4.53b}$$
$$+ \varepsilon H_{\text{cn}} I_{\text{app}}^2 + \varepsilon H_{\text{cp}} I_{\text{app}}^2 + O(\varepsilon^2, \delta^2) \quad \text{in } \Omega.$$

After solving this single one-dimensional model, the potential distribution in the current collectors is

$$\phi_{\text{s,cn}} = -\frac{\varepsilon \mathcal{I}^{(00)}}{L_{\text{cn}} \sigma''_{\text{cn}}} f_{\text{n}} + O(\varepsilon^2, \delta^2), \tag{4.53c}$$

$$\phi_{\text{s,cp}} = V + \frac{\varepsilon \mathcal{I}^{(00)}}{L_{\text{cp}} \sigma''_{\text{cp}}} f_{\text{p}} + O(\varepsilon^2, \delta^2). \tag{4.53d}$$

Recall that in this limit the leading-order current is $\mathcal{I}^{(00)} = I_{\text{app}}/(L_y L_z)$.

4.6.2.4 *An ad-hoc model for the temperature distribution*

The reduced model (4.53) gives the spatial variation of the potential in the current collectors, but only the average cell temperature. An approach sometimes used in the literature is to retain the spatial derivatives in the energy balance equation, but use heat source terms from the averaged one-dimensional electrochemical model (see e.g. [30]). Such an approach corresponds to replacing $\bar{\mathcal{Q}}(\mathcal{I}^{(00)}, T)$ with $\bar{\mathcal{Q}}(\mathcal{I}^{(00)}, \langle T \rangle)$ and replaces (4.53b) with

$$\mathcal{C}_{\text{th}} \frac{\partial T}{\partial t} = \nabla_\perp^2 T + \mathcal{B} \bar{\mathcal{Q}}(\mathcal{I}^{(00)}, \langle T \rangle) - \frac{(h'_{\text{cn}} + h'_{\text{cp}})}{L} T$$
$$+ \frac{\mathcal{B} L_{\text{cn}} \sigma''_{\text{cn}}}{\varepsilon L} |\nabla_\perp \phi_{\text{s,cn}}|^2 + \frac{\mathcal{B} L_{\text{cp}} \sigma''_{\text{cp}}}{\varepsilon L} |\nabla_\perp \phi_{\text{s,cp}}|^2 \tag{4.54a}$$
$$\text{in } \Omega,$$

$$- \nabla_\perp T \cdot \boldsymbol{n} = \varepsilon \overline{h'''} T \quad \text{on } \partial \Omega. \tag{4.54b}$$

This model captures the variation due to Ohmic heating in the current collectors and cooling at the boundaries, but neglects the spatial variation of the heat source within the cell.

4.7 NUMERICAL COMPARISON

In this section, we provide a numerical comparison of the full pouch cell model with the reduced models (4.37) and (4.53). For ease of exposition, we focus on the case in which all variables are uniform in y, so that the full model is two-dimensional, and the reduced model (4.37) has a one-dimensional current collector (in the z-direction), at each point of which we solve a one-dimensional DFN model (we refer to this as a 1+1D model, though since the DFN is already a pseudo-two-dimensional model, perhaps it is more properly a 1+1+1D model). We refer to the very-high conductivity limit model (4.53) as the DFNCC model, to indicate that it involves a single (averaged) DFN model with an additional (uncoupled) problem for the distribution of potential in the current collectors (from which the resistance and heat source can be calculated).

Numerical simulations of the full model were performed using the commercial software COMSOL [33], while the reduced models were implemented in PyBaMM [86]. All simulations were performed on a desktop computer (i5, 2.1 GHz) with 16 Gb of RAM. The model equations in COMSOL are discretised in space using the finite-element method, while in PyBaMM the equations are discretised using the finite-volume method. Both solvers use an adaptive, variable-order backward differentiation formula for the time integration, with both relative and absolute tolerances set to 10^{-6}. Since we aim to compare the full and reduced models and not the merits of any particular numerical approach, we provide a comparison of the solutions of the standard one-dimensional DFN model produced by both COMSOL and PyBaMM in Appendix A.6. Whilst this does not fully quantify differences introduced by employing two different numerical solution methods, it does provide context for our comparisons that follow.

Typical dimensional parameter values for a battery comprising a carbon negative current collector, graphite negative electrode, LiPF$_6$ in EC:DMC electrolyte, LCO positive electrode, and aluminium positive current collector are given in Tables 2.1, 2.2, and Table 4.1. These translate into the dimensionless parameters in Tables 3.3, 3.4, 4.2, and 4.3. From there we see that

$$h \approx 3.8 \times 10^{-5}, \quad \delta \approx 1.6 \times 10^{-3}.$$

The dimensionless conductivities σ_{cn} and σ_{cp} depend on the charge/discharge rate (the so-called C-rate). To give an idea of the typical asymptotic regime batteries operate in, at a C-rate of 3 we find that

$$\sigma_{\mathrm{cn}} \approx 9.5 \times 10^7, \quad \sigma_{\mathrm{cp}} \approx 5.6 \times 10^7. \tag{4.55}$$

We compare the results of the 2D DFN model with the 1+1D DFN and DFNCC models for a 3 C constant current discharge, with both

positive and negative tabs placed at the top of the cell (i.e. at $z = L_z$). In Figures 4.2, 4.3, 4.4 and 4.5 we present comparisons for the potential in the negative current collector, the potential in the positive current collector, the through-cell current density and the x-averaged temperature respectively. Solutions from the full model are shown as a function of space in time in panel (a), with snapshots at a series of times throughout the discharge shown in panel (b). The time- and space-averaged absolute errors (by "error" we mean the difference between the numerical solution of the reduced model in PyBaMM and the COMSOL solution of the full model) are shown in panels (c) and (d), respectively.

We see in Figures 4.2 and 4.3 that the electrical conductivity of the current collectors is sufficiently high that the potentials remain fairly uniform in space, and both the 1+1D DFN and DFNCC models accurately capture the potential distribution in the current collectors. The error is of a similar size to that between the numerical solutions of
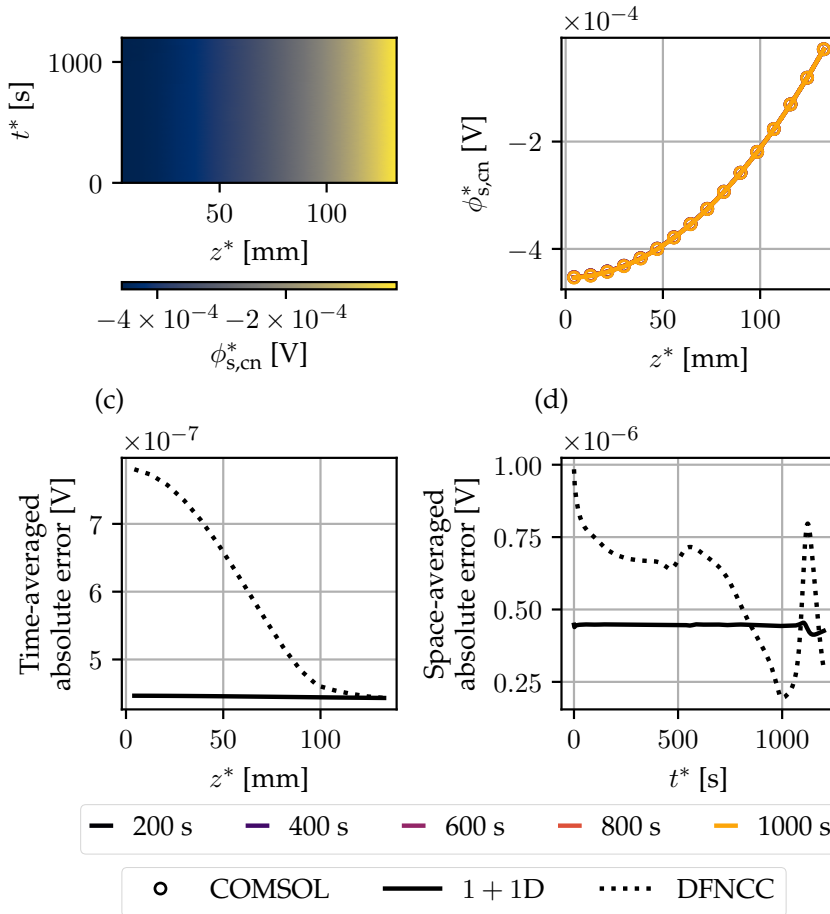
Figure 4.2: Potential in the negative current collector. (a) the COMSOL solution; (b) comparison with the reduced models at various times during discharge; (c) time-averaged absolute errors; (d) z-averaged absolute errors.
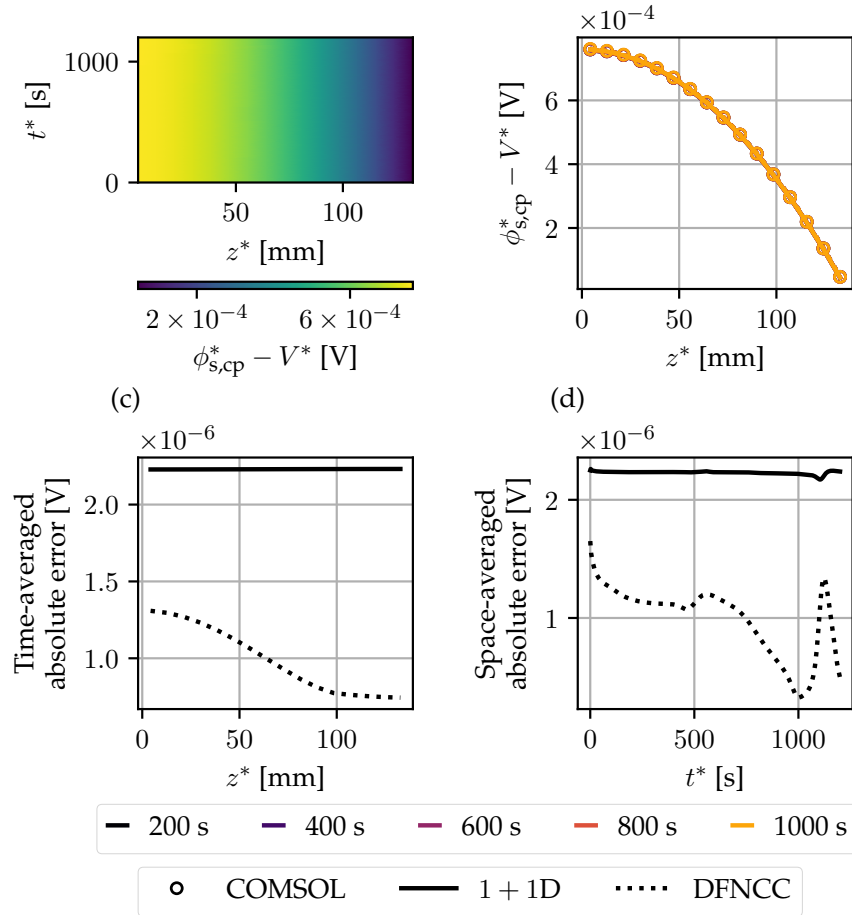
Figure 4.3: Potential in the positive current collector (with the terminal voltage subtracted off). (a) the COMSOL solution; (b) comparison with the reduced models at various times during discharge; (c) time-averaged absolute errors; (d) z-averaged absolute errors.

the 1D DFN obtained using COMSOL and PyBaMM (Appendix A.6), so that little additional error has been introduced as a result of the asymptotic reduction.

In Figure 4.4(a) we see that positioning both tabs at the top of the cell means that for most of the simulation the current preferentially travels through the upper part of the cell. Eventually, as the cell continues to discharge, this part becomes more (de)lithiated until the resultant local increase in through-cell resistance is sufficient for it to become preferential for the current to travel further down the current collectors and through the lower part of the cell (as seen in the final time shown in Figure 4.4(b)). This behaviour is well captured by the 1+1D model, with space-averaged absolute errors in the through-cell current on the order of $10^{-3}\,\mathrm{A\,m^{-2}}$ for most of the discharge, as displayed in Figure 4.4(d). The largest error is found towards the end of the discharge where the OCV becomes highly nonlinear. However, this is also where the greatest discrepancy in the solution between COMSOL and PyBaMM in 1D is
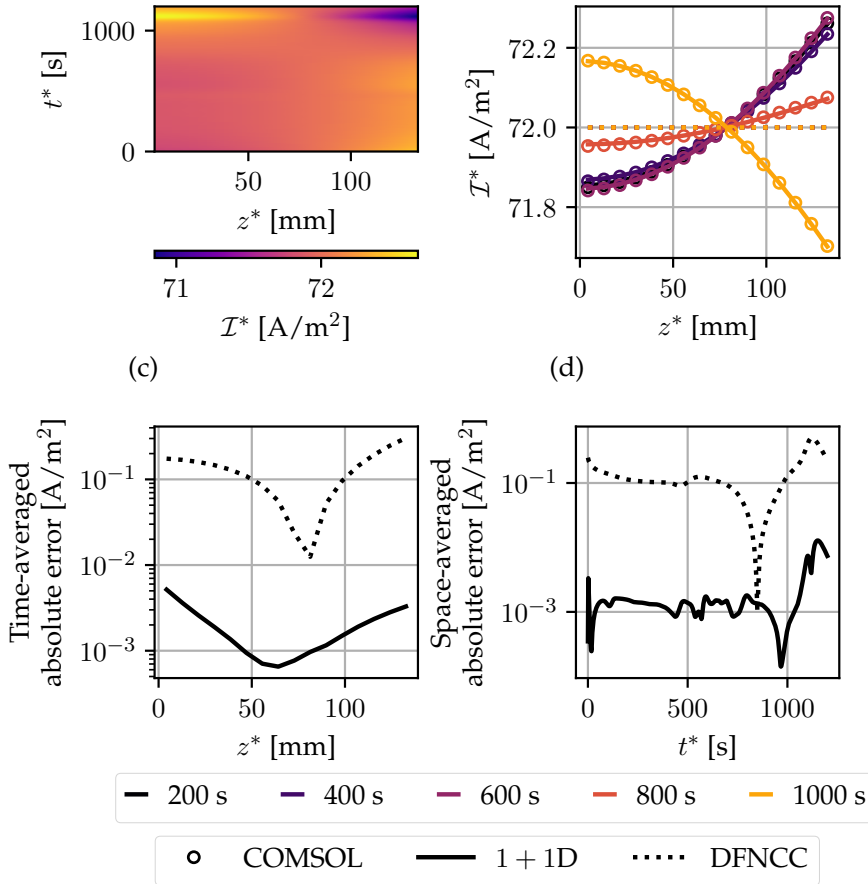
Figure 4.4: Through-cell current density. (a) the COMSOL solution; (b) comparison with the reduced models at various times during discharge; (c) time-averaged absolute errors; (d) z-averaged absolute errors.

found (see the 1C result in Figure A.4). In the DFNCC formulation, the through-cell current density is assumed uniform, so the greatest error is found at the ends of the current collectors where the current density deviates most from its average.

For the parameters in Tables 2.1, 2.2, and 4.1, we find that the temperature exhibits a relatively weak variation along the length of the current collectors, as shown in Figure 4.5. The 1+1D model captures the temperature distribution well.

Since the temperature rise is moderate (and the variation of temperature in space is small), the uniform temperature predicted by the DFNCC model gives a good estimate of the temperature in the full model.

In Table 4.4, we give the normalised RMS error in the current collector potentials, through-cell current, temperature, and voltage obtained by solving the model in PyBaMM as the mesh is refined. The RMS error was computed against the solution obtained using COMSOL's "fine" mesh (450 elements in each current collector, 1650 elements in
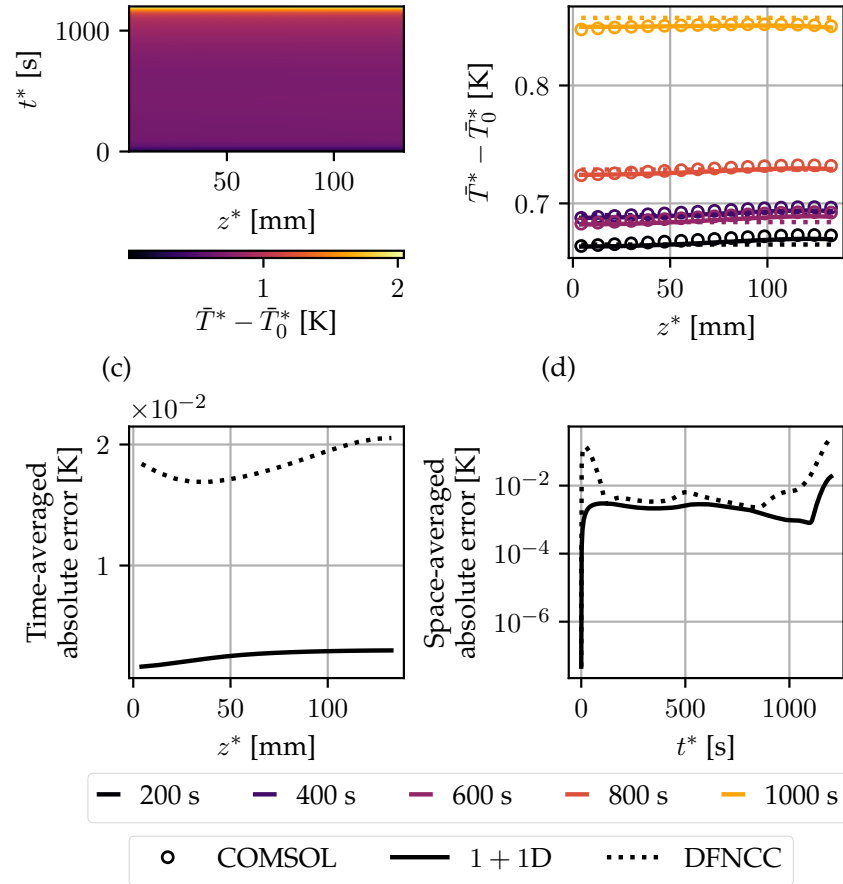
Figure 4.5: The x^*-averaged temperature (a) the COMSOL solution; (b) comparison with the reduced models at various times during discharge; (c) time-averaged absolute errors; (d) z^*-averaged absolute errors.

each electrode, 450 elements in the separator), which was typically solved in around 5376 s. It can be seen that the error in the through-cell current density $\mathcal{I}^*$ for the DFNCC model is much larger than that of the $1 + 1$D model, and remains unchanged as the mesh is refined: this is the asymptotic error inherent in the model. However, other quantities, such as the terminal voltage, are predicted equally well by the DFNCC model at a fraction of the computation time. Depending on the quantities of interest the simpler DFNCC model may well be sufficient for a range of applications.

Finally, to illustrate the asymptotic convergence of the DFNCC model we fix $\sigma_{\mathrm{cn}} = \sigma_{\mathrm{cp}} = \sigma$ and solve for a range of values of σ. The normalised RMS error between the 2D solution in COMSOL and the 1+1D DFN and DFNCC solutions in PyBaMM for a selection of model variables are shown in Figure 4.6.
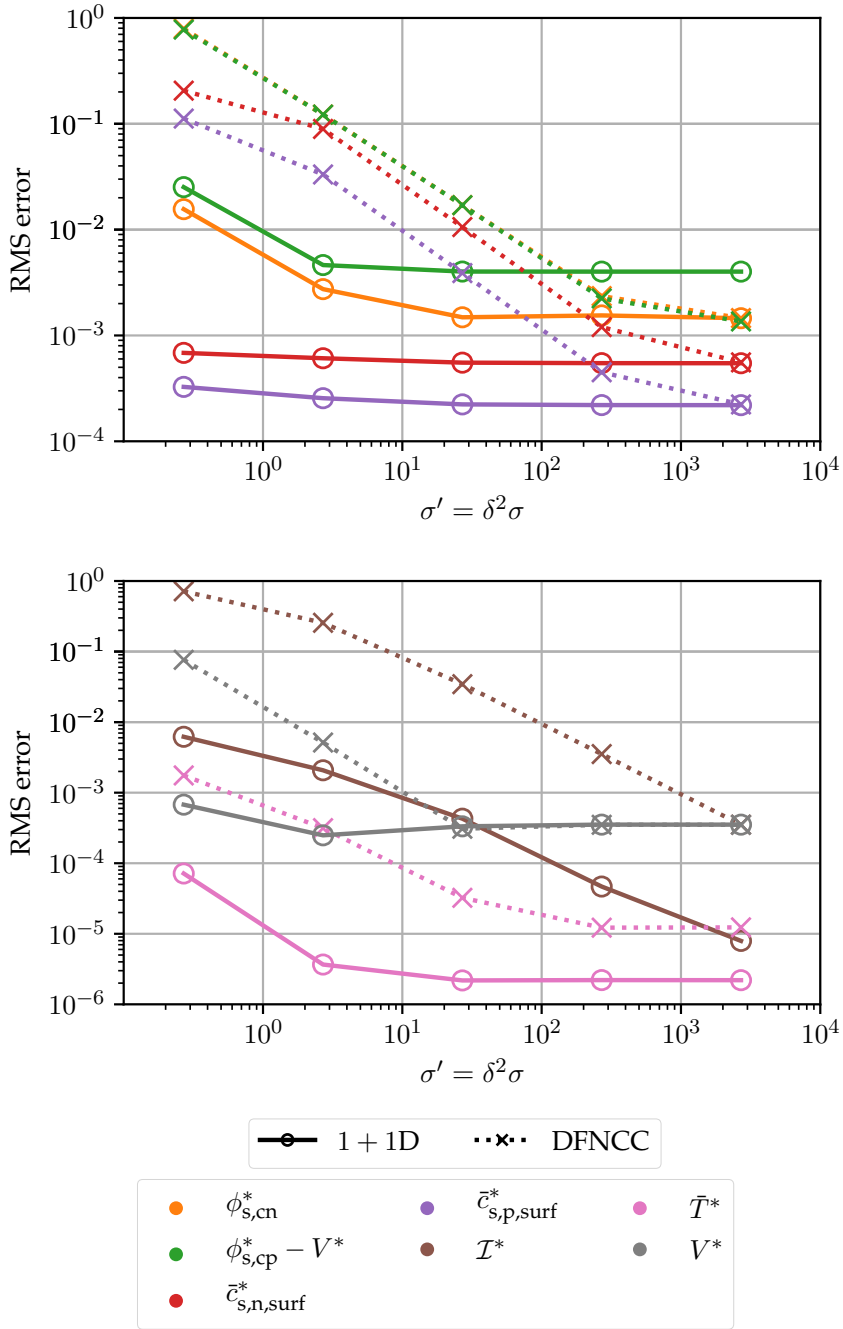
Figure 4.6: Normalised RMS error between the 2D solution in COMSOL and the 1+1D DFN and DFNCC solutions in PyBaMM for a selection of model variables as the non-dimensional conductivity σ is varied, with $\sigma_{cn} = \sigma_{cp} = \sigma$. The quantities plotted for a variable ψ were computed as $\mathrm{RMS}(\psi_{\mathrm{PyBaMM}} - \psi_{\mathrm{COMSOL}})/\mathrm{RMS}(\psi_{\mathrm{COMSOL}})$.

				1+1D				
N	$\phi_{\text{s,cn}}^*$	$\phi_{\text{s,cp}}^* - V^*$	$\bar{c}_{\text{s,n,surf}}^*$	$\bar{c}_{\text{s,p,surf}}^*$	$\mathcal{I}^*$	$\bar{T}^*$	V^*	Solution time [s]
4	2.148×10^{-2}	6.420×10^{-2}	1.646×10^{-2}	2.676×10^{-3}	3.954×10^{-4}	1.024×10^{-4}	2.341×10^{-3}	0.6115
8	5.377×10^{-3}	1.605×10^{-2}	5.767×10^{-3}	7.584×10^{-4}	1.015×10^{-4}	3.030×10^{-5}	6.864×10^{-4}	1.323
16	1.345×10^{-3}	4.011×10^{-3}	1.815×10^{-3}	2.082×10^{-4}	3.249×10^{-5}	7.772×10^{-6}	1.774×10^{-4}	9.446
32	3.421×10^{-4}	1.004×10^{-3}	5.231×10^{-4}	5.459×10^{-5}	2.665×10^{-5}	3.056×10^{-6}	4.412×10^{-5}	85.97
				DFNCC				
N	$\phi_{\text{s,cn}}^*$	$\phi_{\text{s,cp}}^* - V^*$	$\bar{c}_{\text{s,n,surf}}^*$	$\bar{c}_{\text{s,p,surf}}^*$	$\mathcal{I}^*$	$\bar{T}^*$	V^*	Solution time [s]
4	2.172×10^{-2}	2.172×10^{-2}	1.650×10^{-2}	2.703×10^{-3}	2.120×10^{-3}	1.202×10^{-4}	2.339×10^{-3}	0.24
8	5.725×10^{-3}	5.725×10^{-3}	5.895×10^{-3}	8.527×10^{-4}	2.294×10^{-3}	8.622×10^{-5}	6.801×10^{-4}	0.41
16	1.948×10^{-3}	1.948×10^{-3}	2.194×10^{-3}	4.437×10^{-4}	2.330×10^{-3}	8.612×10^{-5}	1.728×10^{-4}	0.99
32	1.262×10^{-3}	1.262×10^{-3}	1.241×10^{-3}	3.963×10^{-4}	2.334×10^{-3}	8.724×10^{-5}	4.931×10^{-5}	2.9

Table 4.4: Normalised RMS error between the 2D solution in COMSOL and the 1+1D DFN and DFNCC solutions in PyBaMM for a selection of model variables. The tabulated quantities for a variable ψ were computed as $\text{RMS}(\psi_{\text{PyBaMM}} - \psi_{\text{COMSOL}})/\text{RMS}(\psi_{\text{COMSOL}})$. Here N is the number of mesh cells per spatial dimension in PyBaMM. The 2D solution was evaluated on a "fine" mesh (450 elements in each current collector, 1650 elements in each electrode, 450 elements in the separator) in COMSOL. Both time stepping routines used a relative and absolute tolerance of 10^{-6}.

4.8 A SUITE OF REDUCED-ORDER MODELS

In this section, we combine the asymptotic analysis conducted in this chapter with the analysis conducted in Chapter 3 to develop a suite of reduced-order models of a lithium-ion pouch cell. These models are displayed pictorially in Figure 4.7. The 2+1D DFN, the most complex model we consider, is shown in the top-left panel. Proceeding downwards in Figure 4.7, represents making simplifications to the transverse model (i.e. the current collectors), which corresponds to the asymptotic analysis conducted earlier in this chapter. The first simplification (the middle row) gives rise to a set of models which we label 'CC'. These models consist of a single 'average' through-cell electrochemical model and a second decoupled two-dimensional problem for the current collector resistances (hence the name 'CC') which can be solved 'offline' before solving the through-cell model. On the bottom row of Figure 4.7, the effects of the current collectors are neglected entirely, with only a single representative through-cell electrochemical model being solved. We refer to these as 0D transverse models. Moving to the right in Figure 4.7 represents making simplifications to the through-cell electrochemical model, which corresponds to the asymptotic analysis we performed in Chapter 3. The three through-cell models that we consider are the DFN model, the SPMe, and the SPM. By combining a transverse model with a through-cell electrochemical model, we arrive at one of the nine models in Figure 4.7. For example, by choosing the 'CC' transverse model and the SPMe for the through-cell model, we arrive at the SPMeCC model, which consists of an 'average' SPMe model and decoupled current collector problem. Alternatively, by choosing a 0D transverse model and the SPM through-cell model, we arrive at the classical SPM model.

4.8.1 *Summary of dimensional transverse models*

To make clear the exact model equations associated with the schematics in Figure 4.7, we now state each of the transverse models in dimensional form. Each transverse model consists of a model for the potentials in the current collectors and a model for the cell temperature. These two models are then coupled to a through-cell model through current sources in the current collector model and/or heat sources in the temperature model.

2+1D DFN (P4D)   2+1D SPMe (P3D)   2+1D SPM (P3D)

DFNCC (P2D)   SPMeCC (P1D)   SPMCC (P1D)

DFN (P2D)   SPMe (P1D)   SPM (P1D)
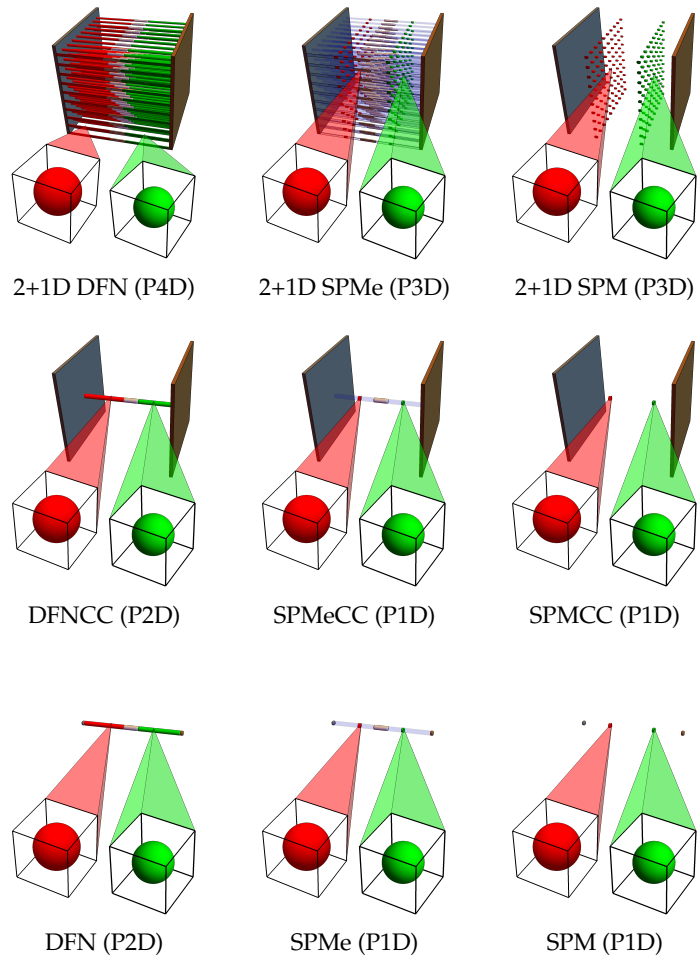
Figure 4.7: Schematic diagram of the reduced-order pouch cell models, and their complexity. DFN corresponds to a one-dimensional problem through the cell, at each point of which there is a radial problem for the concentration of Li in the active material. Thus such a model is pseudo-two-dimensional (P2D). In the 2+1D DFN at every point of the current collectors, a one-dimensional DFN model is solved, leading to a pseudo-four-dimensional (P4D) model. In DFNCC a single DFN model is solved, along with an uncoupled two-dimensional problem in the current collectors. SPM considers a single active particle in each electrode, leading to a one-dimensional model (P1D). In the SPMe an extra one-dimensional equation for the electrolyte is added; such a model remains P1D.

4.8.1.1   *N+1D model*

For the N+1D transverse model, we use (4.37) which we derived earlier in this chapter. The dimensional from of this potential-pair problem is

$$L^*_{\text{cn}}\sigma^*_{\text{cn}}(\nabla^*_\perp)^2\phi^*_{\text{s,cn}} = \mathcal{I}^*, \quad \text{in } \Omega^* \tag{4.56a}$$

$$L^*_{\text{cp}}\sigma^*_{\text{cp}}(\nabla^*_\perp)^2\phi^*_{\text{s,cp}} = -\mathcal{I}^*, \quad \text{in } \Omega^* \tag{4.56b}$$

$$\phi^*_{\text{s,cn}} = 0 \quad \text{on } \partial\Omega^*_{\text{tab,cn},\perp}, \tag{4.56c}$$

$$\nabla^*_\perp\phi^*_{\text{s,cn}} \cdot \boldsymbol{n} = 0 \quad \text{on } \partial\Omega^*_{\text{ext,cn},\perp} \tag{4.56d}$$

$$-\sigma^*_{\text{cp}}\nabla^*_\perp\phi^*_{\text{s,cp}} \cdot \boldsymbol{n} = \frac{I^*_{\text{app}}}{A^*_{\text{tab,cp}}} \quad \text{on } \partial\Omega^*_{\text{tab,cp},\perp}, \tag{4.56e}$$

$$\nabla^*_\perp\phi^*_{\text{s,cp}} \cdot \boldsymbol{n} = 0 \quad \text{on } \partial\Omega^*_{\text{ext,cp},\perp}, \tag{4.56f}$$

with the thermal model given by

$$\rho^*_{\text{eff}}\frac{\partial T^*}{\partial t^*} = \lambda^*_{\text{eff}}(\nabla^*_\perp)^2 T^* + \bar{Q}^* - \frac{(h^*_{\text{cn}} + h^*_{\text{cp}})}{L^*}(T^* - T^*_\infty), \tag{4.56g}$$
$$\text{in } \Omega^*$$

$$-\lambda^*_{\text{eff}}\nabla^*_\perp T^* \cdot \boldsymbol{n} = h^*_{\text{eff}}(T^* - T^*_\infty) \quad \text{on } \partial\Omega^* \tag{4.56h}$$

$$T^*\big|_{t^*=0} = T^*_0. \tag{4.56i}$$

Here, the heat source is given by

$$\bar{Q}^* = \bar{\mathcal{Q}}^* + \frac{L^*_{\text{cn}}}{L^*}\sigma^*_{\text{cn}}|\nabla^*_\perp\phi^*_{\text{s,cn}}|^2 + \frac{L^*_{\text{cp}}}{L^*}\sigma^*_{\text{cp}}|\nabla^*_\perp\phi^*_{\text{s,cp}}|^2, \tag{4.56j}$$

where $\bar{\mathcal{Q}}^*$ is the x^*-averaged heat source from the through-cell electrochemical model. In the above, h^*_{eff} is the dimensional effective edge heat transfer coefficient, and h^*_{cn} and h^*_{cp} are the heat transfer coefficients on the faces of the negative and positive current collectors, respectively. The dimensional effective edge heat transfer coefficient is

$$h^*_{\text{eff}} = \frac{1}{L^*}\int_{-L^*_{\text{cn}}}^{L^*_x + L^*_{\text{cp}}} h^*_{\text{edge}} \, \mathrm{d}x^*,$$

and the dimensional effective volumetric heat capacity and dimensional thermal conductivity are

$$\rho^*_{\text{eff}} = \frac{\sum\limits_k \rho^*_k c^*_{\text{p,k}} L^*_k}{\sum\limits_k L^*_k}, \qquad \lambda^*_{\text{eff}} = \frac{\sum\limits_k \lambda^*_k L^*_k}{\sum\limits_k L^*_k}, \tag{4.56k}$$

respectively.

4.8.1.2 *CC model*

For the 'CC' model, we employ (4.53a), (4.53c)(4.53d), and (4.54). Whilst we derived (4.53) asymptotically, we henceforth use the ad-hoc extension to the thermal model (4.54) because we have found that in practice it a offers significant improvement to accuracy. The dimensional 'CC' model that we use for the rest of this chapter is then

$$V^* = \mathcal{V}^* \left(\mathcal{I}^*, \langle T^* \rangle \right) - R_{\mathrm{cp}}^* I_{\mathrm{app}}^* - R_{\mathrm{cn}}^* I_{\mathrm{app}}^*, \tag{4.57a}$$

$$\rho_{\mathrm{eff}}^* \frac{\partial T^*}{\partial t^*} = \lambda_{\mathrm{eff}}^* (\nabla_\perp^*)^2 T^* + \bar{\mathcal{Q}}^* (\mathcal{I}^*, \langle T \rangle^*)$$
$$- \frac{(h_{\mathrm{cn}}^* + h_{\mathrm{cp}}^*)}{L^*} (T^* - T_\infty^*)$$
$$+ \frac{L_{\mathrm{cn}}^*}{L^*} \sigma_{\mathrm{cn}}^* |\nabla_\perp^* \phi_{\mathrm{s,cn}}^*|^2$$
$$+ \frac{L_{\mathrm{cp}}^*}{L^*} \sigma_{\mathrm{cp}}^* |\nabla_\perp^* \phi_{\mathrm{s,cp}}^*|^2, \quad \text{in } \Omega^* \tag{4.57b}$$

$$- \lambda_{\mathrm{eff}}^* \nabla_\perp^* T^* \cdot \boldsymbol{n} = h_{\mathrm{eff}}^* (T^* - T_\infty^*) \quad \text{on } \partial \Omega^* \tag{4.57c}$$

$$T^* \big|_{t^*=0} = T_0^*. \tag{4.57d}$$

where $\mathcal{V}^*$ is the through-cell voltage and $\bar{\mathcal{Q}}^*$ is the x^*-averaged heat source from the through-cell electrochemical model. In this case, we solve for a single average through-cell model with input current density $\mathcal{I}^* = I_{\mathrm{app}}^* / (L_y^* L_z^*)$. The current collector resistances are given by

$$R_{\mathrm{cn}}^* = \frac{\langle f_{\mathrm{n}}^* \rangle}{L_y^* L_z^* L_{\mathrm{cn}}^* \sigma_{\mathrm{cn}}^*}, \tag{4.57e}$$

$$R_{\mathrm{cp}}^* = \frac{1}{L_y^* L_z^* \sigma_{\mathrm{cp}}^* A_{\mathrm{tab,cp}}^*} \int_{\partial \Omega_{\mathrm{tab,cp},\perp}^*} f_{\mathrm{p}}^* \, \mathrm{d}s^* \tag{4.57f}$$

and the coefficients related to Ohmic heating in the current collectors are

$$H_{\mathrm{cn}}^* = \frac{L_{\mathrm{cn}}^* \langle |\nabla_\perp^* f_{\mathrm{n}}^*|^2 \rangle}{L^* (L_y^* L_z^* L_{\mathrm{cn}}^*)^2 \sigma_{\mathrm{cn}}^*}, \qquad H_{\mathrm{cp}}^* = \frac{L_{\mathrm{cp}}^* \langle |\nabla_\perp^* f_{\mathrm{p}}^*|^2 \rangle}{L^* (L_y^* L_z^* L_{\mathrm{cp}}^*)^2 \sigma_{\mathrm{cp}}^*}, \tag{4.57g}$$

where f_{n}^* and f_{p}^* satisfy the dimensional version of (4.49) which is

$$(\nabla_\perp^*)^2 f_{\mathrm{n}}^* = -1, \quad (\nabla_\perp^*)^2 f_{\mathrm{p}}^* = 1 \quad \text{in } \Omega^*, \tag{4.57h}$$

$$f_{\mathrm{n}}^* = 0 \quad \text{on } \partial \Omega_{\mathrm{tab,cn},\perp}^*, \tag{4.57i}$$

$$\nabla_\perp^* f_{\mathrm{n}}^* \cdot \boldsymbol{n} = 0 \quad \text{on } \partial \Omega_{\mathrm{ext,cn},\perp}^*, \tag{4.57j}$$

$$\nabla_\perp^* f_{\mathrm{p}}^* \cdot \boldsymbol{n} = \frac{L_y^* L_z^* L_{\mathrm{cp}}^*}{A_{\mathrm{tab,cp}}^*} \quad \text{on } \partial \Omega_{\mathrm{tab,cp},\perp}^*, \tag{4.57k}$$

$$\nabla_\perp^* f_{\mathrm{p}}^* \cdot \boldsymbol{n} = 0 \quad \text{on } \partial \Omega_{\mathrm{ext,cp},\perp}^*, \tag{4.57l}$$

$$\langle f_{\mathrm{p}}^* \rangle = 0. \tag{4.57m}$$

The potential distribution in the current collectors is then determined from f_n^* and f_p^* via

$$\phi_{s,cn}^* = -\frac{I_{app}^* f_n^*}{L_y^* L_z^* L_{cn}^* \sigma_{cn}^*}, \qquad \phi_{s,cp}^* = V^* + \frac{I_{app}^* f_p^*}{L_y^* L_z^* L_{cp}^* \sigma_{cp}^*}. \qquad (4.57n)$$

4.8.1.3   *0D model*

In the CC model, the conductivity of the current collectors is high enough that the potential is approximately uniform across them, and the resistances due to the current collectors are calculated as a perturbation. When this perturbation can be ignored, we then have from (4.40) that

$$\phi_{s,cn}^* = 0, \quad \phi_{s,cp}^* = V^*, \qquad (4.58)$$

and we arrive at a model in which the effects of the current collectors are ignored entirely. In this model the cell behaviour is uniform in (y^*, z^*), and the temperature, which is now a function of time only, is governed by the ODE (4.43) which in dimensional form is

$$\rho_{eff}^* \frac{\partial T^*}{\partial t^*} = \bar{\mathcal{Q}}^* \left(\mathcal{I}^*, T^*\right) - \frac{(h_{cn}^* + h_{cp}^*)}{L^*}(T^* - T_\infty^*)$$
$$- \frac{(T^* - T_\infty^*)}{L_y^* L_z^*} \int_{\partial \Omega^*} h_{eff}^* \, ds^* \text{ in } \Omega^*, \qquad (4.59)$$

$$T^*\big|_{t^*=0} = T_0^*. \qquad (4.60)$$

4.8.2   *Summary of dimensional through-cell models*

The dimensional through-cell models that we employ are the DFN ((2.33), (2.35), (2.36), (2.41), and (2.42)), SPMe (3.47), and SPM (3.21). Although, we only considered the isothermal case in Chapter 3, these model equations trivially extend to the thermal case by adding the temperature dependence to the parameters discussed in §4.4. It therefore only remains to state the heat source term, which for each through-cell model is given by

$$\mathcal{Q}_k^* = Q_{Ohm,k}^* + Q_{rxn,k}^* + Q_{rev,k}^*, \qquad (4.61)$$

and accounts for Ohmic heating $Q_{Ohm,k}^*$ due to resistance in the solid and electrolyte, irreverisble heating due to electrochemical reactions

$Q^*_{\text{rxn,k}}$, and reversible heating due to entropic changes in the the electrode $Q^*_{\text{rev,k}}$ [9]. In the electrodes these terms are computed as

$$Q^*_{\text{Ohm,k}} = -\left(i^*_{\text{s,k}}\frac{\partial \phi^*_{\text{s,k}}}{\partial x^*} + i^*_{\text{e,k}}\frac{\partial \phi^*_{\text{e,k}}}{\partial x^*}\right), \qquad \text{k} \in \{\text{n, p}\}, \qquad (4.62)$$

$$Q^*_{\text{rxn,k}} = a^*_{\text{k}}j^*_{\text{k}}\eta^*_{\text{k}}, \qquad \text{k} \in \{\text{n, p}\}, \qquad (4.63)$$

$$Q^*_{\text{rev,k}} = a^*_{\text{k}}j^*_{\text{k}}T^*\frac{\partial U^*_{\text{k}}}{\partial T^*}\bigg|_{T^*=T^*_\infty}, \qquad \text{k} \in \{\text{n, p}\}. \qquad (4.64)$$

However, in the separator there is no heat generation due to electrochemical effects, and we need only consider the Ohmic heat generation term given by

$$Q^*_{\text{Ohm,s}} = -\boldsymbol{i}^*_{\text{e,s}} \cdot \frac{\partial \phi^*_{\text{e,s}}}{\partial x^*}. \qquad (4.65)$$

The x^*-averaged through-cell heat generation is given by

$$\bar{\mathcal{Q}}^* = \frac{1}{L^*}\sum_k L^*_{\text{k}}\bar{\mathcal{Q}}^*_{\text{k}}. \qquad (4.66)$$

In the SPM, the potentials are all independent of space and so the only non-zero contributions to the heating come from the electrochemical reactions $Q^*_{\text{rxn,k}}$ and $Q^*_{\text{rev,k}}$. The Ohmic heating terms appear at higher order, and are included in the SPMe.

4.9 CRITICAL COMPARISON OF ISOTHERMAL MODELS

In this section, we provide a numerical comparison of the models depicted in Figure 4.7. For ease of exposition, we consider the case in which all variables are uniform in y^*, so that each model has one-dimensional current collectors (in z^*). In total we consider 9 models: 1+1D DFN, 1+1D SPM, 1+1D SPMe, DFNCC, SPMeCC, SPMCC, DFN, SPMe and SPM. Each model is implemented within PyBaMM [86]. The model equations are discretised in space using the finite-volume method and integrated in time using an adaptive, variable-order backward differentiation formula. For the spatial discretisation we use the following number of grid points: $N_z = 30$ in the z^*-direction of the current collectors; $N_{r_\text{n}} = 20$ and $N_{r_\text{p}} = 20$ in r^*-direction of the negative and positive particles, respectively; and $N_{x_\text{n}} = 35$, $N_{x_\text{s}} = 20$, and $N_{x_\text{p}} = 35$ in the x-direction negative electrode, separator and positive electrode, respectively. Unless otherwise stated, results are presented for a 1C constant current discharge. To demonstrate the relative computational complexity of each model we present the number of states in each model alongside the solve time in Table 4.5. Here we refer to the number of states required by the part of the model that is integrated in time. That is, we ignore the states in the "CC" part of the problem

which is solved "offline" and is separate from the time integration. We observe a dramatic decrease in both memory requirements and solve times as the complexity of the model is decreased. For example, the SPMeCC requires around 0.2% of the memory required by the 1+1D DFN and is over 400 times faster to solve than the 1+1D DFN.

Model	States	Solve time [ms]
1+1D DFN	49561	8308
1+1D SPMe	3961	1514
1+1D SPM	1261	105
DFN(CC)	1651	259
SPMe(CC)	131	18
SPM(CC)	41	13

Table 4.5: The number of states required for the time integration component of the isothermal version of each model and associated time integration solve time (i.e. excluding any initial time independent solves) for a 1 C constant current disharge with $N_z = 30$, $N_{x_\mathrm{n}} = 35$, $N_{x_\mathrm{s}} = 20$, $N_{x_\mathrm{p}} = 35$, $N_{r_\mathrm{n}} = 20$, and $N_{r_\mathrm{p}} = 20$. Since we have ignored the time independent part of the problem, the results for the "CC" and 1D (no current collector effects) models are the same.

Despite the clear computational benefits of employing a reduced-order model, modelling errors are introduced and must be understood. To help quantify the spatial and temporal errors, we use two measures. The first is the maximum absolute error at each point in z^* defined for a variable Φ^* to be

$$\epsilon_z^* = \max_{t^*} |\Phi_{\text{1+1D DFN}}^* - \Phi_{\text{Reduced}}^*|, \tag{4.67}$$

where $\Phi_{\text{1+1D DFN}}^*$ is the value of variable predicted by the 1+1D DFN model and Φ_{Reduced}^* is the value of the variable predicted by relevant the reduced-order model. The other measure of the error that we use is the maximum absolute error at each point in time in the discharge defined for each variable Φ^* as

$$\epsilon_t^* = \max_{z^*} |\Phi_{\text{1+1D DFN}}^* - \Phi_{\text{Reduced}}^*|. \tag{4.68}$$

Both ϵ_z^* and ϵ_t^* inherit the units of the variable, Φ^*, under study.

The results and conclusions presented below are specific to the parameter values in Tables 2.1, 2.2, and 4.1. One should keep in mind that the most appropriate model is a function of the particular parameter values being used.

4.9.1 *Comparison of terminal voltage*

The most commonly used output of lithium-ion battery models is the terminal voltage. In Figure 4.8 (a), and (b), we present the 1 C terminal voltage predicted by each model and the associated errors between the reduced-order model and the 1+1D DFN. Except for the SPM, the reduced-order models recover the behaviour predicted by the 1+1D DFN at 1 C. However, in Figure 4.8 (b), we observe between a one and two orders of magnitude decrease in the error when using the DFN as the through-cell model, irrespective of the choice of transverse model. This suggests that simplifications in the through-cell electrochemistry result in a greater increase in error than simplifications in the transverse direction. In Figure 4.8 (c), the maximum absolute error in the terminal voltage across the discharge is presented as a function of the C-rate.
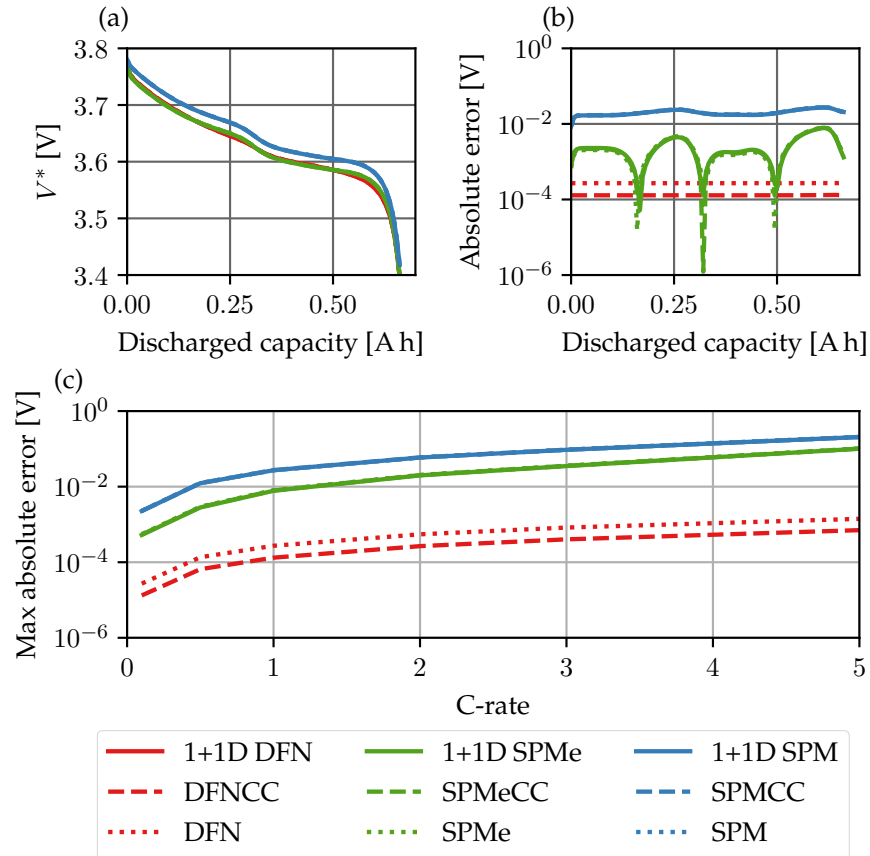
Figure 4.8: Comparison of the predicted terminal voltage: (a) 1 C discharge voltage profile predicted by each model; (b) 1 C discharge voltage profile absolute error between each reduced-order model and the 1+1D DFN; and (c) the maximum absolute error between each reduced-order model and the 1+1D DFN at a range of C-rates. The results for the 1+1D SPMe, SPMeCC, and SPMe are almost indistinguishable and the results for the 1+1D SPM, SPMCC, and SPM are indistinguishable.

As expected, the error increases with increasing C-rate for all of the models considered. Additionally, the error in the models which use the SPM and SPMe increases more quickly with C-rate when compared with the models that use the DFN. This suggests that at higher C-rates retaining a more complex through-cell model becomes increasingly important.

If the terminal voltage is the only quantity of interest then our results suggest that employing a reduced-order model that does not couple the current collector and electrochemical effects is the most appropriate model choice, in the sense the voltage can be accurately predicted at a greatly reduced computational cost. In particular, if one has a larger computational budget and has access to efficient differential-algebraic equation (DAE) solvers then making use of the DFN or DFNCC gives the best prediction of the voltage. However, if the computational budget is more limited the SPMe or SPMeCC may be more appropriate. Finally, we note that the errors between experimental data and more complex through-cell models can be on the order of 10^{-1} V [22], so in practice introducing a modelling error on the order of 10^{-2} V, such as in the SPMeCC, may not affect the ability of the model to replicate experimental results.

4.9.2 *Comparison of particle concentrations*

In Figure 4.9(a), we display the variation in z^* of the surface concentration of the through-cell averaged (x^*-averaged) negative particle predicted by the 1+1D DFN throughout the full discharge. Initially, the surface concentration is uniform in z^*. However, as the discharge proceeds, the upper portion of the cell near the tabs becomes more depleted than the lower portion of the cell. This is due to current preferentially travelling through the upper portion of the cell as the path of least resistance. When the upper portion of the cell is almost fully depleted, the resistances in the upper portion of the cell increase (i.e. it becomes harder to remove more lithium from the negative electrode and harder to insert lithium into the positive electrode) to a sufficient level such that current preferentially travels through the less utilised portions of the cell. This gives rise to a final uniform particle surface concentration. The effect of this on the current can be observed in Figure 4.10(a).

In Figure 4.9(b), we plot the x^*-averaged negative particle surface concentration at 0.17 A h predicted by the 1+1D DFN, the 1+1D SPM, the 1+1D SPM, and the average concentration which is predicted by the models that do not include the z^*-dependence of the concentrations (i.e. the "CC" and 1D models). Given that the variation in surface concentration is on the order of $15 \, \text{mol m}^{-3}$, employing a z^*-averaged model recovers the surface concentrations to 0.1% accuracy. However, as shown in Figures 4.9(c) and (d), an order of magnitude decrease
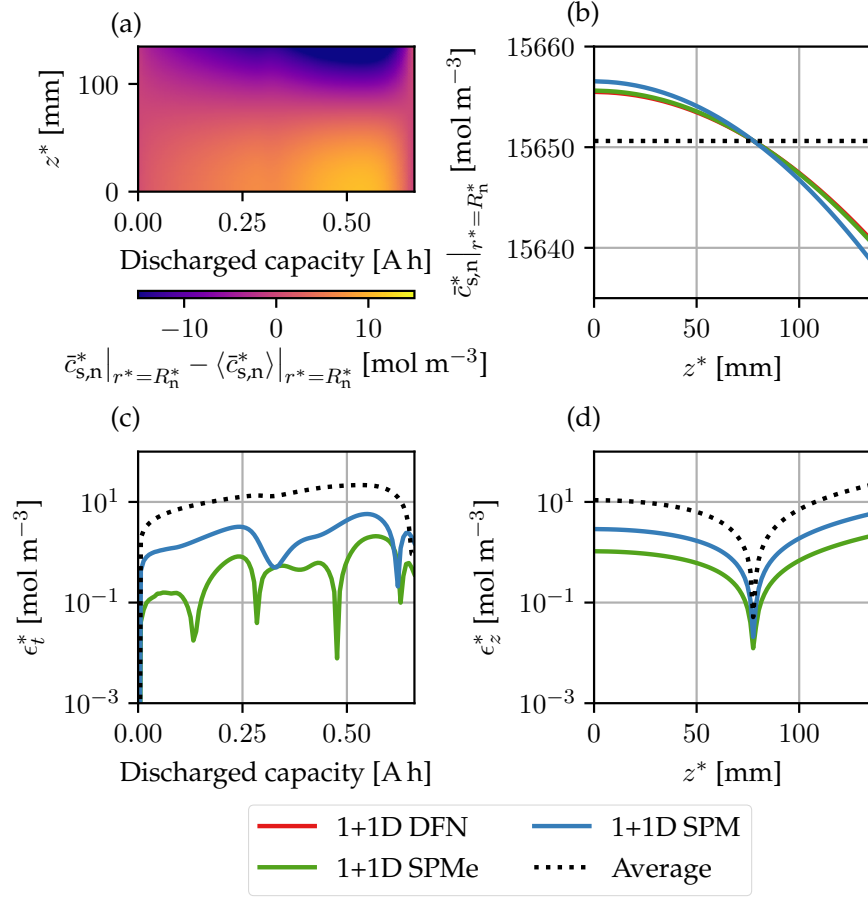
Figure 4.9: Comparison of the x^*-averaged negative particle surface concentra-tion: (a) Variation in the x^*-averaged negative particle surface con-centration predicted by the 1+1D DFN; (b) Snapshot at 0.17 [A h]; (c) Maximum (over z^*) absolute error at each time in the discharge; (d) Maximum (over the entire discharge) absolute error at each z^* location.

in the error can be achieved when using a z^*-resolved model such as the 1+1D SPM or 1+1D SPMe. For situations in which resolving the spatial inhomogeneities (in z^*) in the surface concentration are crucial, a model at least as detailed as the 1+1D SPM should be employed.

A further comparison of the surface concentration variables is pro-vided in Table 4.6. Instead of comparing the x^*-averaged surface con-centration, we now compare the surface concentration at every (x^*,z^*)-location in the cell. Here, we observe that the RMS error in the particle surface concentration is larger for the 1+1D SPM(e) than the 1D DFN and DFNCC. This is because 1+1D SPMe considers a single x^*-averaged particle in the through-cell direction, and in this instance, the through-cell variation in the particle surface concentration is more significant than the z^*-direction variation. This highlights the fact that the best combination of through-cell and transverse simplifications depends on which quantities are of interest: for the results here we find that

the 1+1D SPMe best recovers the through-cell averaged particle surface concentration, but the 1D DFN better approximates the surface concentration at each (x^*, z^*) location.

4.9.3 *Comparison of current distribution*

In Figure 4.10(a), we present the through-cell current density predicted by the 1+1D DFN as a function of z^* and discharge capacity. As discussed in our description of the particle surface concentration variation, we observe that the current preferentially travels through the top of the cell except at particular times where particle concentrations are such that the through-cell resistance makes it preferential for the current to flow more uniformly through the cell (at 0.35 A h) and through the bottom of the cell (at the end of discharge). In Figure 4.10(b), shows the through-cell current density as a function of z at 0.17 A h through
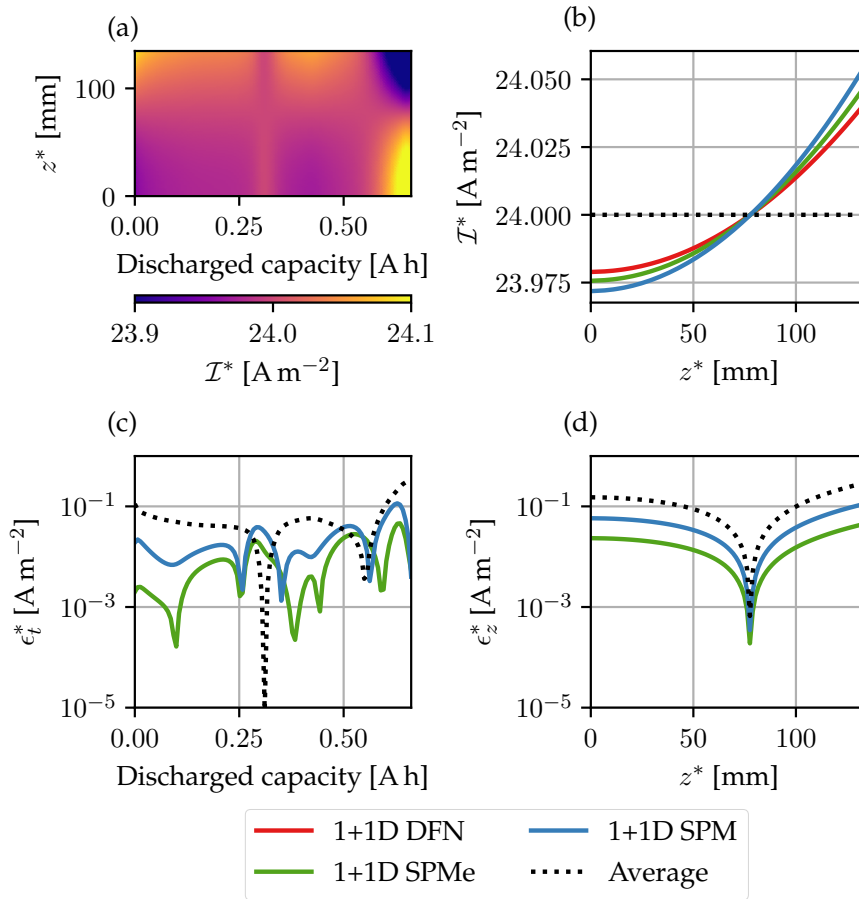
Figure 4.10: Comparison of the through-cell current: (a) Through-cell current predicted by the 1+1D DFN; (b) Snapshot at 0.17 [A h]; (c) Maximum (over z^*) absolute error at each time in the discharge; (d) Maximum (over the entire discharge) absolute error at each z^* location.

the discharge. We observe that the average current (as predicted by the "CC" and 1D models) provides a good first approximation of the through-cell current density which is reasonably uniform (only varying by about $0.04\,\mathrm{A\,m^{-2}}$). However, the 1+1D SPM and 1+1D SPMe both provide an improved estimate of the spatial variation in the through-cell current density, and can give an order of magnitude decrease in the error, as demonstrated in Figures 4.10(c) and (d). In applications where accurately resolving the current distribution is a key objective and the computational budget is limited, the 1+1D SPMe is the best choice in terms of offering good accuracy at low computational costs.

4.9.4   *Comparison of negative potentials*

In Figure 4.11(a), we present the potential in the negative electrode at the point $0.17\,\mathrm{A\,h}$ in the discharge (we display this instead of the current collector potential through time because the current collector potential is approximately constant throughout a $1\,\mathrm{C}$ discharge). In the upper left corner of the electrode, next to the tab, the potential takes values close to the reference value of zero. However, as we move through the cell in the x-direction or down the current collector in the z-direction we observe a drop in the potential. In particular, a greater potential drop is observed in the current collector direction and so current collector Ohmic losses are of greater importance than through-cell electrode Ohmic losses. In Figures 4.11(b), (c), and (d), we compare the negative current collector potential at $0.17\,\mathrm{A\,h}$ as predicted by the 1+1D and "CC" models. Note that the 1D models predict that the potential will simply take on the reference value of 0 everywhere in the current collector. We observe excellent agreement between all models.

4.9.5   *Summary of isothermal comparison*

In this section, we have provided a critical comparison of some of the key outputs predicted by the 1+1D DFN model and the reduced-order models introduced in this paper. In the interest of brevity, we have only presented detailed results for a limited set of variables, but results for other key variables are provided in Table 4.6 for reference.

The key result is that in the isothermal case, choosing a reduced-order model that simplifies the z-direction behaviour (e.g. the DFNCC) instead of the x-direction behaviour (e.g. 1+1D SPMe) provides a better allocation of computational resources. Only in situations where the z-direction variation in variables such as the surface concentrations and through-cell current are essential should simplifications to the through-cell model be made in favour of simplifications to the transverse model. In such situations, the 1+1D SPMe typically provides a good balance of accuracy and computational cost.
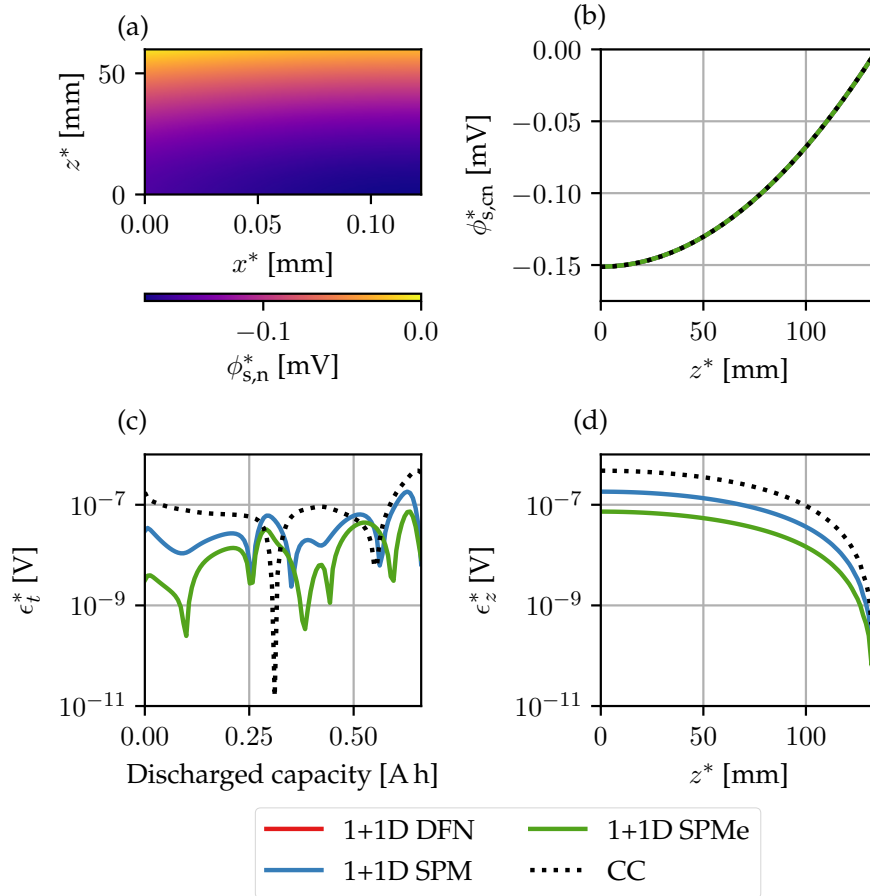
Figure 4.11: Comparison of negative potentials: (a) Snapshot at 0.17 [A.h] of the negative electrode potential predicted by the 1+1D DFN; (b) Snapshot of the negative current collector potential at 0.17[A.h]; (c) Maximum (over z^*) absolute error in the negative current collector potential at each time in the discharge; (d) Maximum (over the entire discharge) absolute error in the negative current collector potential at each z^* location. The results of the DFNCC, SPMeCC, and SPMCC are all represented by CC.

Variable	Units	Typical values	1+1D SPMe	1+1D SPM	DFNCC	SPMeCC	SPMCC	DFN	SPMe	SPM
V^*	V	$3.4 - 3.8$	3.25×10^{-3}	2.04×10^{-2}	1.29×10^{-4}	3.29×10^{-3}	2.05×10^{-2}	2.70×10^{-4}	3.33×10^{-3}	2.06×10^{-2}
$\phi^*_{s,cn}$	V	$-1.5 \times 10^{-4} - 0$	1.44×10^{-8}	3.30×10^{-8}	6.75×10^{-8}	6.75×10^{-8}	6.75×10^{-8}	1.11×10^{-4}	1.11×10^{-4}	1.11×10^{-4}
$\phi^*_{s,n}$	V	$-1.7 \times 10^{-4} - 0$	2.03×10^{-6}	1.53×10^{-5}	7.79×10^{-8}	2.00×10^{-6}	1.53×10^{-5}	1.11×10^{-4}	1.11×10^{-4}	1.24×10^{-4}
$\phi^*_{e,k}$	V	$-0.26 - -0.17$	2.03×10^{-3}	1.20×10^{-2}	3.81×10^{-5}	2.03×10^{-3}	1.20×10^{-2}	1.04×10^{-4}	2.07×10^{-3}	1.20×10^{-2}
$\phi^*_{s,p}$	V	$3.4 - 3.8$	3.25×10^{-3}	2.02×10^{-2}	1.14×10^{-4}	3.25×10^{-3}	2.02×10^{-2}	1.22×10^{-4}	3.28×10^{-3}	2.03×10^{-2}
$\phi^*_{s,cp}$	V	$3.4 - 3.8$	3.25×10^{-3}	2.04×10^{-2}	7.55×10^{-5}	3.27×10^{-3}	2.04×10^{-2}	1.22×10^{-4}	3.28×10^{-3}	2.05×10^{-2}
$\mathcal{I}^*$	$\mathrm{A\,m^{-2}}$	$23.7 - 24.1$	6.11×10^{-3}	1.40×10^{-2}	2.87×10^{-2}	2.87×10^{-2}	2.87×10^{-2}	2.87×10^{-2}	2.87×10^{-2}	2.87×10^{-2}
$c^*_{s,n}\big|_{r^*=R^*_n}$	$\mathrm{mol\,m^{-3}}$	$4804 - 19404$	9.28×10^2	9.28×10^2	6.77	9.28×10^2	9.28×10^2	6.77	9.28×10^2	9.28×10^2
$c^*_{s,p}\big|_{r^*=R^*_p}$	$\mathrm{mol\,m^{-3}}$	$31506 - 48316$	4.14×10^2	4.14×10^2	7.33	4.14×10^2	4.14×10^2	7.33	4.14×10^2	4.14×10^2
$c^*_{e,k}$	$\mathrm{mol\,m^{-3}}$	$800 - 1200$	1.08×10^1	1.14×10^2	1.41×10^{-1}	1.08×10^1	1.14×10^2	1.41×10^{-1}	1.08×10^1	1.14×10^2
$i^*_{e,k}$	$\mathrm{A\,m^{-2}}$	$0.9 - 24$	1.65	1.65	2.11×10^{-2}	1.65	1.65	2.11×10^{-2}	1.65	1.65
j^*_k	$\mathrm{A\,m^{-2}}$	$-2.3 - 2.6$	3.06×10^{-1}	3.06×10^{-1}	2.54×10^{-3}	3.06×10^{-1}	3.06×10^{-1}	2.54×10^{-3}	3.06×10^{-1}	3.06×10^{-1}
η^*_n	V	$0.0014 - 0.008$	1.30×10^{-3}	1.34×10^{-3}	1.01×10^{-5}	1.30×10^{-3}	1.34×10^{-3}	1.01×10^{-5}	1.30×10^{-3}	1.34×10^{-3}
η^*_p	V	$-0.12 - -0.06$	4.20×10^{-3}	4.80×10^{-3}	7.14×10^{-5}	4.20×10^{-3}	4.80×10^{-3}	7.14×10^{-5}	4.20×10^{-3}	4.80×10^{-3}

Table 4.6: RMS errors of key model variables in each of the reduced-order models vs. the 1+1D DFN for a 1 C constant-current discharge.

4.10   CRITICAL COMPARISON OF THERMAL MODELS

We now compare the thermal versions of the models under the conditions of a $3\,\mathrm{C}$ discharge and tab cooling. Tab cooling is simulated by applying

$$\lambda_{\mathrm{eff}}^* \nabla^* T^* \cdot \boldsymbol{n} = -h_{\mathrm{tab}}^* (T^* - T_\infty^*) \tag{4.69}$$

on the tabs and

$$\lambda_{\mathrm{eff}}^* \nabla^* T^* \cdot \boldsymbol{n} = 0 \tag{4.70}$$

on all other boundaries. For this comparison, both tabs are placed at the top of the cell and the value of h_{tab}^* is set to $1000\,\mathrm{W\,m^{-2}\,K^{-1}}$ so that a temperature variation on the order of a few degrees Kelvin is observed across the cell; this is in accordance with experimental results [32]. This approach was taken as a simple way to induce a variation in the temperature in the z^*-direction that is similar to the variation seen in experiments. However, a proper treatment of tab cooling would involve a more complete model of the tabs which are a major heat transfer bottleneck [32].

In Figure 4.12, we display the volume-averaged temperature predicted by each model. By referring to the performance of the 0D transverse model, we observe that it is important to account for transverse effects in order to accurately predict the temperature during tab cooling. This is because using the average temperature in (4.69) leads to a higher rate of cooling. In Figure 4.12, we also observe that models
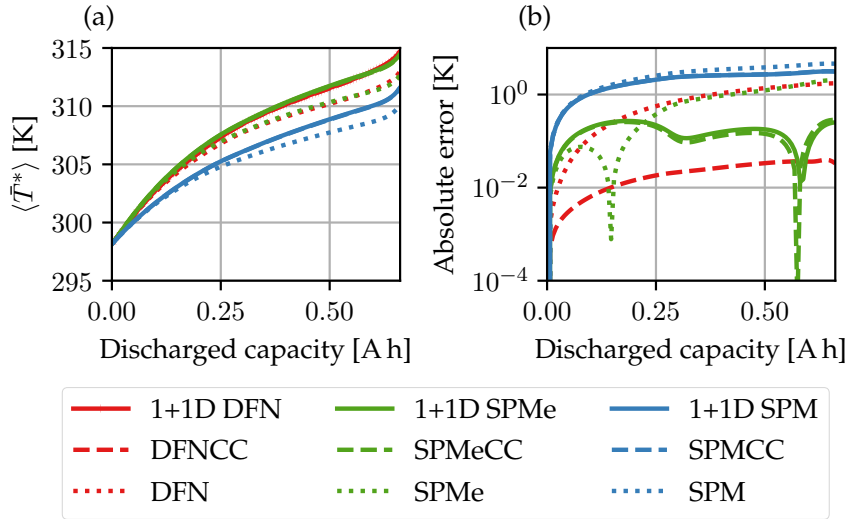
Figure 4.12: Comparison of the volume-averaged cell temperature: (a) predicted volume-averaged cell temperature; (b) absolute error between reduced model and 1+1D DFN.

with an SPM through-cell model perform poorly. This is because they neglect the Ohmic heating in the electrolyte.

The DFN, SPMe, and SPM employ a lumped thermal model with cooling proportional to the difference between the average temperature and the ambient temperature. Since the actual temperature at the tab is lower than the average temperature, these models overpredict the cooling rate, giving a lower volume-averaged cell temperature, as observed in Figure 4.12.

In Figure 4.13, we present the temperature as a function of space and time throughout the discharge. Again we observe that the DFNCC best predicts the temperature profile of the 1+1D DFN, and the greatest error is introduced by using the SPM. Note that the error for the 1+1D and "CC" models is similar, which suggest using a simpler transverse model (that still retains some z^*-dependence).
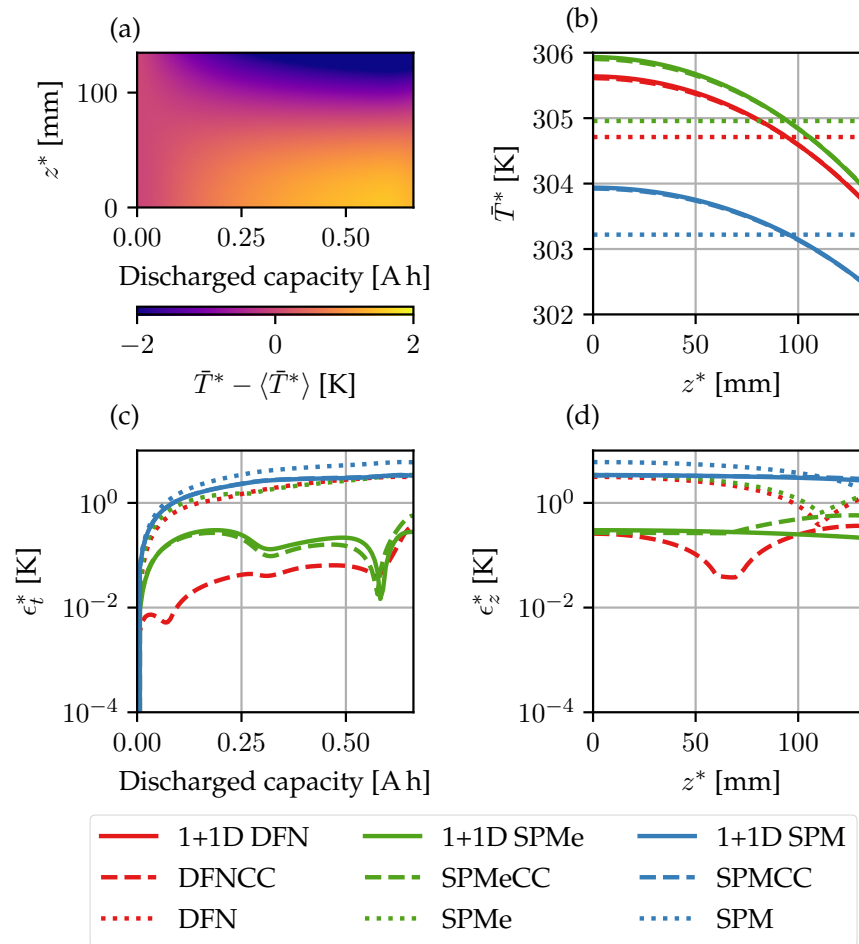
Figure 4.13: Comparison of temperature profiles: (a) x-averaged cell temperature variation through time predicted by the 1+1D DFN; (b) x-averaged cell temperature at 0.17 [A h]; (c) Maximum (over z^*) absolute error at each time in the discharge; (d) Maximum (over the entire discharge) absolute error at each z^* location.

In Figure 4.14, we break the volume-averaged heating into its components to help diagnose where errors in the various reduced models arise. We observe that across all forms of heating, the DFNCC is almost indistinguishable from the results of the 1+1D DFN. Whilst one might initially think that the DFN should produce the same irreversible and reversible reaction heating as the DFNCC, this is not the case because the temperature predicted by the DFN is lower, as mentioned in the discussion of Figure 4.12. The temperature dependence of the electrochemical reactions then means that the 1D DFN overpredicts the reaction heating. The SPMeCC and 1+1D SPMe both capture the general behaviour of the Ohmic and irreversible reaction heating, however, they fail to capture the fluctuations in this general behaviour, particularly in the Ohmic heating. This is a result of failing to capture the though-cell variations in the reaction overpotentials, as well as the variations in the electrolyte potentials. Despite this, both the SPMeCC and 1+1D SPMe perform reasonably well at recovering the total heating.
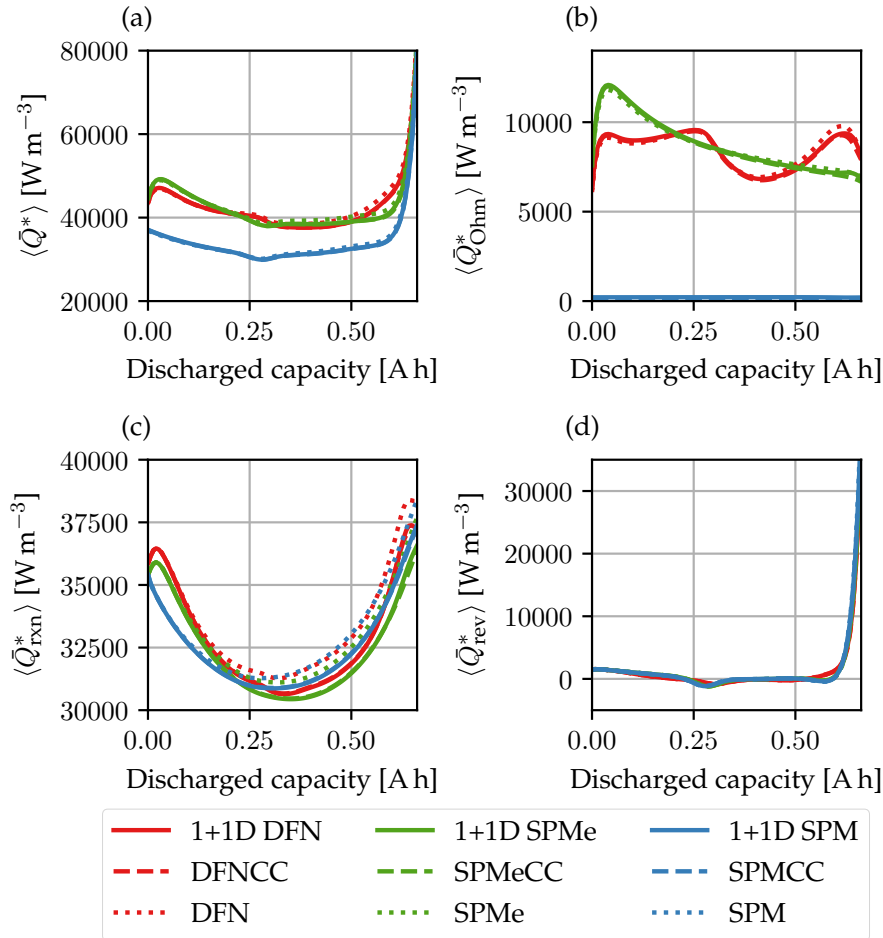
Figure 4.14: Comparison of volume-averaged cell heating: (a) total heating; (b) Ohmic heating; (c) reaction (irreversible) heating; (d) irreversible heating.

The main failing of the SPM and 1+1D SPM is that neither accounts for any though-cell Ohmic heating, with the 1+1D SPM only accounting for current collector Ohmic heating. As a result, these models significantly underpredict cell heating. Therefore it is recommended that a more complicated through-cell model than the SPM is used for thermal studies.

In Figure 4.15 (a), we present the total heating predicted by the 1+1D DFN as a function of z^* and the discharge time. Initially, the cell heats near the top, but as the discharge proceeds heating mainly occurs near the bottom of the cell. This may seem in contrast to what we would expect given the isothermal current profiles in Figure 4.10. However, as shown in Figure 4.16, the current profile can be very different for the tab cooling scenario considered here. We now see that the current
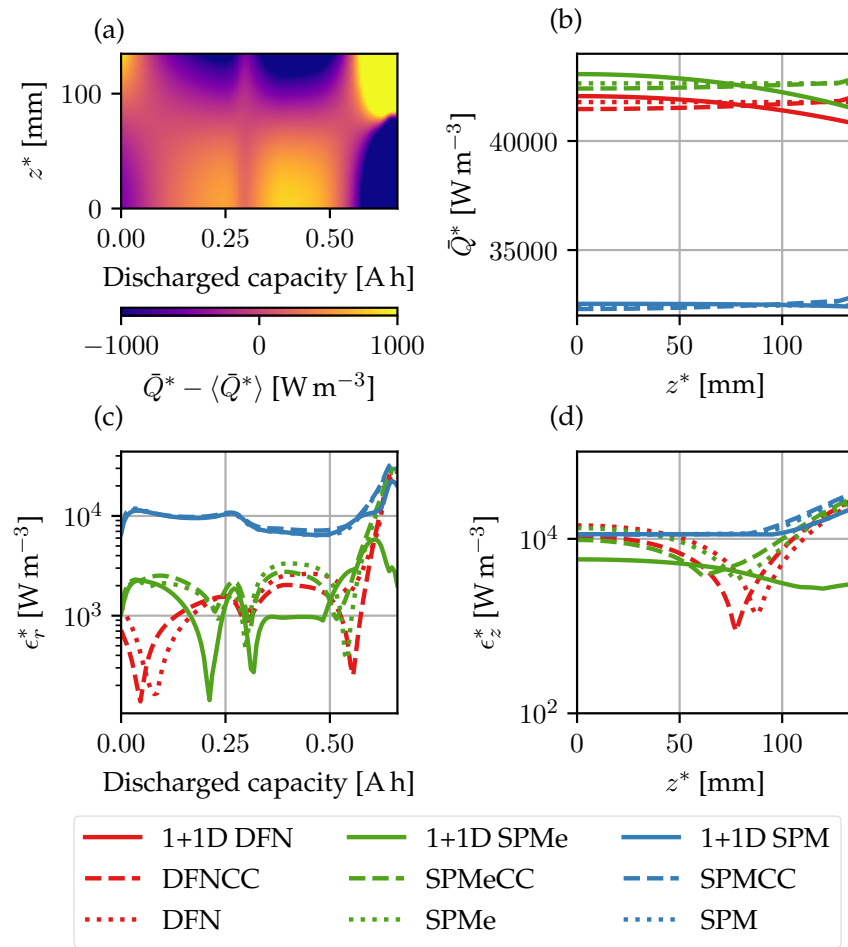
Figure 4.15: Comparison of x^*-averaged total heating, $\bar{Q}^*$: (a) The variation in the heat generation profile throughout the discharge predicted by the 1+1D DFN; (b) x^*-averaged heat generation at 0.17[A.h]; (c) Maximum (over z^*) absolute error at each time in the discharge; (d) Maximum (over the entire discharge) absolute error at each z^* location.

now preferentially travels through the bottom of the cell for most of the discharge, and the increased current leads to increased heating. This is an effect of the temperature dependence of the parameters in the through-cell models and as a results higher temperature leads to lower through-cell resistance. In Figures 4.15 (b), (c), and (d), we compare the heat generation predicted by each reduced order model with that of the 1+1D DFN. We observe that all reduced models give rise to around a 10% error in the total heating.
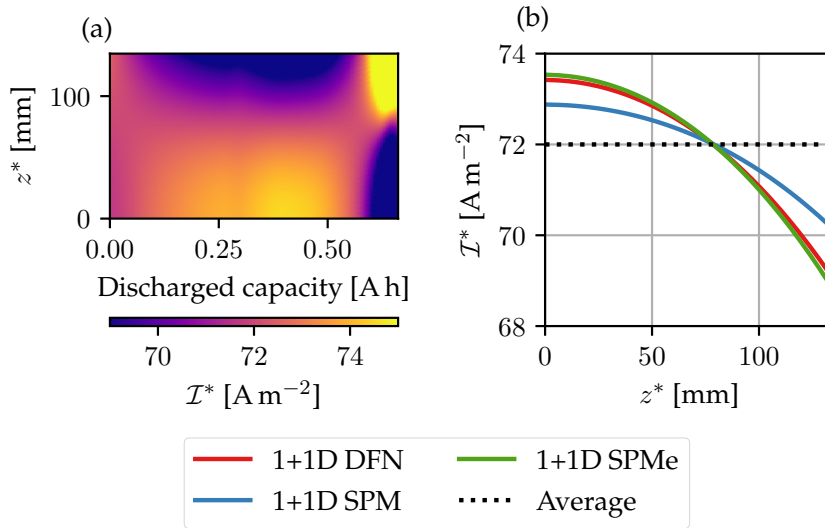
Figure 4.16: Current distribution during the discharge of a tab-cooled cell.

4.10.1 *Drive cycle comparison*

The constant current discharges that we have investigated throughout this chapter are useful for comparing models. However, they are not fully representative of a realistic usage scenario. To give an example of how the models perform under more realistic conditions, we compare the performance of each model on a portion of the US06 drive cycle. Here, we just consider the measured terminal voltage and the average temperature of the cell, as shown in Figure 4.17. We observe that similar to our previous results, the main errors are introduced by making simplifications to the through-cell electrochemical model. Therefore to most accurately capture the temperature rises, computational effort should be placed upon using a more detailed through-cell model like the DFN with a CC or 0D transverse model, rather than in using a detailed 1+1D transverse model and a simplified through-cell model like the SPM.
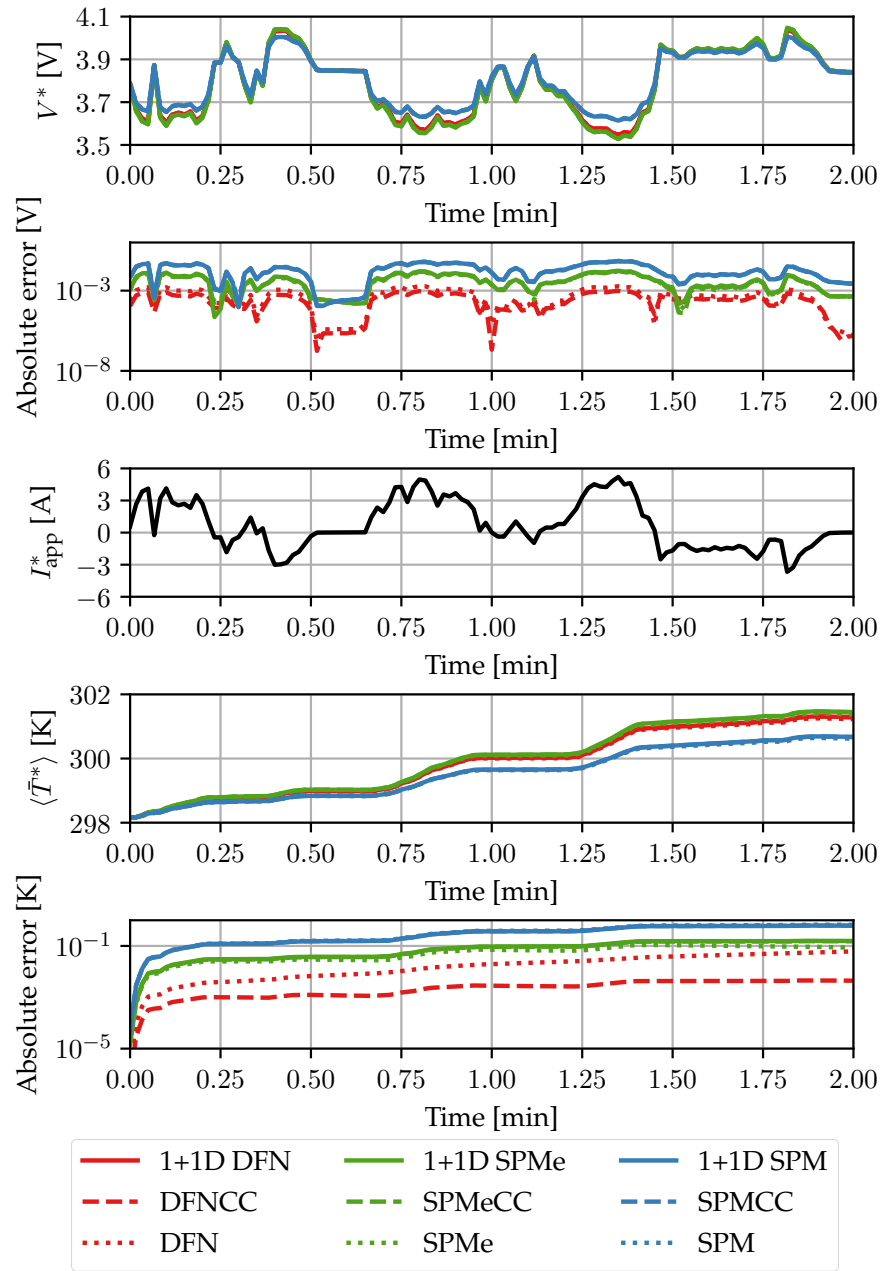
Figure 4.17: Comparison of model performance on US06 drive cycle. Solve times were: 1+1D DFN 154s, 1+1D SPMe 83s, 1+1D SPM 11s, DFN(CC) 25s, SPMe(CC) 1s, SPM(CC) 0.23s

4.11 COMPARISON SUMMARY

In the previous sections, we have provided a detailed comparison of the nine models in Figure 4.7. In Table 4.7, we have condensed this information into a concise format. Whilst the recommendations presented in Table 4.7 are informed by the quantitative performance of the models in each of the comparisons in the previous sections, they are to some degree qualitative in nature.

The first two columns in the table correspond to the solve time and the number of states required to solve that model. The solve times should only be considered relative to one another, as one could achieve speedups by employing different numerical methods or hardware. Similarly, the number of states should only be considered as representative of the spatial complexity of each model as different discretisation methods lead to a different number of states. Solve times in green are on the order of 10ms, orange on the order of 100ms, and red on the order of 1000ms, so that a green model is approximately 100 times faster than a red model. We similarly colour the states of each model so that a red model requires around 10 times more memory than an orange model and around 100 times more memory than a green model.

The second set of columns summarises the ability of each model to accurately predict key output variables during a $1\,\mathrm{C}$ discharge: the current distribution, $\mathcal{I}^*$; the negative current collector potential, $\phi_{\mathrm{s,cn}}^*$; the x-averaged negative particle surface concentration, $\bar{c}_{\mathrm{s,n}}^*$; and the average cell temperature, $\langle \bar{T}^* \rangle$. We adopt a traffic light system for each of these variables as described in Table 4.8. The system is designed to divide the predictions of each variable into three categories, where green is most accurate and red is least accurate. This is done with reference to the results presented throughout this chapter. Generally, moving from one colour to the next represents an order of magnitude difference in error, but this wasn't always the most appropriate division and we refer the reader to Table 4.8 for precise details. To be clear, red does not indicate that the model should not be used, but that this model is less accurate than the other models. Since we refer to the 1+1D DFN model for calculation of errors in models, the 1+1D DFN is always coloured green.

The third set of columns considers the ability of each model to predict the terminal voltage under low current, medium current, and high current conditions. We again adopt a traffic light system where a maximum absolute error of $< 1 \times 10^{-3}\,\mathrm{V}$ is coloured green, $< 1 \times 10^{-1}\,\mathrm{V}$ is coloured orange, and $< 1\,\mathrm{V}$ is coloured red. For this column, we have used the data in Figure 4.8(c). Again, since we refer to the 1+1D DFN model for the calculation of model errors, the 1+1D DFN is always coloured green.

Model	Solve time [ms]	States	$\mathcal{I}^*$	1C $\phi^*_{s,cn}$	$\bar{c}^*_{s,n}$	3C $\langle\bar{T}^*\rangle$	V^* $I^*_{app} < 1\,$C	$1\,$C $< I^*_{app} < 4\,$C	$I^*_{app} > 4C$
1+1D DFN	8377	49561	🟢	🟢	🟢	🟢	🟢	🟢	🟢
1+1D SPMe	1519	3961	🟢	🟢	🟢	🟠	🟠	🟠	🔴
1+1D SPM	102	1261	🟠	🟠	🟠	🔴	🟠	🔴	🔴
DFNCC	248	1651	🔴	🟠	🔴	🟢	🟢	🟢	🟢
SPMeCC	10	131	🔴	🟠	🔴	🟠	🟠	🟠	🔴
SPMCC	5	41	🔴	🟠	🔴	🔴	🟠	🔴	🔴
DFN	248	1651	🔴	🔴	🔴	🔴	🟢	🟢	🟢
SPMe	10	131	🔴	🔴	🔴	🔴	🟠	🟠	🔴
SPM	5	41	🔴	🔴	🔴	🔴	🟠	🔴	🔴

Table 4.7: Qualitative evaluation of the suite of reduced-order models. In the variables, we employed the traffic light system described in Table 4.8. For the final set of columns (current dependence), we make use of the results in Figure 4.8(c) with the following traffic light system for the maximum absolute errors: $< 1 \times 10^{-3}\,$V (green), $< 1 \times 10^{-1}\,$V (orange), $< 1\,$V (red).

	V^* [V]	$\mathcal{I}^*$ [A m^{-2}]	$\phi_{s,cn}^*$ [V]	$\bar{c}_{s,n}^*$ [mol m^{-3}]	$\langle \bar{T} \rangle^*$ [K]
🟢	$< 10^{-3}$	$< 5 \times 10^{-2}$	$< 10^{-7}$	< 5	$< 10^{-1}$
🟠	$< 10^{-1}$	$< 10^{-1}$	$< 10^{-6}$	< 10	< 1
🔴	< 1	< 1	$< 10^{-3}$	< 100	< 10

Table 4.8: Traffic light system key. The numbers refer to ranges in the absolute errors obtained for a 1 C discharge (3 C for temperature). For the variables, V^*, $\mathcal{I}^*$, $\phi_{s,cn}^*$, and $\bar{c}_{s,n}^*$ these errors refer to the isothermal case. For the variable $\langle \bar{T}^* \rangle$, the errors refer to the thermal case.

We now interpret the summary presented in Table 4.7. Firstly, by employing the 1+1D SPMe instead of the 1+1D DFN, we can achieve similar performance in terms of predicting the current, current collector potential, and y^*-z^* concentration variation while reducing memory requirements by an order of magnitude. This is achieved at the expense of a slight reduction in accuracy of the terminal voltage prediction and average cell temperature. The model is most appropriate in the low to medium C-rate range. Employing the 1+1D SPM sees a similar reduction in memory requirements, but with an additional reduction in solve time by an order of magnitude. However, this is achieved at the expense of less accurate predictions of all of the variables as well as being limited to low C-rates.

The DFNCC offers a reduction in both solve time and memory requirements by an order of magnitude without loss of accuracy in both the terminal voltage and average cell temperature. Further, there is only a small reduction in accuracy of the current collector potential. However, it achieves this reduction in solve time and memory requirements at the expense of accuracy in the estimates of the through-cell current density, and x^*-averaged negative particle concentration. The DFNCC recovers the terminal voltage well across the range of C-rates we investigated. The SPMeCC drops the solve time and memory requirements by a further order of magnitude relative to the DFNCC. To achieve this, a small amount of accuracy is sacrificed in the terminal voltage and average temperature estimates. Additionally, the SPMeCC is limited to low and medium C-rates. The solve time and memory requirements of the SPMCC are similar to that of the SPMeCC, but the predictions of the voltage and average temperature are less accurate. Further, the SPMCC is limited to low C-rates.

The DFN, SPMe, and SPM all offer orders of magnitude reductions in solve time and memory requirements compared to the models that account for current collector effects, but all do so at the expense of accuracy in the predictions of through-cell current density, current collector potential, x^*-averaged concentration, and average temperature. However, the DFN can accurately predict the terminal voltage, and recovers the terminal voltage well across the full range of C-rates we considered. The SPMe performed moderately at recovering the terminal voltage

at low to medium C-rates. The SPM was the worst performing model across all variables, and is best applied at low C-rates.

Table 4.7 highlights the trade-off that must be made between computational complexity and accuracy. However, we see that through the appropriate choice of a model, one can choose where accuracy is sacrificed in favour of reduced complexity. For example, in a study of spatially dependant degradation within a lithium-ion pouch cell, it makes more sense to employ the 1+1D SPMe or the 1+1D SPM instead of the DFN or DFNCC, because they retain greater accuracy in the y^*-z^*-dependent variables for a similar computational budget. Alternatively, in pack or module level simulations where one is only interested in the average temperature and voltage outputs of a cell, the DFNCC or the SPMeCC is more appropriate. Further, where computational constraints are really strict such as in model-based control, simple models such as the SPM and SPMe are most appropriate (the SPMCC and the SPMeCC could also be used in a limited form). In applying these simple models, it is important to understand their limitations so that they can be used appropriately. As a general rule, if integrated quantities, such as the terminal voltage, are important then the most detailed through-cell model that the budget can afford should be used. On the other hand, if capturing variations in the transverse directions is important then a 1+1D model is an appropriate choice.

4.12   SUMMARY

In this chapter, we have developed a full three-dimensional model of a lithium-ion pouch cell inspired by the one-dimensional DFN model. We then provided a systematic asymptotic derivation of the 2+1D DFN battery model from the full 3D DFN model, identifying the key dimensionless parameters controlling the reduction. Our findings are in agreement with other works that employ the 2+1D approach in an ad-hoc fashion (e.g. [25], [38], [40], [42]). Moreover, we have shown that, in a suitable parameter regime, the model can be simplified further to the DFNCC comprising a single representative 1D model describing the electrochemistry in the through-cell direction with an uncoupled two-dimensional problem to solve for the distribution of potential in the current collectors, from which resistances and heat generation can be determined. This latter approximation reduces the model from pseudo-four-dimensional to pseudo-two-dimensional, dramatically reducing the computational cost. By identifying the parameters which control the asymptotic reduction our analysis highlights the parameter regimes in which the 2+1D DFN and DFNCC models are appropriate, and quantifies the error a priori. This informs practical design choices for key cell parameters (such as current collector thickness or tab placement) in order that the cell discharge uniformly. Our systematic analysis also makes clear that the simplifications are independent of the model used

for the through-cell current so that they can be combined with other through-cell asymptotic simplifications in a systematic and mathematically consistent way. This led us to develop a suite of reduced-order pouch cell models which combined the limit taken in this chapter with that taken in Chapter 3.

Through a series of comparisons, it was demonstrated that choosing a reduced-order model depends on the variables of interest for a particular application. For instance, in many control or systems-level applications, one is only concerned with obtaining integrated quantities, such as the terminal voltage and volume-averaged cell temperature. In such cases, it is best to select the highest fidelity through-cell models the computational budget allows, combined with a simpler transverse model (e.g. the SPMeCC). However, if distributed (in y^*-z^*) quantities are of interest, such as in trying to model non-uniform degradation, then it is necessary to choose a more complicated transverse model (e.g. the 1+1D SPMe).

In contrast to the simplifications to the through-cell model that we pursued here, more complicated through-cell models could also be used by extending the DFN to include additional physics such as degradation mechanisms, particle size distributions, non-spherical particles, etc. The 2+1D DFN model provides a framework into which such additional physical effects can be straightforwardly incorporated. This provides a computationally efficient way of investigating how non-uniform cell use affects degradation, for example, and helps to rapidly assess new cell designs that aim to mitigate non-uniform ageing of cells.

MATHEMATICAL MODELLING OF THE SEI

5.1 INTRODUCTION

Whilst a large number of degradation mechanisms occur within lithium-ion batteries (see [10]), we focus our attention on the growth of the solid–electrolyte interphase (SEI) [7], [83], [94]. The SEI is a layer that forms on the surface of the negative electrode particles as a result of parasitic side reactions which consume lithium ions and solvent molecules from the electrolyte [7], [59], [81], [83], [94]. Experiments indicate that the SEI grows quickly during the first few cycles of a lithium-ion cell and slowly thereafter [15], [82]. Being able to predict the long-term growth rate of the SEI is of particular commercial interest because degradation occurs on the timescale of years and is highly cell dependent, rendering direct experiment infeasible and raising questions around extrapolation for data-driven approaches, such as machine learning. Therefore, we develop physics-based models of the SEI focused on capturing the long-term growth rate.

Physics-based SEI models broadly fall into one of three categories: detailed first principles density functional theory (DFT) models, continuum-level models, and zero-dimensional growth models. DFT models are used to provide key insights into the important properties of the SEI such as the diffusion coefficients of particular species [8], [79], and the chemical composition of the SEI [46]. However, these models are computationally expensive and are not appropriate for application in cell level simulations. On the other hand, zero-dimensional growth models, neglect most of the complexity of the SEI and instead model a single 'limiting' mechanism (e.g. diffusion of a single species). The goal of these zero-dimensional models is to capture the key long-term SEI growth behaviour whilst remaining sufficiently computationally simple to be incorporated into a full battery model such as (2.32)-(2.36). Continuum-level models offer a bridge between some of the complexity of DFT models and the simplicity of the zero-dimensional SEI model. We develop a detailed continuum model of the SEI that is informed by results from DFT models and then employ asymptotic methods to systematically simplify this model and develop a set of reduced-order models with the complexity of the zero-dimensional growth models. We will then adopt one of these reduced models and re-write it in terms of measurable electrochemical quantities. Upon doing this we validate this reduced model by comparing it with experimental capacity fade data. Finally, we integrate this validated SEI model into a simple full

cell model of a lithium-ion battery to study the impact dynamic loads have on the rate of SEI growth.

5.2   OVERVIEW OF THE SEI

The SEI is generally considered to consist of two layers of differing composition: a porous outer layer of organic materials (e.g $(CH_2OCO_2Li)_2$) and a dense inner layer of inorganic materials (e.g. Li_2CO_3) [4], [5], [93]. There is some debate over the typical thicknesses of each layer. A recent study of a 20 nm thick SEI has reported the porous outer layer to be 5 nm thick with the majority of the SEI being dense and impermeable to the electrolyte [45]. However, it has also been reported that the outer layer can be up to 100 nm thick with the inner layer a few nanometers thick [3]. This discrepancy is likely a result of the high dependency of the SEI on the particular chemistry of a cell. Several fundamental studies on the structure, composition, and other key features of the SEI have been conducted — reviews of which can be found in [4], [93], [97].
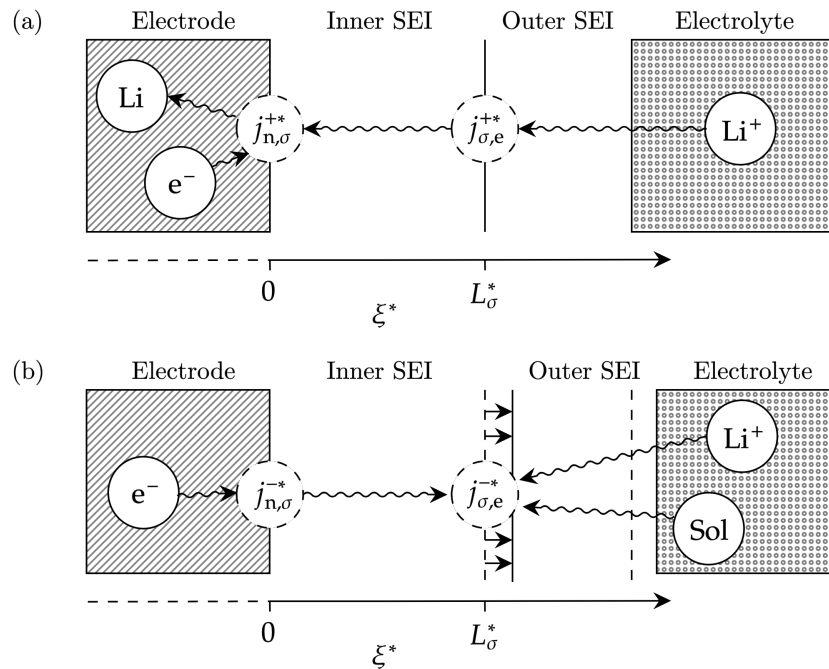
Figure 5.1: Schematic of the SEI and associated electrochemical reactions: (a) lithium intercalation reaction path (during charging); (b) SEI growth reaction path.

A schematic of the inner an outer layer structure of the SEI is presented in Figure 5.1. There are two main sets of processes that occurs through the SEI. The first set of processes, depicted in Figure 5.1 (a), is associated with lithium intercalation and consists of lithium ions being transferred from the electrolyte into the inner SEI and then to the electrode where they combine with an electron to form intercalated

lithium (and vice versa). The second set of processes is associated with SEI growth and is depicted in Figure 5.1 (b). This consists of electrons jumping from the electrode into the inner SEI and then combining with a lithium ion and solvent molecule at the interface between the inner and outer SEI to form fresh SEI.

5.3 LITERATURE REVIEW

All of the zero-dimensional SEI growth models that we are aware of choose to model one or two components of the processes involved in the growth of SEI depicted in Figure 5.1(b) and neglect the effects that the intercalation process, as presented in Figure 5.1(a), may have on the growth rate. The common zero-dimensional SEI growth models fall into the following categories: solvent-diffusion-limited growth [66], electron-migration-limited growth [19], [59], reaction-limited growth [44], [69], and solvent diffusion with reactions [63]. Other authors have considered alternative methods of transport for electrons through the inner SEI in the form of: electron tunnelling [43], or being carried by neutral lithium atom interstitials [82]. Two review papers compare each of these zero-dimensional growth models with SEI growth experiments [82], [87]. Both conclude that solvent diffusion through the outer SEI, reactions, and electron tunnelling are unlikely to be the rate-limiting mechanism in the long-term growth of SEI. Solvent diffusion is eliminated because it does not predict the experimentally observed potential dependence of the SEI growth rate. The reaction-limited and electron-tunnelling cases are eliminated because they do not predict the $t^{1/2}$ growth rate that is observed experimentally. In [82], the authors consider electron transport via neutral lithium atom interstitials to be the most likely candidate for the rate-limiting mechanism but the authors also note in a previous paper that interstitial concentrations found from DFT results are insufficient to drive SEI formation at reasonable rates [81]. In [87], the authors conclude that no current zero-dimensional growth model is fully consistent with their experimental results. They eliminate the electron-migration-limited growth model based upon an experiment which increased the flow of electrolyte to the surface upon which SEI was being created. In doing this, they observed an increase in the growth rate of SEI which they believe could only be explained if the rate-limiting species was contained within the electrolyte. They hypothesise that a charged solvent species could explain their results.

There are only a hand-full of continuum-level studies of SEI growth. In [81], a continuum model of the SEI is developed which treats the SEI as a porous structure within through which electrons are transported. Electrolyte floods the pores of this structure allowing lithium ions and solvent molecules to be transported within the SEI. An SEI formation reaction is assumed to occur throughout the SEI and decrease the porosity where it occurs. From their full model, they derive zero-dimensional

models for the SEI growth rate for the cases of electron-migration-limited growth and solvent-diffusion-limited growth. For the electron migration limited growth case, their SEI model predicts the presence of a single dense layer, which we recognise as the inner SEI. In contrast, the solvent-diffusion-limited growth case predicts the presence of a single porous layer, which we recognise as the outer SEI. By considering the dependence of these two expressions upon the porosity and tortuosity of the SEI, [81] conclude that solvent diffusion is unlikely to be the rate-limiting mechanism. Instead, transport through the inner SEI is considered the key mechanism to study to determine the long term growth rate.

Whilst the continuum model developed in [81] accounts for electron transport within the inner SEI, the transport of lithium ions is neglected. Therefore, the reduced-order expressions developed in [81] neglects the interactions between these species without justification. This may help explain some of the inconsistencies that are observed between zero-dimensional growth models and experimental results. In both [18] and [20] detailed continuum models of the inner SEI that account for the transport of electrons, vacancies and lithium ion interstitials are developed. However, these models are significantly more computationally expensive than the zero-dimensional growth models and therefore their application in full cell and multi-cell simulations is limited. In our work, we develop a detailed model of the inner SEI that accounts for the interactions between the key species in the layer and then used asymptotic methods to derive simplified expressions for the growth of the inner SEI.

5.4   MATHEMATICAL MODEL OF THE INNER SEI

In this section, we develop a mathematical model of the growth of the inner SEI by considering a detailed description of electron and lithium ion interstitial transport within a layer of pure Li_2CO_3 coupled to electrochemical reactions at the surfaces. Our model takes inspiration from [18], in which electroneutrality is enforced by balancing the concentrations of lithium-ion interstitials and lattice vacancies. In [80], density functional theory calculations were performed for Li_2CO_3 and it was found that the concentrations of electrons and lithium-ion interstitials are orders of magnitude greater than those of other species for the typical potential drops seen across the surface of the negative electrode particle $\sim$0.2 V. Therefore, we have chosen to enforce electroneutrality by instead balancing the concentrations of lithium ion interstitials and electrons. We note in passing that electroneutrality may not hold in a significant portion of the SEI as the Debye length is $\sim$2.4 nm for 10^{-3} M of lithium ion interstitials and electrons and the SEI itself has a thickness of $\sim$10–100 nm [18].

5.4.1   *Transport model*

We consider the transport of two species within the inner SEI: negatively charged electrons and positively charged lithium ion interstitials. We model the two species using the Nernst–Plank theory of electrolytes introduced in §2.4.2, where the electrons take up the role of the anionic species. That is, we assume that each species is driven down concentration gradients according to Fick's law and by gradients in the electric potential. Therefore, the fluxes of lithium ion interstitials and electrons are

$$N_\sigma^{*+} = -D_\sigma^{*+} \left(\frac{\partial c_\sigma^*}{\partial \xi^*} + \frac{F^*}{R_g^* T^*} c_\sigma^* \frac{\partial \phi_\sigma^*}{\partial \xi^*} \right), \tag{5.1a}$$

$$N_\sigma^{*-} = -D_\sigma^{*-} \left(\frac{\partial c_\sigma^*}{\partial \xi^*} - \frac{F^*}{R_g^* T^*} c_\sigma^* \frac{\partial \phi_\sigma^*}{\partial \xi^*} \right), \tag{5.1b}$$

respectively. Here, $D_\sigma^{*+}, D_\sigma^{*-}$ are the (constant) diffusivities of lithium ion interstitials and electrons, c_σ^* is the concentration of both lithium ion interstitials and electrons (set equal by our assumption of electroneutrality), $\xi^* \in [0, L_\sigma^*]$ is the spatial coordinate within the inner SEI (where L_σ^* is the thickness of the SEI), F^* is Faraday's constant, R_g^* is the gas constant, T^* is temperature, and ϕ_σ^* is the electric potential in the SEI. For this section, we choose to work with the fluxes of the individual species instead of the current and an effective flux as in §2.31.

5.4.2   *Electrochemical reactions*

On the surfaces of the inner SEI layer, electrochemical reactions take place which are dependent upon the concentrations, and potential differences across the surfaces. The first set of reactions are the lithium intercalation reactions that we are familiar with from earlier chapters. On the graphite–SEI interface, lithium intercalated in the graphite electrode can form a lithium ion interstitial in the SEI and an electron in the negative electrode and vice versa. Therefore, we have

$$\mathrm{Li_n} \rightleftharpoons \mathrm{Li}_\sigma^+ + \mathrm{e}_n^-,$$

where, $\mathrm{Li_n}$ represents lithium in the graphite particle, e_n^- represents the electrons in the graphite particle, Li_σ^+ represents lithium ion interstitials in the SEI. We capture this reaction mathematically by considering the forward and backward reactions to obtain

$$\begin{aligned} j_{n,\sigma}^{*+} = {} & m_{n,\sigma}^{*+} c_{s,n}^* \exp \left(\frac{F^*}{2R_g^* T_\infty^*} (\phi_{s,n}^* - \phi_\sigma^*) \right) \\ & - m_{\sigma,n}^{*+} (c_{s,n,\max}^* - c_{s,n}^*) c_\sigma^* \exp \left(-\frac{F^*}{2R_g^* T_\infty^*} (\phi_{s,n}^* - \phi_\sigma^*) \right) \Bigg|_{\xi^*=0}, \end{aligned} \tag{5.2}$$

where $j_{n,\sigma}^{*+}$ is the interfacial current density of the intercalation reaction at the graphite–SEI interface, and $m_{n,\sigma}^{*+}$ and $m_{\sigma,n}^{*+}$ are the forward and backward reaction constants, respectively. Here, $c_{s,n}^*$ is the lithium concentration in the graphite, $c_{s,n,max}^*$ is the maximum lithium concentration in graphite, and $\phi_{s,n}^*$ is the negative electrode potential.

On the SEI–electrolyte surface (we will neglect the outer SEI for simplicity), lithium ion interstitials can become lithium ions in the electrolyte and vice versa. Therefore, we have

$$\mathrm{Li}_\sigma^+ \rightleftharpoons \mathrm{Li}_e^+,$$
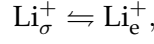
where Li_e^+ represents lithium ions in the electrolyte. We represent this reaction mathematically using

$$
\begin{aligned}
j_{\sigma,e}^{*+} =& m_{\sigma,e}^{*+} c_\sigma^* \exp\left(\frac{F^*}{2R_g^* T_\infty^*}(\phi_\sigma^* - \hat{\phi}_{e,n}^*) \right) \\
&- m_{e,\sigma}^{*+} c_{e,n}^* \exp\left(-\frac{F^*}{2R_g^* T_\infty^*}(\phi_\sigma^* - \hat{\phi}_{e,n}^*) \right) \Bigg|_{\xi^* = L_\sigma^*(t^*)},
\end{aligned}
\tag{5.3}
$$

where $j_{\sigma,e}^{*+}$ is the interfacial current density of the lithium ion reaction at the SEI–electrolyte interface, and $m_{\sigma,e}^{*+}$ and $m_{e,\sigma,n}^{*+}$ are the forward and backward reaction constants, respectively. Here, $c_{e,n}^*$ is the lithium ion concentration in the electrolyte and $\hat{\phi}_{e,n}^*$ is the true electrolyte potential (not the electrochemical potential, see §2.4.1).

In addition to the lithium intercalation reactions, there is also a reaction on the graphite–SEI surface that transfers electrons between then graphite and the SEI, given by

$$\mathrm{e}_n^- \rightleftharpoons \mathrm{e}_\sigma^-,$$
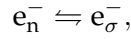
where e_n represents electrons in the graphite and e_σ^- represents electrons in the SEI. This reaction is captured by

$$
\begin{aligned}
j_{n,\sigma}^{*-} =& -m_{n,\sigma}^{*-} \exp\left(-\frac{F^*}{2R_g^* T_\infty^*}(\phi_{s,n}^* - \phi_\sigma^*) \right) \\
&+ m_{\sigma,n}^{*-} c_\sigma^* \exp\left(\frac{F^*}{2R_g^* T_\infty^*}(\phi_{s,n}^* - \phi_\sigma^*) \right) \Bigg|_{\xi^* = 0},
\end{aligned}
\tag{5.4}
$$

where $j_{n,\sigma}^{*-}$ is the interfacial current density of the electron transfer reaction at the graphite–SEI interface, and $m_{n,\sigma}^{*-}$ and $m_{\sigma,n}^{*-}$ are the forward and backward reaction constants, respectively. Note that the forward reaction is negative and the backward is positive in this expression because electrons are negatively charged.

Finally, on the SEI–electrolyte surface, the SEI formation reaction takes place. The reaction consumes a lithium ion from the electrolyte, a

solvent molecule from the electrolyte, and an electron from the SEI to create pure Li_2CO_3, written as

$$Li_e^+ + EC_e + e_\sigma^- \rightarrow Li_2CO_3$$
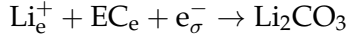
where Li_e^+ represents lithium ions in the electrolyte, EC_e represents ethylene carbonate (an example of a solvent) in the electrolyte, and e_σ^- represents electrons in the SEI. Here, we only consider the forward reaction, thus we have

$$j_{\sigma,e}^{*-} = -m_{\sigma,e}^{*-} c_{e,n}^* c_{sol}^* c_\sigma^* \exp\left(-\frac{F^*}{2R_g^* T_\infty^*}(\phi_\sigma^* - \hat{\phi}_{e,n}^*)\right)\bigg|_{\xi^*=L_\sigma^*}, \qquad (5.5)$$

where $j_{\sigma,e}^{*-}$ is the interfacial current density of the SEI formation reaction, $m_{e,\sigma}^{*-}$ is the reaction rate constant, and c_{sol}^* is the concentration of solvent in the electrolyte. Note that this reaction induces a negative interfacial current density because negatively charged electrons flow into the reaction from the SEI (we have been using the convention that a positive current corresponds to the flow of positive charge from the negative electrode, through the SEI and electrolyte, and towards the positive electrode).

5.4.3 *Full model*

Using the expressions for the fluxes and electrochemical reactions given by (5.1)-(5.5), we formulate the SEI growth model. Within the SEI, we have conservation of both lithium ion interstitials and electrons, which gives

$$\frac{\partial c_\sigma^*}{\partial t^*} = -\frac{\partial N_\sigma^{*+}}{\partial \xi^*} \qquad (5.6a)$$

$$\frac{\partial c_\sigma^*}{\partial t^*} = -\frac{\partial N_\sigma^{*-}}{\partial \xi^*}. \qquad (5.6b)$$

We take the initial concentration of lithium ion interstitials and electrons to be given by

$$c_\sigma^*\big|_{t^*=0} = c_{\sigma,0}^* \qquad (5.6c)$$

where $c_{\sigma,0}^*$ is a constant. On the graphite–SEI interface the flux of lithium into the SEI is given by

$$N_\sigma^{*+}\big|_{\xi^*=0} = \frac{j_{n,\sigma}^{*+}}{F^*}, \qquad (5.6d)$$

and the flux of electrons into the SEI is given by

$$N_\sigma^{*-}\big|_{\xi^*=0} = -\frac{j_{n,\sigma}^{*-}}{F^*}, \qquad (5.6e)$$

where the minus sign accounts for the negative charge of the electrons in the conversion of the interfacial current density into a molar flux.

On the SEI–electrolyte boundary, we need to account for the effect of the moving boundary. Within newly created SEI, there may be some concentration of lithium ion interstitials and electrons present. In general, this could depend upon the potential at which a reaction occurs, the concentrations of particular reaction products, and thermal effects. However, for simplicity, we shall assume that the concentration in fresh SEI is zero. Other concentrations could be considered but these must be chosen carefully to avoid issues with the conservation of mass. We shall see shortly that making this assumption of zero concentration in fresh SEI does not affect our results. Under this assumption, within in a small region $[L_\sigma^*(t^*) - \Delta\xi^*, L_\sigma^*(t^*)]$ of constant concentration, there will be a loss of

$$\frac{\mathrm{d}L_\sigma^*}{\mathrm{d}t^*} c_\sigma^* \big|_{\xi^* = L_\sigma^*(t^*)}^*$$

moles per metre squared per second from the region due only to the movement of the region (from the growth of the SEI). Accounting for this in the flux of lithium out of the SEI at the SEI–electrolyte interface, we have

$$N_\sigma^{*+} \big|_{\xi^* = L_\sigma^*} = \frac{j_{\sigma,\mathrm{e}}^{*+}}{F^*} + \frac{\mathrm{d}L_\sigma^*}{\mathrm{d}t^*} c_\sigma^* \big|_{\xi^* = L_\sigma^*(t^*)}. \tag{5.6f}$$

Similarly, the flux of electrons out of the SEI at the SEI interface is given by

$$N_\sigma^{*-} \big|_{\xi^* = L_\sigma^*} = -\frac{j_{\mathrm{n},\sigma}^{*-}}{F^*} + \frac{\mathrm{d}L_\sigma^*}{\mathrm{d}t^*} c_\sigma^* \big|_{\xi^* = L_\sigma^*(t^*)}, \tag{5.6g}$$

where the minus sign in front of the reaction terms accounts for the negative charge of the electrons.

Finally, the SEI grows at a rate proportional to the interfacial current density of the SEI growth reaction and the partial molar volume of SEI, $\bar{V}_\sigma^*$ (a higher partial molar volume means each mole of SEI has greater volume, leading to a greater increase in thickness). Therefore, we have

$$\frac{\mathrm{d}L_\sigma^*}{\mathrm{d}t^*} = -\bar{V}_\sigma^* \frac{j_{\sigma,\mathrm{e}}^{*-}}{F^*}. \tag{5.6h}$$

with the initial thickness of the SEI given by

$$L_\sigma^* \big|_{t^* = 0} = 0. \tag{5.6i}$$

The full set of dimensional parameters in this model is presented in Tables 5.1, 5.2. We have reported parameter values where available. However, one should be aware that many of these values are mearly 'educated' guesses from previous modelling papers.

Parameter	Units	Description	Value	Reference
$m_{\mathrm{n},\sigma}^{*+}$	$\mathrm{A\,m\,mol^{-1}}$	Graphite–SEI intercalation forward reaction rate	9.841×10^4	[18]
$m_{\sigma,\mathrm{n}}^{*+}$	$\mathrm{A\,m^4\,mol^{-2}}$	Graphite–SEI intercalation backward reaction rate	1.03×10^{10}	[18]
$m_{\sigma,\mathrm{e}}^{*+}$	$\mathrm{A\,m\,mol^{-1}}$	SEI–electrolyte lithium transfer forward reaction rate	-	
$m_{\mathrm{e},\sigma}^{*-}$	$\mathrm{A\,m\,mol^{-1}}$	SEI–electrolyte lithium transfer backward reaction rate	-	
$m_{\mathrm{n},\sigma}^{*-}$	$\mathrm{A\,m^{-2}}$	Graphite–SEI electron transfer forward reaction rate	0.964	[18]
$m_{\sigma,\mathrm{n}}^{*-}$	$\mathrm{A\,m\,mol^{-1}}$	Graphite–SEI electron transfer backward reaction rate	9.64×10^{-8}	[18]
$m_{\sigma,\mathrm{e}}^{*-}$	$\mathrm{A\,m^7\,mol^{-3}}$	SEI–electrolyte SEI formation reaction rate	-	
D_{σ}^{*+}	$\mathrm{m^2\,s^{-1}}$	Lithium ion interstitial diffusivity in SEI	2×10^{-14}	[20]
D_{σ}^{*-}	$\mathrm{m^2\,s^{-1}}$	Electron diffusivity in SEI	5×10^{-19}	[20]

Table 5.1: Dimensional parameters in the SEI model (Part 1).

Parameter	Units	Description	Value	Reference
$\bar{V}_\sigma^*$	$m^3\,mol^{-1}$	Partial molar volume of Li_2CO_3	3.5019×10^{-5}	[20]
$c_{\sigma,0}^*$	$mol\,m^{-3}$	Initial lithium ion interstitial and electron concentration in SEI	10	[20]
$L_{\sigma,\mathrm{typ}}^*$	nm	Typical SEI thickness	10	[80]
c_{sol}^*	$mol\,m^{-3}$	Electrolyte solvent concentration	4.5×10^3	[81]
F^*	$C\,mol^{-1}$	Faraday's constant	96487	
R_g^*	$J\,mol^{-1}\,K^{-1}$	Universal gas constant	8.314	
T_∞^*	K	Reference temperature	298.15	
$c_{\mathrm{s,n}}^*$	$mol\,m^{-3}$	Negative electrode lithium concentration	1.2491×10^4	$c_{\mathrm{s,n,max}}^*/2$
$c_{\mathrm{s,n,max}}^*$	$mol\,m^{-3}$	Maximum negative electrode lithium concentration	2.4983×10^4	[51]
$c_{\mathrm{e,n}}^*$	$mol\,m^{-3}$	Negative electrolyte lithium ion concentration	1000	§3
$\phi_{\mathrm{s,n}}^*$	V	Negative electrode potential	0	§3
$\hat{\phi}_{\mathrm{e,n}}^*$	V	Negative electrolyte potential	-	

Table 5.2: Dimensional parameters in the SEI model (Part 2).

5.4.4 *Nondimensionalisation*

To facilitate our asymptotic analysis, we nondimensionalise the SEI model by introducing typical scalings. The through-SEI position, ξ^*, and the thickness of the SEI, L_σ^*, are scaled with the typical thickness of the SEI. We scale time with the SEI growth timescale, as stated in Table 5.3. The concentration is scaled with the initial value and the electric potential is scaled by the magnitude of the total potential drop across the SEI layer. The flux of lithium ion intersitials is scaled naturally by the diffusion flux and the interfacial current densities are scaled similarly. Likewise, the electron flux and associated interfacial current densities are scaled naturally with the electron diffusion. The scalings are summarised as

$$
\xi^* = L_{s,\text{typ}}^* \xi, \quad L_\sigma^* = L_{\sigma,\text{typ}}^* L_\sigma, \quad t^* = \tau_{\text{grow}}^* t
$$

$$
c_\sigma^* = c_{\sigma,0}^* c_\sigma, \quad \phi_\sigma^* = |\phi_{s,n}^* - \phi_{e,n}^*| \phi_\sigma + \hat{\phi}_{e,n}^*,
$$

$$
N_\sigma^{*+} = \frac{D_\sigma^{*+} c_{\sigma,0}^*}{L_{\sigma,\text{typ}}^*} N_\sigma^+, \quad N_\sigma^{*-} = \frac{D_\sigma^{*-} c_{\sigma,0}^*}{L_{\sigma,\text{typ}}^*} N_\sigma^-,
$$

$$
j_{n,\sigma}^{*+} = \frac{F^* D_\sigma^{*+} c_{\sigma,0}^*}{L_{\sigma,\text{typ}}^*} j_{n,\sigma}^+, \quad j_{n,\sigma}^{*-} = \frac{F^* D_\sigma^{*-} c_{\sigma,0}^*}{L_{\sigma,\text{typ}}^*} j_{n,\sigma}^-,
$$

$$
j_{\sigma,e}^{*+} = \frac{F^* D_\sigma^{*+} c_{\sigma,0}^*}{L_{\sigma,\text{typ}}^*} j_{\sigma,e}^+, \quad j_{\sigma,e}^{*-} = \frac{F^* D_\sigma^{*-} c_{\sigma,0}^*}{L_{\sigma,\text{typ}}^*} j_{\sigma,e}^-.
$$

$$(5.7)$$

After making these scalings we identify a set of dimensionless parameters in the model which are presented in Tables 5.4 and 5.2 alongside their interpretation and derived values. We also present key timescales for the model in Table 5.3.

Symbol	Expression	Interpretation	Value (s)
τ_{grow}^*	$(L_{\sigma,\text{typ}}^*)^2/(D_\sigma^{*-} \bar{V}_\sigma^* c_{\sigma,0}^*)$	SEI growth timescale	5.711×10^5
τ_{Li}^*	$(L_{\sigma,\text{typ}}^*)^2/D_\sigma^{*+}$	Lithium ion interstitial diffusion timescale	5×10^{-3}
$\tau_{e^-}^*$	$(L_{\sigma,\text{typ}}^*)^2/D_\sigma^{*-}$	Electron diffusion timescale	200

Table 5.3: Timescales associated with the physical process in the SEI model. The SEI growth time scale is chosen to be associated with the diffusion timescale of electrons through the SEI as this is often reported to be the rate-limiting mechanism and not the electrochemical reaction. (Note we have omitted the reaction timescales from this table).

Parameter	Expression	Description	Value
$m_{\mathrm{n},\sigma}^{+}$	$m_{\mathrm{n},\sigma}^{*+}c_{\mathrm{s,n}}^{*}L_{\sigma,\mathrm{typ}}^{*}/(D_{\sigma}^{*+}c_{\sigma,0}^{*}F^{*})$	Ratio of interstitial diffusion timescale and graphite–SEI intercalation forward reaction timescale	6.37×10^{8}
$m_{\sigma,\mathrm{n}}^{+}$	$m_{\sigma,\mathrm{n}}^{*+}(c_{\mathrm{s,n,max}}^{*} - c_{\mathrm{s,n}}^{*})L_{\sigma,\mathrm{typ}}^{*}/(D_{\sigma}^{*+}F^{*})$	Ratio interstitial diffusion timescale and graphite–SEI intercalation backward reaction timescale	6.67×10^{14}
$m_{\sigma,\mathrm{e}}^{+}$	$m_{\sigma,\mathrm{e}}^{*+}L_{\sigma,\mathrm{typ}}^{*}/(D_{\sigma}^{*+}F^{*})$	Ratio of interstitial diffusion timescale and SEI–electrolyte lithium transfer forward reaction timescale	-
$m_{\mathrm{e},\sigma}^{+}$	$m_{\mathrm{e},\sigma}^{*-}c_{\mathrm{e,n}}^{*}L_{\sigma,\mathrm{typ}}^{*}/(D_{\sigma}^{*+}c_{\sigma,0}^{*}F^{*})$	Ratio of interstitial diffusion timescale and SEI–electrolyte lithium transfer backward reaction timescale	-
$m_{\mathrm{n},\sigma}^{-}$	$m_{\mathrm{n},\sigma}^{-}L_{\sigma,\mathrm{typ}}^{*}/(D_{\sigma}^{*-}c_{\sigma,0}^{*}F^{*})$	Ratio of electron diffusion timescale and graphite–SEI electron transfer forward reaction timescale	1.99×10^{4}
$m_{\sigma,\mathrm{n}}^{-}$	$m_{\sigma,\mathrm{n}}^{-}L_{\sigma,\mathrm{typ}}^{*}/(D_{\sigma}^{*-}F^{*})$	Ratio of electron diffusion timescale and graphite–SEI electron transfer backward reaction timescale	1.99×10^{-3}
$m_{\sigma,\mathrm{e}}^{*-}$	$m_{\sigma,\mathrm{e}}^{-}c_{\mathrm{e,n}}^{*}c_{\mathrm{sol}}^{*}L_{\sigma,\mathrm{typ}}/(D_{\sigma}^{*-}F^{*})$	Ratio of electron diffusion timescale and SEI–electrolyte SEI formation reaction timescale	-

Table 5.4: Dimensionless parameters in SEI model (Part 1).

Parameter	Expression	Description	Value
$\mathcal{C}_{\text{Li}}$	$\tau_{\text{Li}}^* / \tau_{\text{grow}}^*$	Ratio of lithium interstitial and SEI growth timescales	8.75×10^{-9}
$\mathcal{C}_{\text{e}^-}$	$\tau_{\text{e}^-}^* / \tau_{\text{grow}}^*$	Ratio of electron transport and SEI growth timescales	3.5×10^{-4}
λ	$F^* |\phi_{\text{s,n}} - \phi_{\text{e,n}}| / (R_g^* T_\infty)$	Ratio of magnitude of potential difference across SEI to the thermal voltage	11.677
Φ	$\text{sgn}(\phi_{\text{s,n}} - \phi_{\text{e,n}})$	Sign of potential difference across SEI	$1, -1$

Table 5.5: Dimensionless parameters in SEI model (Part 2).

In the following we state the dimensionless version of the SEI model (5.1a)-(5.6) which we arrive at after applying (5.7). The lithium ion interstitials are governed by

$$
\mathcal{C}_{\mathrm{Li}} \frac{\partial c_\sigma}{\partial t} = -\frac{\partial N_\sigma^+}{\partial \xi}, \quad N_\sigma^+ = -\left(\frac{\partial c_\sigma}{\partial \xi} + \lambda c_\sigma \frac{\partial \phi_\sigma}{\partial \xi} \right),
\tag{5.8a}
$$

$$
N_\sigma^+ \big|_{\xi=0} = j_{\mathrm{n},\sigma}^+, \quad N_\sigma^+ \big|_{\xi=L_\sigma} = j_{\sigma,\mathrm{e}}^+ + \mathcal{C}_{\mathrm{Li}} \frac{\mathrm{d}L_\sigma}{\mathrm{d}t} c_\sigma \big|_{\xi=L_\sigma(t)},
\tag{5.8b}
$$

with the associated electrochemical reactions given by

$$
\begin{aligned}
j_{\mathrm{n},\sigma}^+ &= m_{\mathrm{n},\sigma}^+ \exp\left(\frac{\lambda}{2} (\Phi - \phi_\sigma) \right) \\
&\quad - m_{\sigma,\mathrm{n}}^+ c_\sigma \exp\left(-\frac{\lambda}{2} (\Phi - \phi_\sigma) \right) \Big|_{\xi=0},
\end{aligned}
\tag{5.8c}
$$

$$
j_{\sigma,\mathrm{e}}^+ = m_{\sigma,\mathrm{e}}^+ c_\sigma \exp\left(\frac{\lambda \phi_\sigma}{2} \right) - m_{\mathrm{e},\sigma}^+ \exp\left(-\frac{\lambda \phi_\sigma}{2} \right) \Big|_{\xi=L_\sigma(t)}.
\tag{5.8d}
$$

The electrons are governed by

$$
\mathcal{C}_{\mathrm{e}^-} \frac{\partial c_\sigma}{\partial t} = -\frac{\partial N_\sigma^-}{\partial \xi} \quad N_\sigma^- = -\left(\frac{\partial c_\sigma}{\partial \xi} - \lambda c_\sigma \frac{\partial \phi_\sigma}{\partial \xi} \right),
\tag{5.8e}
$$

$$
N_\sigma^- \big|_{\xi=0} = -j_{\mathrm{n},\sigma}^-, \quad N_\sigma^- \big|_{\xi=L_\sigma} = -j_{\mathrm{n},\sigma}^- + \mathcal{C}_{\mathrm{e}^-} \frac{\mathrm{d}L_\sigma}{\mathrm{d}t} c_\sigma \big|_{\xi=L_\sigma(t)},
\tag{5.8f}
$$

with the electrochemical reactions given by

$$
\begin{aligned}
j_{\mathrm{n},\sigma}^- &= -m_{\mathrm{n},\sigma}^- \exp\left(-\frac{\lambda}{2} (\Phi - \phi_\sigma) \right) \\
&\quad + m_{\sigma,\mathrm{n}}^- c_\sigma \exp\left(\frac{\lambda}{2} (\Phi - \phi_\sigma) \right) \Big|_{\xi=0},
\end{aligned}
\tag{5.8g}
$$

$$
j_{\sigma,\mathrm{e}}^- = -m_{\sigma,\mathrm{e}}^- c_\sigma \exp\left(-\frac{\lambda \phi_\sigma}{2} \right) \Big|_{\xi=L_\sigma(t)}.
\tag{5.8h}
$$

The initial concentration of both interstitials and electrons is given by

$$
c_\sigma \big|_{t=0} = 1.
\tag{5.8i}
$$

Finally the SEI thickness is given by

$$
\frac{\mathrm{d}L_\sigma}{\mathrm{d}t} = -j_{\sigma,\mathrm{e}}^-, \quad L_\sigma \big|_{t=0} = 0.
\tag{5.8j}
$$

5.4.5 *Pseudo steady-state model*

We now develop a pseudo steady-state version of the SEI model (5.8) for which we later consider various asymptotic limiting cases. To develop this model we rescale our spatial coordinates onto a fixed domain and the take the limit of a rapid timescale of transport within the SEI

relative to the SEI growth timescale. Since we investigate effects on the timescale of SEI growth, the model that we develop is pseudo steady-state in the sense that transport of species within the inner SEI is in steady state but the domain itself is growing. We first scale

$$\xi = L_\sigma(t)\hat{\xi}, \tag{5.9}$$

so that $\hat{\xi} \in [0, 1]$. Under this transformation, the partial derivatives become

$$\left(\frac{\partial}{\partial \xi}\right)_t = \frac{1}{L_\sigma(t)}\left(\frac{\partial}{\partial \hat{\xi}}\right)_t,$$
$$\left(\frac{\partial}{\partial t}\right)_\xi = \left(\frac{\partial}{\partial t}\right)_{\hat{\xi}} - \frac{\hat{\xi}}{L_\sigma(t)}\frac{\mathrm{d}L_\sigma}{\mathrm{d}t}\left(\frac{\partial}{\partial \hat{\xi}}\right)_t \tag{5.10}$$

where the subscript indicates the variable that is being held fixed when the partial derivate is taken. Therefore (5.8) becomes as follows. The lithium ion interstitials are governed by

$$\mathcal{C}_{\mathrm{Li}}\left(\frac{\partial c_\sigma}{\partial t} - \frac{\hat{\xi}}{L_\sigma(t)}\frac{\mathrm{d}L}{\mathrm{d}t}\frac{\partial c_\sigma}{\partial \hat{\xi}}\right) = -\frac{1}{L_\sigma(t)}\frac{\partial N_\sigma^+}{\partial \hat{\xi}}, \tag{5.11a}$$

$$N_\sigma^+ = -\frac{1}{L_\sigma(t)}\left(\frac{\partial c_\sigma}{\partial \hat{\xi}} + \lambda c_\sigma \frac{\partial \phi_\sigma}{\partial \hat{\xi}}\right), \tag{5.11b}$$

$$N_\sigma^+\big|_{\hat{\xi}=0} = j_{\mathrm{n},\sigma}^+, \quad N_\sigma^+\big|_{\hat{\xi}=1} = j_{\sigma,\mathrm{e}}^+ + \mathcal{C}_{\mathrm{Li}}\frac{\mathrm{d}L_\sigma}{\mathrm{d}t}c_\sigma\big|_{\hat{\xi}=1}, \tag{5.11c}$$

with the associated electrochemical reactions given by

$$j_{\mathrm{n},\sigma}^+ = m_{\mathrm{n},\sigma}^+ \exp\left(\frac{\lambda}{2}(\Phi - \phi_\sigma)\right)$$
$$\quad - m_{\sigma,\mathrm{n}}^+ c_\sigma \exp\left(-\frac{\lambda}{2}(\Phi - \phi_\sigma)\right)\bigg|_{\hat{\xi}=0}, \tag{5.11d}$$

$$j_{\sigma,\mathrm{e}}^+ = m_{\sigma,\mathrm{e}}^+ c_\sigma \exp\left(\frac{\lambda\phi_\sigma}{2}\right) - m_{\mathrm{e},\sigma}^+ \exp\left(-\frac{\lambda\phi_\sigma}{2}\right)\bigg|_{\hat{\xi}=1}. \tag{5.11e}$$

The electrons are governed by

$$\mathcal{C}_{\mathrm{e}^-}\left(\frac{\partial c_\sigma}{\partial t} - \frac{\hat{\xi}}{L_\sigma(t)}\frac{\mathrm{d}L}{\mathrm{d}t}\frac{\partial c_\sigma}{\partial \hat{\xi}}\right) = -\frac{1}{L_\sigma(t)}\frac{\partial N_\sigma^-}{\partial \hat{\xi}}, \tag{5.11f}$$

$$N_\sigma^- = -\frac{1}{L_\sigma(t)}\left(\frac{\partial c_\sigma}{\partial \hat{\xi}} - \lambda c_\sigma \frac{\partial \phi_\sigma}{\partial \hat{\xi}}\right), \tag{5.11g}$$

$$N_\sigma^-\big|_{\hat{\xi}=0} = -j_{\mathrm{n},\sigma}^-, \quad N_\sigma^-\big|_{\hat{\xi}=1} = -j_{\mathrm{n},\sigma}^- + \mathcal{C}_{\mathrm{e}^-}\frac{\mathrm{d}L_\sigma}{\mathrm{d}t}c_\sigma\big|_{\hat{\xi}=1}, \tag{5.11h}$$

with the associated electrochemical reactions given by

$$j_{\mathrm{n},\sigma}^- = -m_{\mathrm{n},\sigma}^- \exp\left(-\frac{\lambda}{2}(\Phi - \phi_\sigma)\right)$$
$$+ m_{\sigma,\mathrm{n}}^- c_\sigma \exp\left(\frac{\lambda}{2}(\Phi - \phi_\sigma)\right)\Bigg|_{\hat\xi=0}, \tag{5.11i}$$

$$j_{\sigma,\mathrm{e}}^- = -m_{\sigma,\mathrm{e}}^- c_\sigma \exp\left(-\frac{\lambda\phi_\sigma}{2}\right)\Bigg|_{\hat\xi=1} \tag{5.11j}$$

The initial concentration of both interstitials and electrons are given by

$$c_\sigma\big|_{t=0} = 1. \tag{5.11k}$$

Finally the SEI thickness is given by

$$\frac{\mathrm{d}L_\sigma}{\mathrm{d}t} = -j_{\sigma,\mathrm{e}}^-, \quad L_\sigma\big|_{t=0} = 0. \tag{5.11l}$$

We now take the limit of a rapid timescale of transport within the SEI relative to the SEI growth timescale, which is supported by the values reported in Tables 5.4 and 5.2. This reduces our problem to a pseudo steady-state problem. To do this, we introduce a single small parameter ε such that

$$\mathcal{C}_{\mathrm{Li}} = \mathcal{O}(\varepsilon), \quad \mathcal{C}_{\mathrm{e}^-} = \mathcal{O}(\varepsilon)$$

and take all other dimensionless parameters in the model to be $\mathcal{O}(1)$. We note in passing that the parameter values for the dimensionless reactions rates in Tables 5.4 and 5.2 suggest that some of the electrochemical reactions occur many orders of magnitude faster than transport of both lithium ion interstitials and electrons through the SEI, which lead to these reactions being in equilibrium. However, for now, we study the case where electrochemical reactions and transport processes occur on a similar timescale and leave further reductions for later. We then make regular asymptotic expansion in each of the model variables of the form

$$c_\sigma = c_\sigma^{(0)} + \varepsilon c_\sigma^{(1)} + \mathcal{O}(\varepsilon^2),$$

and take $\varepsilon \to 0$. At leading order in ε, (5.11) becomes the following, where we have dropped the asymptotic order superscript. The lithium ion interstitials are governed by

$$\frac{\partial N_\sigma^+}{\partial \hat\xi} = 0, \tag{5.12a}$$

$$N_\sigma^+ = -\frac{1}{L_\sigma(t)}\left(\frac{\partial c_\sigma}{\partial \hat\xi} + \lambda c_\sigma \frac{\partial \phi_\sigma}{\partial \hat\xi}\right), \tag{5.12b}$$

$$N_\sigma^+\big|_{\hat\xi=0} = j_{\mathrm{n},\sigma}^+, \quad N_\sigma^+\big|_{\hat\xi=1} = j_{\sigma,\mathrm{e}}^+, \tag{5.12c}$$

with the associated electrochemical reactions given by

$$
j_{n,\sigma}^+ = m_{n,\sigma}^+ \exp\left(\frac{\lambda}{2}(\Phi - \phi_\sigma)\right)
$$
$$
- m_{\sigma,n}^+ c_\sigma \exp\left(-\frac{\lambda}{2}(\Phi - \phi_\sigma)\right)\bigg|_{\hat{\xi}=0},
$$
(5.12d)

$$
j_{\sigma,e}^+ = m_{\sigma,e}^+ c_\sigma \exp\left(\frac{\lambda\phi_\sigma}{2}\right) - m_{e,\sigma}^+ \exp\left(-\frac{\lambda\phi_\sigma}{2}\right)\bigg|_{\hat{\xi}=1}.
$$
(5.12e)

The electrons are governed by

$$
\frac{\partial N_\sigma^-}{\partial \hat{\xi}} = 0,
$$
(5.12f)

$$
N_\sigma^- = -\frac{1}{L_\sigma(t)}\left(\frac{\partial c_\sigma}{\partial \hat{\xi}} - \lambda c_\sigma \frac{\partial \phi_\sigma}{\partial \hat{\xi}}\right),
$$
(5.12g)

$$
N_\sigma^-\big|_{\hat{\xi}=0} = -j_{n,\sigma}^-, \quad N_\sigma^-\big|_{\hat{\xi}=1} = -j_{n,\sigma}^-
$$
(5.12h)

with the associated electrochemical reactions given by

$$
j_{n,\sigma}^- = -m_{n,\sigma}^- \exp\left(-\frac{\lambda}{2}(\Phi - \phi_\sigma)\right)
$$
$$
+ m_{\sigma,n}^- c_\sigma \exp\left(\frac{\lambda}{2}(\Phi - \phi_\sigma)\right)\bigg|_{\hat{\xi}=0},
$$
(5.12i)

$$
j_{\sigma,e}^- = -m_{\sigma,e}^- c_\sigma \exp\left(-\frac{\lambda\phi_\sigma}{2}\right)\bigg|_{\hat{\xi}=1}
$$
(5.12j)

Finally the SEI thickness is given by

$$
\frac{dL_\sigma}{dt} = -j_{\sigma,e}^-, \quad L_\sigma\big|_{t=0} = 0.
$$
(5.12k)

In making this expansion, we have removed the time derivatives from the problems for the fluxes of lithium ion interstitials and electrons. Therefore, the initial condition on the lithium ion interstitial and electron concentration is no longer required. We have neglected the transient effects of the lithium ion interstitials to obtain a pseudo steady-state model. To capture transient effects and in particular the transition from the initial conditions, we can consider a short time problem by rescaling time with the lithium ion interstitial diffusion timescale but we shall not consider this analysis. On this timescale, the full complexity of (5.11) is recovered with the exception that the SEI thickness is fixed.

To simplify the analysis in the following sections, we re-write (5.12) as a system of algebraic equations for the fluxes, boundary concentrations,

and boundary potentials, coupled to a single ODE for the SEI thickness. To do this, we add (5.12b) and (5.12g) to get

$$-2\frac{\partial c_\sigma}{\partial \hat{\xi}} = L_\sigma(N_\sigma^+ + N_\sigma^-), \tag{5.13}$$

and then integrate with respect to $\hat{\xi}$, to obtain

$$c_\sigma = c_\sigma\big|_{\hat{\xi}=0} - \frac{L_\sigma}{2}(N_\sigma^+ + N_\sigma^-)\xi. \tag{5.14}$$

We also subtract (5.12g) from (5.12b) to obtain

$$-2\lambda c_\sigma\frac{\partial \phi_\sigma}{\partial \hat{\xi}} = L_\sigma(N_\sigma^+ - N_\sigma^-). \tag{5.15}$$

We then multiply the left hand side of (5.13) by the right hand side of (5.15), and the right hand side of (5.13) by the left hand side of (5.15), divide through by c_σ, and integrate with respect to $\hat{\xi}$, to get

$$\phi_\sigma = \phi_\sigma\big|_{\hat{\xi}=0} + \frac{1}{\lambda}\frac{N_\sigma^+ - N_\sigma^-}{N_\sigma^+ + N_\sigma^-}\log\left(\frac{c_\sigma}{c_\sigma\big|_{\hat{\xi}=0}}\right). \tag{5.16}$$

Equations (5.14) and (5.16) are exact expressions for c_σ and ϕ_σ and we can determine them after we have obtained asymptotic expressions for the remaining variables. Evaluating (5.14) and (5.16) on $\hat{\xi} = 1$ then gives

$$c_\sigma\big|_{\hat{\xi}=1} = c_\sigma\big|_{\hat{\xi}=0} - \frac{L_\sigma}{2}(N_\sigma^+ + N_\sigma^-), \tag{5.17a}$$

$$\phi_\sigma\big|_{\hat{\xi}=1} = \phi_\sigma\big|_{\hat{\xi}=0} + \frac{1}{\lambda}\frac{N_\sigma^+ - N_\sigma^-}{N_\sigma^+ + N_\sigma^-}\log\left(\frac{c_\sigma\big|_{\hat{\xi}=1}}{c_\sigma\big|_{\hat{\xi}=0}}\right). \tag{5.17b}$$

The problem is therefore reduced to an algebraic problem for $c_\sigma\big|_{\hat{\xi}=0}$, $c_\sigma\big|_{\hat{\xi}=1}$ $\phi_\sigma\big|_{\hat{\xi}=0}$, and $\phi_\sigma\big|_{\hat{\xi}=1}$.

5.5   ASYMPTOTIC REDUCTION OF PSEUDO STEADY-STATE SEI MODEL

In this section, we consider six limiting cases of (5.12) in which simple algebraic expressions for SEI growth can be derived. The first case corresponds to applying a large positive potential difference across the layer, $(\phi_{s,n}^* - \phi_{e,p}^*) \gg 0$, and the second to applying a large negative potential difference across the layer $(\phi_{s,n}^* - \phi_{e,n}^*) \ll 0$. In the third case, we take the timescale for the transport of lithium ion interstitials and electrons within the SEI to be short in comparison to the timescale

for the electrochemical reactions to occur. We refer to this third case as the reaction-limited case. In the fourth case, we take the timescale for the transport of lithium ion interstitials and electrons to be much longer than the timescale for the electrochemical reactions. We refer to this case as the diffusion-limited case. In the fifth case, we will assume that the timescales of electron transport through the SEI and the lithium intercalation reaction at the graphite–SEI surface to be longer than the other timescales in the model. We refer to this case as the electron diffusion and lithium intercalation reaction (graphite–SEI) limited case. In the sixth case, we will assume that the timescales of electron transport through the SEI and the lithium intercalation reaction at the SEI–electrolyte surface to be longer than the other timescales in the model. We refer to this case as the electron diffusion and lithium intercalation reaction (SEI–electrolyte) limited case. Consulting the parameter values in Tables 5.4 and 5.5 suggests that the diffusion-limited case is the limit that is most consistent with the reported parameter values. However, it should be noted that SEI parameters are notoriously difficult to obtain so these values are only estimates. Throughout this section, we assume that the pseudo steady-state approximation (5.12) holds.

5.5.1 *Large positive potential difference*

We first consider the case in which a large positive potential difference is applied across the layer. This corresponds to taking

$$\Phi = 1, \quad \lambda \to \infty.$$

We cannot simply make a regular asymptotic expansion in this limit. Therefore, we first consider balancing the model equations in order to inform our asymptotic expansions. We assume that the flux of lithium through the cell is $\mathcal{O}(1)$ and show this to be the case later. Given this, we balance (5.12d) by taking

$$\phi\big|_{\hat{\xi}=0} = 1 + \mathcal{O}\left(\frac{1}{\lambda}\right).$$

We also balance (5.12e) by assuming that the concentration on the SEI–electrolyte boundary is exponentially small

$$c_\sigma\big|_{\hat{\xi}=1} = \mathcal{O}(\exp(-\lambda\alpha)),$$

where we will determine α shortly in terms of the leading-order component of $\phi_\sigma\big|_{\hat{\xi}=1}$. By taking these balances in the lithium reactions, we then have from (5.12j) that

$$j_{\text{se}}^- = \mathcal{O}(\exp(-2\lambda\alpha)) \tag{5.18}$$

Informed by these balances, we make the following asymptotic expansions

$$c_\sigma\big|_{\hat{\xi}=1} = \exp(-\lambda\alpha)\left(c_\sigma^{(0)}\big|_{\hat{\xi}=1} + \frac{1}{\lambda}c_\sigma^{(1)}\big|_{\hat{\xi}=1} + \mathcal{O}\left(\frac{1}{\lambda^2}\right)\right)$$

$$N_\sigma^- = \exp(-2\lambda\alpha)\left(N_\sigma^{-(0)} + \frac{1}{\lambda}N_\sigma^{-(1)} + \mathcal{O}\left(\frac{1}{\lambda^2}\right)\right)$$

$$j_{n,\sigma}^- = \exp(-2\lambda\alpha)\left(j_{n,\sigma}^{-(0)} + \frac{1}{\lambda}j_{n,\sigma}^{-(1)} + \mathcal{O}\left(\frac{1}{\lambda^2}\right)\right)$$

with all other variables in the model expanded as

$$c_\sigma\big|_{\hat{\xi}=0} = c_\sigma^{(0)}\big|_{\hat{\xi}=0} + \frac{1}{\lambda}c_\sigma^{(1)}\big|_{\hat{\xi}=0} + \mathcal{O}\left(\frac{1}{\lambda^2}\right),$$

etc. Substituting these expansions into (5.12e), we can now see that

$$\alpha = \frac{\phi_\sigma^{(0)}\big|_{\hat{\xi}=1}}{2} \tag{5.19}$$

chosen such that the term

$$m_{\sigma,e}^+ c_\sigma^{(1)}\big|_{\hat{\xi}=1}\exp(-\lambda\alpha)\exp\left(\frac{\lambda\phi_\sigma^{(0)}\big|_{\hat{\xi}=1}}{2}\right)\exp\left(\frac{\phi_\sigma^{(1)}\big|_{\hat{\xi}=1}}{2}\right)$$

is $\mathcal{O}(1)$.

At $\mathcal{O}(1)$, (5.17b) is

$$\phi_\sigma^{(0)}\big|_{\hat{\xi}=1} = 1 - \alpha \tag{5.20}$$

where the factor of α on the right hand side arises from the term

$$\log\left(\frac{c_\sigma^{(0)}\big|_{\hat{\xi}=1}\exp(-\lambda\alpha)}{c_\sigma^{(0)}\big|_{\hat{\xi}=0}}\right) = \log\left(\frac{c_\sigma^{(0)}\big|_{\hat{\xi}=1}}{c_\sigma^{(0)}\big|_{\hat{\xi}=0}}\right) - \lambda\alpha.$$

Therefore, given (5.19) and (5.20), we obtain

$$\phi_\sigma^{(0)}\big|_{\hat{\xi}=1} = \frac{2}{3}, \quad \alpha = \frac{1}{3}. \tag{5.21}$$

At $\mathcal{O}(1)$, (5.17a) gives

$$N_\sigma^{+(0)} = \frac{2c_\sigma^{(0)}\big|_{\hat{\xi}=0}}{L_\sigma}. \tag{5.22}$$

The graphite–SEI electron transfer reaction (5.12i) at $\mathcal{O}(1)$ is

$$0 = -m_{n,\sigma}^-\exp\left(\frac{\phi_\sigma^{(1)}\big|_{\hat{\xi}=0}}{2}\right) + m_{\sigma,n}^- c_\sigma^{(0)}\big|_{\hat{\xi}=0}\exp\left(-\frac{\phi_\sigma^{(1)}\big|_{\hat{\xi}=0}}{2}\right) \tag{5.23}$$

and therefore we have

$$c_\sigma^{(0)}\big|_{\hat{\xi}=0} = \frac{m_{\text{n},\sigma}^-}{m_{\sigma,\text{n}}^-} \exp\left(\phi_\sigma^{(1)}\big|_{\hat{\xi}=0}\right). \tag{5.24}$$

Now at $\mathcal{O}(1)$ the graphite–SEI lithium intercalation reaction (5.12d) becomes

$$j_{\text{n},\sigma}^{+(0)} = m_{\text{n},\sigma}^+ \exp\left(-\frac{\phi_\sigma^{(1)}\big|_{\hat{\xi}=0}}{2}\right) - m_{\sigma,\text{n}}^+ c_\sigma^{(0)}\big|_{\hat{\xi}=0} \exp\left(\frac{\phi_\sigma^{(1)}\big|_{\hat{\xi}=0}}{2}\right). \tag{5.25}$$

Substituting (5.12c), (5.22), and (5.24) into (5.25), we obtain

$$\begin{aligned}
\frac{2c_\sigma^{(0)}\big|_{\hat{\xi}=0}}{L_\sigma} &= \frac{m_{\text{n},\sigma}^+ (m_{\text{n},\sigma}^-)^{1/2}}{(m_{\sigma,\text{n}}^-)^{1/2}}(c_\sigma^{(0)}\big|_{\hat{\xi}=0})^{-1/2} \\
&\quad - \frac{m_{\sigma,\text{n}}^+ (m_{\sigma,\text{n}}^-)^{1/2}}{(m_{\text{n},\sigma}^-)^{1/2}}(c_\sigma^{(0)}\big|_{\hat{\xi}=0})^{3/2}.
\end{aligned} \tag{5.26}$$

By making the transformation

$$c_\sigma^{(0)}\big|_{\hat{\xi}=0} = \frac{4m_{\text{n},\sigma}^-}{L_\sigma^2 (m_{\sigma,\text{n}}^+)^2 m_{\sigma,\text{n}}^-}\hat{c}^2, \tag{5.27}$$

we get an algebraic equation for $\hat{c}$,

$$\hat{c}^4 + \hat{c}^3 = a \tag{5.28}$$

where

$$a = \frac{L_\sigma^4 m_{\text{n},\sigma}^+ (m_{\sigma,\text{n}}^+)^3 m_{\sigma,\text{n}}^-}{16 m_{\text{n},\sigma}^-}. \tag{5.29}$$

Algebraic expressions for the four solutions to (5.28) can be obtained using the formula for the roots of a quartic polynomial. However we do not present these expressions here because they are long and do not offer insight. Two of the solutions have an imaginary component for positive real values of a and so we discard these as non-physical. The third solution is negative, which corresponds to a nonphysical negative values of $(c_\sigma^{(0)})^{1/2}$ in (5.26). The remaining physical solution is presented in Figure 5.2.

To determine $\phi_\sigma^{(1)}\big|_{\hat{\xi}=1}$ and $c_\sigma^{(0)}\big|_{\hat{\xi}=1}$, we consider the $\mathcal{O}(1)$ component of the SEI–electrolyte lithium reaction (5.12e), which is given by

$$j_{\sigma,\text{e}}^{+(0)} = m_{\sigma,\text{e}}^+ c_\sigma^{(0)}\big|_{\hat{\xi}=1} \exp\left(\frac{\phi_\sigma^{(1)}\big|_{\hat{\xi}=1}}{2}\right). \tag{5.30}$$
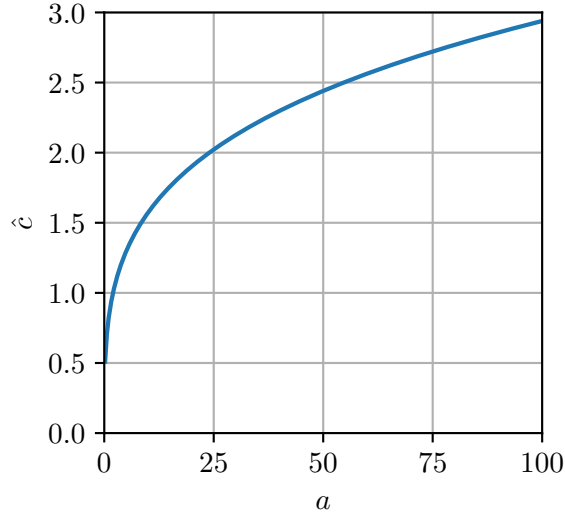
Figure 5.2: The positive real solution of (5.28) as a function of a.

Then using (5.22), we have

$$c_\sigma^{(0)}\big|_{\hat{\xi}=1} = \frac{2c_\sigma^{(0)}\big|_{\hat{\xi}=0}}{m_{\sigma,e}^+ L_\sigma} \exp\left(-\frac{\phi_\sigma^{(1)}\big|_{\hat{\xi}=1}}{2}\right). \tag{5.31}$$

Now, (5.17b) at $\mathcal{O}(1/\lambda)$ is

$$\phi_\sigma^{(1)}\big|_{\hat{\xi}=1} = \phi_\sigma^{(1)}\big|_{\hat{\xi}=0} + \log\left(\frac{c_\sigma^{(0)}\big|_{\hat{\xi}=1}}{c_\sigma^{(0)}\big|_{\hat{\xi}=0}}\right). \tag{5.32}$$

Substituting (5.31) into (5.32) yields

$$\phi_\sigma^{(1)}\big|_{\hat{\xi}=1} = \frac{2}{3}\phi_\sigma^{(1)}\big|_{\hat{\xi}=0} + \frac{2}{3}\log\left(\frac{2}{m_{\sigma,e}^+ L_\sigma}\right). \tag{5.33}$$

Since we now know both $c_\sigma^{(0)}\big|_{\hat{\xi}=1}$ and $\phi_\sigma^{(1)}\big|_{\hat{\xi}=1}$ in terms of $\hat{c}$, we can calculate the SEI growth reaction rate, which is determined by the $\mathcal{O}(\exp(-2\lambda\alpha))$ component of (5.12j) as

$$j_{\sigma,e}^{-(0)} = -m_{\sigma,e}^- c_\sigma^{(0)}\big|_{\hat{\xi}=1}, \tag{5.34}$$

which upon substitution of the previous calculated terms is

$$j_{\sigma,e}^{-(0)} = -m_{\sigma,e}^- \left(\frac{2c_\sigma^{(0)}\big|_{\hat{\xi}=0}}{m_{\sigma,e}^+ L_\sigma}\right)^{2/3} \left(\frac{m_{n,\sigma}^-}{m_{\sigma,n}^-}\right)^{1/3} \tag{5.35}$$

Finally, we can now determine the leading-order contributions to both ϕ_σ and c_σ by using (5.14) and (5.16). We have

$$c_\sigma = \frac{L_\sigma N_\sigma^{+(0)}}{2}(1 - \xi) + \mathcal{O}\left(\frac{1}{\lambda}\right),$$ (5.36)

$$\phi_\sigma = 1 + \frac{\phi_\sigma^{(1)}\big|_{\hat{\xi}=1}}{\lambda}$$
$$+ \frac{1}{\lambda}\log\left(\frac{\frac{L_\sigma N_\sigma^{+(0)}}{2}(1 - \xi) + c_\sigma^{(0)}\big|_{\hat{\xi}=1}\exp\left(-\frac{\lambda}{3}\right)}{c_\sigma^{(0)}\big|_{\hat{\xi}=0}}\right)$$ (5.37)
$$+ \mathcal{O}\left(\frac{1}{\lambda}\right),$$

where we have included the exponentially small boundary concentration within the log term to prevent blow up of ϕ_σ at $\hat{\xi} = 1$. Away from $\hat{\xi} = 1$, this term is insignificant and so we can add it whilst retaining $\mathcal{O}(1/\lambda)$ accuracy. To demonstrate that this addition also retains $\mathcal{O}(1/\lambda)$ in a small boundary layer of size $\mathcal{O}\left(\exp(-\lambda/3)\right)$, we consider

$$\tilde{\xi} := (1 - \hat{\xi})\exp\left(\frac{\lambda}{3}\right), \quad \tilde{\xi} = \mathcal{O}(1).$$

We then have that

$$\frac{1}{\lambda}\log\left(\frac{\left(\frac{L_\sigma N_\sigma^{+(0)}}{2}\tilde{\xi} + c_\sigma^{(0)}\big|_{\hat{\xi}=1}\right)\exp\left(-\frac{\lambda}{3}\right)}{c_\sigma^{(0)}\big|_{\hat{\xi}=0}}\right) = -\frac{1}{3} + \mathcal{O}\left(\frac{1}{\lambda}\right).$$

Therefore, we can see that within the boundary layer we obtain the same solution up to $\mathcal{O}(1/\lambda)$ regardless of whether we append the value on the right boundary.

In Figure 5.3, we compare the asymptotic and numerical solutions for the fluxes and boundary values for a range of values of λ with all other parameters taken to be $\mathcal{O}(1)$ values. We observe that the asymptotic solution excellently recovers the numerical solution for sufficiently large values of λ. In Figures 5.3 (b), (d), and (f) we plot the absolute errors of each of the solutions alongside a dotted line to indicate the scalings of the errors. From this we observe that the errors in N_σ^+, $c_\sigma\big|_{\hat{\xi}=0}$, $\phi_\sigma\big|_{\hat{\xi}=0}$, and $\phi_\sigma\big|_{\hat{\xi}=1}$ are $\mathcal{O}(\exp(-\lambda/3))$, whilst the errors in N_σ^- and $c_\sigma\big|_{\hat{\xi}=1}$ are $\mathcal{O}(\exp(-\lambda/3)/\lambda)$. This is significantly better than the $\mathcal{O}(1/\lambda)$ errors that our asymptotics predicts for some variables and suggests that many of the higher-order terms in the expansion are zero (for this particular set of parameters). For completeness, we also compare the asymptotic and numerical solutions for the concentration and potential within the SEI in Figure 5.4. We again observe excellent agreement in the two solutions, with the measured errors being of size 10^{-7}–10^{-6} and the predicted asymptotic error being $\exp(-\lambda/3) \approx 10^{-6}$.
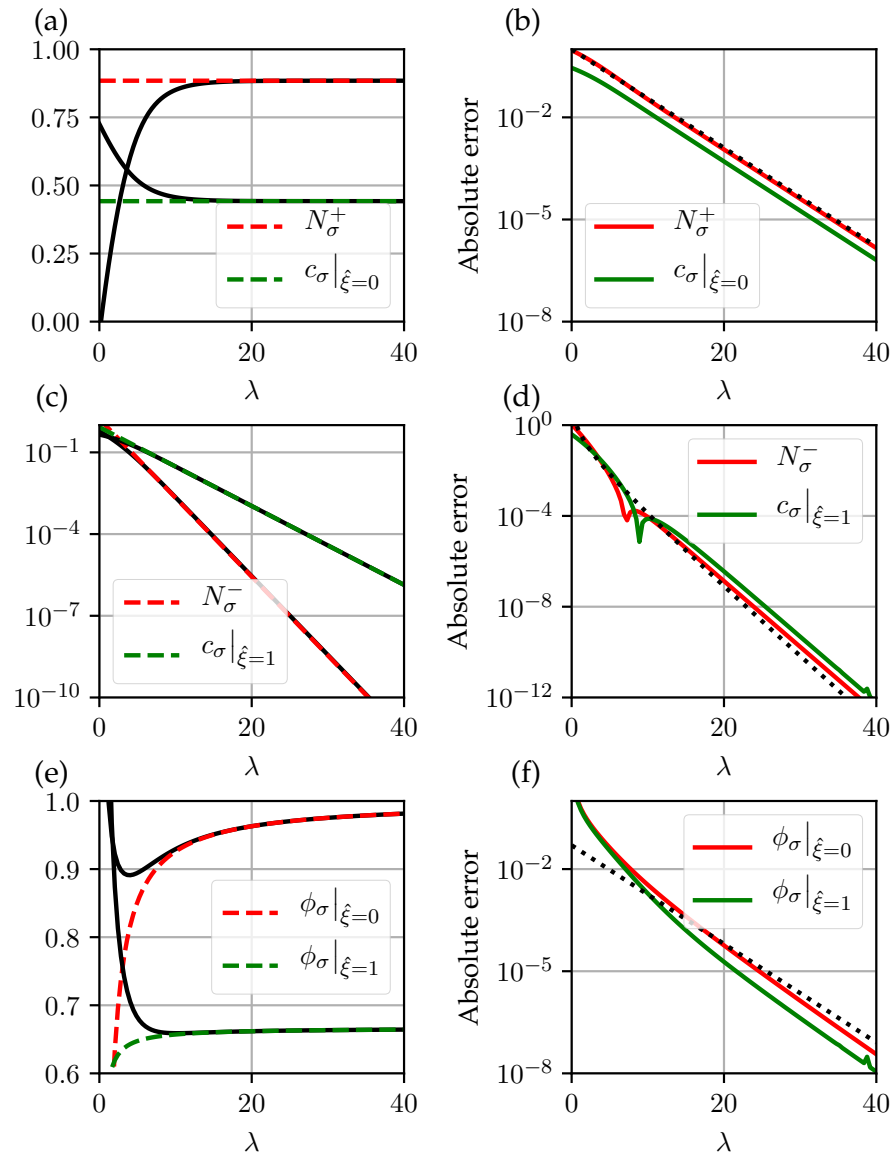
Figure 5.3: Comparison of asymptotic (from §5.5.1) (dashed in (a), (c), (e)) and numerical (5.12) (solid in (a), (c), and (e)) solutions where all parameters except λ are taken to be $\mathcal{O}(1)$: (a) predicted values of lithium flux and graphite–SEI boundary conentration; (b) absolute errors with dotted line $\exp(-\lambda/3)$ for reference; (c) predicted values of electron flux and SEI–electrolyte boundary concentration; (d) absolute errors with dotted line $\exp(-\lambda/3)/\lambda$ for reference; (e) predicted boundary potentials; (f) absolute errors with dotted line $(5 \times 10^{-2})\exp(-\lambda/3)$ for reference.
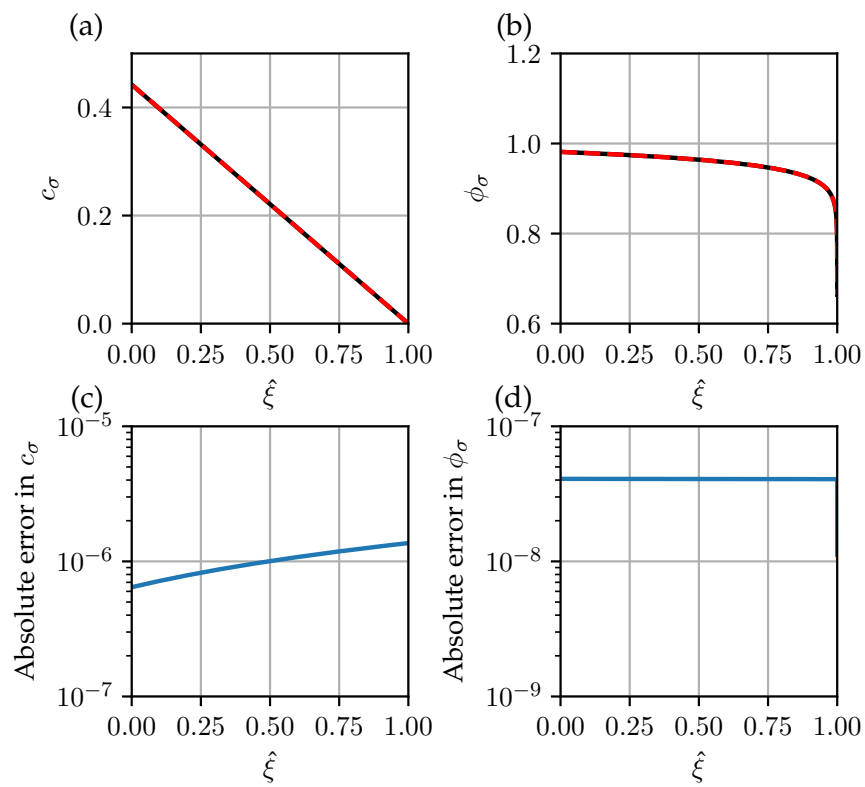
Figure 5.4: Comparison of asymptotic (from §5.5.1) and numerical (5.12) concentrations and potentials within the SEI for $\lambda = 40$. Note that $\exp(-\lambda/3) \approx 10^{-6}$.

5.5.2 *Large negative potential difference*

We now consider the case of a large applied negative potential difference, $(\phi_{s,n}^* - \phi_{e,n}^*) \ll 0$. This corresponds to taking

$$\Phi = -1, \quad \lambda \to \infty.$$

In this case, we take the lithium-ion and electron fluxes to be $\mathcal{O}(\lambda)$. We then create an $\mathcal{O}(\lambda)$ balance in (5.12d) by taking

$$\phi_\sigma\big|_{\hat{\xi}=0} = -1 + \frac{2\log(\lambda)}{\lambda} + \mathcal{O}\left(\frac{1}{\lambda}\right).$$

Similarly, we balance (5.12j) by taking

$$\phi_\sigma\big|_{\hat{\xi}=1} = -\frac{2\log(\lambda)}{\lambda} + \mathcal{O}\left(\frac{1}{\lambda}\right).$$

By introducing these $\log(\lambda)/\lambda$ terms in the expansions of the boundary potentials, we must then balance (5.17b) at $\mathcal{O}(\log(\lambda)/\lambda)$, which informs us to make the following asymptotic expansions

$$N_\sigma^+ = \lambda \sum_{i=0}^{\infty} \sum_{j=0}^{i} \frac{\log(\lambda)^j}{\lambda^i} N_\sigma^{+(i,j)},$$

$$N_\sigma^- = \lambda \sum_{i=0}^{\infty} \sum_{j=0}^{i} \frac{\log(\lambda)^j}{\lambda^i} N_\sigma^{-(i,j)},$$

$$\phi_\sigma\big|_{\hat{\xi}=0} = -1 + \frac{2\log(\lambda)}{\lambda} + \frac{\phi_\sigma^{(1,0)}\big|_{\hat{\xi}=0}}{\lambda} + \sum_{i=2}^{\infty} \sum_{j=0}^{i} \frac{\log(\lambda)^j}{\lambda^i} \phi_\sigma^{(i,j)}\big|_{\hat{\xi}=0},$$

$$\phi_\sigma\big|_{\hat{\xi}=1} = -\frac{2\log(\lambda)}{\lambda} + \frac{\phi_\sigma^{(1,0)}\big|_{\hat{\xi}=1}}{\lambda} + \sum_{i=2}^{\infty} \sum_{j=0}^{i} \frac{\log(\lambda)^j}{\lambda^i} \phi_\sigma^{(i,j)}\big|_{\hat{\xi}=1},$$

$$c_\sigma\big|_{\hat{\xi}=0} = \sum_{i=0}^{\infty} \sum_{j=0}^{i} \frac{\log(\lambda)^j}{\lambda^i} c_\sigma^{(i,j)}\big|_{\hat{\xi}=0},$$

$$c_\sigma\big|_{\hat{\xi}=1} = \sum_{i=0}^{\infty} \sum_{j=0}^{i} \frac{\log(\lambda)^j}{\lambda^i} c_\sigma^{(i,j)}\big|_{\hat{\xi}=1}.$$

Here the order of magnitude of the terms (from large to small) is

$$\lambda, \log(\lambda), \frac{\log(\lambda)}{\lambda}, \frac{1}{\lambda}, \frac{\log(\lambda)^2}{\lambda^2}, \frac{\log(\lambda)}{\lambda^2}, \frac{1}{\lambda^2}, \cdots$$

After making these expansions, (5.17a) at $\mathcal{O}(\lambda)$, $\mathcal{O}(\log(\lambda))$, and $\mathcal{O}(1)$ gives

$$N_\sigma^{-(0,0)} = -N_\sigma^{+(0,0)} \tag{5.38a}$$

$$N_\sigma^{-(0,1)} = -N_\sigma^{+(0,1)} \tag{5.38b}$$

$$c_\sigma^{(0,0)}\big|_{\hat{\xi}=1} = c_\sigma^{(0,0)}\big|_{\hat{\xi}=0} - \frac{L_\sigma}{2}\left(N_\sigma^{+(1,0)} + N_\sigma^{-(1,0)}\right) \tag{5.38c}$$

and the electrochemical reactions (5.12d), (5.12e), (5.12i), and (5.12j) at $\mathcal{O}(\lambda)$ give

$$j_{\mathrm{n},\sigma}^{+(0,0)} = -m_{\sigma,\mathrm{n}}^+ c_\sigma^{(0,0)}\big|_{\hat{\xi}=0} \exp\left(\frac{\phi_\sigma^{(1,0)}\big|_{\hat{\xi}=0}}{2}\right) \tag{5.39a}$$

$$j_{\sigma,\mathrm{e}}^{+(0,0)} = -m_{\mathrm{e},\sigma}^+ \exp\left(-\frac{\phi_\sigma^{(1,0)}\big|_{\hat{\xi}=1}}{2}\right) \tag{5.39b}$$

$$j_{\mathrm{n},\sigma}^{-(0,0)} = -m_{\mathrm{n},\sigma}^+ \exp\left(\frac{\phi_\sigma^{(1,0)}\big|_{\hat{\xi}=0}}{2}\right) \tag{5.39c}$$

$$j_{\sigma,\mathrm{e}}^{-(0,0)} = -m_{\sigma,\mathrm{e}}^- c_\sigma^{(0,0)}\big|_{\hat{\xi}=1} \exp\left(-\frac{\phi_\sigma^{(1,0)}\big|_{\hat{\xi}=1}}{2}\right). \tag{5.39d}$$

Then using (5.12c), (5.12h), and (5.38a) we can use (5.39a) with (5.39c) and (5.39b) with (5.39d) to obtain

$$c_\sigma^{(0,0)}\big|_{\hat{\xi}=0} = \frac{m_{\mathrm{n},\sigma}^-}{m_{\sigma,\mathrm{n}}^+}, \quad c_\sigma^{(0,0)}\big|_{\hat{\xi}=1} = \frac{m_{\mathrm{e},\sigma}^+}{m_{\sigma,\mathrm{e}}^-}. \tag{5.40}$$

Therefore (5.38c) gives

$$N_\sigma^{+(1,0)} + N_\sigma^{-(0,0)} = \frac{2}{L_\sigma}\left(\frac{m_{\mathrm{n},\sigma}^-}{m_{\sigma,\mathrm{n}}^+} - \frac{m_{\mathrm{e},\sigma}^+}{m_{\sigma,\mathrm{e}}^-}\right). \tag{5.41}$$

Equation (5.21) at $\mathcal{O}(1)$ gives

$$0 = -1 + \frac{2N_\sigma^{+(0,0)}}{N_\sigma^{(1,0)} + N_\sigma^{-(1,0)}} \log\left(\frac{c_\sigma^{(0,0)}\big|_{\hat{\xi}=1}}{c_\sigma^{(0,0)}\big|_{\hat{\xi}=0}}\right). \tag{5.42}$$

Substituting (5.40) and (5.41) into (5.42) then gives

$$N_\sigma^{+(0,0)} = \frac{m_{\mathrm{n},\sigma}^- m_{\sigma,\mathrm{e}}^- - m_{\mathrm{e},\sigma}^+ m_{\sigma,\mathrm{n}}^+}{L_\sigma m_{\sigma,\mathrm{e}}^- m_{\sigma,\mathrm{n}}^+ \log\left(\frac{m_{\mathrm{e},\sigma}^+ m_{\sigma,\mathrm{n}}^+}{m_{\mathrm{n},\sigma}^- m_{\sigma,\mathrm{e}}^-}\right)}. \tag{5.43}$$

We now use (5.38a), (5.39), and (5.43), to obtain

$$\phi_\sigma^{(1,0)}\big|_{\hat{\xi}=0} = 2\log\left(\frac{m_{\text{e},\sigma}^+ m_{\sigma,\text{n}}^+ - m_{\text{n},\sigma}^- m_{\sigma,\text{e}}^-}{L_\sigma m_{\text{n},\sigma}^- m_{\sigma,\text{e}}^- m_{\sigma,\text{n}}^+ \log\left(\frac{m_{\text{e},\sigma}^+ m_{\sigma,\text{n}}^+}{m_{\text{n},\sigma}^- m_{\sigma,\text{e}}^-}\right)}\right), \qquad (5.44\text{a})$$

$$\phi_\sigma^{(1,0)}\big|_{\hat{\xi}=1} = -2\log\left(\frac{m_{\text{e},\sigma}^+ m_{\sigma,\text{n}}^+ - m_{\text{n},\sigma}^- m_{\sigma,\text{e}}^-}{L_\sigma m_{\text{e},\sigma}^+ m_{\sigma,\text{e}}^- m_{\sigma,\text{n}}^+ \log\left(\frac{m_{\text{e},\sigma}^+ m_{\sigma,\text{n}}^+}{m_{\text{n},\sigma}^- m_{\sigma,\text{e}}^-}\right)}\right), \qquad (5.44\text{b})$$

which concludes the leading-order solution. We now continue to the next order in the expansion to increase the solution accuracy. Firstly, (5.17a) at $\mathcal{O}(\log(\lambda)^2/\lambda)$, $\mathcal{O}(\log(\lambda)/\lambda)$, and $\mathcal{O}(1/\lambda)$ gives

$$N_\sigma^{-(2,2)} = -N_\sigma^{+(2,2)}, \qquad (5.45\text{a})$$

$$c_\sigma^{(1,1)}\big|_{\hat{\xi}=1} = c_\sigma^{(1,1)}\big|_{\hat{\xi}=0} - \frac{L_\sigma}{2}\left(N_\sigma^{+(2,1)} + N_\sigma^{-(2,1)}\right), \qquad (5.45\text{b})$$

$$c_\sigma^{(1,0)}\big|_{\hat{\xi}=1} = c_\sigma^{(1,0)}\big|_{\hat{\xi}=0} - \frac{L_\sigma}{2}\left(N_\sigma^{+(2,0)} + N_\sigma^{-(2,0)}\right). \qquad (5.45\text{c})$$

At $\mathcal{O}(\log(\lambda)^2)$ the electrochemical reactions (5.12d), (5.12e), (5.12i), and (5.12j) give

$$0 = -\frac{1}{2}m_{\sigma,\text{n}}^+ c_\sigma^{(0,0)}\big|_{\hat{\xi}=0} \exp\left(\frac{\phi_\sigma^{(1,0)}\big|_{\hat{\xi}=0}}{2}\right)\phi_\sigma^{(2,2)}\big|_{\hat{\xi}=0}, \qquad (5.46\text{a})$$

$$0 = \frac{1}{2}m_{\text{e},\sigma}^+ \exp\left(\frac{\phi_\sigma^{(1,0)}\big|_{\hat{\xi}=1}}{2}\right)\phi_\sigma^{(2,2)}\big|_{\hat{\xi}=1}, \qquad (5.46\text{b})$$

$$0 = \frac{1}{2}m_{\text{n},\sigma}^- \exp\left(-\frac{\phi_\sigma^{(1,0)}\big|_{\hat{\xi}=0}}{2}\right)\phi_\sigma^{(2,2)}\big|_{\hat{\xi}=0}, \qquad (5.46\text{c})$$

$$0 = -\frac{1}{2}m_{\sigma,\text{e}}^- c_\sigma^{(0,0)}\big|_{\hat{\xi}=1} \exp\left(-\frac{\phi_\sigma^{(1,0)}\big|_{\hat{\xi}=1}}{2}\right)\phi_\sigma^{(2,2)}\big|_{\hat{\xi}=1}, \qquad (5.46\text{d})$$

and therefore we have

$$\phi_\sigma^{(2,2)}\big|_{\hat{\xi}=0} = 0, \quad \phi_\sigma^{(2,2)}\big|_{\hat{\xi}=1} = 0. \qquad (5.47)$$

Now at $\mathcal{O}(\log(\lambda))$ the electrochemical reactions (5.12d), (5.12e), (5.12i), and (5.12j) give

$$j_{\mathrm{n},\sigma}^{+(1,1)} = -\frac{1}{2}m_{\sigma,\mathrm{n}}^{+}\left(2c_{\sigma}^{(1,1)}\big|_{\hat{\xi}=0} + c_{\sigma}^{(0,0)}\big|_{\hat{\xi}=0}\phi_{\sigma}^{(2,1)}\big|_{\hat{\xi}=0}\right)$$
$$\times \exp\left(\frac{\phi_{\sigma}^{(1,0)}\big|_{\hat{\xi}=0}}{2}\right), \tag{5.48a}$$

$$j_{\sigma,\mathrm{e}}^{+(1,1)} = \frac{1}{2}m_{\mathrm{e},\sigma}^{+}\phi_{\sigma}^{(2,1)}\big|_{\hat{\xi}=1}\exp\left(-\frac{\phi_{\sigma}^{(1,0)}\big|_{\hat{\xi}=1}}{2}\right), \tag{5.48b}$$

$$j_{\mathrm{n},\sigma}^{-(1,1)} = -\frac{1}{2}m_{\mathrm{n},\sigma}^{-}\phi_{\sigma}^{(2,1)}\big|_{\hat{\xi}=0}\exp\left(\frac{\phi_{\sigma}^{(1,0)}\big|_{\hat{\xi}=0}}{2}\right), \tag{5.48c}$$

$$j_{\sigma,\mathrm{e}}^{-(1,1)} = -\frac{1}{2}m_{\sigma,\mathrm{e}}^{+}\left(2c_{\sigma}^{(1,1)}\big|_{\hat{\xi}=1} - c_{\sigma}^{(0,0)}\big|_{\hat{\xi}=1}\phi_{\sigma}^{(2,1)}\big|_{\hat{\xi}=1}\right)$$
$$\times \exp\left(\frac{\phi_{\sigma}^{(1,0)}\big|_{\hat{\xi}=1}}{2}\right). \tag{5.48d}$$

Substituting (5.12c), (5.12h), (5.38b), (5.40), and (5.44) into (5.48a) and (5.48c) gives

$$c_{\sigma}^{(1,1)} = 0. \tag{5.49}$$

We can then substitute (5.12c), (5.12h), (5.38b), (5.40), (5.44), and (5.49) into (5.48a) and (5.48b) to obtain

$$\phi_{\sigma}^{(2,1)}\big|_{\hat{\xi}=1} = \phi_{\sigma}^{(2,1)}\big|_{\hat{\xi}=0}. \tag{5.50}$$

Then substituting (5.12c), (5.12h), (5.38b), (5.40), (5.44), and (5.50) into (5.48b) and (5.48d), we obtain

$$c_{\sigma}^{(1,1)}\big|_{\hat{\xi}=1} = 0. \tag{5.51}$$

It now just remains to determine, $\phi_{\sigma}^{(2,1)}\big|_{\hat{\xi}=0}$, and $N_{\sigma}^{+(1,1)}$. Upon substitution of our previously derived expressions into (5.21) at $\mathcal{O}(\log(\lambda)/\lambda)$, we obtain

$$0 = 4 + \frac{\phi_{\sigma}^{(2,1)}\big|_{\hat{\xi}=0}}{2}. \tag{5.52}$$

Therefore, we have

$$\phi_{\sigma}^{(2,1)}\big|_{\hat{\xi}=0} = -8, \quad \phi_{\sigma}^{(2,1)}\big|_{\hat{\xi}=1} = 8. \tag{5.53}$$

Finally, substituting (5.44) and (5.53) into (5.48b), we get

$$N_{\sigma}^{+(1,1)} = -4N_{\sigma}^{(0,0)}, \tag{5.54}$$

which concludes our first-order analysis.

In summary, our combined leading- and first-order solution is

$$c_\sigma\big|_{\hat{\xi}=0} = \frac{m_{\mathrm{n},\sigma}^-}{m_{\sigma,\mathrm{n}}^+} + \mathcal{O}\left(\frac{1}{\lambda}\right), \tag{5.55a}$$

$$c_\sigma\big|_{\hat{\xi}=1} = \frac{m_{\mathrm{e},\sigma}^+}{m_{\sigma,\mathrm{e}}^-} + \mathcal{O}\left(\frac{1}{\lambda}\right), \tag{5.55b}$$

$$N_\sigma^+ = (\lambda - 4\log(\lambda)) \frac{m_{\mathrm{n},\sigma}^- m_{\sigma,\mathrm{e}}^- - m_{\mathrm{e},\sigma}^+ m_{\sigma,\mathrm{n}}^+}{L_\sigma m_{\sigma,\mathrm{e}}^- m_{\sigma,\mathrm{n}}^+ \log\left(\frac{m_{\mathrm{e},\sigma}^+ m_{\sigma,\mathrm{n}}^+}{m_{\mathrm{n},\sigma}^- m_{\sigma,\mathrm{e}}^-}\right)}$$
$$+ \mathcal{O}(1), \tag{5.55c}$$

$$N_\sigma^- = - (\lambda - 4\log(\lambda)) \frac{m_{\mathrm{n},\sigma}^- m_{\sigma,\mathrm{e}}^- - m_{\mathrm{e},\sigma}^+ m_{\sigma,\mathrm{n}}^+}{L_\sigma m_{\sigma,\mathrm{e}}^- m_{\sigma,\mathrm{n}}^+ \log\left(\frac{m_{\mathrm{e},\sigma}^+ m_{\sigma,\mathrm{n}}^+}{m_{\mathrm{n},\sigma}^- m_{\sigma,\mathrm{e}}^-}\right)}$$
$$+ \mathcal{O}(1), \tag{5.55d}$$

$$\phi_\sigma\big|_{\hat{\xi}=0} = -1 + \frac{2\log(\lambda)}{\lambda}$$
$$+ \frac{2}{\lambda} \log\left(\frac{m_{\mathrm{e},\sigma}^+ m_{\sigma,\mathrm{n}}^+ - m_{\mathrm{n},\sigma}^- m_{\sigma,\mathrm{e}}^-}{L_\sigma m_{\mathrm{n},\sigma}^- m_{\sigma,\mathrm{e}}^- m_{\sigma,\mathrm{n}}^+ \log\left(\frac{m_{\mathrm{e},\sigma}^+ m_{\sigma,\mathrm{n}}^+}{m_{\mathrm{n},\sigma}^- m_{\sigma,\mathrm{e}}^-}\right)}\right)$$
$$- \frac{8\log(\lambda)}{\lambda^2} + \mathcal{O}\left(\frac{1}{\lambda^2}\right), \tag{5.55e}$$

$$\phi_\sigma\big|_{\hat{\xi}=1} = -\frac{2\log(\lambda)}{\lambda}$$
$$- \frac{2}{\lambda} \log\left(\frac{m_{\mathrm{e},\sigma}^+ m_{\sigma,\mathrm{n}}^+ - m_{\mathrm{n},\sigma}^- m_{\sigma,\mathrm{e}}^-}{L_\sigma m_{\mathrm{e},\sigma}^+ m_{\sigma,\mathrm{e}}^- m_{\sigma,\mathrm{n}}^+ \log\left(\frac{m_{\mathrm{e},\sigma}^+ m_{\sigma,\mathrm{n}}^+}{m_{\mathrm{n},\sigma}^- m_{\sigma,\mathrm{e}}^-}\right)}\right)$$
$$+ \frac{8\log(\lambda)}{\lambda^2} + \mathcal{O}\left(\frac{1}{\lambda^2}\right). \tag{5.55f}$$

We also write the expressions for the through-SEI concentration (5.13) and potential (5.15). For the through SEI concentration, we have

$$c_\sigma = c_\sigma\big|_{\hat{\xi}=0} + \left(c_\sigma\big|_{\hat{\xi}=1} - c_\sigma\big|_{\hat{\xi}=0}\right)\hat{\xi} + \mathcal{O}\left(\frac{1}{\lambda}\right), \tag{5.55g}$$

and for the through-SEI potential we have

$$\phi_\sigma = \phi_\sigma\big|_{\hat{\xi}=0} + \frac{2}{\lambda L_\sigma} \frac{N_\sigma^+ - N_\sigma^-}{c_\sigma\big|_{\hat{\xi}=0} - c_\sigma\big|_{\hat{\xi}=1}} \log\left(\frac{c_\sigma\big|_{\hat{\xi}=1}}{c_\sigma\big|_{\hat{\xi}=0}}\right) + \mathcal{O}\left(\frac{1}{\lambda}\right). \tag{5.55h}$$

We now compare our asymptotic solution (5.55) with the numerical solution to (5.12). In Figure 5.5, we compare the solutions for the fluxes and boundary concentrations and potentials for a range of values of λ and $\Phi = -1$. We observe excellent agreement between the numerical and asymptotic solutions for sufficiently high values of λ. In Figure 5.5
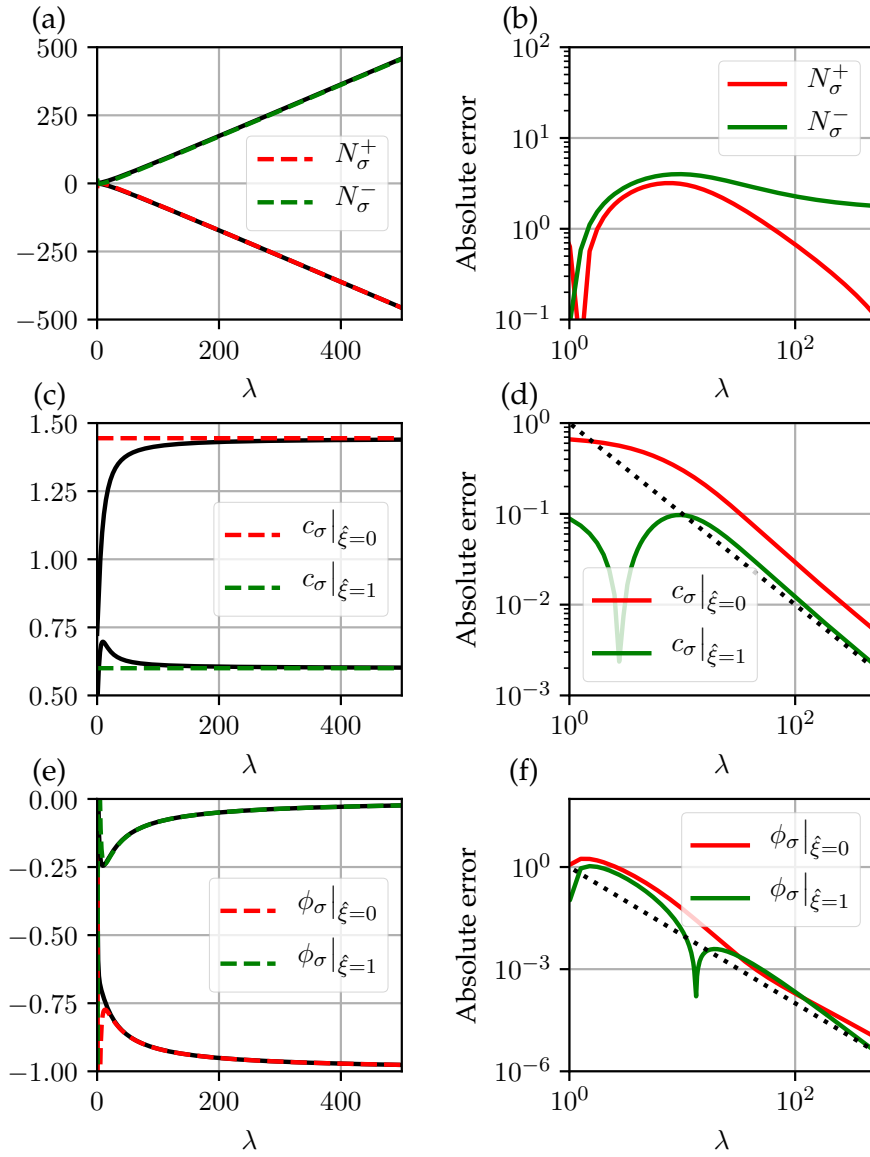
Figure 5.5: Comparison of asymptotic (§5.5.2) (dashed in (a), (c), (e)) and numerical (5.12) (solid in (a), (c), (e)) solution where all parameter except λ are taken to be $\mathcal{O}(1)$: (a) predicted values of lithium and electron fluxes; (b) absolute errors in fluxes; (c) predicted values of boundary concentrations; (d) absolute errors in concentrations with dotted line $1/\lambda$ for reference; (e) predicted values of boundary potentials; (f) absolute errors in potentials with dotted line $1/\lambda^2$ for reference.

(b), (d), and (f), we observe that the asymptotic errors for the fluxes are at most $\mathcal{O}(1)$, the asymptotic error in the boundary concentrations is $\mathcal{O}(1/\lambda)$, and the asymptotic error in the boundary potentials is $\mathcal{O}(1/\lambda^2)$ as predicted in (5.55). We also see better performance in the prediction of N_σ^+, which suggests that the $\mathcal{O}(1)$ lithium flux may be zero for this particular parameter set (however we have not confirmed this). For completeness, we also present the through-SEI concentration and potential profiles in Figure 5.6. Here, we again observe good agreement between the asymptotic and numerical solutions with errors consistent with the asymptotic $\mathcal{O}(1/\lambda)$ error.
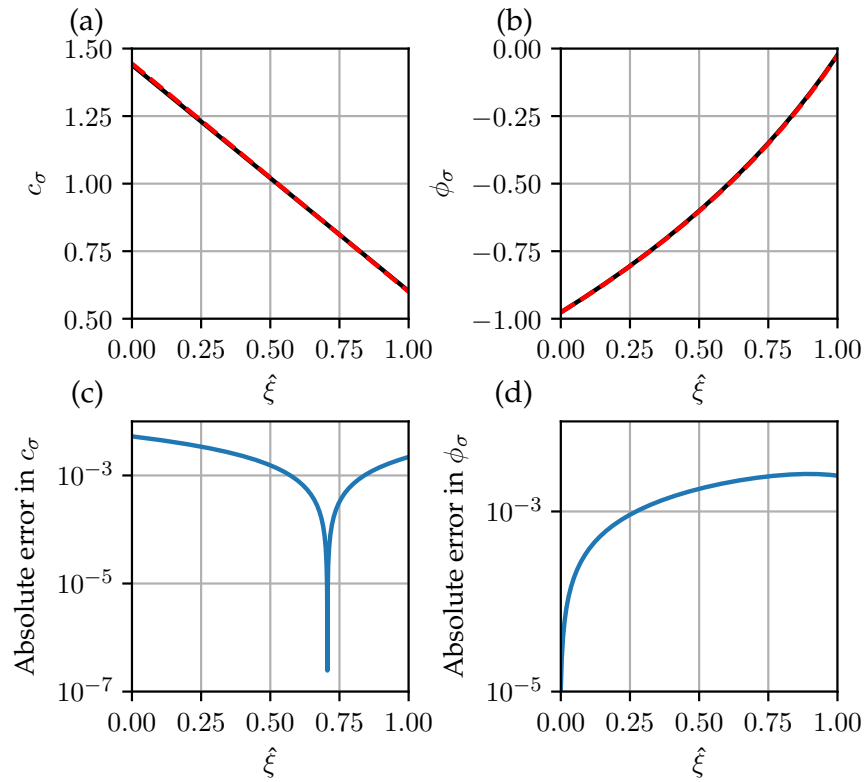

Figure 5.6: Comparison of asymptotic (§5.5.2) and numerical (5.12) concentrations and potentials within the SEI for $\lambda = 500$. Note that $1/500 \approx 10^{-3}$

5.5.3 *Reaction-limited growth*

In this section, we consider the case of reaction-limited growth. To do this, we introduce a parameter m such that

$$m_{n,\sigma}^+ = m\hat{m}_{n,\sigma}^+, \quad m_{\sigma,n}^+ = m\hat{m}_{\sigma,n}^+, \quad m_{\sigma,e}^+ = m\hat{m}_{\sigma,e}^+,$$
$$m_{e,\sigma}^+ = m\hat{m}_{e,\sigma}^+, \quad m_{n,\sigma}^- = m\hat{m}_{n,\sigma}^+, \quad m_{\sigma,n}^- = m\hat{m}_{\sigma,n}^+,$$
$$m_{\sigma,e}^- = m\hat{m}_{\sigma,e}^+,$$

with each of the 'hat' terms being $\mathcal{O}(1)$. We also assume that all other parameters in the problem are $\mathcal{O}(1)$. We make regular asymptotic expansions of the form

$$N_\sigma^+ = N_\sigma^{+(0)} + mN_\sigma^{+(1)} + \ldots$$

in each of the variables and then take the limit $m \to 0$.

At leading order in m, the electrochemical reactions (5.12d), (5.12e), (5.12i), and (5.12j) give

$$j_{n,\sigma}^{+(0)} = j_{\sigma,e}^{+(0)} = j_{n,\sigma}^{-(0)} = j_{\sigma,e}^{-(0)} = 0 \tag{5.56}$$

and therefore we also have

$$N_\sigma^{+(0)} = N_\sigma^{-(0)} = 0. \tag{5.57}$$

Then at leading order in m, (5.17a) and (5.17b) give

$$c_\sigma^{(0)}\big|_{\hat{\xi}=1} = c_\sigma^{(0)}\big|_{\hat{\xi}=1}, \quad \phi_\sigma^{(0)}\big|_{\hat{\xi}=1} = \phi_\sigma^{(0)}\big|_{\hat{\xi}=0}. \tag{5.58}$$

At $\mathcal{O}(m)$, the electrochemical reactions (5.12d), (5.12e), (5.12i), and (5.12j) give

$$j_{n,\sigma}^{+(1)} = \hat{m}_{n,\sigma}^+ \exp\left(\frac{\lambda}{2}(\Phi - \phi_\sigma^{(0)}\big|_{\hat{\xi}=0})\right)$$
$$- \hat{m}_{\sigma,n}^+ c_\sigma^{(0)}\big|_{\hat{\xi}=0} \exp\left(-\frac{\lambda}{2}(\Phi - \phi_\sigma^{(0)}\big|_{\hat{\xi}=0})\right), \tag{5.59a}$$

$$j_{\sigma,e}^{+(1)} = \hat{m}_{\sigma,e}^+ c_\sigma^{(0)}\big|_{\hat{\xi}=1} \exp\left(\frac{\lambda\phi_\sigma^{(0)}\big|_{\hat{\xi}=1}}{2}\right)$$
$$- \hat{m}_{e,\sigma}^+ \exp\left(-\frac{\lambda\phi_\sigma^{(0)}\big|_{\hat{\xi}=1}}{2}\right), \tag{5.59b}$$

$$j_{\text{n},\sigma}^{-(1)} = -\hat{m}_{\text{n},\sigma}^{-} \exp\left(-\frac{\lambda}{2}(\Phi - \phi_\sigma^{(0)}\big|_{\hat{\xi}=0})\right)$$
$$+ \hat{m}_{\sigma,\text{n}}^{-} c_\sigma^{(0)}\big|_{\hat{\xi}=0} \exp\left(\frac{\lambda}{2}(\Phi - \phi_\sigma^{(0)}\big|_{\hat{\xi}=0})\right), \tag{5.59c}$$

$$j_{\sigma,\text{e}}^{-(1)} = -\hat{m}_{\sigma,\text{e}}^{-} c_\sigma^{(0)}\big|_{\hat{\xi}=1} \exp\left(-\frac{\lambda\phi_\sigma^{(0)}\big|_{\hat{\xi}=1}}{2}\right). \tag{5.59d}$$

Using that $N_\sigma^+ = j_{\text{n},\sigma}^+ = j_{\sigma,\text{e}}^+$ and $N_\sigma^- = -j_{\text{n},\sigma}^- = -j_{\sigma,\text{e}}^-$ we equate (5.59a) with (5.59b) and (5.59c) with (5.59d) and use (5.58) to find

$$c_\sigma^{(0)}\big|_{\hat{\xi}=0} = \sqrt{\frac{\hat{m}_{\text{n},\sigma}^+}{\left(\hat{m}_{\sigma,\text{e}}^- + \hat{m}_{\sigma,\text{n}}^- \exp\left(\lambda\Phi/2\right)\right)}}$$
$$\times \sqrt{\frac{\left(\hat{m}_{\text{e},\sigma}^+ + \hat{m}_{\text{n},\sigma}^+ \exp\left(\lambda\Phi/2\right)\right)}{\left(\hat{m}_{\sigma,\text{n}}^+ + \hat{m}_{\sigma,\text{e}}^+ \exp\left(\lambda\Phi/2\right)\right)}} \tag{5.60a}$$

$$\phi_\sigma^{(0)}\big|_{\hat{\xi}=0} = \frac{\Phi}{2} + \frac{1}{2\lambda} \log\left(\frac{\left(\hat{m}_{\text{e},\sigma}^+ + \hat{m}_{\text{n},\sigma}^+ \exp\left(\lambda\Phi/2\right)\right)}{\left(\hat{m}_{\sigma,\text{n}}^+ + \hat{m}_{\sigma,\text{e}}^+ \exp\left(\lambda\Phi/2\right)\right)}\right)$$
$$+ \frac{1}{2\lambda} \log\left(\hat{m}_{\sigma,\text{e}}^- + \hat{m}_{\sigma,\text{n}}^- \exp\left(\lambda\Phi/2\right)\right). \tag{5.60b}$$

Substituting (5.60) into (5.59) we then get

$$N_\sigma^{+(1)} = \frac{\left(\hat{m}_{\text{n},\sigma}^-\right)^{1/4}}{\left(\hat{m}_{\text{e},\sigma}^+ + \hat{m}_{\text{n},\sigma}^+ \exp\left(\lambda\Phi/2\right)\right)^{1/4}}$$
$$\times \frac{\left(\hat{m}_{\text{n},\sigma}^+ \hat{m}_{\sigma,\text{e}}^+ \exp\left(\lambda\Phi\right) - \hat{m}_{\text{e},\sigma}^+ \hat{m}_{\sigma,\text{n}}^+\right)}{\left(\hat{m}_{\sigma,\text{e}}^- + \hat{m}_{\sigma,\text{n}}^- \exp\left(\lambda\Phi/2\right)\right)^{1/4}}$$
$$\times \frac{\exp\left(-\lambda\Phi/4\right)}{\left(\hat{m}_{\sigma,\text{n}}^+ + \hat{m}_{\sigma,\text{e}}^+ \exp\left(\lambda\Phi/2\right)\right)^{3/4}}, \tag{5.61a}$$

$$N_\sigma^{-(1)} = \frac{\hat{m}_{\sigma,\text{e}}^-(\hat{m}_{\text{n},\sigma}^-)^{3/4} \exp\left(-\lambda\Phi/4\right)}{\left(\hat{m}_{\sigma,\text{e}}^- + \hat{m}_{\sigma,\text{n}}^- \exp\left(\lambda\Phi/2\right)\right)^{3/4}}$$
$$\times \frac{\left(\hat{m}_{\text{e},\sigma}^+ + \hat{m}_{\text{n},\sigma}^+ \exp\left(\lambda\Phi/2\right)\right)^{1/4}}{\left(\hat{m}_{\sigma,\text{n}}^+ + \hat{m}_{\sigma,\text{e}}^+ \exp\left(\lambda\Phi/2\right)\right)^{1/4}} \tag{5.61b}$$

which concludes our analysis. In summary, we have

$$N_\sigma^+ = m N_\sigma^{+(1)} + \mathcal{O}(m^2), \tag{5.62a}$$
$$N_\sigma^- = m N_\sigma^{-(1)} + \mathcal{O}(m^2), \tag{5.62b}$$
$$c_\sigma = c_\sigma^{(0)}\big|_{\hat{\xi}=0} + \mathcal{O}(m), \tag{5.62c}$$
$$\phi_\sigma = \phi_\sigma^{(0)}\big|_{\hat{\xi}=0} + \mathcal{O}(m), \tag{5.62d}$$

where the concentration and potential are constant within the inner SEI up to terms of size $\mathcal{O}(m)$. In Figure 5.7, we compare our asymptotic solution (5.62) with the numerical solution of (5.12). We observe excellent agreement between asymptotic and numerical solutions for each of the variables with the errors scaling as predicted in (5.62).

5.5.4 *Diffusion-limited growth*

We now consider the case in which the timescales for diffusion of lithium ion interstitials and electrons through the inner SEI layer are significantly longer than the timescales of the electrochemical reactions. We again introduce the parameter m such that

$$m_{n,\sigma}^+ = m\hat{m}_{n,\sigma}^+, \quad m_{\sigma,n}^+ = m\hat{m}_{\sigma,n}^+, \quad m_{\sigma,e}^+ = m\hat{m}_{\sigma,e}^+,$$
$$m_{e,\sigma}^+ = m\hat{m}_{e,\sigma}^+, \quad m_{n,\sigma}^- = m\hat{m}_{n,\sigma}^+, \quad m_{\sigma,n}^- = m\hat{m}_{\sigma,n}^+,$$
$$m_{\sigma,e}^- = m\hat{m}_{\sigma,e}^+,$$

with each of the 'hat' terms being $\mathcal{O}(1)$ and also take every other parameter in the model to be $\mathcal{O}(1)$. We then take the limit $m \to \infty$. However, we first consider balancing the model equations to inform our asymptotic expansions. We shall assume that the fluxes are $\mathcal{O}(1)$. On the $\hat{\xi} = 0$ boundary, this is achieved by balancing the forward and backwards reactions by simply having $c_\sigma|_{\hat{\xi}=0} = \mathcal{O}(1)$ and $\phi_\sigma|_{\hat{\xi}=0} = \mathcal{O}(1)$. However, on the $\hat{\xi} = 1$ boundary, (5.12j) only contains a forward reaction and so a balance cannot be achieved in this way. Instead, we consider

$$c_\sigma|_{\hat{\xi}=1} \sim m^\alpha, \quad \phi_\sigma|_{\hat{\xi}=1} \sim \beta \log(m), \tag{5.63}$$

which upon substitution into (5.12e) and (5.12j) gives

$$\mathcal{O}(1) = \hat{m}_{\sigma,e}^+ m^{1+\alpha+\beta\lambda/2} - \hat{m}_{e,\sigma}^+ m^{1-\beta\lambda/2}, \tag{5.64a}$$
$$\mathcal{O}(1) = -\hat{m}_{\sigma,e}^- m^{1+\alpha-\beta\lambda/2}. \tag{5.64b}$$

We choose to balance the forward and backward reactions in (5.64a) and we balance the left and right hand sides of (5.64b). We then have the conditions

$$1 + \alpha + \frac{\beta\lambda}{2} = 1 - \frac{\beta\lambda}{2}, \quad 0 = 1 + \alpha - \frac{\beta\lambda}{2} \tag{5.65}$$

which give

$$\alpha = -\frac{2}{3}, \quad \beta = \frac{2}{3\lambda}. \tag{5.66}$$

With these balances the first non-zero component of (5.12e) is $\mathcal{O}(m^{2/3})$, which is a balance of the forward and backwards reactions.
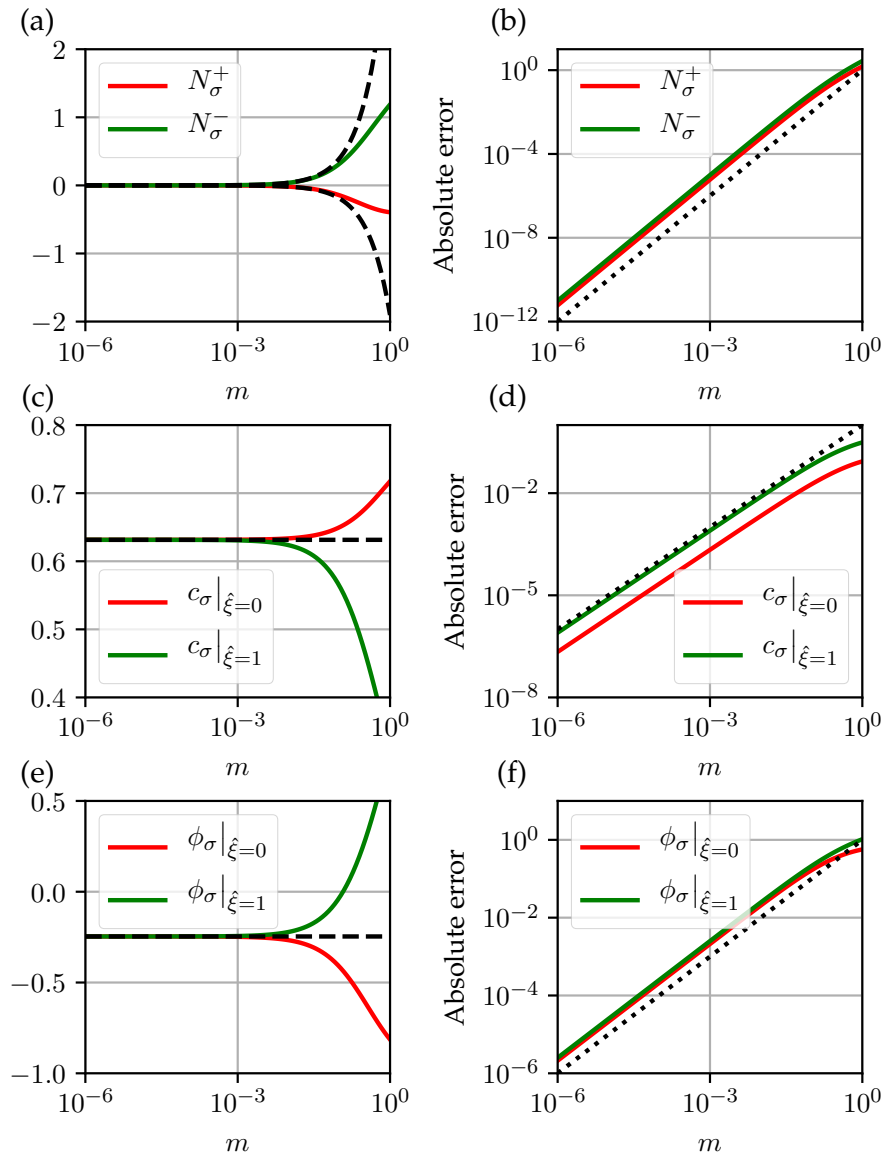
Figure 5.7: Comparison of asymptotic (5.62) (dashed in (a), (c), (e)) and numerical (5.12) (solid in (a), (c), (e)) solution where all parameter except m are taken to be $\mathcal{O}(1)$ and $\Phi = -1$: (a) predicted values of lithium and electron fluxes; (b) absolute errors in fluxes with dotted line m^2 for reference; (c) predicted values of boundary concentrations; (d) absolute errors in concentrations with dotted line m for reference; (e) predicted values of boundary potentials; (f) absolute errors in potentials with dotted line m for reference.

Informed by this balance we make the following asymptotic expansions

$$c_\sigma\big|_{\hat{\xi}=0} = c_\sigma^{(0)}\big|_{\hat{\xi}=0} + \frac{1}{m}c_\sigma^{(1)} + \dots$$

$$\phi_\sigma\big|_{\hat{\xi}=0} = \phi_\sigma^{(0)}\big|_{\hat{\xi}=0} + \frac{1}{m}\phi_\sigma^{(1)} + \dots$$

$$c_\sigma\big|_{\hat{\xi}=1} = m^{-2/3}\left(c_\sigma^{(1)}\big|_{\hat{\xi}=1} + \frac{1}{\log(m)}c_\sigma^{(2)}\big|_{\hat{\xi}=1}\dots\right)$$

$$\phi_\sigma\big|_{\hat{\xi}=1} = \frac{2}{3\lambda}\log(m) + \phi_\sigma^{(0)}\big|_{\hat{\xi}=1} + \frac{1}{\log(m)}\phi_\sigma^{(1)}\big|_{\hat{\xi}=1} + \dots \qquad (5.67)$$

$$N_\sigma^+ = N_\sigma^{+(0)} + \frac{1}{\log(m)}N_\sigma^{+(1)} + \dots$$

$$N_\sigma^- = N_\sigma^{-(0)} + \frac{1}{\log(m)}N_\sigma^{-(1)} + \dots$$

and then take $m \to \infty$.

At $\mathcal{O}(m)$, (5.12d) and (5.12i) give

$$0 = \hat{m}_{\mathrm{n},\sigma}^+ \exp\left(\frac{\lambda}{2}(\Phi - \phi_\sigma^{(0)}\big|_{\hat{\xi}=0})\right)$$
$$- \hat{m}_{\sigma,\mathrm{n}}^+ c_\sigma^{(0)}\big|_{\hat{\xi}=0} \exp\left(-\frac{\lambda}{2}(\Phi - \phi_\sigma^{(0)}\big|_{\hat{\xi}=0})\right), \qquad (5.68)$$

$$0 = -\hat{m}_{\mathrm{n},\sigma}^- \exp\left(-\frac{\lambda}{2}(\Phi - \phi_\sigma^{(0)}\big|_{\hat{\xi}=0})\right)$$
$$+ \hat{m}_{\sigma,\mathrm{n}}^- c_\sigma^{(0)}\big|_{\hat{\xi}=0} \exp\left(\frac{\lambda}{2}(\Phi - \phi_\sigma^{(0)}\big|_{\hat{\xi}=0})\right). \qquad (5.69)$$

From which we obtain

$$c_\sigma^{(0)}\big|_{\hat{\xi}=0} = \sqrt{\frac{\hat{m}_{\mathrm{n},\sigma}^- \hat{m}_{\mathrm{n},\sigma}^+}{\hat{m}_{\sigma,\mathrm{n}}^- \hat{m}_{\sigma,\mathrm{n}}^+}}, \qquad (5.70)$$

$$\phi_\sigma^{(0)}\big|_{\hat{\xi}=0} = \Phi + \frac{1}{2\lambda}\log\left(\frac{\hat{m}_{\mathrm{n},\sigma}^+ \hat{m}_{\sigma,\mathrm{n}}^-}{\hat{m}_{\mathrm{n},\sigma}^- \hat{m}_{\sigma,\mathrm{n}}^+}\right). \qquad (5.71)$$

Now at $\mathcal{O}(\log(m))$, (5.17b) becomes

$$\frac{2}{3\lambda} = -\frac{2}{3\lambda}\frac{N_\sigma^{+(0)} - N_\sigma^{-(0)}}{N_\sigma^{+(0)} + N_\sigma^{-(0)}}. \qquad (5.72)$$

Therefore we must have

$$N_\sigma^{+(0)} = 0. \qquad (5.73)$$

Then from (5.17a) at $\mathcal{O}(1)$ we obtain

$$N_\sigma^{-(0)} = \frac{2c_\sigma^{(0)}\big|_{\hat{\xi}=0}}{L_\sigma}. \qquad (5.74)$$

Equation (5.12e) at $\mathcal{O}(m^{2/3})$ and (5.12j) at $\mathcal{O}(1)$ give

$$0 = \hat{m}_{\sigma,e}^+ c_\sigma^{(1)}\big|_{\hat{\xi}=1} \exp\left(\frac{\lambda\phi_\sigma^{(0)}\big|_{\hat{\xi}=1}}{2}\right)$$

$$- m_{e,\sigma}^+ \exp\left(-\frac{\lambda\phi_\sigma^{(0)}\big|_{\hat{\xi}=1}}{2}\right), \tag{5.75}$$

$$N_\sigma^{-(0)} = -m_{\sigma,e}^- c_\sigma^{(1)}\big|_{\hat{\xi}=1} \exp\left(-\frac{\lambda\phi_\sigma^{(0)}\big|_{\hat{\xi}=1}}{2}\right). \tag{5.76}$$

Solving (5.75) for $c_\sigma^{(1)}\big|_{\hat{\xi}=1}$ and $\phi_\sigma^{(0)}\big|_{\hat{\xi}=1}$ and using (5.70) and (5.74) then gives

$$c_\sigma^{(1)}\big|_{\hat{\xi}=1} = \left(\frac{2}{\hat{m}_{\sigma,e}^- L_\sigma}\right)^{2/3} \left(\frac{\hat{m}_{e,\sigma}^+ \hat{m}_{n,\sigma}^- \hat{m}_{n,\sigma}^+}{\hat{m}_{\sigma,e}^+ \hat{m}_{\sigma,n}^- \hat{m}_{\sigma,n}^+}\right)^{1/3}, \tag{5.77a}$$

$$\phi_\sigma^{(0)}\big|_{\hat{\xi}=1} = \frac{2}{3\lambda} \log\left(\frac{\hat{m}_{e,\sigma}^+ \hat{m}_{\sigma,e}^-}{2\hat{m}_{\sigma,e}^+} \sqrt{\frac{\hat{m}_{\sigma,n}^- \hat{m}_{\sigma,n}^+}{\hat{m}_{n,\sigma}^- \hat{m}_{n,\sigma}^+}}\right). \tag{5.77b}$$

We now develop an expression for the first non-zero component of the lithium flux. To do this, we consider the $\mathcal{O}(1)$ component of (5.17b) which is given by

$$\phi_\sigma^{(0)}\big|_{\hat{\xi}=1} = \phi_\sigma^{(0)}\big|_{\hat{\xi}=0} - \frac{1}{\lambda} \log\left(\frac{c_\sigma^{(1)}\big|_{\hat{\xi}=1}}{c_\sigma^{(0)}\big|_{\hat{\xi}=0}}\right) - \frac{4}{3\lambda} \frac{N_\sigma^{+(1)}}{N_\sigma^{-(0)}}. \tag{5.78}$$

We then solve (5.78) for $N_\sigma^{+(1)}$ and use the expressions that we have derived for the other variables to obtain

$$N_\sigma^{+(1)} = \frac{3}{2L_\sigma} \sqrt{\frac{\hat{m}_{n,\sigma}^- \hat{m}_{n,\sigma}^+}{m_{\sigma,n}^- m_{\sigma,n}^+}} \left(\lambda\Phi + \log\left(\frac{\hat{m}_{n,\sigma}^+ \hat{m}_{\sigma,e}^+}{\hat{m}_{e,\sigma}^+ \hat{m}_{\sigma,n}^+}\right)\right). \tag{5.79}$$

Finally, at $\mathcal{O}(1/\log(m))$, (5.17a) gives

$$N_\sigma^{-(1)} = -N_\sigma^{+(1)}. \tag{5.80}$$

In summary, we have

$$c_\sigma\big|_{\hat{\xi}=0} = c_\sigma^{(0)}\big|_{\hat{\xi}=0} + \mathcal{O}\left(\frac{1}{m}\right), \tag{5.81a}$$

$$\phi_\sigma\big|_{\hat{\xi}=0} = \phi_\sigma^{(0)}\big|_{\hat{\xi}=0} + \mathcal{O}\left(\frac{1}{m}\right), \tag{5.81b}$$

$$c_\sigma\big|_{\hat{\xi}=1} = m^{-2/3}c_\sigma^{(1)}\big|_{\hat{\xi}=1} + \mathcal{O}\left(\frac{1}{m^{2/3}\log(m)}\right), \tag{5.81c}$$

$$\phi_\sigma\big|_{\hat{\xi}=1} = \frac{2}{3\lambda}\log(m) + \phi_\sigma^{(0)}\big|_{\hat{\xi}=1} + \mathcal{O}\left(\frac{1}{\log(m)}\right), \tag{5.81d}$$

$$N_\sigma^+ = \frac{1}{\log(m)}N_\sigma^{+(1)} + o\left(\frac{1}{\log(m)}\right), \tag{5.81e}$$

$$N_\sigma^- = N_\sigma^{-(0)} + \frac{1}{\log(m)}N_\sigma^{-(1)} + o\left(\frac{1}{\log(m)}\right), \tag{5.81f}$$

$$c_\sigma = (m^{-2/3}c_\sigma^{(1)}\big|_{\hat{\xi}=1} - c_\sigma^{(0)}\big|_{\hat{\xi}=0})\hat{\xi} + c_\sigma^{(0)}\big|_{\hat{\xi}=0} \\ + \mathcal{O}\left(\frac{1}{m^{2/3}\log(m)}\right), \tag{5.81g}$$

$$\phi_\sigma = \phi_\sigma^{(0)}\big|_{\hat{\xi}=0} \\ + \frac{1}{\lambda}\left(\frac{N_\sigma^{+(1)} - N_\sigma^{-(1)}}{\log(m)N_\sigma^{-(0)}} - 1\right)\log\left(\frac{c_\sigma}{c_\sigma^{(0)}\big|_{\hat{\xi}=0}}\right) \\ + \mathcal{O}\left(\frac{1}{\log(m)}\right). \tag{5.81h}$$

Where a big-$\mathcal{O}$ notation error is reported, we have continued our asymptotic expansion in a computational algebra package to confirm this error. Where a little-o error is reported, we have not continued the expansion to determine the error.

We now compare our asymptotic solution (5.81) with the numerical solution of (5.12). Our results for the six variables in the algebraic version of the problem are presented in Figure 5.8. We observe good agreement between our asymptotic solution and the numerical solution with the magnitude of the errors scaling as we would expect from our asymptotic errors predicted in (5.81). For N_σ^+, and N_σ^- we expect (but have not rigorously confirmed) that the error decays a rate similar to $(1/\log(m))^2$ and have therefore provided this as a reference on the error plot. For $\phi_\sigma\big|_{\hat{\xi}=1}$, the slow error decay is a result of the log-dependent errors. Continuing to significantly higher values of m will reduce this error but the convergence of the numerical solution to (5.81) could not be achieved. For completeness, we present the concentration and potential within the SEI for $m = 1000$ in Figure 5.9. We again see that the concentration and potential profiles predated by our solution capture the numerical solution up to errors of the magnitude predicted in (5.81).
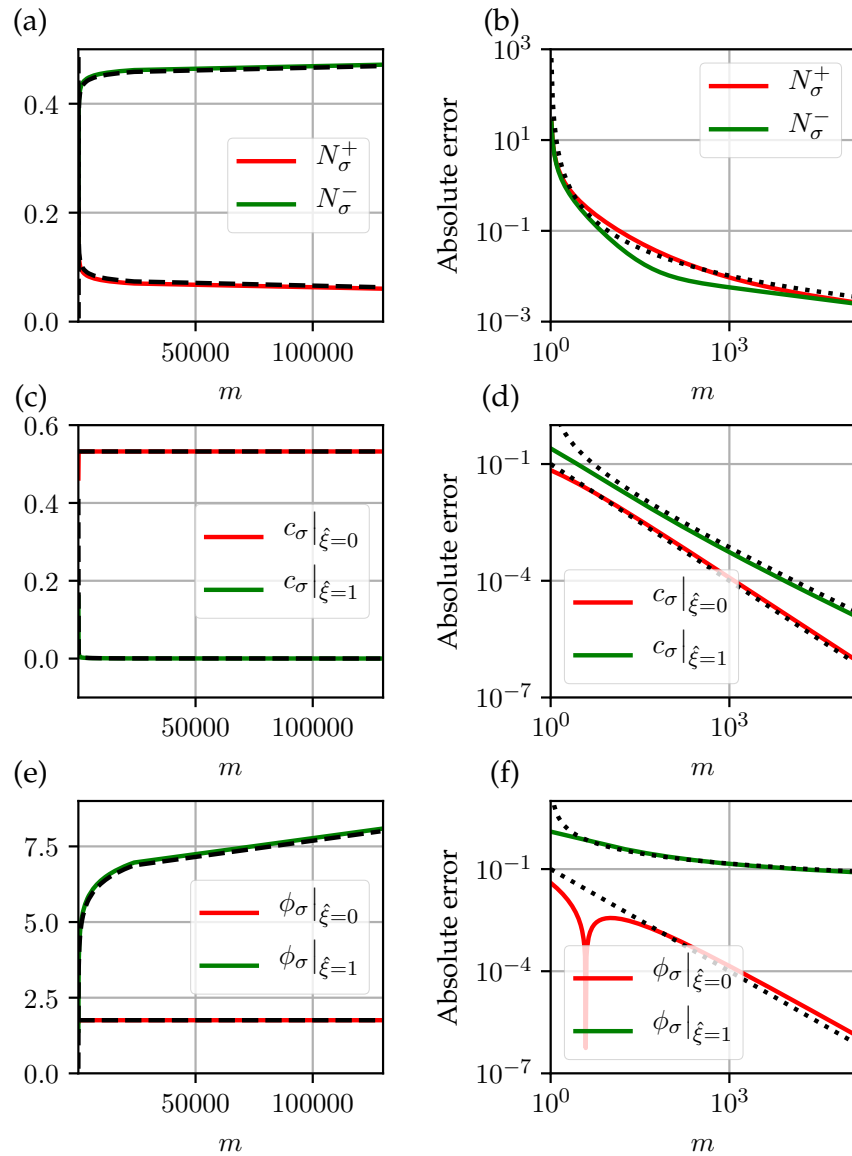
Figure 5.8: Comparison of asymptotic (5.81) (dashed in (a), (c), (e)) and numerical (5.12) (solid in (a), (c), (e)) solution where all parameter except m are taken to be $\mathcal{O}(1)$ and $\Phi = 1$: (a) predicted values of lithium and electron fluxes; (b) absolute errors in fluxes with dotted line $(1/\log(m))^2$ for reference; (c) predicted values of boundary concentrations; (d) absolute errors in concentrations with dotted lines $m^{-2/3}/\log(m)$ (upper) and $1/m$ (lower) for reference; (e) predicted values of boundary potentials; (f) absolute errors in potentials with dotted lines $1/\log(m)$ (upper) and $1/m$ (lower) for reference.
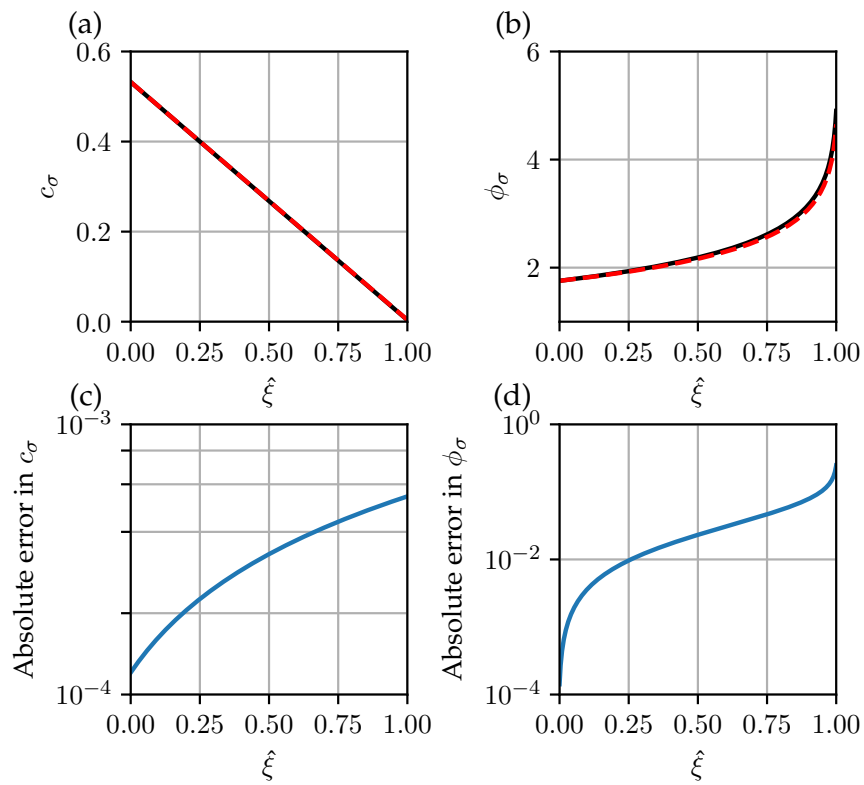
Figure 5.9: Comparison of asymptotic (5.81) and numerical (5.12) concentration and potential within the SEI for $m = 1000$, $\Phi = 1$ and all other parameters $\mathcal{O}(1)$. Here the expected errors are $m^{-2/3}/\log(m) \approx 10^{-3}$ for the concentration and $1/\log(m) \approx 10^{-1}$ for the potential.

5.5.5 *Electron migration with graphite–SEI intercalation reaction*

We now consider the case in which the SEI growth is limited by migration of electrons through the SEI but lithium intercalation is limited by the reaction on the graphite–SEI boundary. This corresponds to taking

$$m_{n,\sigma}^+ = \hat{m}_{n,\sigma}^+/m, \quad m_{\sigma,n}^+ = \hat{m}_{\sigma,n}^+/m, \quad m_{\sigma,e}^+ = \hat{m}_{\sigma,e}^+,$$
$$m_{e,\sigma}^+ = \hat{m}_{e,\sigma}^+, \quad m_{n,\sigma}^- = m\hat{m}_{n,\sigma}^+, \quad m_{\sigma,n}^- = m\hat{m}_{\sigma,n}^+,$$
$$m_{\sigma,e}^- = m\hat{m}_{\sigma,e}^+,$$

with each of the 'hat' terms being $\mathcal{O}(1)$, every other parameter in the model to be $\mathcal{O}(1)$, and taking the limit $m \to \infty$. The analysis is very similar to that of the diffusion-limited growth case so we just state the leading-order solution which is

$$c_\sigma|_{\hat{\xi}=0} = \sqrt{\frac{m_{e,\sigma}^+ m_{n,\sigma}^-}{m_{\sigma,e}^+ m_{\sigma,n}^-}} \exp\left(-\frac{\lambda\Phi}{2}\right), \tag{5.82a}$$

$$c_\sigma|_{\hat{\xi}=1} = \left(\frac{2m_{e,\sigma}^+}{L_\sigma m_{\sigma,e}^- m_{\sigma,e}^+}\right)^{2/3} \left(\frac{m_{n,\sigma}^-}{m_{\sigma,n}^-}\right)^{1/3} \exp\left(-\frac{\lambda\Phi}{3}\right), \tag{5.82b}$$

$$\phi_\sigma|_{\hat{\xi}=0} = \frac{\Phi}{2} + \frac{1}{2\lambda} \log\left(\frac{m_{e,\sigma}^+ m_{\sigma,n}^-}{m_{\sigma,e}^+ m_{n,\sigma}^-}\right) \tag{5.82c}$$

$$\phi_\sigma|_{\hat{\xi}=1} = \frac{\Phi}{3} + \frac{2}{3\lambda} \log\left(L_\sigma m_{\sigma,e}^-\right) + \frac{1}{3\lambda} \log\left(\frac{m_{e,\sigma}^+ m_{\sigma,n}^-}{m_{\sigma,e}^+ m_{n,\sigma}^-}\right), \tag{5.82d}$$

$$N_\sigma^- = \frac{2}{L_\sigma} \sqrt{\frac{m_{e,\sigma}^+ m_{n,\sigma}^-}{m_{\sigma,e}^+ m_{\sigma,n}^-}} \exp\left(-\frac{\lambda\Phi}{2}\right), \tag{5.82e}$$

$$N_\sigma^+ = \left(\frac{m_{e,\sigma}^+ m_{\sigma,n}^-}{m_{\sigma,e}^+ m_{n,\sigma}^-}\right)^{1/4} \exp\left(-\frac{\lambda\Phi}{4}\right)$$
$$\times \left(m_{n,\sigma}^+ \left(\frac{m_{n,\sigma}^- m_{\sigma,e}^+}{m_{\sigma,n}^- m_{e,\sigma}^+}\right)^{1/2} \exp\left(\frac{\lambda\Phi}{2}\right) \right.$$
$$\left. -m_{\sigma,n}^+ \left(\frac{m_{n,\sigma}^- m_{e,\sigma}^+}{m_{\sigma,n}^- m_{\sigma,e}^+}\right)^{1/2} \exp\left(-\frac{\lambda\Phi}{2}\right)\right), \tag{5.82f}$$

where we have recombined m with the 'hat' terms. This asymptotic solution and the numerical solution of (5.12) are compared in Figure 5.10. We observe good agreement between the two solutions with the errors scaling with at least $m^{-2/3}$.
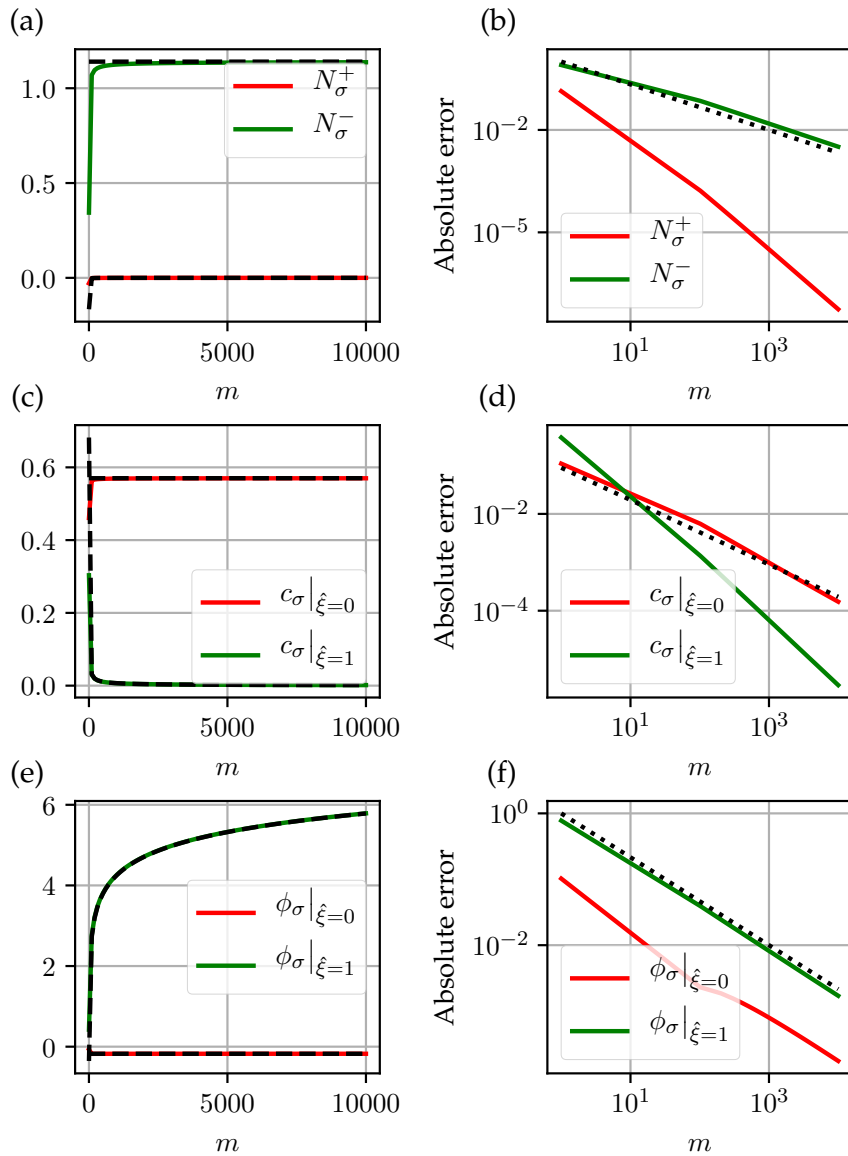
Figure 5.10: Comparison of asymptotic solution (5.82) (dashed in (a), (c), (e)) and numerical solution to (5.12) (solid in (a), (c), (e)) where all parameter except m are taken to be $\mathcal{O}(1)$ and $\Phi = -1$: (a) predicted values of lithium and electron fluxes; (b) absolute errors in fluxes with dotted line $m^{-2/3}$ for reference; (c) predicted values of boundary concentrations; (d) absolute errors in concentrations with dotted lines $m^{-2/3}$ for reference; (e) predicted values of boundary potentials; (f) absolute errors in potentials with dotted lines $m^{-2/3}$ for reference.

5.5.6   *Electron diffusion and SEI–electrolyte intercalation reaction*

We also consider the case in which SEI growth is limited migration of electrons through the SEI and lithium intercalation is limited by the reaction on the SEI–electrolyte boundary. This corresponds to taking

$$m_{n,\sigma}^+ = \hat{m}_{n,\sigma}^+, \quad m_{\sigma,n}^+ = \hat{m}_{\sigma,n}^+, \quad m_{\sigma,e}^+ = \hat{m}_{\sigma,e}^+/m,$$
$$m_{e,\sigma}^+ = \hat{m}_{e,\sigma}^+/m, \quad m_{n,\sigma}^- = m\hat{m}_{n,\sigma}^+, \quad m_{\sigma,n}^- = m\hat{m}_{\sigma,n}^+,$$
$$m_{\sigma,e}^- = m\hat{m}_{\sigma,e}^+,$$

with each of the 'hat' terms being $\mathcal{O}(1)$ and also take every other parameter in the model to be $\mathcal{O}(1)$. We will then take the limit $m \to \infty$. The analysis is very similar to that of the diffusion-limited growth case so we again simply state the leading-order solution, which is

$$c_\sigma\big|_{\hat\xi=0} = \sqrt{\frac{m_{n,\sigma}^- m_{n,\sigma}^+}{m_{\sigma,n}^- m_{\sigma,n}^+}}, \tag{5.83a}$$

$$c_\sigma\big|_{\hat\xi=1} = \left(\frac{2m_{n,\sigma}^+}{L_\sigma m_{\sigma,e}^- m_{\sigma,n}^+}\right)^{2/3} \left(\frac{m_{n,\sigma}}{m_{\sigma,n}}\right)^{1/3} \exp\left(\frac{\lambda\Phi}{3}\right), \tag{5.83b}$$

$$\phi_\sigma\big|_{\hat\xi=0} = \Phi + \frac{1}{2\lambda} \log\left(\frac{m_{n,\sigma}^+ m_{\sigma,n}^-}{m_{\sigma,n}^+ m_{n,\sigma}^-}\right), \tag{5.83c}$$

$$\phi_\sigma\big|_{\hat\xi=1} = \frac{2\Phi}{3} + \frac{2}{3\lambda} \log\left(L_\sigma m_{\sigma,e}^-\right)$$
$$+ \frac{1}{3\lambda} \log\left(\frac{m_{n,\sigma}^+ m_{\sigma,n}^-}{4m_{\sigma,n}^+ m_{n,\sigma}^-}\right), \tag{5.83d}$$

$$N_\sigma^- = \frac{2}{L_\sigma} \sqrt{\frac{m_{n,\sigma}^- m_{n,\sigma}^+}{m_{\sigma,n}^- m_{\sigma,n}^+}}, \tag{5.83e}$$

$$N_\sigma^+ = \left(\frac{2}{L_\sigma m_{\sigma,e}^-}\right)^{1/3} \exp\left(\frac{\lambda\Phi}{6}\right)$$
$$\times \left(\frac{1}{m_{n,\sigma}^- m_{n,\sigma}^+ m_{\sigma,n}^- m_{\sigma,n}^+}\right)^{1/6}$$
$$\times \left(m_{n,\sigma}^+ m_{\sigma,e}^+ \left(\frac{m_{n,\sigma}^-}{(m_{\sigma,n}^+)^2}\right)^{1/3} \exp\left(\frac{\lambda\Phi}{2}\right)\right.$$
$$\left. - m_{e,\sigma}^+ \left(m_{n,\sigma}^- m_{\sigma,n}^+\right)^{1/3} \exp\left(-\frac{\lambda\Phi}{2}\right)\right). \tag{5.83f}$$

Here, we have recombined the 'm' and 'hat' terms. As before, we compare our asymptotic solution (5.83) with the numerical solution of (5.12) in Figure 5.11. We observe good agreement between the solutions with the error in the electron scaling as $m^{-2/3}$ and the errors in the other terms (with the exception of $\phi_\sigma\big|_{\hat\xi=1}$) decaying at a faster rate. The errors in $\phi_\sigma\big|_{\hat\xi=1}$ decay slightly slower than $m^{-2/3}$.
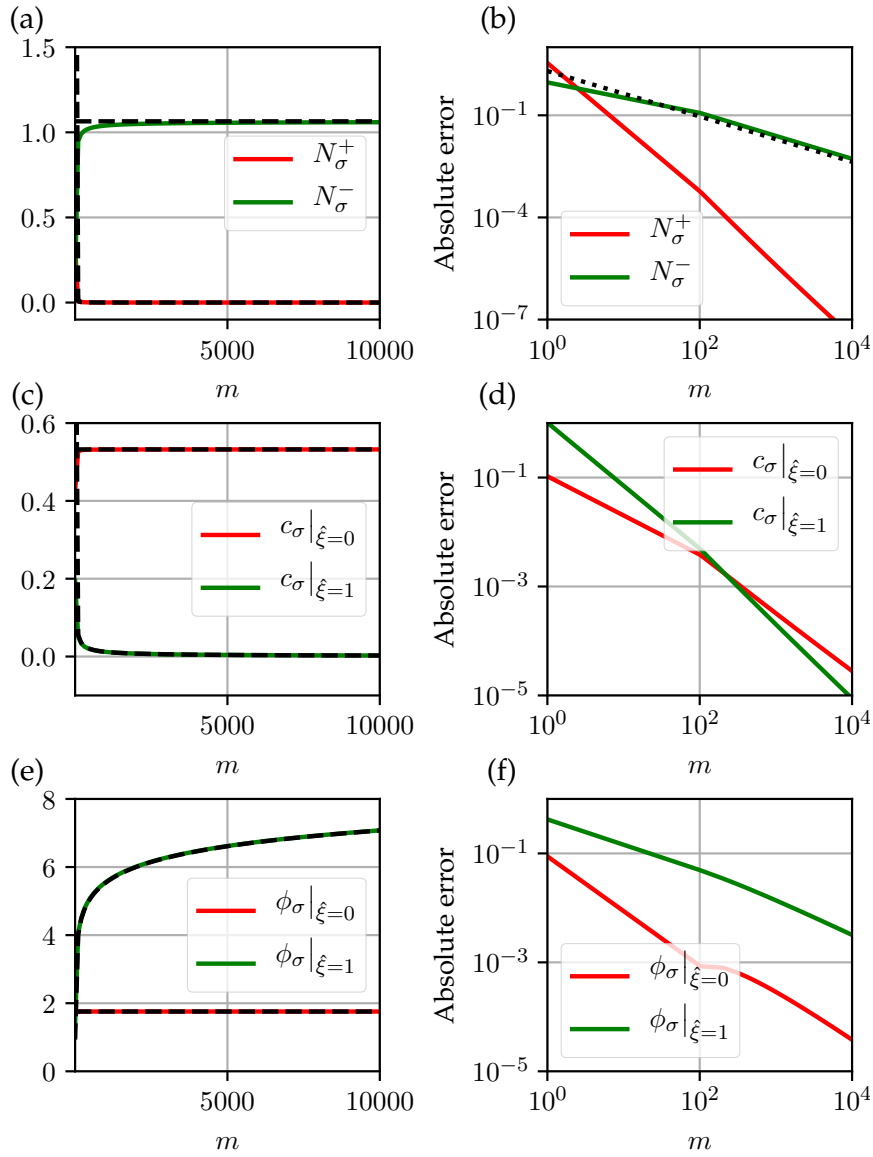
Figure 5.11: Comparison of asymptotic solution (5.83) (dashed in (a), (c), (e)) and numerical solution to (5.12) (solid in (a), (c), (e)) where all parameter except m are taken to be $\mathcal{O}(1)$ and $\Phi = 1$: (a) predicted values of lithium and electron fluxes; (b) absolute errors in fluxes with dotted line $m^{-2/3}$ for reference; (c) predicted values of boundary concentrations; (d) absolute errors in concentrations; (e) predicted values of boundary potentials; (f) absolute errors in potentials.

5.6   VALIDATION OF A REDUCED SEI MODEL

In this section, we compare the reduced SEI model that we developed in the electron migration with graphite–SEI intercalation reaction limit (5.82) with experimental data and set it within the context of the ad-hoc zero-dimensional SEI growth models from the literature. A similar study could be undertaken for the other reduced-order models that we have developed. However, we chose to investigate this particular candidate because it recovers a square-root of time SEI growth dependence, an exponential dependence upon the potential drop across the layer (which we expected would recover SoC dependence), and retains a Butler–Volmer-like structure for the intercalation reaction. We begin by dimensionalising the model and writing it in terms of measurable electrochemical properties as well as variables that are employed in full lithium-ion cell models such as the DFN. We then adopt the experimentally motivated battery model developed in [82] to compare our SEI model with experimental data that captures the time, temperature, and SoC dependence of capacity fade within a lithium-ion cell. We follow this with a discussion of how our SEI model compares to other ad-hoc SEI models in the literature and conclude that our model is one of only two growth models that can well recover observed cell capacity fade.

5.6.1   *Redimensionalisation*

We begin by redimensionalising (5.82). Here, we are only concerned with two quantities, the intercalation flux N_σ^+ and the electron flux N_σ^-. Applying the scalings in (5.7), we obtain

$$
\begin{aligned}
N_\sigma^{*+} = {} & \frac{1}{F^*} \left(\frac{m_{e,\sigma}^{*+} m_{\sigma,n}^{*-} c_{e,n}^*}{m_{\sigma,e}^{*+} m_{n,\sigma}^{*-}} \right)^{1/4} \\
& \times \exp\left(-\frac{F^*}{4 R_g^* T^*} (\phi_{s,n}^* - \hat{\phi}_{e,n}^*) \right) \\
& \times \left[m_{n,\sigma}^{*+} c_{s,n}^* \left(\frac{m_{n,\sigma}^{*-} m_{\sigma,e}^{*+}}{m_{\sigma,n}^{*-} m_{e,\sigma}^{*+} c_{e,n}^*} \right)^{1/2} \right. \\
& \qquad \times \exp\left(\frac{F^*}{2 R_g^* T^*} (\phi_{s,n}^* - \hat{\phi}_{e,n}^*) \right) \\
& \quad - m_{\sigma,n}^{*+} (c_{s,n,max}^* - c_{s,n}^*) \left(\frac{m_{n,\sigma}^{*-} m_{e,\sigma}^{*+} c_{e,n}^*}{m_{\sigma,n}^{*-} m_{\sigma,e}^{*+}} \right)^{1/2} \\
& \qquad \left. \times \exp\left(-\frac{F^*}{2 R_g^* T^*} (\phi_{s,n}^* - \hat{\phi}_{e,n}^*) \right) \right],
\end{aligned}
\tag{5.84a}
$$

$$N_\sigma^{*-} = \frac{2D_\sigma^{*-}}{L_\sigma^*} \sqrt{\frac{m_{e,\sigma}^{*+}m_{n,\sigma}^{*-}c_{e,n}^*}{m_{\sigma,e}^{*+}m_{\sigma,n}^{*-}}}$$
$$\times \exp\left(-\frac{F^*}{2R_g^*T^*}(\phi_{s,n}^* - \hat\phi_{e,n}^*)\right). \tag{5.84b}$$

The key measureable electrochemical quantity is the OCP of the negative electrode with respect to a lithium reference electrode. As a step towards this, we first write (5.84a) in terms of the OCP of the negative electrode vs. the potential in the electrolyte, $\hat U_n^*(c_{s,n}^*, c_e^*)$. By taking the intercalation reaction to be in equilibrium ($N_\sigma^{*+} = 0$, $\hat U_n^*(c_{s,n}^*, c_e^*) = \phi_{s,n}^* - \hat\phi_{e,n}^*$), (5.84a) gives

$$\hat U_n^*(c_{e,n}^*, c_{e,n}^*) = \frac{R_g^*T^*}{F^*}\log\left(\frac{m_{\sigma,n}^{*-}m_{e,\sigma}^{*+}(c_{s,n,\max}^* - c_{s,n}^*)c_{e,n}^*}{m_{n,\sigma}^{*-}m_{\sigma,e}^{*+}c_{s,n}^*}\right). \tag{5.85}$$

Following a similar approach to that taken in §2.4.1, we can then write (5.84a) as

$$N_\sigma^{*+} = \frac{2}{F^*}(m_{n,\sigma}^{*+}m_{\sigma,n}^{*+})^{1/2}(c_{s,n}^*)^{1/2}(c_{s,n,\max}^* - c_{s,n}^*)^{1/2}$$
$$\times \left(\frac{m_{e,\sigma}^{*+}m_{n,\sigma}^{*-}c_{e,n}^*}{m_{\sigma,e}^{*+}m_{\sigma,n}^{*-}}\right)^{1/4}$$
$$\times \exp\left(-\frac{F^*}{4R_g^*T^*}(\phi_{s,n}^* - \hat\phi_{e,n}^*)\right)$$
$$\times \sinh\left(\frac{F^*}{2R_g^*T^*}(\phi_{s,n}^* - \hat\phi_{e,n}^* - \hat U_n^*(c_{s,n}^*, c_{e,n}^*))\right). \tag{5.86}$$

To write our expressions in terms of the OCP relative to a lithium reference electrode, $U_n^*(c_n^*)$, we use (2.13). Mathematical models of full cells are also written in terms of the electrochemical potential in the electrolyte, ϕ_e^*, instead of the true potential in the electrolyte, $\hat\phi_e^*$ (see §2.4.1 for more details). We write (5.84) in terms of ϕ_e^* instead of $\hat\phi_e^*$ using (2.12). Finally, to be consistent with our formulation of full cell models in earlier chapters, we write the reduced SEI model as interfacial current densities defined to be

$$j_n^* := F^*N_\sigma^{*+}, \quad j_\sigma^* = -F^*N_\sigma^{*-}. \tag{5.87}$$

Following this process, (5.84) becomes

$$j_n^* = j_{0,n}^*\sinh\left(\frac{F^*\eta_n^*}{2R_g^*T^*}\right), \tag{5.88a}$$

$$j_\sigma^* = -\frac{2F^*D_\sigma^{*-}}{L_\sigma^*}c_{\sigma,\text{ref}}^*\exp\left(-\frac{F^*}{2R_g^*T^*}(\phi_{s,n}^* - \phi_{e,n}^*)\right), \tag{5.88b}$$

where

$$
\begin{aligned}
j_{0,n}^* = {} & m_n^*(c_{s,n}^*)^{1/2}(c_{s,n,\max}^* - c_{s,n}^*)^{1/2}\left(c_{\sigma,\mathrm{ref}}^*\right)^{1/2} \\
& \times \exp\left(-\frac{F^*(\phi_{s,n}^* - \phi_{e,n}^*)}{4R_g^*T^*}\right),
\end{aligned}
\tag{5.88c}
$$

$$
\eta_{s,n}^* = \phi_{s,n}^* - \phi_{e,n}^* - U_n^*(c_{s,n}^*),
\tag{5.88d}
$$

are the intercalation exchange current density and intercalation overpotential. Two lumped constants have been introduced here

$$
m_n^* = 2(m_{n,\sigma}^+)^{1/2}(m_{\sigma,n}^{*+})^{1/2}
\tag{5.88e}
$$

which is an effective reaction rate similar to that introduced in §2.4.1 with units of $\mathrm{A\,m^{-2}\,(m^3\,mol^{-1})^{1.5}}$, and

$$
c_{\sigma,\mathrm{ref}}^* = \sqrt{\frac{m_{n,\sigma}^{*-}m_{\mathrm{Li,e}}^*m_{e,\sigma}^{*+}}{m_{\sigma,n}^{*-}m_{e,\mathrm{Li}}^*m_{\sigma,e}^{*+}}},
\tag{5.88f}
$$

which has units of $\mathrm{mol\,m^{-3}}$ and corresponds to the concentration of electrons (and lithium-ion interstitials) at the graphite–SEI interface when $\phi_{s,n}^* = \phi_{e,n}^*$. As an aside, the actual electron concentration at the graphite–SEI interface is obtained from

$$
c_{\sigma,\mathrm{ref}}^* \exp\left(-\frac{F^*}{2R_g^*T^*}(\phi_{s,n}^* - \phi_{e,n}^*)\right).
$$

From the structure of (5.88), we can see that the standard Butler–Volmer relation for intercalation (introduced in §2.4.1) is only slightly modified with the exchange current density now dependent upon the concentration of lithium-ion interstitials at the graphite-SEI interface instead of the concentration of lithium-ions in the electrolyte. As a result, this introduces a potential dependence to the exchange current density which was not previously present. The main characteristics of the SEI growth reaction, j_σ^*, are that it is proportional to the diffusivity of electrons within the SEI as well as the concentration of electrons at the graphite–SEI interface, and inversely proportional to the thickness of the SEI. Since the concentration of electrons at the graphite–SEI interface is dependent upon the potential difference across the SEI, this introduces an SoC dependence into the model. Additionally, the inverse proportionality to the SEI thickness results in a square-root of time decay of the SEI growth rate, which is often reported in capacity fade experiments [15], [63]. These characteristics make the model a promising candidate for capturing SEI growth accurately.

5.6.2 *Experimentally motivated model*

To compare our SEI model with the experimental data from [35], we require some model of the lithium-ion cell. The experimental results in [35] demonstrate that it is crucial to employ the graphite OCP measured for a particular cell to accurately predict capacity fade. This quantity is provided in [35] as a function of SoC, i.e. $U_n^*(\text{SoC})$. However, the physics-based models that we have previously been using require the graphite OCP as a function of the surface concentration of the graphite particles, $U_n^*(c_{s,n}^*)$. It is not immediately clear how to convert from SoC to $c_{s,n}^*$ without knowledge of the concentrations at SoC $= 0, 1$. Further, we are not provided with many other key parameters for this particular cell that are required in full physics-based models. To avoid these difficulties, we employ the experimentally motivated approach taken in [82] to perform our comparison. This is approach involves making several ad-hoc assumptions to link our model to the concepts of 'capacity' and 'SoC'.

We first assume that the capacity loss of the cell is equal to the lithium lost due to SEI formation. It should be noted that the loss of lithium and the capacity fade is not necessarily equal. This is because the loss of lithium results in stochiometric offsets between the electrodes which cause the upper and lower voltage limits (from which capacity is defined) to correspond to different balances of the electrode concentrations [10]. However, in [10] these offsets appear small so this is likely a reasonable first assumption. The capacity of the cell is then given by

$$\frac{\partial Q^*}{\partial t^*} = A^* j_\sigma^*, \quad Q^*\big|_{t^*=0} = Q_0^*, \tag{5.89a}$$

where Q^* is the cell capacity (in Coulombs), Q_0^* is the initial cell capacity, and A^* is the total surface area of the negative electrode.

The second assumption is that during storage the SoC of the cell decays at the same rate as the relative capacity Q^*/Q_0^* of the cell. The thinking here is that when the capacity fades by a particular amount, the same amount of charge stored in the cell must also be lost. The factor of Q_0^* converts the total stored charge into SoC (referenced to the initial capacity of the cell). Therefore, we have

$$\frac{\partial \text{SoC}}{\partial t^*} = \frac{A^*}{Q_0^*} j_\sigma^*, \quad \text{SoC}\big|_{t^*=0} = \text{SoC}_0, \tag{5.89b}$$

where SoC_0 is the SoC at the beginning of the experiment.

In the experimental procedure in [35] a checkup experiment was performed after 1.9 months, 3.8 months, 6.5 months, and 9.5 months of storage to measure the capacity of the cells. After this checkup, the cells were returned to the initial SoC but this is now the SoC measured with respect the newly measured capacity of the cell, Q^*, instead of the

initial capacity of the cell, Q_0^*. Within the model, we account for this resetting of the SoC using

$$\text{SoC}_{\text{reset}} = \text{SoC}_0 \frac{Q^*}{Q_0^*}. \tag{5.89c}$$

Numerically, we simply update the SoC during storage with (5.89b), read out Q^* at the allotted checkup times, apply (5.89c), and repeat until the end of the experiment.

We describe the evolution of the thickness of the SEI using (5.6h) but assume that a small layer of SEI of thickness, $L_{\sigma,0}^*$, has formed on the short timescales that we have previously, neglected. Therefore, we have

$$\frac{\partial L_\sigma^*}{\partial t^*} = -\frac{\bar{V}_\sigma^*}{F^*} j_\sigma^*, \quad L_\sigma^*\big|_{t^*=0} = L_{\sigma,0}^*. \tag{5.89d}$$

We also assume that the intercalation reaction is almost in equilibrium (we will justify this assumption more formally later) so that $\phi_{\text{s,n}}^* - \phi_{\text{e,n}}^* \approx U_{\text{n}}^*(\text{SoC})$, such that (5.88b) becomes

$$j_\sigma^* = -\frac{2F^* D_\sigma^{*-}}{L_\sigma^*} c_{\sigma,\text{ref}}^* \exp\left(-\frac{F^*}{2R_{\text{g}}^* T^*} U_{\text{n}}^*(\text{SoC})\right). \tag{5.89e}$$

Equations (5.89) then forms a closed system of ordinary differential equations which we solve numerically. Values for each of the parameters except $c_{\sigma,\text{ref}}^*$, $L_{\sigma,0}^*$, and $\bar{V}_\sigma^*$ are provided in Tables 5.1 and 5.2. We shall modify these values only slightly taking $L_{\sigma,0}^* = 1\,\text{nm}$ instead of $15\,\text{nm}$. We also take $\bar{V}_\sigma^*$ and $c_{\sigma,\text{ref}}^*$ to be fitting parameters. To capture the temperature dependence of the SEI growth rate, we assume that the diffusivity of electrons within the SEI follows an Arrhenius relation of the form

$$D_\sigma^{*-} = D_{\sigma,\text{ref}}^{*-} \exp\left(\frac{E_{\text{D},\sigma}^*}{R_{\text{g}}^*}\left(\frac{1}{T_{\text{ref}}^*} - \frac{1}{T^*}\right)\right), \tag{5.89f}$$

where we shall take $T_{\text{ref}}^* = 323.15\,\text{K}$ (50 °C) and will employ $E_{\text{D},\sigma}^*$ as an additional fitting parameter.

5.6.3   *Comparison with experiments*

In [35], calendar ageing (long-term storage without charge/discharge) is studied at different temperatures across 16 different SoCs. The capacity of these cells was measured at the start of the experiment and then after 1.9 months, 3.8 months, 6.5 months, and 9.5 months, giving the time dependence of capacity fade. Three types of lithium-ion cell with graphite negative electrodes were studied but we shall only consider the cell with a Nickel-Cobalt-Aluminum (NCA) positive electrode.

Since the study of capacity fade is conducted on full cells, degradation mechanisms other than SEI formation are also likely occurring within the cell. However, for our comparisons, we will proceed with the assumption that SEI is the only degradation mechanism and comment on where this assumption is appropriate in light of our comparison results.

We employ least squares to fit (5.89) to the experimental data from [35], treating $\bar{V}_\sigma^*$, $c_{\sigma,\text{ref}}^*$, and $E_{\text{D},\sigma}^*$ as adjustable parameters. All other parameters are taken from Tables 5.1 and 5.2 and we take $L_{\sigma,0}^* = 1\,\text{nm}$. We first hold the temperature fixed at $50\,^\circ\text{C}$ and fit $\bar{V}_\sigma^*$ and $c_{\sigma,\text{ref}}^*$ to the full set of SoC and time dependent experimental results (as displayed in Figure 5.12 (b)) to find $c_{\sigma,\text{ref}}^* = 0.967\,\text{mol}\,\text{m}^3$, $\bar{V}_\sigma^* = 1.16 \times 10^{-5}\,\text{m}^3\,\text{mol}^{-1}$. We then hold these values fixed and adjust $E_{\text{D},\sigma}^*$ such that our model fits the SoC and temperature dependent data (as displayed in Figure 5.12(c)). Doing this, we find the value $E_{\text{D},\sigma}^* = 41\,851\,\text{J}\,\text{mol}^{-1}$.

In Figure 5.12, we compare the capacity fade prediction from our SEI model with experimental data. For SoCs greater than 0.2, our model excellently recovers the SoC, temporal, and temperature dependence of the experimental results. In particular, the model captures well the sudden reduction in capacity that occurs around SoC=0.6. This reflects the step change in the OCP at around SoC=0.6. The mostly flat regions of the OCP also give rise to similar rates of capacity fade in both the experimental and model results.

At low SoCs, our model fails to capture the capacity fade predicted by experiment. It is possible that the model we adopted for resetting the SoC (5.89) is not accurate at low SoCs. Experimentally, the OCP will shift as a function of SoC as lithium is lost [10]. However, we do not fully account for these shifts. Experimentally remeasuring the OCP at each checkup may help reduce this uncertainty. Another possible reason is that there are additional degradation mechanisms that are important at low SoC. In [82], a linear rate of degradation representing any other unidentified mechanisms is introduced in conjunction with an SEI growth model. For demonstration purposes, we also do this by replacing (5.89a) and (5.89b) with

$$\frac{\partial Q^*}{\partial t^*} = A^* j_\sigma^* - \gamma^*, \quad Q^*\big|_{t^*=0} = Q_0^* \tag{5.90a}$$

$$\frac{\partial \text{SoC}}{\partial t^*} = \frac{A^*}{Q_0^*} j_\sigma^* - \frac{\gamma^*}{Q_0^*}, \quad \text{SoC}\big|_{t^*=0} = \text{SoC}_0, \tag{5.90b}$$

where γ^* is a fitting parameter with units of A that encompasses other degradation mechanisms. By treating γ^* as an additional fitting parameter alongside $\bar{V}_\sigma^*$ and $c_{\sigma,\text{ref}}^*$, for the data for $50\,^\circ\text{C}$ after 9.5 months, we obtain the results in Figure 5.13. Here, we observe a much improved performance at capturing capacity fade at low SoCs. Therefore our SEI model is consistent with the hypothesis that other degradation mechanisms drive degradation at low SoCs.
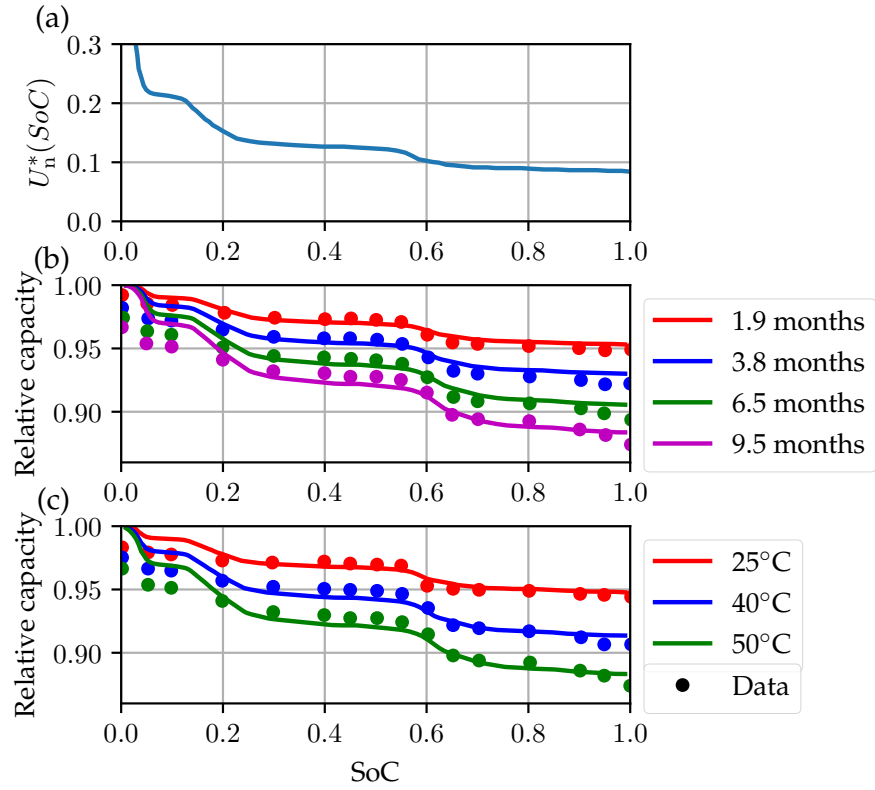
Figure 5.12: Fit of (5.89) to experimental data from [35]: (a) Negative electrode OCP as a function SoC reported in [35]; (b) Time and SoC dependence of capacity fade at 50 °C; (c) Temperature and SoC dependence of capacity fade after 9.5 months of storage. The fitted parameter values are $c^*_{\sigma,\text{ref}} = 0.967\,\text{mol m}^{-3}$, $\bar{V}^*_\sigma = 1.16 \times 10^{-5}\,\text{m}^3\,\text{mol}^{-1}$, $E^*_{\text{D},\sigma} = 41\,851\,\text{J mol}^{-1}$ and the initial SEI thickness was taken to be 1 nm. All other parameter values are from Tables 5.1 and 5.2.
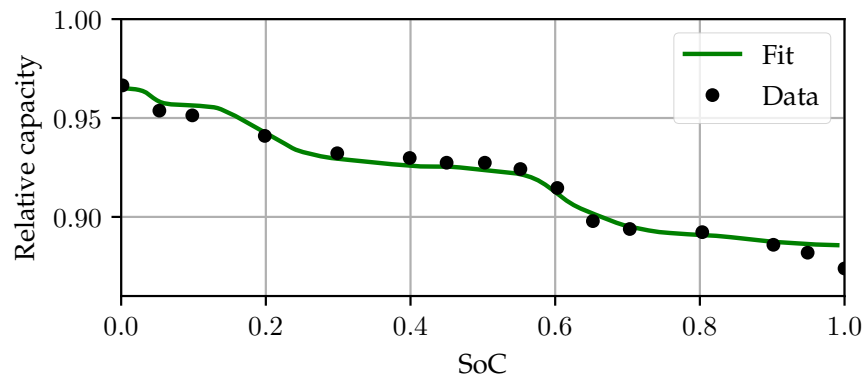

Figure 5.13: Comparison between (5.89) with (5.90) and experimental data from [35] at 50 °C after 9.5 months. Fitted parameter values are: $c^*_{\sigma,\text{ref}} = 1.68\,\text{mol m}^{-3}$, $\bar{V}^*_\sigma = 8 \times 10^{-9}\,\text{m}^3\,\text{mol}^{-1}$, and $\gamma = 1.4 \times 10^{-5}$.

5.6.4   *Relation to zero-dimensional SEI growth models*

In §5.3 we discussed the ad-hoc zero-dimensional models of SEI growth that have been developed in the literature. A numerical comparison of these zero-dimensional SEI growth models was provided [82] but we will discuss the key features of each here to demonstrate similarities and differences with our asymptotically derived SEI growth model. There are four models that we will discuss. The first is solvent diffusion-limited growth. In this case, solvent molecules in the electrolyte are slow to transport through the outer SEI layer to the reaction site. Therefore, the rate at which they do so determines the SEI growth rate. The model that is commonly written is (see [66], [87])

$$j^*_{\text{solvent}} = -\frac{F^* D^*_{\text{sol}} c^*_{\text{sol}}}{L^*_\sigma}, \tag{5.91}$$

where D^*_{sol} is the diffusivity of solvent molecules within the outer SEI, c^*_{sol} is the concentration of solvent in the bulk electrolyte, and L^*_σ is the thickness of the outer SEI. Here the rate of growth is inversely proportional to the thickness of the SEI and therefore can replicate the square root of time dependence of capacity fade observed experimentally [15], [63]. However, this model crucially does not contain a dependence upon the potential difference across the SEI. Therefore, it cannot recover the SoC dependence observed in the experimental results of [35].

The second common SEI growth mechanism is reaction-limited growth. Here, solvent molecules and electrons are available in abundance at the reaction site and it is the SEI reaction itself that determines the growth rate of the SEI. The model that is commonly written down is (see [69], [71])

$$j^*_{\text{reaction}} = j_{0,\sigma} \exp\left(\frac{F^* \eta^*_\sigma}{R^*_g T^*}\right) \tag{5.92}$$

where $j^*_{0,\sigma}$ is the SEI exchange current density (a constant),

$$\eta^*_\sigma = \phi^*_{\text{s,n}} - \phi^*_{\text{e,n}} - U^*_\sigma - r^*_\sigma L^*_\sigma (j^*_{\text{n}} + j^*_{\text{reaction}}) \tag{5.93}$$

is the SEI reaction overpotential, U^*_σ is the SEI OCP, and r^*_σ is the SEI resistivity. Unlike the solvent diffusion-limited growth model, this model will give rise to an SoC dependent growth rate. However, since the SEI resistivity is typically small, the growth rate is only weakly dependent upon the thickness of the SEI. As a result the model predicts a linear capacity fade [71] which contrasts with the slowing rate of capacity fade observed experimental in [15].

Electron-migration-limited growth assumes that transport of electrons through the inner SEI determines the growth rate of the SEI. This the same case that we consider in the development of our asymptotic

SEI growth model. However, the commonly written ad-hoc model differs significantly from the model that we have derived. This ad-hoc model takes the form (see [82], [87])

$$j_{\text{electron}}^* = \kappa_\sigma^* \frac{\eta_\sigma^*}{L_\sigma^*}, \tag{5.94}$$

where κ_σ^* is the conductivity of the SEI,

$$\eta_\sigma^* = \phi_{\text{s,n}}^* - \phi_{\text{e,n}}^* - U_\sigma^* \tag{5.95}$$

is the SEI overpotential, and U_σ^* is the OCP of the SEI growth reaction. The model is inversely proportional to the thickness of the SEI and so recovers the observed square root of time capacity fade rate of [15]. Additionally, this model contains a potential dependence and therefore will produce an SoC dependent capacity fade. The SoC dependence of the capacity fade predicted by this model was studied in [82]. It was found that this model does not fit well to the SoC dependence of the experimental capacity fade data of [35] even when only a single temperature and checkup time was considered.

A final novel model of SEI growth was proposed in [82] to explain the SoC dependence of capacity fade. In this model, the authors propose that diffusion of lithium ion interstitials (which carry electrons to the SEI reaction site) is the limiting mechanism in SEI growth. The model that they develop takes the form

$$j_{\text{inter}}^* = -\frac{F^* D_{\text{Li,i}}^*}{L_\sigma^*} c_{\text{Li,i,0}}^* \exp\left(-\frac{F^*}{R_{\text{g}}^* T^*}(\phi_{\text{s,n}}^* - \phi_{\text{s,e}}^*)\right), \tag{5.96}$$

where $D_{\text{Li,i}}^*$ is the diffusivity of lithium ion interstitials in the inner SEI, and $c_{\text{Li,i,0}}^*$ is the concentration of lithium ion interstitials in the inner SEI when $\phi_{\text{s,n}}^* = \phi_{\text{e,n}}^*$. This model is very similar in structure to our asymptotic expression for SEI growth, with the only difference being a factor of $1/2$ within the exponential.

In summary, of the ad-hoc zero-dimensional SEI models, it appears that only one model, lithium ion interstitial growth, is consistent with the available capacity fade data. Since both our SEI model and the lithium atom interstitial model can explain the available data fairly well, are of very similar forms, and accurate parameter values are difficult to obtain for these models, it is difficult at this stage to determine which model is a more accurate representation of the true physical process. One benefit of our approach, however, is that we have consistently developed an associated intercalation reaction. Of the available literature, we have not observed any other models that attempts to do this for growth limited by processes within the inner SEI.

5.7 DYNAMIC LOADS

We now introduce our SEI model into a full physics-based model of a lithium-ion cell motivated by those derived in §3. This allows us to study the effects of dynamic load profiles on cell degradation and therefore suggest ways to use a cell that reduce degradation. We begin by introducing our model in dimensional form and then introduce scalings to write it in dimensionless form. After introducing our model, we study the cases of a fixed throughput, fixed depth-of-discharge (DoD), and SEI growth during a realistic drive cycle. We also develop a map of 'safe' and 'dangerous' operating conditions for degradation in lithium-ion cells. Throughout this section, we employ notation that has been previously introduced in this thesis.

5.7.1 *Dimensional model*

We will employ the simplest physics-based model of a lithium-ion cell because this illustrates the key extensions that must be made to include SEI growth into a full cell model. This also allows our model to be computationally inexpensive so that we can efficiently compute degradation over periods of a year whilst still resolving the effects of cycling on the timescale of hours. We arrive at this model by taking the limit of fast diffusion within the active material particles in the SPM (3.21). In taking this limit, the concentration within each particle become uniform and we can replace the diffusion equation within each of the particles with a single ODE. Therefore, the evolution of the concentrations within the particles is described by

$$\frac{\partial c_{s,n}^*}{\partial t^*} = -\frac{3j_n^*}{F^* R_n^*}, \quad c_{s,n}^*\big|_{t^*=0} = c_{s,n,0}^*, \tag{5.97a}$$

$$\frac{\partial c_{s,p}^*}{\partial t^*} = -\frac{3j_p^*}{F^* R_p^*}, \quad c_{s,p}^*\big|_{t^*=0} = c_{s,p,0}^*. \tag{5.97b}$$

We note that lithium can only enter or leave the negative particle via the intercalation reaction, j_n^*. The SEI formation reaction therefore does not directly consume lithium from the particle. However, lithium may be transported from the particle into the electrolyte and then consumed by the SEI formation reaction. We capture this effect by noting that the SEI consumes a portion of the applied current. Therefore, across the surface of the negative electrode particles, we have

$$j_n^* + j_\sigma^* = \frac{\mathcal{I}^*}{a_n^* L_n^*}. \tag{5.97c}$$

As before, the SEI thickness is given by

$$\frac{\partial L_\sigma^*}{\partial t^*} = -\frac{\bar{V}_\sigma^*}{F^*} j_\sigma^*, \quad L_\sigma^*\big|_{t^*=0} = L_{\sigma,0}^*. \tag{5.97d}$$

On the positive electrode, only the intercalation reaction occurs and therefore we simply have

$$j_{\mathrm{p}}^* = -\frac{\mathcal{I}^*}{a_{\mathrm{p}}^* L_{\mathrm{p}}^*}. \tag{5.97e}$$

The model is then closed with our derived expressions for the negative electrode intercalation and SEI reactions (5.88), which we restate here for clarity

$$j_{\mathrm{n}}^* = j_{0,\mathrm{n}}^* \sinh\left(\frac{F^* \eta_{\mathrm{n}}^*}{2 R_{\mathrm{g}}^* T^*}\right), \tag{5.97f}$$

$$j_{\sigma}^* = -\frac{2 F^* D_{\sigma}^{*-}}{L_{\sigma}^*} c_{\sigma,\mathrm{ref}}^* \exp\left(-\frac{F^*}{2 R_{\mathrm{g}}^* T^*}(\phi_{\mathrm{s,n}}^* - \phi_{\mathrm{e,n}}^*)\right), \tag{5.97g}$$

where

$$j_{0,\mathrm{n}}^* = m_{\mathrm{n}}^*(c_{\mathrm{s,n}}^*)^{1/2}(c_{\mathrm{s,n,max}}^* - c_{\mathrm{s,n}}^*)^{1/2}\left(c_{\sigma,\mathrm{ref}}^*\right)^{1/2}$$
$$\times \exp\left(-\frac{F^*(\phi_{\mathrm{s,n}}^* - \phi_{\mathrm{e,n}}^*)}{4 R_{\mathrm{g}}^* T^*}\right), \tag{5.97h}$$

$$\eta_{\mathrm{s,n}}^* = \phi_{\mathrm{s,n}}^* - \phi_{\mathrm{e,n}}^* - U_{\mathrm{n}}^*(c_{\mathrm{s,n}}^*), \tag{5.97i}$$

and we have taken $\phi_{\mathrm{s,n}}^* = 0$ as the reference potential. Other key variables, such as the terminal voltage, can be recovered by trivial modifications of the expressions presented for the SPM (3.21) however, these are not important for this study. Equations (5.97) form a model of the full lithium-ion cell that is spatially independent, which dramatically reduces computational costs. However, the introduction of the SEI side reaction results in an additional algebraic constraint (5.97c). Therefore (5.97) is a system of differential algebraic equations (DAEs).

5.7.2 *Nondimensionalisation*

We now nondimensionalise (5.97) to improve numerical performance. Without doing this, the large exponential dependence within the algebraic constraint (5.97c) can result in convergence issues. For the full cell variables, we employ the scalings in (3.1) as well as the dimensionless parameters defined in Tables 3.3 and 3.4. We introduce the following scalings for variables associated with SEI growth as follows

$$L_{\sigma}^* = L_{\sigma,0}^* L_{\sigma}, \quad j_{\sigma}^* = \frac{2 F^* D_{\sigma}^{*-} c_{\sigma,\mathrm{ref}}^*}{L_{\sigma,\mathrm{typ}}^*} \exp\left(-\frac{F^* U_{\mathrm{n,ref}}^*}{2 R_{\mathrm{g}}^* T^*}\right) j_{\sigma}, \tag{5.98}$$

and introduce the dimensionless parameters

$$\bar{V}_\sigma = \frac{2\bar{V}_\sigma^* D_\sigma^{*-} c_{\sigma,\text{ref}}^* \exp\left(-\frac{F^* U_{\text{n,ref}}^*}{2R_\text{g}^* T^*}\right) \tau_\text{d}^*}{(L_{\sigma,0}^*)^2}, \tag{5.99}$$

$$C_\sigma = \frac{\tau_\sigma^*}{\tau_\text{d}^*} \tag{5.100}$$

where τ_d^* is the discharge timescale defined in Table 3.2 and

$$\tau_\sigma^* = \frac{2c_{\text{s,n,max}}^* L_{\sigma,0}^*}{D_\sigma^{-*} a_\text{n}^* c_{\sigma,\text{ref}}^* \exp\left(-\frac{F^* U_{\text{n,ref}}^*}{2R_\text{g}^* T^*}\right)} \tag{5.101}$$

is the timescale for the SEI formation reaction. With these scalings, (5.97) becomes

$$\frac{\partial c_{\text{s,n}}}{\partial t} = -\frac{3j_\text{n}}{a_\text{n}}, \quad c_{\text{s,n}}\big|_{t=0} = c_{\text{s,n},0}, \tag{5.102a}$$

$$\frac{\partial c_{\text{s,p}}}{\partial t} = -\frac{3j_\text{p}}{a_\text{p}\gamma_\text{p}}, \quad c_{\text{s,p}}\big|_{t=0} = c_{\text{s,p},0} \tag{5.102b}$$

$$\frac{\partial L_\sigma}{\partial t} = -\bar{V}_\sigma j_\sigma, \quad L_\sigma\big|_{t=0} = 1, \tag{5.102c}$$

$$j_\text{n} + \frac{1}{C_\sigma}j_\sigma = \frac{\mathcal{I}}{L_\text{n}}, \tag{5.102d}$$

$$j_\text{n} = \frac{1}{C_{r_\text{n}}} c_{\text{s,n}}^{1/2}(1 - c_{\text{s,n}})^{1/2}\exp\left(-\frac{1}{4}(\phi_{\text{s,n}} - \phi_{\text{e,n}})\right)$$
$$\times \sinh\left(\frac{\eta_\text{n}}{2}\right), \tag{5.102e}$$

$$j_\sigma = -\frac{1}{L_\sigma}\exp\left(-\frac{1}{2}(\phi_{\text{s,n}} - \phi_{\text{e,n}})\right), \tag{5.102f}$$

$$\eta_\text{n} = \phi_{\text{s,n}} - \phi_{\text{e,n}} - U_\text{n}(c_{\text{s,n}}), \tag{5.102g}$$

$$\phi_{\text{s,n}} = 0, \tag{5.102h}$$

$$j_\text{p} = -\frac{\mathcal{I}}{L_\text{p}}. \tag{5.102i}$$

In the remainder of this section, we will make use of the parameter values from the fit in Figure 5.12 as well as those in Tables 2.1, 2.2, 5.1, and 5.2. As a result, we have

$$\bar{V}_\sigma = \frac{0.0109}{\mathcal{C}}, \quad C_\sigma = 590290.95\mathcal{C} \tag{5.103}$$

where $\mathcal{C}$ is the C-rate. There is one remaining unknown parameter, C_{r_n} the coefficient in our updated intercation reaction (5.102e). We have scaled this equation in exactly the same way as we did in §3. Since the coefficient in the original intercalation reaction, which we will label $C_{r_\text{n},\text{std}}$, was determined experimentally, we will simply relate this parameter to our new parameter through equating the two exchange

current densities at a reference state of $\phi_{s,n}^* - \phi_{e,n}^* = U_n^*(c_{s,n,ref}^*)$, where $c_{s,n,ref}^*$ is the concentration in the negative electrode at this reference state. We shall take $c_{s,n,ref} = 0.5$. Doing this gives the value

$$\mathcal{C}_{r_n} = 0.033\mathcal{C}. \tag{5.104}$$

This is related to the standard prefactor by

$$\mathcal{C}_{r_n} = \mathcal{C}_{r_n,std} \exp\left(-\frac{U_n(c_{s,n,ref})}{4}\right). \tag{5.105}$$

To properly obtain this parameter value, we would require access to the raw experimental data for the exchange current density. Since we do not have this, we have adopted the approach presented above to obtain a parameter value of the correct order of magnitude.

5.7.3 *Results*

We now solve (5.102) numerically using PyBaMM. We start by imposing a sinusoidal input current of the form

$$I_{app}^*(t^*) = I_{max}^* \sin\left(2\pi\omega^* t^*\right) \tag{5.106}$$

where I_{max} is the maximum amplitude of the applied current, and ω^* is the frequency of the applied current. The first case that we study is that of a fixed total throughput of current through the cell. This corresponds to the condition

$$\int_0^{t_{final}^*} |I_{app}^*(t^*)|\, dt^* = a^*, \tag{5.107}$$

where $t_{final}^* > 0$ is the final time of the simulation and $a^* > 0$ is constant. This is enforced by taking

$$I_{max}^* = \frac{a^* 2\sqrt{2\pi}}{\sqrt{4\pi t_{final}^* - \frac{1}{\omega^*}\sin\left(4\pi\omega^* t_{final}^*\right)}}. \tag{5.108}$$

By considering this case we remove the concern that the different usage conditions that we consider lead to different rates of degradation because the cell is being used more (rather than how it is being used). We then choose a^* such that an applied current with a frequency of $\omega^* = 1/(1\,\text{h})$ discharges the cell from $c_{s,n} = 0.8$ to $c_{s,n} = 0.2$ in 30 min. We display our results for a frequency of $\omega^* = 1/(10\,\text{min})$ for initial conditions of $c_{s,n} = 0.2$, 0.4, 0.6, 0.8 and a frequency of $\omega^* = 1/(1\,\text{h})$ for initial conditions $c_{s,n} = 0.8$ in Figure 5.14. We choose to investigate only one case with a frequency of $\omega^* = 1/(1\,\text{h})$ because the cell would fully discharge at lower intial stoichiometries and the case we studied was representative of the key behaviour.
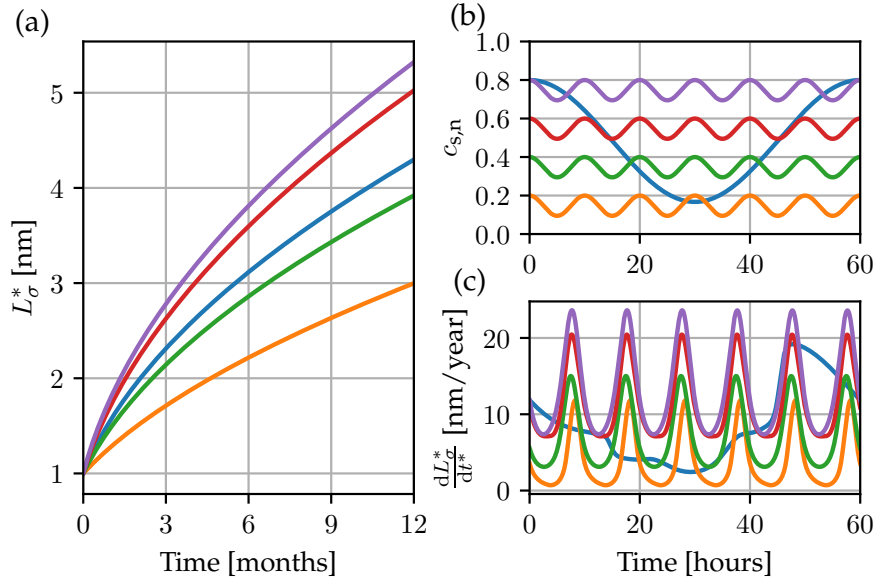
(a)

(b)

(c)

Figure 5.14: SEI growth results for the input current (5.106) with (5.108) for a selection of initial conditions and frequencies (as indicated in (b)): (a) Predicted SEI thickness through time; (b) Negative particle stochiometry profiles in first hour; (c) SEI growth rates during the first hour of cycling (i.e. for 1 nm thick SEI layer). Colouring is consistent across (a), (b), and (c).

In Figure 5.14 (a), we present the predicted thickness of the SEI during a twelve-month simulation of SEI growth. For all frequencies and initial conditions, we observe the characteristic slowing growth rate as the thickness of the layer increase. We also observe a strong dependence on the initial conditions of the cell. By referring to the negative particle stochiometries in Figure 5.14 (b) in conjunction with (a), we can see that higher negative particle stochiometries correspond to a thicker SEI. This aligns with the calendar ageing results for high SoCs in the previous section. For the current with a period of 1 hour (blue), less time is spent at higher negative particle stochiometries than the currents with a period of 10 minutes that are initially at $c_{s,n} = 0.6, 0.8$ (red, purple). However, it also spends less time at low negative particle stochiometries than the currents with a period of 10 minutes that are initially at $c_{s,n} = 0.2, 0.4$ (yellow, green). Therefore, we observe a medium rate of growth for this case. By referring to Figure 5.14 (c), we confirm that negative particle stochiometry (and therefore the negative OCP) is the main determinant of relative SEI growth rates (i.e. a higher stochiometry leads to more growth than a lower stochiometry). However, we also observe that the rate of growth is highly dependent upon the applied current. In particular, charging the cell leads to much higher growth rates than discharging the cell. Therefore, whilst important, stochiometry is not the sole determining factor in the growth rate of SEI upon the application of dynamic loads.

To investigate further the dependence of the SEI growth rate on the magnitude of the applied current, we consider the case in which we hold the depth of discharge, that is the maximum and minimum values of $c_{s,n}$ obtained during a cycle, fixed and vary the magnitude of the current. To do this, we now apply a current I_{max}^* and then set the frequency through

$$\omega^* = \frac{3I_{max}^*}{\pi(c_{s,n,0} - c_{s,n,min})c_{s,n,max}^* a_n^* L_n^* F^* R_n^* L_y^* L_z^*},\tag{5.109}$$

where $c_{s,n,0}$ is the initial stochiometry in the negative particle and $c_{s,n,min}$ is the desired minimum stochiometry. The relation (5.109) is derived by assuming that the intercalation current density is approximately equal to the applied current averaged across the electrode and then integrating the negative particle concentration equation with respect to time from $t^* = 0$ to $t^* = 1/(2\omega^*)$.
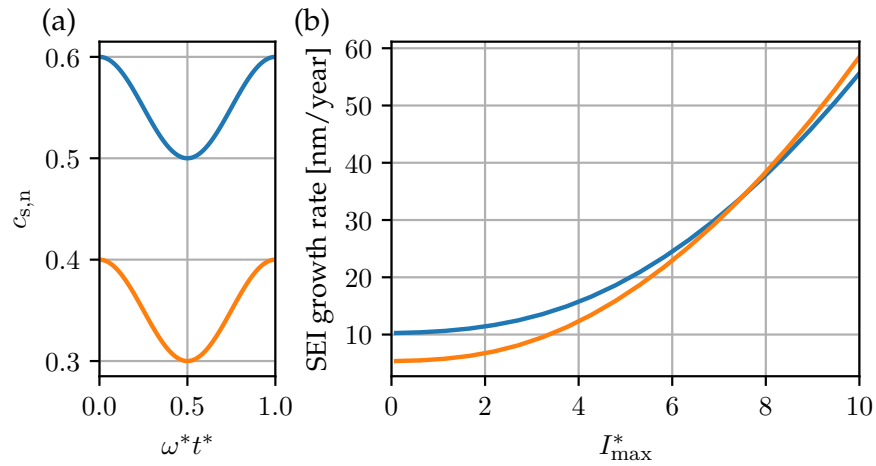

Figure 5.15: Average SEI growth rate over the first cycle (with SEI film of thickness 1 nm) for the input current (5.106) with (5.109) and two cases: $c_{s,n,0} = 0.6$ with $c_{s,n,min} = 0.5$ and $c_{s,n,0} = 0.4$ with $c_{s,n,min} = 0.3$. (a) Negative particle stochiometry; (b) Average SEI growth rate over first cycle.

In Figure 5.15, we consider two cases: $c_{s,n,0} = 0.6$ with $c_{s,n,min} = 0.5$ and $c_{s,n,0} = 0.4$ with $c_{s,n,min} = 0.3$ for (5.106) with (5.109). In both cases the DoD is the same and therefore the total current throughput is also the same. The concentration profiles throughout a single period as displayed in Figure 5.15 (a). In Figure 5.15 (b), we present the average rate of SEI growth during a cycle as a function of the applied current. For both set of initial conditions we observe an increasing rate of SEI growth for higher applied current. Therefore the harder you drive the cell the greater the degradation. For this particular case, we also interestingly see that for high enough currents the stochiometry (and the associated OCP) become relatively less important compared to internal resistances in the cell. We can observe this effect by comparing
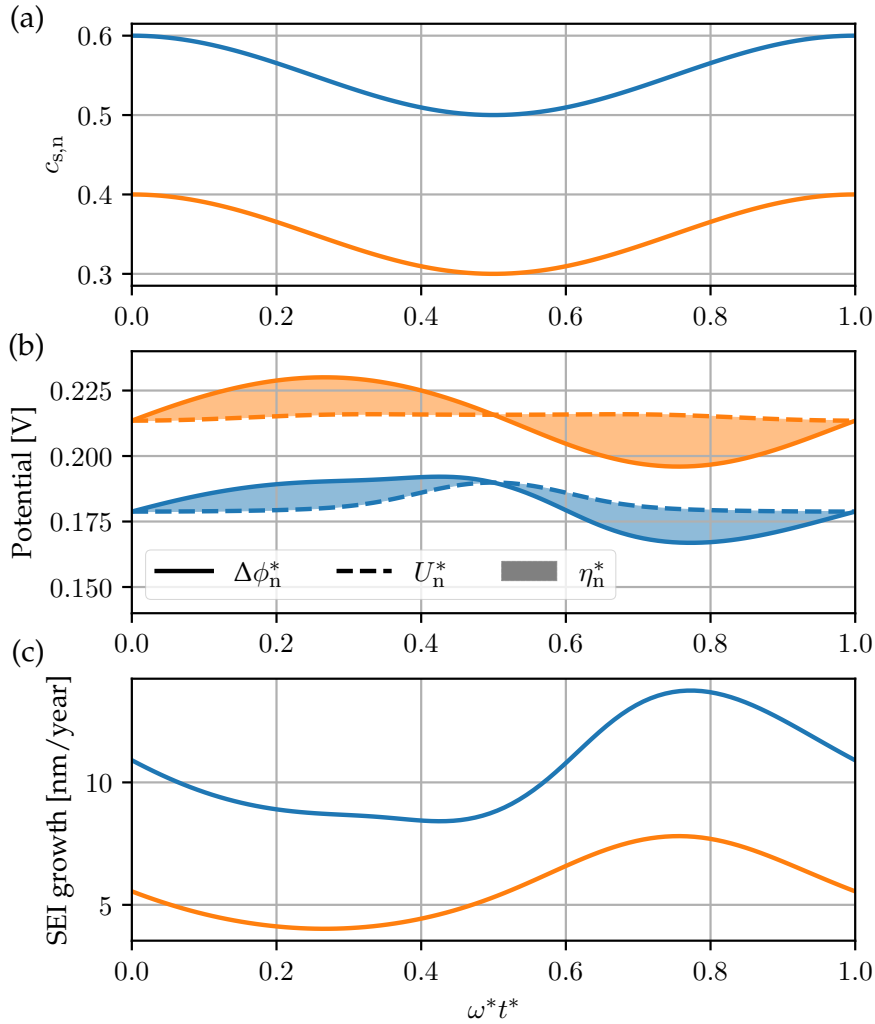
Figure 5.16: SEI growth rate over the first cycle (with SEI film of thickness 1 nm) for the input current (5.106) with (5.109) and $I_{max}^* = 1\,A$ and two cases: $c_{s,n,0} = 0.6$ with $c_{s,n,min} = 0.5$, and $c_{s,n,0} = 0.4$ with $c_{s,n,min} = 0.3$. (a) Negative particle stochiometry; (b) Breakdown of surface potential difference into components; (c) SEI growth rate.

Figure 5.17: SEI growth rate over the first cycle (with SEI film of thickness 1 nm) for the input current (5.106) with (5.109) and $I_{max}^* = 10\,\mathrm{A}$ and two cases: $c_{s,n,0} = 0.6$ with $c_{s,n,min} = 0.5$, and $c_{s,n,0} = 0.4$ with $c_{s,n,min} = 0.3$. (a) Negative particle stochiometry; (b) Breakdown of surface potential difference into components; (c) SEI growth rate.
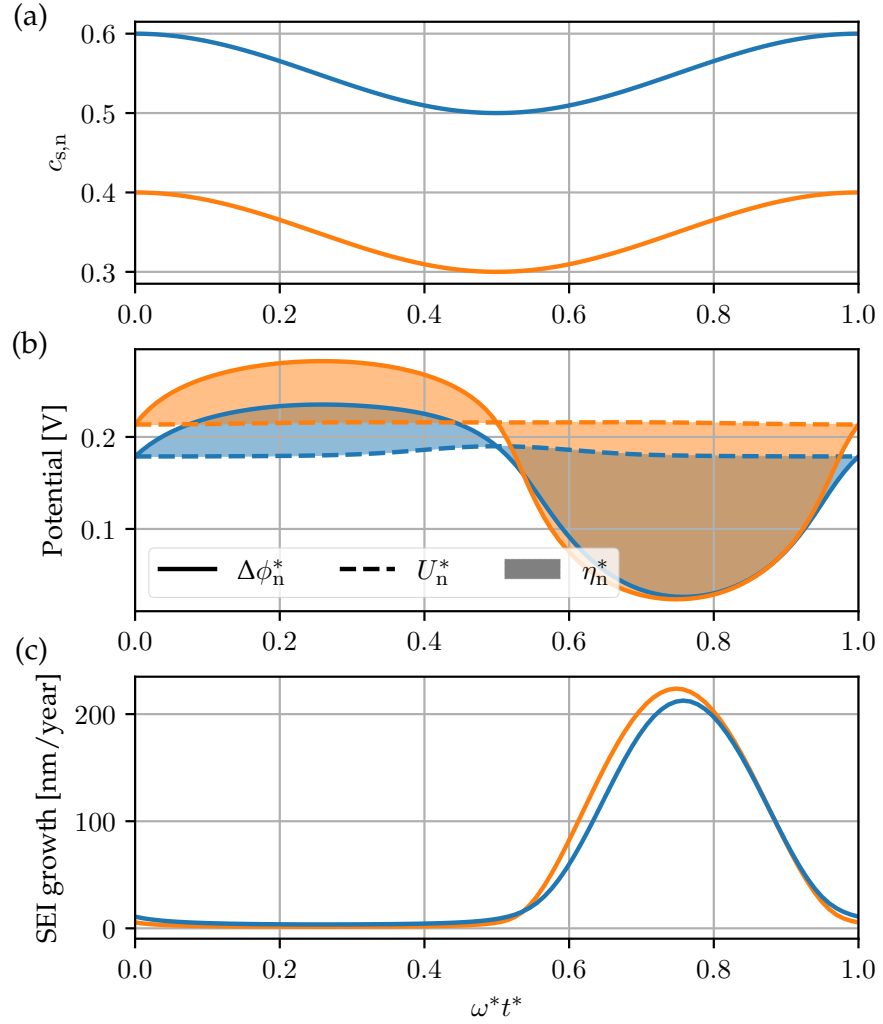
Figure 5.16 for an applied current with $I^*_{\max} = 1$ A and Figure 5.17 for an applied current with $I^*_{\max} = 10$ A.

For the 1 A case, we can observe in Figure 5.16(b) that the size of the reaction overpotentials are small relative to the difference in the OCPs and for the most part the potential difference across the negative particle surface is determined by the OCP. This OCP then drives the observed SEI growth rate presented in Figure 5.16(c) with a lower potential corresponding to higher growth rates. Here we also observe that the overpotentials are such that they increase the surface potential difference during discharge and increase it during charge giving rise to higher SEI growth during charge. In contrast to the 1 A case, in the 10 A, we can observe in Figure 5.17 (b), that the reaction overpotentials contribute significantly more to the surface potential difference. For this particular case, we observe that the overpotentials associated with the $c_{s,n,0} = 0.6$ with $c_{s,n,\min} = 0.5$ case are smaller than those in the $c_{s,n,0} = 0.4$ with $c_{s,n,\min} = 0.3$. As a result, the surface potential difference is lower for the $c_{s,n,0} = 0.4$ with $c_{s,n,\min} = 0.3$ case for much of the critical charge portion of the cycle. In turn, we then observe a higher rate of SEI growth in Figure 5.17 (c) during charge and leads to a higher average SEI growth rate. The reaction overpotential is, in general, a function of SoC and applied current, with the exact form given from the intercalation reaction (5.102e) and the SEI growth reaction. Therefore, this result does not apply generally.

To summarise the dependence of the SEI growth rate upon stochiometry and the applied current, we consider (5.102d)–(5.102g) in isolation of the rest of the model. We set the SEI thickness to be 1 nm but note that growth rates for other thickness can be approximated well by simply scaling the growth rates here by $(1\,\text{nm})/L^*_\sigma$, where L^*_σ is the desired SEI thickness because $\mathcal{C}_\sigma \gg 1$. We then perform a parameter sweep through $c_{s,n}$ and $I^*_{\max}$. The growth rate results are presented in Figure 5.18 (b). Here, we observe that typically larger values of $c_{s,n}$ and more negative values of I^*_{app} (corresponding to charging) give rise to greater rates of SEI growth. The main exception to this is that very low states of charge result in large SEI growth rates. This is because of the form of the intercalation exchange current density, $j^*_{0,n}$ which approaches zero as $c_{s,n}$ approaches zero and leads to high resistances. By comparing Figure 5.18 (a) and (b), we can see that steps in the OCP (e.g. at 0.2, 0.5, and 0.9) correspond to steps in the predicted growth rate. These steps remain a key feature across different currents.
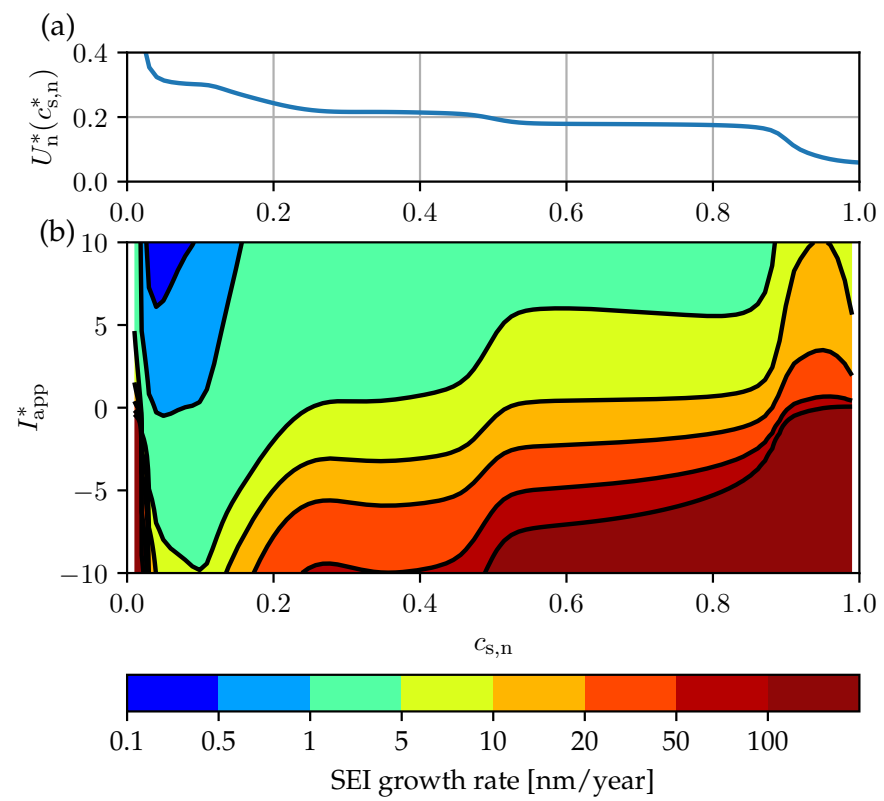
Figure 5.18: SEI growth predicted by (5.102d)–(5.102g) with a 1 nm SEI film: (a) OCP of graphite vs negative particle stochiometry; (b) SEI growth rate vs applied current and negative particle stochiometry.

Finally, as an indication of how the model might be used to explore degradation in other environments, we consider SEI growth in a more realistic situation by applying a US06 drive cycle profile to (5.102). Our results are presented in Figure 5.19. We again observe that the SEI growth rate is highest during charging (through regenerative braking during the drive cycle) and lowest during discharging. From Figure 5.19 (c) we observe that the OCP does not vary over the timeframe of the drive cycle. Therefore, the variations in growth that we observe over the drive cycle are the result of changes in the reaction overpotential at different currents. It remains to be seen if this predicted behaviour is observed in reality.
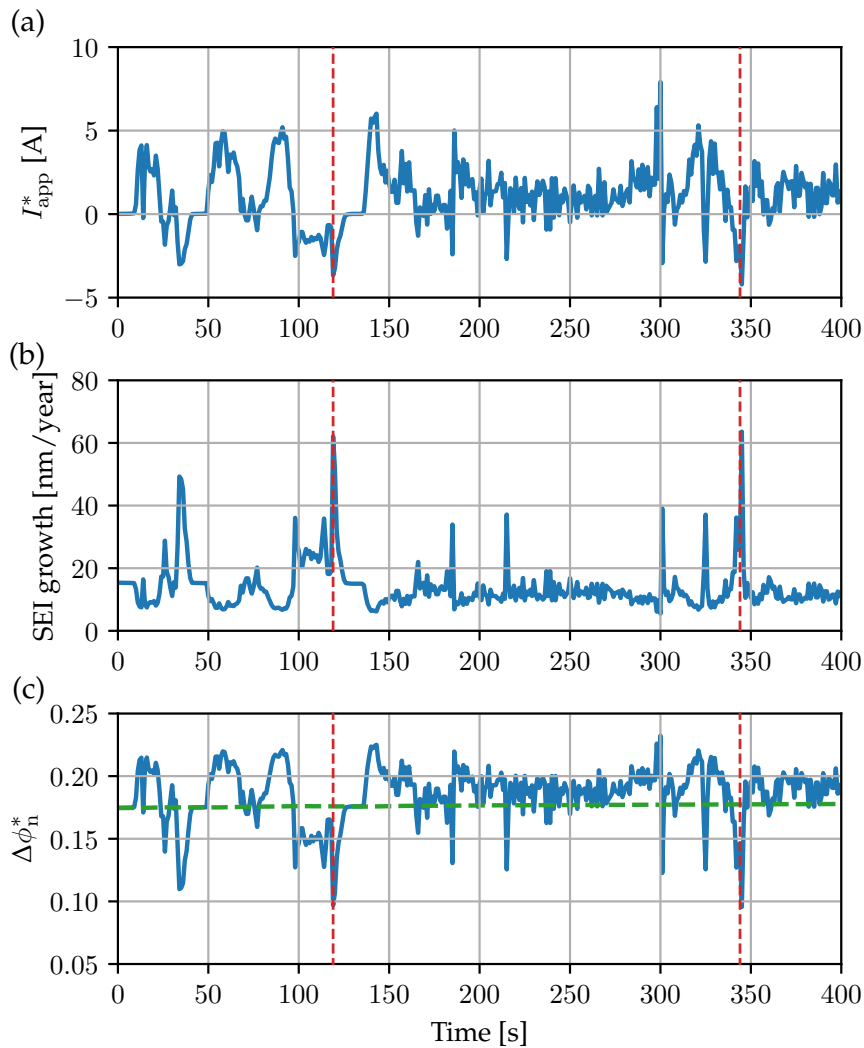

Figure 5.19: Full cell model with SEI growth (5.102) run with drive cycle input: (a) Applied current from US06 data; (b) SEI growth rate; (c) Negative electrode surface potential difference (negative OCP indicated by green dashed line). Points of high SEI growth are indicated by red dashed lines.

5.8   SUMMARY

In this chapter, we have introduced a detailed continuum model of the SEI influenced by DFT calculations. We then performed an extensive asymptotic analysis to develop a set of simple models valid in various limiting cases. Following this, we re-wrote one of these asymptotically reduced models in terms of known electrochemical quantities and then verified this model by comparing it to experimental data to confirm that this model can recover the SoC, temporal, and temperature dependence of the capacity fade of lithium-ion batteries. Finally, we incorporated this validated SEI model into a simplified model of a full lithium-ion cell that is inspired by the full cell battery models that we derived in §3. This allowed us to study SEI growth under the imposition of different dynamic load profiles. The SEI growth rates observed in our numerical experiments were highly dependent upon the potential difference across the surface of the negative particles and in turn the negative OCP and intercalation overpotential. Depending upon the applied current, the relative importance of the OCP and reaction overpotential changed. We mapped out this dependence in Figure 5.18, which serves a guide to 'safe' and 'dangerous' operating conditions for degradation. To accurately model SEI growth it is critical to capture the negative OCP and intercalation overpotentials correctly. Since we have made the assumption of fast diffusion in the particle in the chapter, our simple full cell model does not accurately capture the particle surface concentration. Therefore, the results within the dynamic load section should be viewed only qualitatively and as a demonstration of principle. Ongoing collaborations are taking place to include SEI growth into PyBaMM so that SEI growth can be studied within the context of more detailed cell models. The approach, however, remains the same as that taken here.

6

CONCLUSIONS

In this chapter, we first summarise the main results obtained within this thesis. We follow this with a brief discussion of possible future work on this topic and then conclude with some closing remarks.

6.1 SUMMARY OF RESULTS

This thesis has been directed towards addressing two key challenges in the development of the understanding of degradation in lithium-ion batteries. The first is the development of mathematical models of lithium-ion batteries that can be employed to simulate the performance of a full lithium-ion efficiently. The second challenge is the development of accurate models of the key degradation mechanisms. We addressed the first of these challenges in Chapters 3 and 4 of this thesis and we addressed the second challenge in Chapter 5. To allow the work in this thesis to be taken on and employed by others in the battery community, all of the models developed in this thesis were implemented within an easy-to-use open-source battery modelling software called PyBaMM.

In Chapter 2, we introduced the standard one-dimensional model of a lithium-ion battery, referred to as the Doyle–Fuller–Newman (DFN) model. Then in Chapter 3, we simplified the DFN model by considering the limit of a long electrolyte diffusion timescale relative to the discharge timescale. We derived the classical SPM and a new model that accounts for an additional electrolyte correction, which we referred to as the SPMe. We quantified the asymptotic errors in terms of key ratios of parameters and then provided a full numerical comparison of the models that we derived. We found that the SPMe offers an order of magnitude reduction in solve time compared to the DFN with only a small increase in error. Further, the solve time of the SPM was comparable to the SPMe but the SPMe offered a significant increase in accuracy. We then considered ad-hoc variants of the SPMe from the literature and compared their performance with that of our asymptotic SPMe. We found that our asymptotic SPMe performed better than these model and identified that the reason for this improvement lay in the failure of ad-hoc models to recognise that the single particle in the SPMe represents a theoretical averaged particle and not any one particular particle. As a result, the overpotential terms in our model were written with reference to electrode-averaged quantities whereas those of ad-hoc models were written with reference to particular points in the lithium-ion cell. In addition to this, we also identified the cause of a discrepancy between the SPMe and DFN, which occurred when

the OCP had a large second derivative. In response to this, we proposed a further extension to the SPMe that corrected this behaviour and identified the additional computation effort required to address the discrepancy.

In Chapter 4, we turned our attention to three-dimensional effects in lithium-ion pouch cells. Here, we proposed a three-dimensional thermal model of a lithium-ion pouch cell inspired by the one-dimensional DFN model. We then took the limit of high conductivity in the current collectors to derive a model with a 2+1D structure (2D current collectors with a 1D through-cell model at every point). We provided a numerical comparison of the full and reduced model, and found that the results were equivalent up to errors of a similar size to numerical errors. Henceforth we adopted the 2+1D model. We then proceeded by considering lower-order truncations of the asymptotic expansion in this same limit. At leading order, we then recovered the standard one-dimensional DFN model and then at first order we obtained an 'in-between' model that accounted for some of the higher dimensional effects but utilised just one averaged through-cell model. We then considered different combinations of the asymptotic limits taken in this chapter and the asymptotic limits taken in Chapter 3 to develop a suite of reduced-order models of a lithium-ion pouch cell. We provided a full numerical comparison of this suite of models. We found that in general the computational budget should be allocated towards a more detailed through-cell model instead of models that account for higher-dimensional effects. However, when thermal effects are included accurately capturing higher dimensional effects can be essential. In which case, we found that a model such as the SPMeCC offers a good balance between numerical simplicity and accuracy. We also found that thermal effects could not be properly captured by using the classical SPM because electrolyte Ohmic heating accounted for a significant proportion of the heat generation in the cell.

Finally, in Chapter 5, we developed a detailed electrochemical model of the inner SEI based upon observations in DFT simulations. We then conducted asymptotic analysis for several physically relevant limits to simplify this model. We choose to consider one of these limits in detail, namely the limit of slow electron migration with a slow lithium intercalation reaction on the graphite–SEI interface, and re-wrote the model in terms of measurable electrochemical quantities. Upon doing this, we adopted a simple experimentally motivated model of a lithium-ion battery to allow us to compare our SEI model with experimental capacity fade data for calendar aged cells. We found that our model could recover the temporal, thermal, and SoC dependence of capacity fade excellently for medium to high SoCs. However, at low SoC our model failed to capture capacity fade adequately, which we conjectured to be the result of other degradation mechanisms. We then combined our work on full cell models from Chapter 3 and the work developing

the SEI growth model to incorporate SEI growth into a simple model of a full lithium-ion cell. We then studied the effect of dynamic load profiles on the rate of SEI growth. Here, we found that SEI grows greatest at high SoCs and high charging currents, a finding that is highly relevant for mitigating degradation caused by the fast charging of electric vehicles.

6.2   FUTURE WORK

The study of degradation in lithium-ion batteries is a highly complex topic with many of the degradation mechanisms still little understood. A few of the key mechanisms that we haven't touched upon in this thesis are

- lithium plating

- dendrite formation

- loss of active material (through mechanical cracking)

- current collector dissolution

- binder decomposition.

Each of these mechanisms can be included as an extension to the full cell models that we introduced in Chapters 2 and 3. Throughout this thesis, we have assumed that diffusion in the particles is governed by Fick's law. However, there is evidence to suggest that the particles more likely behave as phase-changing material and so it is of interest to consider extensions for different particle physics. From including SEI growth into a full cell model, it is apparent that there is a clear separation of the discharge timescale and the timescale for SEI growth. A multiple scales based approach to solving this problem would therefore likely offer a more efficient approach to simulating long-term degradation than the direct numerical approach we adopted. Such an approach would also be of interest for efficiently modelling other degradation mechanisms.

6.3   CLOSING REMARKS

The work in this thesis has been motivated by the need to understand degradation in lithium-ion batteries. To this end, we addressed two key challenges within this topic: the development of efficient mathematical models and the development of accurate models of key degradation mechanisms. To address the first of these challenges, we have developed a suite of reduced-order models of a lithium-ion battery, characterised the domain of applicability of each model, and further implemented these models within an easy-to-use open-source battery modelling software so that these models are readily available for use by other researchers and industry. In the second of these challenges,

we choose to focus our attention on modelling the key degradation mechanism: SEI growth. This model was able to accurately recover the SoC, thermal, and temporal dependence of SEI growth. We were then able to employ the model to provide insights into operating conditions that give rise to higher rates of degradation.

Whilst much work remains for a full understanding of the degradation of lithium-ion batteries to be achieved, we have made significant contributions to the required mathematical framework. Further, we have promoted a collaborative approach to research through the development of open-source software, which we believe is essential to tackle this complex problem.

PYBAMM

With lithium-ion batteries emerging as a key technology of the 21st century and the battery modelling research community growing rapidly [57], there is a need to bring together battery research in a coherent way. To address this need, PyBaMM's mission is as follows:

> PyBaMM's mission is to accelerate battery modelling research by providing an open-source framework for multi-institutional interdisciplinary collaboration.

By being open-source, PyBaMM removes two important factors that can hinder software collaboration. The first factor is the cost of usage. It is not uncommon for there to be limited licenses available in university departments for commercial software and many start-ups cannot afford the costs of commercial software. The second factor lies in the ability to modify source code. By allowing this, researchers are not limited by the functionality deemed most important by a commercial software development team and can instead add features as they require.

PyBaMM offers improved collaboration and research impact in battery modelling by providing a modular framework through which either existing or new tools can be combined in order to solve continuum models for batteries. For example, PyBaMM can easily be adapted to incorporate new models, alternative spatial discretisations, new time-stepping algorithms, and new experimental protocols. Any such additions can then immediately be used with the existing suite of models already implemented, and comparisons can be made between different models, discretisations, or algorithms with variables such as hardware, software and implementation details held fixed. Similarly, additional physics can be incorporated into the existing models, without needing to start from scratch to study each new effect. This facilitates the simultaneous study of a range of extensions to the standard battery models, for example by coupling together several degradation mechanisms.

A.1 IMPLEMENTATION AND ARCHITECTURE

PyBaMM's architecture is based around two core components. The first is the expression tree, which encodes mathematical equations symbolically (see Figure A.1). Each expression tree consists of a set of symbols, each of which represents either a variable, parameter, mathematical operation, matrix, or vector. Every battery model in PyBaMM is then defined as a collection of symbolic expression trees. The expression trees

in each model are organised within Python dictionaries representing the governing equations, boundary equations, and initial conditions of the model. An example of implementing a simple diffusion model using expression trees is provided in Appendix A.4.

$$\nabla \cdot (D \nabla u) \longleftrightarrow$$
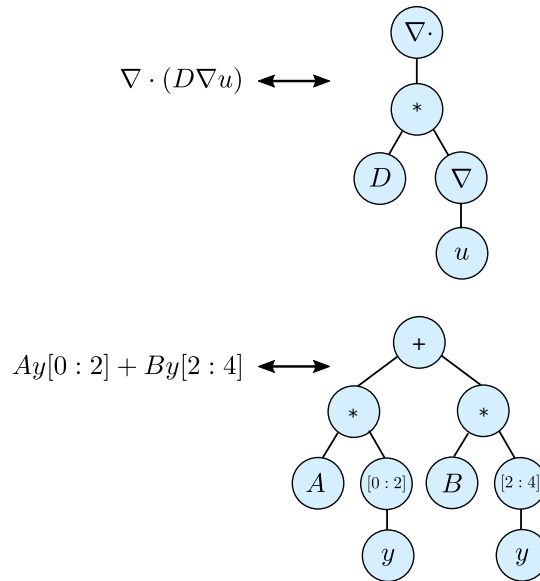
$$Ay[0:2] + By[2:4] \longleftrightarrow$$

Figure A.1: Models are encoded and passed down the pipeline using a symbolic expression tree data-structure. Leafs in the tree represent parameters, variables, matrices etc., while internal nodes represent either basic operators such multiplication or division, or continuous operators such as divergence or gradients.

The second core component of PyBaMM's architecture is the pipeline process (see Figure A.2). In the pipeline process different modular components operate on the model in turn. The pipeline is constructed using Python classes, so that users have full control over the entire process, and can customise the pipeline or insert their own components at any stage. Figure A.2 depicts a typical pipeline with the following stages:

1. Define a battery model and geometry using PyBaMM's syntax. This generates a collection of expression trees representing the model.

2. Parse the expression trees for the battery model and geometry, replacing any parameters with their provided numerical values. For convenience, parameter values may be provided in a csv file.

3. Mesh the geometry and discretise the model on this mesh with user-defined spatial methods. This process parses each expression tree converting variables into state vectors, and spatial operators (e.g. gradient and divergence) into matrices (accounting for the boundary conditions of the model).

4. Solve the model using a time-stepping algorithm. PyBaMM offers a consistent interface to a number of ODE and DAE solvers (including SciPy [95] and SUNDIALS [28], [29], [47]). One of the main benefits of PyBaMM's expression tree structure is that it provides the capability to automatically compute the Jacobian for any model, using symbolic differentiation, which significantly improves the performance of the numerical solvers.

5. Post-processes the solution. Built-in post-processing utilities provided access to any user-defined output variables at any solution time or state. Additionally, PyBaMM includes several visualisation utilities which allow for easy plotting and comparison of any of the model variables (for example output, see Figure A.3).

An example of employing the PyBaMM pipeline process to solve a model is provided in Appendix A.5.
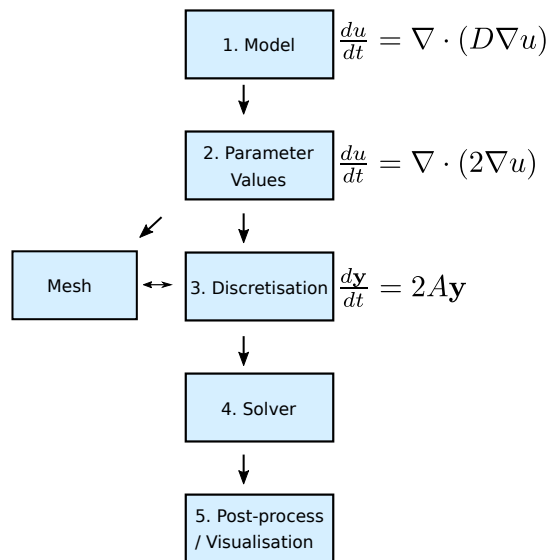

Figure A.2: PyBaMM is designed around a pipeline approach. Models are initially defined using mathematical expressions encoded as expression trees. These models are then passed to a class which sets the parameters of the model, before being discretised into linear algebra expressions, and finally solved using a time-stepping class.

A.2 QUALITY CONTROL

Tests in PyBaMM are performed within the `unittest` framework. We follow a test-driven development process, and unit tests are implemented for every class with unit test code coverage consistently above 98%. In addition, a smaller set of integration tests are implemented to ensure the end-to-end reliability of the code. The integration tests consist of tests that check every model in PyBaMM can be processed and
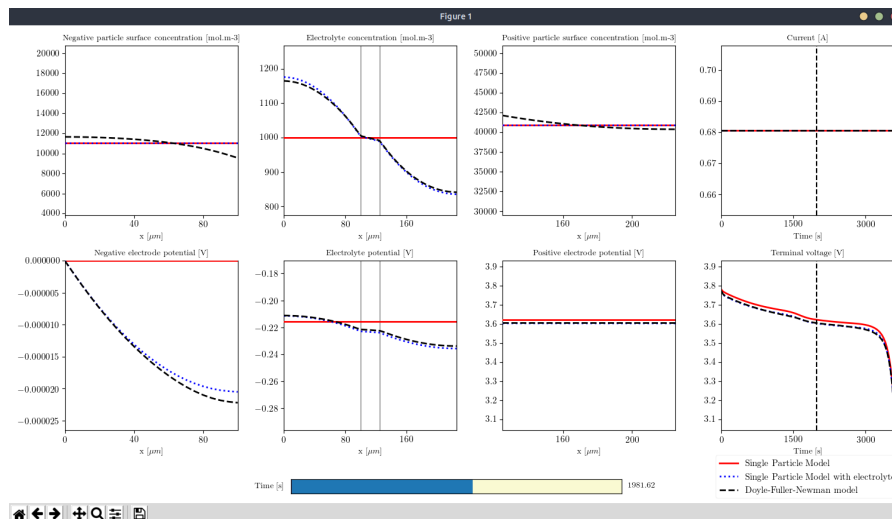
Figure A.3: Interactive output of inbuilt visualisation. The user can select the time at which to view the output using the time-slider bar at the bottom. For a given list of variables and solved models, such plots are automatically generated.

solved for a set of default inputs, convergence tests between reduced-order and full-order models, convergence tests for each spatial method, and tests for each solver type. PyBaMM is developed using git version control, with all unit and integration tests being run using GitHub actions for Linux (Ubuntu 18.04), macOS Big Sur and Windows 10 every time a pull request is made and every night. The main PyBaMM repository contains a selection of Jupyter Notebooks that serve as a "getting started" documentation for PyBaMM, and a useful set of examples on how to use PyBaMM for different tasks such as creating a new battery model, running the existing models, or changing the default parameters. These are tested along with the main PyBaMM code to ensure they are up to date. To ensure contributions to the code are of high quality, all pull requests are peer-reviewed by other contributors and must be approved before being merged into the main code branch. Further to ensure stability, PyBaMM has a working develop branch and a stable master (release) branch. More information can be found within the `CONTRIBUTING.md` file in the PyBaMM repository.

A.3   AVAILABILITY AND INSTALLATION

PyBaMM can be run on any Linux, MacOS, and Windows systems that has Python 3.6 or higher installed. PyBaMM is available on PyPI, the standard python package repository and can, therefore, be installed simply using `pip install pybamm`. In addition to a simple local install, PyBaMM is also available to use within a browser via Google Colab. Making PyBaMM simple to install and easy to try within a browser has had the effect of lowering the barriers to usage of the software. This

increases the numbers of possible users within the battery research community. For more information, please see the PyBaMM GitHub repository.

In this section, we present an example of how to enter a simple diffusion model in PyBaMM. This model serves as a good representation of the types of models that arise in battery modelling because it contains most of the key components: spatial operators, parameters, Dirichlet and Neumann boundary conditions, and initial conditions.

We consider the concentration of some species c, on a spatial domain $x \in [0, 1]$, and at some time $t \in [0, \infty)$. The concentration of the species is taken to evolve according to a nonlinear diffusion process with the concentration being fixed at $x = 0$ and a constant inward flux of species imposed at $x = 1$. Mathematically, the model is stated as

$$\frac{\partial c}{\partial t} = \nabla \cdot (D(c)\nabla c) \qquad \text{in } 0 < x < 1, \quad t > 0, \qquad \text{(A.1a)}$$

$$c = 1 \qquad \text{at } x = 0, \qquad \text{(A.1b)}$$

$$D(c)\frac{\partial c}{\partial x} = 1 \qquad \text{at } x = 1, \qquad \text{(A.1c)}$$

$$c = x + 1 \qquad \text{at } t = 0, \qquad \text{(A.1d)}$$

where $D(c) = k(1 + c)$ is the diffusion coefficient and k is a parameter, which we will refer to as the diffusion parameter.

In Listing A.1, we provide the PyBaMM code implementing (A.1). Note that operator overloading of $*$ and $+$ allows symbols to be intuitively combined to produce expression trees. A more detailed and up-to-date introduction to the syntax is provided in the online examples available on GitHub.

The model is now represented by a collection of expression trees and can, therefore, be solved by passing it through the pipeline just like any other model in PyBaMM. Additionally, extending the model to include additional physics is simple and intuitive due to the simple symbolic representation of the underlying mathematical equations. For example, we can add a source term to the governing equation (A.1a) by only modifying one line of code (line 10 of Listing A.1) and still obtain useful properties of the model such as the analytical Jacobian.

Listing A.1: Defining a model in PyBaMM.

```python
1   # 1. Initialise model
2   model = pybamm.BaseModel()
3
4   # 2. Define parameters and variables
5   c = pybamm.Variable("c", domain="unit line")
6   k = pybamm.Parameter("Diffusion parameter")
7
8   # 3. State governing equations
9   D = k * (1 + c)
10  dcdt = pybamm.div(D * pybamm.grad(c))
11  model.rhs = {c: dcdt}
12
13  # 4. State boundary conditions
14  D_right = pybamm.BoundaryValue(D, "right")
15  model.boundary_conditions = {
16    c: {
17      "left": (1, "Dirichlet"),
18      "right": (1/D_right, "Neumann")
19    }
20  }
21
22  # 5. State initial conditions
23  x = pybamm.SpatialVariable("x", domain="unit line")
24  model.initial_conditions = {c: x + 1}
```

A.5 SOLVING A MODEL

We now consider an example of solving a PyBaMM model by passing it through the pipeline process. Here, we solve the Doyle-Fuller-Newman (DFN) model, which is the standard model of a lithium-ion battery [21]. The code is presented in Listing A.2. Please see the PyBaMM documentation for more detailed and up-to-date examples.

The common interface of all PyBaMM models makes it easy to perform the pipeline process as illustrated here upon multiple models or the same model with different options activated. Therefore, comparing the results of different models, mesh types, discretisations, and solvers then becomes straightforward within the PyBaMM framework.

A.6 COMPARISON WITH COMSOL

Here we give a brief comparison of the numerical solution of the standard 1D DFN model obtained using PyBaMM with that from COMSOL, to give an estimate of the effect of the different in spatial discretisation methods and time-stepping routines used by the two software packages.

In Figure A.4, we present the computed terminal voltage and volume-averaged temperature across a range of C-rates. Panels (c) and (d) show the differences between the two solutions. It can be seen that the difference in the terminal voltage is no more than $\mathcal{O}(10^{-4})$ V. Similarly, the difference in the computed average cell temperature is also at most

Listing A.2: Solving a model in PyBaMM.

```python
# 1. Load model and geometry
model = pybamm.lithium_ion.DFN()
geometry = model.default_geometry

# 2. Process parameters
param = model.default_parameter_values
param.process_model(model)
param.process_geometry(geometry)

# 3. Set mesh
mesh = pybamm.Mesh(
        geometry,
        model.default_submesh_types,
        model.default_var_pts
    )

# 4. Discretise model
disc = pybamm.Discretisation(
        mesh, model.default_spatial_methods
    )
disc.process_model(model)

# 5. Solve model
t_eval = numpy.linspace(0, 0.2, 100)
solution = model.default_solver.solve(model, t_eval)
```

$\mathcal{O}(10^{-4})$ K. At low to moderate C-rates, a large spike in the difference is observed towards the end of the simulation where the OCV in highly non-linear. Both meshes were refined until the solutions converged, but the differences still persisted, which leads us to believe the discrepancy is due to slight differences in the time-stepping strategy and approach used to couple the micro- and macro-scale problems.

To investigate the influence of the mesh size in the PyBaMM implementation of the DFN model a number of simulations were performed with an increasing number of finite volumes per domain. Table A.1 shows the normalised root mean square (RMS) error in the potentials, concentrations, voltage and temperature obtained by solving the model in PyBaMM as the number of finite volumes N is increased. The RMS error was computed with respect to the solution obtained using COMSOL's "extremely fine" mesh (45 elements in each electrode, 11 elements in the separator), which was typically solved in around 70s.
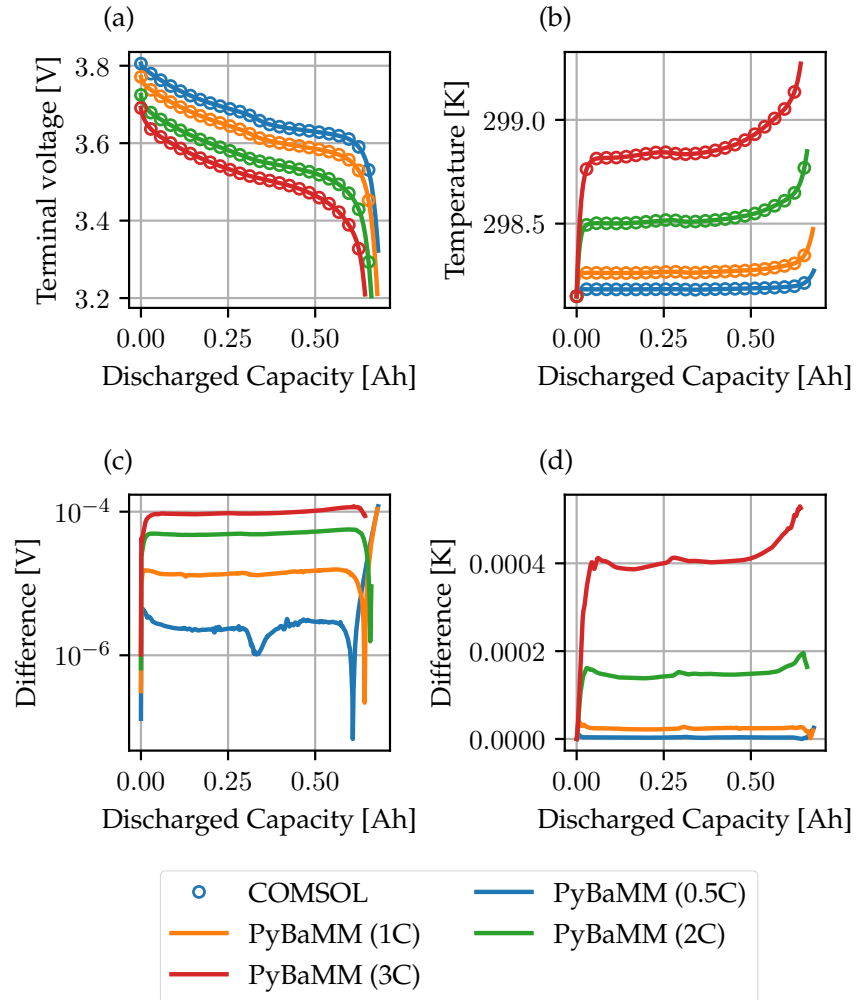
Figure A.4: Comparison of (a) the terminal voltage and (b) the temperature obtained from the solution of the 1D DFN model from PyBaMM and COMSOL for a range of C-rates. The differences in the voltage and temperature between the two solutions are shown in panels (c) and (d), respectively. Note the logarithmic scale in panel (c). Here we used 128 finite volumes per domain in the PyBaMM model and the COMSOL model was solved on an "extremely fine" mesh (45 elements in each electrode, 11 elements in the separator). Both time-stepping routines used a relative tolerance of 10^{-6}.

N	$\phi_{\text{s,n}}^*$	$\phi_{\text{s,p}}^* - V^*$	ϕ_{e}^*	$c_{\text{s,n,surf}}^*$	$c_{\text{s,p,surf}}^*$	c_{e}^*	V^*	T^*	Solution time [s]
4	2.56×10^{-2}	6.59×10^{-2}	6.06×10^{-3}	8.62×10^{-3}	3.72×10^{-3}	2.53×10^{-3}	4.60×10^{-3}	2.86×10^{-5}	0.1712
8	6.86×10^{-3}	1.64×10^{-2}	1.75×10^{-3}	2.57×10^{-3}	9.51×10^{-4}	6.47×10^{-4}	1.37×10^{-3}	8.53×10^{-5}	0.1925
16	2.05×10^{-3}	4.11×10^{-3}	6.32×10^{-4}	9.43×10^{-4}	2.56×10^{-4}	1.75×10^{-4}	4.04×10^{-4}	2.45×10^{-6}	0.3027
32	8.78×10^{-4}	1.03×10^{-3}	3.48×10^{-4}	5.50×10^{-4}	8.26×10^{-5}	6.30×10^{-5}	1.40×10^{-4}	7.74×10^{-7}	0.6790
64	6.27×10^{-4}	2.71×10^{-4}	2.78×10^{-4}	4.64×10^{-4}	4.00×10^{-5}	4.26×10^{-5}	7.43×10^{-5}	3.60×10^{-7}	2.119
128	5.76×10^{-4}	1.08×10^{-4}	2.61×10^{-4}	4.45×10^{-4}	2.98×10^{-5}	3.87×10^{-5}	6.80×10^{-5}	2.59×10^{-7}	7.49

Table A.1: Normalised RMS difference between the PyBaMM and COMSOL solution of the 1D DFN model for a selection of model variables. The tabulated quantities for a variable ψ were computed as $\text{RMS}(\psi_{\text{PyBaMM}} - \psi_{\text{COMSOL}})/\text{RMS}(\psi_{\text{COMSOL}})$. Here N is the number of finite volumes per domain in the PyBaMM model. The PyBaMM solution was compared to the COMSOL solution on an "extremely fine" mesh (45 elements in each electrode, 11 elements in the separator). Both time stepping routines used a relative tolerance of 10^{-6}.

BIBLIOGRAPHY

[1] D. P. Abraham, M. M. Furczon, S. H. Kang, D. W. Dees, and A. N. Jansen, "Effect of electrolyte composition on initial cycling and impedance characteristics of lithium-ion cells," *Journal of Power Sources*, vol. 180, no. 1, pp. 612–620, 2008.

[2] A. Aitio, S. G. Marquis, P. Ascencio, and D. Howey, "Bayesian parameter estimation applied to the Li-ion battery single particle model with electrolyte dynamics," *arXiv preprint*, vol. arXiv, p. 2001.09890, 2020, (Accepted to IFAC 2020).

[3] A. M. Andersson, A. Henningson, H. Siegbahn, U. Jansson, and K. Edström, "Electrochemically lithiated graphite characterised by photoelectron spectroscopy," *Journal of Power Sources*, vol. 119, pp. 522–527, 2003.

[4] D. Aurbach, "Review of selected electrode-solution interactions which determine the performance of Li and Li ion batteries," *Journal of Power Sources*, vol. 89, no. 2, pp. 206–218, 2000.

[5] D. Aurbach, Y. Ein-Ely, and A. Zaban, "The surface chemistry of lithium electrodes in alkyl carbonate solutions," *Journal of The Electrochemical Society*, vol. 141, no. 1, pp. L1–L3, 1994.

[6] D. R. Baker and M. W. Verbrugge, "Temperature and current distribution in thin-film batteries," *Journal of The Electrochemical Society*, vol. 146, no. 7, pp. 2413–2424, 1999.

[7] A. Barré, B. Deguilhem, S. Grolleau, M. Gérard, F. Suard, and D. Riu, "A review on lithium-ion battery ageing mechanisms and estimations for automotive applications," *Journal of Power Sources*, vol. 241, pp. 680–689, 2013.

[8] L. Benitez and J. M. Seminario, "Ion diffusivity through the solid electrolyte interphase in lithium-ion batteries," *Journal of The Electrochemical Society*, vol. 164, no. 11, E3159–E3170, 2017.

[9] D. Bernardi, "A general energy balance for battery systems," *Journal of The Electrochemical Society*, vol. 132, no. 1, p. 5, 1985.

[10] C. R. Birkl, M. R. Roberts, E. McTurk, P. G. Bruce, and D. A. Howey, "Degradation diagnostics for lithium ion cells," *Journal of Power Sources*, vol. 341, pp. 373–386, 2017.

[11] A. M. Bizeray, D. A. Howey, and C. W. Monroe, "Resolving a discrepancy in diffusion potentials, with a case study for Li-ion batteries," *Journal of The Electrochemical Society*, vol. 163, no. 8, E223–E229, 2016.

[12]   A. M. Bizeray, J. H. Kim, S. R. Duncan, and D. A. Howey, "Identifiability and parameter estimation of the single particle lithium-ion battery model," *IEEE Transactions on Control Systems Technology*, vol. 27, no. 5, pp. 1862–1877, 2018.

[13]   A. M. Bizeray, S. Zhao, S. R. Duncan, and D. A. Howey, "Lithium-ion battery thermal-electrochemical model-based state estimation using orthogonal collocation and a modified extended Kalman filter," *Journal of Power Sources*, vol. 296, pp. 400–412, 2015.

[14]   A. Bizeray, "State and Parameter Estimation of Physics-Based Lithium-ion Battery Models," PhD thesis, University of Oxford, 2016.

[15]   M. Broussely, S. Herreyre, P. Biensan, P. Kasztejna, K. Nechev, and R. J. Staniewicz, "Aging mechanism in Li ion cells and calendar life predictions," *Journal of Power Sources*, vol. 97-98, pp. 13–21, 2001.

[16]   J. Brédas, J. M. Buriak, F. Caruso, *et al.*, "An electrifying choice for the 2019 Chemistry Nobel prize: Goodenough, Whittingham, and Yoshino," *Chemistry of Materials*, vol. 31, no. 21, pp. 8577–8581, 2019.

[17]   H. S. Carslaw and J. C. Jaeger, *Conduction of heat in solids*. Clarendon P, 1959.

[18]   J. Christensen and J. Newman, "A mathematical model for the lithium-ion negative electrode solid electrolyte interphase," *Journal of The Electrochemical Society*, vol. 151, no. 11, A1977–A1988, 2004.

[19]   J. Christensen and J. Newman, "Cyclable Lithium and Capacity Loss in Li-Ion Cells," *Journal of The Electrochemical Society*, vol. 152, no. 4, A818, 2005.

[20]   A. M. Colclasure, K. A. Smith, and R. J. Kee, "Modeling detailed chemistry and transport for solid-electrolyte-interface (SEI) films in Li–ion batteries," *Electrochimica Acta*, vol. 58, no. 1, pp. 33–43, 2011.

[21]   M. Doyle, T. F. Fuller, and J. Newman, "Modeling of galvanostatic charge and discharge of the lithium/polymer/insertion cell," *Journal of the Electrochemical society*, vol. 140, no. 6, pp. 1526–1533, 1993.

[22]   M. Ecker, S. Käbitz, I. Laresgoiti, and D. U. Sauer, "Parameterization of a physico-chemical model of a lithium-ion battery: II. Model validation," *Journal of The Electrochemical Society*, vol. 162, no. 9, A1849–A1857, 2015.

[23]   M. Farag, H. Sweity, M. Fleckenstein, and S. Habibi, "Combined electrochemical, heat generation, and thermal model for large prismatic lithium-ion batteries in real-time applications," *Journal of Power Sources*, vol. 360, pp. 618–633, 2017.

[24] R. Fong, U. Von Sacken, and J. R. Dahn, "Studies of lithium intercalation into carbons using nonaqueous electrochemical cells," *Journal of The Electrochemical Society*, vol. 137, no. 7, p. 2009, 1990.

[25] R. E. Gerver and J. P. Meyers, "Three-dimensional modeling of electrochemical performance and heat generation of lithium-ion batteries in tabbed planar configurations," *Journal of The Electrochemical Society*, vol. 158, no. 7, A835, 2011.

[26] M. Guo, G. Sikha, and R. E. White, "Single-particle model for a lithium-ion cell: Thermal behavior," *Journal of The Electrochemical Society*, vol. 158, no. 2, A122–A132, 2011.

[27] X. Han, M. Ouyang, L. Lu, and J. Li, "Simplification of physics-based electrochemical model for lithium ion battery on electric vehicle. Part II: Pseudo-two-dimensional model simplification and state of charge estimation," *Journal of Power Sources*, vol. 278, pp. 814–825, 2015.

[28] A. C. Hindmarsh, "The PVODE and IDA algorithms," Lawrence Livermore National Lab., CA (US), Tech. Rep., 2000.

[29] A. C. Hindmarsh, P. N. Brown, K. E. Grant, S. L. Lee, R. Serban, D. E. Shumaker, and C. S. Woodward, "SUNDIALS: Suite of nonlinear and differential/algebraic equation solvers," *ACM Transactions on Mathematical Software (TOMS)*, vol. 31, no. 3, pp. 363–396, 2005.

[30] E. Hosseinzadeh, R. Genieser, D. Worwood, A. Barai, J. Marco, and P. Jennings, "A systematic approach for electrochemical-thermal modelling of a large format lithium-ion battery for electric vehicle application," *Journal of Power Sources*, vol. 382, pp. 77–94, 2018.

[31] X. Hu, S. Li, and H. Peng, "A comparative study of equivalent circuit models for Li-ion batteries," *Journal of Power Sources*, vol. 198, pp. 359–367, 2012.

[32] I. A. Hunt, Y. Zhao, Y. Patel, and G. J. Offer, "Surface cooling causes accelerated degradation compared to tab cooling for lithium-ion pouch cells," *Journal of The Electrochemical Society*, vol. 163, no. 9, A1846–A1852, 2016.

[33] C. Inc., *COMSOL multiphysics reference manual, version 5.4*, 2018.

[34] F. P. Incropera, D. P. DeWitt, T. L. Bergman, and A. S. Lavine, *Fundamentals of heat and mass transfer*. John Wiley & Sons, 2007.

[35] P. Keil, S. F. Schuster, J. Wilhelm, J. Travi, A. Hauser, R. C. Karl, and A. Jossen, "Calendar aging of lithium-ion batteries," *Journal of The Electrochemical Society*, vol. 163, no. 9, A1872, 2016.

[36] P. Kemper and D. Kum, "Extended single particle model of li-ion batteries towards high current applications," in *Vehicle Power and Propulsion Conference (VPPC)*, IEEE, 2013, pp. 1–6.

[37]   G. H. Kim, J. Gonder, J. Lustbader, and A. Pesaran, "Thermal management of batteries in advanced vehicles using phase-change materials," *World Electric Vehicle Journal*, vol. 2, no. 2, pp. 46–59, 2008.

[38]   G. H. Kim, K. Smith, K. J. Lee, S. Santhanagopalan, and A. Pesaran, "Multi-domain modeling of lithium-ion batteries encompassing multi-physics in varied length scales," *Journal of The Electrochemical Society*, vol. 158, no. 8, A955, 2011.

[39]   T. L Kirk, J. Evans, C. P. Please, and S. J. Chapman, "Modelling electrode heterogeneity in lithium-ion batteries: Unimodal and bimodal particle-size distributions," *arXiv preprint*, vol. arXiv, p. 2006.12208, 2020.

[40]   S. Kosch, Y. Zhao, J. Sturm, J. Schuster, G. Mulder, E. Ayerbe, and A. Jossen, "A computationally efficient multi-scale model for lithium-ion cells," *Journal of The Electrochemical Society*, vol. 165, no. 10, A2374–A2388, 2018.

[41]   X. Lai, Y. Zheng, and T. Sun, "A comparative study of different equivalent circuit models for estimating state-of-charge of lithium-ion batteries," *Electrochimica Acta*, vol. 259, pp. 566–577, 2018.

[42]   K. J. Lee, K. Smith, A. Pesaran, and G. H. Kim, "Three dimensional thermal-, electrical-, and electrochemical-coupled model for cylindrical wound large format lithium-ion batteries," *Journal of Power Sources*, vol. 241, pp. 20–32, 2013.

[43]   D. Li, D. Danilov, Z. Zhang, H. Chen, Y. Yang, and P. H. L. Notten, "Modeling the SEI-formation on graphite electrodes in LiFePO4 batteries," *Journal of the Electrochemical Society*, vol. 162, no. 6, A858–A869, 2015.

[44]   L. Liu, J. Park, X. Lin, A. M. Sastry, and W. Lu, "A thermal-electrochemical model that gives spatial-dependent growth of solid electrolyte interphase in a li-ion battery," *Journal of Power Sources*, vol. 268, pp. 482–490, 2014.

[45]   P. Lu and S. J. Harris, "Lithium transport within the solid electrolyte interphase," *Electrochemistry Communications*, vol. 13, no. 10, pp. 1035–1037, 2011.

[46]   P. Lu, C. Li, E. W. Schneider, and S. J. Harris, "Chemistry, impedance, and morphology evolution in solid electrolyte interphase films during formation in lithium ion batteries," *Journal of Physical Chemistry C*, vol. 118, no. 2, pp. 896–903, 2014.

[47]   B. Malengier, P. Kišon, J. Tocknell, C. Abert, F. Bruckner, and M. A. Bisotti, "ODES: A high level interface to ODE and DAE solvers," *The Journal of Open Source Software*, vol. 3, no. 22, p. 165, 2018.

[48] S. G. Marquis, V. Sulzer, R. Timms, C. P. Please, and S. J. Chapman, "An asymptotic derivation of a single particle model with electrolyte," *Journal of The Electrochemical Society*, vol. 166, no. 15, A3693–A3706, 2019.

[49] S. G. Marquis, R. Timms, V. Sulzer, C. P. Please, and S. J. Chapman, "A suite of reduced-order models of a single-layer lithium-ion pouch cell," *arXiv preprint*, vol. arXiv, p. 2008.03691, 2020, (Submitted to Journal of The Electrochemical Society).

[50] R. N. Methekar, V. Ramadesigan, J. C. Pirkle, and V. R. Subramanian, "A perturbation approach for consistent initialization of index-1 explicit differential-algebraic equations arising from battery model simulations," *Computers and Chemical Engineering*, vol. 35, no. 11, pp. 2227–2234, 2011.

[51] S. J. Moura, *FastDFN*, GitHub repository, 2016, (github.com/scott-moura/fastDFN).

[52] S. J. Moura, F. B. Argomedo, R. Klein, A. Mirtabatabaei, and M. Krstic, "Battery state estimation for a single particle model with electrolyte dynamics," *IEEE Transactions on Control Systems Technology*, vol. 25, no. 2, pp. 453–468, 2017.

[53] I. R. Moyles, M. G. Hennessy, T. G. Myers, and B. R. Wetton, "Asymptotic reduction of a porous electrode model for lithium-ion batteries," *SIAM Journal on Applied Mathematics*, vol. 79, no. 4, pp. 1528–1549, 2019.

[54] J. Newman, *DUALFOIL*, 2014, (www.cchem.berkeley.edu/jsngrp/fortran.html).

[55] J. Newman and K. E. Thomas-Alyea, *Electrochemical systems*. John Wiley & Sons, 2012.

[56] P. W. C. Northrop, M. Pathak, D. Rife, S. De, S. Santhanagopalan, and V. R. Subramanian, "Efficient simulation and model reformulation of two-dimensional electrochemical thermal behavior of lithium-ion batteries," *Journal of the Electrochemical Society*, vol. 162, no. 6, A940–A951, 2015.

[57] E. P. Office, *Greg Clark announces Faraday Institution*, EPSRC, Ed., 2017, (epsrc.ukri.org/newsevents/news/faradayinstitution/).

[58] K. K. Patel, J. M. Paulsen, and J. Desilvestro, "Numerical simulation of porous networks in relation to battery electrodes and separators," *Journal of Power Sources*, vol. 122, no. 2, pp. 144–152, 2003.

[59] E. Peled, "The electrochemical behavior of alkali and alkaline earth metals in nonaqueous battery systems—the solid electrolyte interphase model," *Journal of The Electrochemical Society*, vol. 126, no. 12, p. 2047, 1979.

[60] D. Pelzer, D. Ciechanowicz, and A. Knoll, "Energy arbitrage through smart scheduling of battery energy storage considering battery degradation and electricity price forecasts," *Innovative Smart Grid Technologies-Asia (ISGT-Asia), 2016 IEEE*, pp. 472–477, 2016.

[61] H. E. Perez, X. Hu, and S. J. Moura, "Optimal charging of batteries via a single particle model with electrolyte and thermal dynamics," in *American Control Conference (ACC)*, 2016, pp. 4000–4005.

[62] S. B. Peterson, J. Apt, and J. F. Whitacre, "Lithium-ion battery cell degradation resulting from realistic vehicle and vehicle-to-grid utilization," *Journal of Power Sources*, vol. 195, no. 8, pp. 2385–2392, 2010.

[63] M. B. Pinson and M. Z. Bazant, "Theory of SEI formation in rechargeable batteries: Capacity fade, accelerated aging and lifetime prediction," *Journal of the Electrochemical Society*, vol. 160, no. 2, A243–A250, 2012.

[64] G. L. Plett, *Battery management systems, Volume I: Battery modeling*. Artech House, 2015.

[65] G. L. Plett, *Battery management systems, Volume II: Equivalent-circuit methods*. Artech House, 2015.

[66] H. J. Ploehn, P. Ramadass, and R. E. White, "Solvent diffusion model for aging of lithium-ion battery cells," *Journal of The Electrochemical Society*, vol. 151, no. 3, A456–A462, 2004.

[67] E. Prada, D. Di Domenico, Y. Creff, J. Bernard, V. Sauvant-Moynot, and F. Huet, "Simplified electrochemical and thermal model of LiFePO4-graphite Li-ion batteries for fast charge applications," *Journal of The Electrochemical Society*, vol. 159, no. 9, A1508–A1519, 2012.

[68] S. K. Rahimian, S. Rayman, and R. E. White, "Extension of physics-based single particle model for higher charge–discharge rates," *Journal of Power Sources*, vol. 224, pp. 180–194, 2013.

[69] P. Ramadass, B. Haran, P. M. Gomadam, R. White, and B. N. Popov, "Development of first principles capacity fade model for Li-ion cells," *Journal of the Electrochemical Society*, vol. 151, no. 2, A196–A203, 2004.

[70] R. Ranom, "Mathematical modelling of lithium ion batteries," PhD thesis, University of Southampton, 2014.

[71] J. M. Reniers, G. Mulder, and D. A. Howey, "Review and performance comparison of mechanical-chemical degradation models for lithium-ion batteries," *Journal of The Electrochemical Society*, vol. 166, no. 14, A3189–A3200, 2019.

[72] J. M. Reniers, G. Mulder, S. Ober-Blöbaum, and D. A. Howey, "Improving optimal control of grid-connected lithium-ion batteries through more accurate battery and degradation modelling," *Journal of Power Sources*, vol. 379, pp. 91–102, 2018.

[73] G. Richardson, G. Denuault, and C. P. Please, "Multiscale modelling and analysis of lithium-ion battery charge and discharge," *Journal of Engineering Mathematics*, vol. 72, no. 1, pp. 41–72, 2012.

[74] G. Richardson and J. R. King, "Time-dependent modelling and asymptotic analysis of electrochemical cells," *Journal of Engineering Mathematics*, vol. 59, no. 3, pp. 239–275, 2007.

[75] G. Richardson, I. Korotkin, R. Ranom, M. Castle, and J. M. Foster, "Generalised single particle models for high-rate operation of graded lithium-ion electrodes: Systematic derivation and validation," *Electrochimica Acta*, vol. 339, p. 135 862, 2020.

[76] F. Röder, S. Sonntag, D. Schröder, and U. Krewer, "Simulating the impact of particle size distribution on the performance of graphite electrodes in lithium-ion batteries," *Energy Technology*, vol. 4, no. 12, pp. 1588–1597, 2016.

[77] A. Romero-Becerril and L. Alvarez-Icaza, "Comparison of discretization methods applied to the single-particle model of lithium-ion batteries," *Journal of Power Sources*, vol. 196, no. 23, pp. 10 267–10 279, 2011.

[78] A. Seaman, T. S. Dao, and J. McPhee, "A survey of mathematics-based equivalent-circuit and electrochemical battery models for hybrid and electric vehicle simulation," *Journal of Power Sources*, vol. 256, pp. 410–423, 2014.

[79] S. Shi, P. Lu, Z. Liu, Y. Qi, L. G. Hector Jr, H. Li, and S. J. Harris, "Direct calculation of Li-ion transport in the solid electrolyte interphase," *Journal of the American Chemical Society*, vol. 134, no. 37, pp. 15 476–15 487, 2012.

[80] S. Shi, Y. Qi, H. Li, and L. G. Hector, "Defect thermodynamics and diffusion mechanisms in Li2CO3 and implications for the solid electrolyte interphase in Li-ion batteries," *The Journal of Physical Chemistry C*, vol. 117, no. 17, pp. 8579–8593, 2013.

[81] F. Single, B. Horstmann, and A. Latz, "Revealing SEI morphology: In-depth analysis of a modeling approach," *Journal of The Electrochemical Society*, vol. 164, no. 11, E3132–E3145, 2017.

[82] F. Single, A. Latz, and B. Horstmann, "Identifying the mechanism of continued growth of the solid–electrolyte interphase," *ChemSusChem*, vol. 11, no. 12, pp. 1950–1955, 2018.

[83] K. Smith, Y. Shi, and S. Santhanagopalan, "Degradation mechanisms and lifetime prediction for lithium-ion batteries; A control perspective," in *American Control Conference (ACC)*, 2015, pp. 728–730.

[84]   V. Sulzer, "Mathematical Modelling of Lead-Acid Batteries," PhD thesis, University of Oxford, 2019.

[85]   V. Sulzer, S. J. Chapman, C. P. Please, D. A. Howey, and C. W. Monroe, "Faster lead-acid battery simulations from porous-electrode theory: Part II. asymptotic analysis," *Journal of The Electrochemical Society*, vol. 166, no. 12, A2372, 2019.

[86]   V. Sulzer, S. G. Marquis, R. Timms, M. Robinson, and S. J. Chapman, "Python Battery Mathematical Modelling (PyBaMM)," *ECSarXiv*, vol. 7, 2020, (Submitted to the Journal of Open Research Software).

[87]   M. Tang, S. Lu, and J. Newman, "Experimental and Theoretical Investigation of Solid-Electrolyte-Interphase Formation Mechanisms on Glassy Carbon," *Journal of the Electrochemical Society*, vol. 159, no. 11, A1775–A1785, 2012.

[88]   T. R. Tanim, C. D. Rahn, and C. Y. Wang, "A temperature dependent, single particle, lithium ion cell model including electrolyte diffusion," *Journal of Dynamic Systems, Measurement, and Control*, vol. 137, no. 1, p. 011 005, 2015.

[89]   T. R. Tanim, C. D. Rahn, and C. Y. Wang, "State of charge estimation of a lithium ion cell based on a temperature dependent and electrolyte enhanced single particle model," *Energy*, vol. 80, pp. 731–739, 2015.

[90]   R. Timms, S. G. Marquis, I. Korotkin, V. Sulzer, G. Richardson, R. Ranom, M. Castle, J. M. Foster, C. P. Please, and S. J. Chapman, "Corrigendum to "generalised single particle models for high-rate operation of graded lithium-ion electrodes: Systematic derivation and validation"[electrochimica acta 339 (2020) 135862]," *Electrochimica Acta*, vol. 351, p. 136 371, 2020.

[91]   R. Timms, S. G. Marquis, V. Sulzer, C. P. Please, and S. J. Chapman, "Asymptotic reduction of a lithium-ion pouch cell model," *arXiv preprint*, vol. arXiv, p. 2005.05127, 2020, (Submitted to SIAM).

[92]   T. G. Tranter, R. Timms, T. Heenan, *et al.*, "Probing heterogeneity in li-ion batteries with coupled multiscale models of electrochemistry and thermal transport using tomographic domains," *Journal of The Electrochemical Society*, vol. 167, no. 11, p. 110 538, 2020.

[93]   P. Verma, P. Maire, and P. Novák, "A review of the features and analyses of the solid electrolyte interphase in Li-ion batteries," *Electrochimica Acta*, vol. 55, no. 22, pp. 6332–6341, 2010.

[94]   J. Vetter, P. Novák, M. R. Wagner, C. Veit, K. C. Möller, J. O. Besenhard, M. Winter, M. Wohlfahrt-Mehrens, C. Vogler, and a. Hammouche, "Ageing mechanisms in lithium-ion batteries," *Journal of Power Sources*, vol. 147, no. 1-2, pp. 269–281, 2005.

[95] P. Virtanen, R. Gommers, T. E. Oliphant, M. Haberland, T. Reddy, D. Cournapeau, E. Burovski, P. Peterson, W. Weckesser, J. Bright, *et al.*, "SciPy 1.0: Fundamental Algorithms for Scientific Computing in Python," *Nature Methods*, vol. 17, pp. 261–272, 2020.

[96] C. P. Wang, S. D. Lopatin, R. Z. Bachrach, and G. Sikha, *Graded electrode technologies for high energy lithium-ion batteries, US Patent App. 12/953,143*, 2011.

[97] W. Y. Xuan, *Lithium-ion batteries: solid-electrolyte interphase*. World Scientific, 2004.